2008

Probability density methods for modeling local and global aspects of intracellular calcium signaling

G. S. Blair Williams
College of William & Mary - Arts & Sciences

Probability Density Methods for Modeling Local and Global Aspects of
Intracellular Calcium Signaling

George S. B. Williams

Staunton, Virginia

Master of Science, The College of William & Mary, 2005
Master of Arts, The College of William & Mary, 2003
Bachelor of Science, The College of William & Mary, 2001

A Dissertation presented to the Graduate Faculty
of the College of William and Mary in Candidacy for the Degree of
Doctor of Philosophy
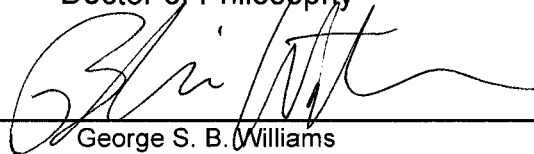
Department of Applied Science

The College of William & Mary
May, 2008

APPROVAL PAGE

This Dissertation is submitted in partial fulfillment of
the requirements for the degree of

Doctor of Philosophy

George S. B. Williams

Approved by the Committee, April, 2008

Committee Chair
Gregory D. Smith, The College of William & Mary

Carey K. Bagdassarian, The College of William & Mary

Eric L. Bradley, The College of William & Mary

Eric A. Sobie, Mount Sinai School of Medicine

ABSTRACT PAGE

Considerable insight into intracellular calcium (Ca) responses has been obtained through the development of whole cell models that are based on molecular mechanisms, e.g., the kinetics of intracellular Ca channels and the feedback of Ca upon these channels. However, a limitation of most deterministic whole cell models to date is the assumption that channels are globally coupled by a single [Ca], when in fact channels experience localized "domain" Ca concentrations. More realistic stochastic Monte Carlo simulations are capable of representing individual domain Ca concentrations but suffer from increased computational demand. This dissertation introduces a novel probability approach which captures important aspects of local Ca signaling while improving computational efficiency.

In many cell types calcium release is mediated by diffusely distributed 1,4,5-trisphosphate receptors (IP3Rs). In Chapter 2 a Monte Carlo whole cell model is presented where each IP3R has a local cytosolic and luminal domain [Ca]. The Monte Carlo model is used to validate a probability density approach where local cytosolic and luminal domains Ca concentrations are represented as bivariate probability densities jointly distributed with IP3R state. Using this probability density approach, analysis shows that the time scale of Ca domain formation and collapse (both cytosolic and luminal) influences global Ca oscillations. Additionally, two reduced models of Ca signaling are derived that are valid when there is a separation of time scales between the stochastic gating of IP3Rs and the dynamics of domain Ca. These reduced whole cell models account for the influence of local Ca signaling on global Ca dynamics and are therefore more realistic than other conventional deterministic whole cell models.

In cardiac myocytes, Ca influx through voltage gated channels causes the release of intracellular Ca, a process known as Ca -induced Ca release (CICR). In Chapter 3 a probability density approach to CICR is derived from advection-reaction equations relating the time-dependent probability density of subsarcolemmal subspace and junctional sarcoplasmic reticulum [Ca] conditioned on "Ca release unit" state. When these equations are coupled to ordinary differential equations for the bulk myoplasmic and sarcoplasmic reticulum [Ca], a realistic but minimal whole cell model is produced. Modeling Ca release unit activity using this probability density approach avoids the computationally demanding task of resolving spatial aspects of global Ca signaling, while accurately representing heterogeneous local Ca signals in a population of diadic subspaces and junctional sarcoplasmic reticulum domains. The probability density approach is validated and benchmarked for computational efficiency by comparison to traditional Monte Carlo simulations. However, a probability density calculation can be significantly faster than the corresponding Monte Carlo simulation, especially when cellular parameters are such that univariate rather than multivariate probability densities may be employed.

Expanding upon the computational advantages of the probability density approach, a moment closure technique is introduced in Chapter 4 which facilitates whole cell modeling of cardiac myocytes when the dynamics of subspace [Ca] are much faster than those of junctional SR [Ca]. The method begins with the derivation of a system of ODEs describing the time-evolution of the moments of the univariate probability density functions for junctional SR [Ca] jointly distributed with CaRU state. This open system of ODEs is then closed using an algebraic relationship that expresses the third moment of junctional SR [Ca] in terms of the first and second moments. Benchmark simulations indicate that the moment closure approach is nearly 10,000-times more computationally efficient than corresponding Monte Carlo simulations while leading to nearly identical results.

Contents

Acknowledgments

I acknowledge all of the individuals who have supported me during my tenure at the College of William & Mary. Specifically, I thank Gregory D. Smith who has been an invaluable advisor during my doctoral work. I would also like to thank my Master's thesis advisor, Carey K. Bagdassarian, without whom my graduate career might not have been possible.

I also acknowledge my parents who have encouraged me throughout my life as I strive to achieve my goals. I am extremely grateful for my occasionally annoying friends and colleagues – Ronald A. Quinlan, Jeffrey R. Groff, M. Drew LaMar, and Marco A. Huertas – who have contributed substantially to my achievements. I especially thank Hilary DeRemigio who has been a resolute supporter and an important factor in my success.

This dissertation would not have been possible without the assistance and valuable input from our collaborators, M. Saleet Jafri and Eric A. Sobie. I would also like to acknowledge Marco A. Huertas for his work in the development of the moment closure technique presented in Chapter 4.

The work contained within this manuscript was funded by the National Science Foundation under Grants No. 0133132 and 0443843.

List of Tables

List of Figures

Chapter 1

Introduction

Calcium (Ca^{2+}) is a divalent cation essential to living organisms. In vertebrates, Ca^{2+} plays an important role in the formation and maintenance of bones and teeth. Calcium is also a ubiquitous second messenger responsible for such vital tasks as adhesion, fertilization, cell differentiation, and muscle contraction [Berridge, 1998, Berridge, 1993]. One reason that calcium is such a versatile second messenger is that cells are able to decode information from the spatial and temporal dimensions, and amplitude of Ca^{2+} signals in multiple dimensions (e.g., space, time, and amplitude) [Berridge, 1998, Berridge et al., 2000]. Cells have evolved the ability to mix and tune these Ca^{2+} signals to suit their physiology using a "toolkit" comprised of various signaling, regulatory, and sensory mechanisms [Berridge et al., 2000, Berridge et al., 2003].

The fertilization of mammalian oocytes involves Ca^{2+} waves crossing the egg following sperm entry [Whitaker, 2006]. Following fertilization, when the one-cell embryo is ready to divide, a single Ca^{2+} transient triggers the division into two daughter cells. During development and throughout life, both gene activation and transcription are known to be sensitive to the amplitude and duration of Ca^{2+} signals [Berridge, 1998, Dolmetsch et al., 1997]. In neurons, Ca^{2+} is responsible for triggering the re-

1

lease of neurotransmitters by binding with the synaptic vesicle protein Synaptotagmin I [Fernández-Chacón et al., 2001, Burgoyne and Morgan, 1998]. Cellular metabolism is influenced by Ca^{2+} since mitochondria rely on cytosolic Ca^{2+} signals to tune their metabolic activity [Hajnóczky et al., 1995].

In muscle cells, Ca^{2+} governs the cycle of contraction and relaxation [Bers, 2002, Wier, 1990]. Action potentials trigger the cell-wide release of intracellular Ca^{2+} which then binds to troponin C to produce a conformational change in the greater troponin complex. This conformational change allows the myosin motor protein to bind to actin and initiate muscle contraction. Localized Ca^{2+} signals can however produce completely different results. For example, in smooth muscle cells, Ca^{2+} sparks located just under the plasma membrane cause the cell to relax by activating potassium (K^+) channels [Berridge, 1998]. Temporal aspects of Ca^{2+} release are also important for muscle cells. In cardiac myocytes, dys-synchronous release of Ca^{2+} can cause pathological phenomena such as alternans and arrhythmias [Wilson et al., 2006, Dibb et al., 2007, Jiang et al., 2007, Chelu and Wehrens, 2007].

Just as Ca^{2+} is essential for cell life, it can also be a signal for cell death. In addition to being toxic to the cell at high levels for long periods, Ca^{2+} can also initiate the process of programmed cell death (apoptosis). Apoptosis aids in the formation of various tissue patterns during normal development and also plays a role in diseased conditions such as cancer, AIDS, and Alzheimer's [Berridge, 1998]. Calcium's exact function in apoptosis is complex, however, calcium is known to initiate cell death in response to various pathological conditions (for more information see [Berridge et al., 2000]).

1.1 Calcium homeostasis

Ca^{2+} homeostasis – the regulation of a stable intracellular $[Ca^{2+}]$ – would be impossible without the presence of semipermeable lipid bilayers that constitute the cell's outer and inner membranes. This barrier contains a wide variety of biological molecules but primarily consists of proteins and lipids. Phospholipids (typically the most common constituent of cell membranes) consist of a hydrophilic, polar head and a non-polar, hydrophobic tail. It is the polar head group which makes the membrane impermeable to charged molecules and ions such as Ca^{2+}. Since Ca^{2+} cannot freely pass across membranes the cell can use them to create $[Ca^{2+}]$ gradients. For example, the endoplasmic reticulum (ER), a continuous membrane-delimited intracellular compartment, contains levels of Ca^{2+} several fold greater than the cytosol.

The Ca^{2+} concentrations found inside the cell are regulated by numerous processes, usually consisting of a membrane bound protein actively or passively moving Ca^{2+} ions. There are three main types of proteins involved in the transport of Ca^{2+}: channels, pumps, and exchangers. Ca^{2+} channels are typically an assembly of several sub-unit proteins which combine to form a "pore" through the plane of the membrane. Often passage of ions through these pores is regulated by a "gate" which may be opened or closed by chemical or electrical signals, temperature, or mechanical force, depending on the type of channel. For example, the ryanodine receptor calcium channel (RyR) is activated by a chemical signal (Ca^{2+}) while the dihydropyridine receptor calcium channel (DHPR) is activated by a depolarization of the plasma membrane.

Pumps and exchangers act to balance the passive transport of ion channels. Pumps act by using energy from a variety of sources, including adenosine 5'-triphosphate (ATP), to drive the flow of ions against their concentration gradient. For example, the plasma membrane Ca^{2+}-ATPase (PMCA) which resides on the cell's outer membrane acts to move Ca^{2+} ions from cytosol to the extracellular space. Another important

Ca^{2+} pump is the sarco-endoplasmic reticulum Ca^{2+}-ATPase (SERCA) which resides on the ER/SR membrane and transfers Ca^{2+} from the cytosol to the space contained within the ER/SR membrane known as the lumen.

Similar to pumps, exchangers also act to drive ions against their concentration gradient. However, instead of using an energy source such as ATP, an exchanger uses the energy from the electrochemical gradient of another ion. For example, the sodium-calcium exchanger (NCX) located on the plasma membrane allows three sodium (Na^+) ions to flow down their electrochemical gradient into cell in exchange for the extrusion a single Ca^{2+} ion from the cell.

Because prolonged exposure to elevated Ca^{2+} concentrations can be toxic or even fatal to cells, the previously mentioned pumps, channels and exchangers are tuned to maintain the proper Ca^{2+} homeostasis. Typically, cytosolic $[Ca^{2+}]$ is between 10 - 100 nM, noticeably lower than the 1 - 2 mM $[Ca^{2+}]$ outside the cell and the 10 - 1000 μM $[Ca^{2+}]$ within intracellular Ca^{2+} reservoirs, such as the endoplasmic reticulum (ER) or in muscle cells the sarcoplasmic reticulum (SR) [Hille, 2001]. Figure 1.1 shows the typical cellular compartments and various components of the Ca^{2+} signaling "toolkit" discussed above.
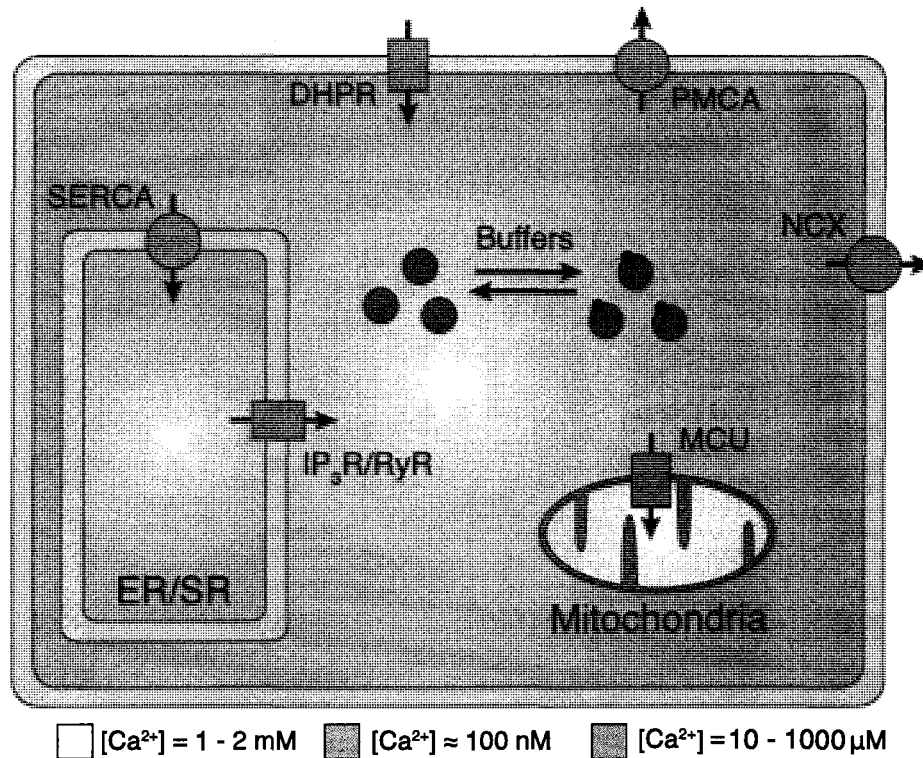
Figure 1.1: Diagram of typical intracellular Ca^{2+} signaling components. Entry of Ca^{2+} into the cell is through store operated or voltage gated Ca^{2+} channels such as the dihydropyridine receptor (DHPR). Ca^{2+} entry into the cell is balanced by the removal of Ca^{2+} via the plasma membrane Ca^{2+}-ATPase (PMCA) pump and sodium-calcium exchanger (NCX). Intracellular release is typically mediated by inositol 1,4,5-trisphosphate receptors (IP$_3$R) and ryanodine receptors (RyR). Ca^{2+} is resequestered to the ER/SR by the sarco-endoplasmic reticulum Ca^{2+}-ATPase (SERCA) pump. Ca^{2+} entry into the mitochondria is mediated by the mitochondrial Ca^{2+} uniporter (MCU) which is currently thought to be a highly selective ion channel [Kirichok et al., 2004].

1.2 Calcium induced calcium release

As a common second messenger, Ca^{2+} regulates many different types of ion channels in both excitable and non-excitable cells. The release of calcium from intracellular stores is regulated primarily by two types of Ca^{2+}-activated Ca^{2+} channels; inositol 1,4,5-trisphosphate receptors (IP_3R) and ryanodine receptors (RyR) [Fill and Copello, 2002, Bezprozvanny, 2005, Foskett et al., 2007b]. IP_3R's name is derived from its ability to bind with the co-agonist, inositol 1,4,5-trisphosphate (IP_3). IP_3 is generated from phosphatidylinositol 4,5-bisphosphate (PIP_2) by the action of the membrane bound enzyme phospholipase C (PLC) [Berridge, 1998]. IP_3Rs can be activated by either IP_3, Ca^{2+}, or both. RyRs are so named due to their affinity for the poisonous plant alkaloid ryanodine which was the first agonist used in the purification of RyR ion channel. Unlike IP_3, ryanodine is not naturally found in vertebrate cells and therefore does not play an important role in normal Ca^{2+} signaling. The process of Ca^{2+} activating IP_3Rs or RyRs to release intracellular Ca^{2+} is commonly referred to as calcium-induced calcium release (CICR).

Both the IP_3R and the RyR families contain three major isoforms differing only slightly in their genetic makeup. The RyR family is slightly larger at 560 kDa versus IP_3R's 310 kDa [Lai et al., 1989, Foskett et al., 2007a]. IP_3Rs are expressed in a wide range of cell types but are most abundant in neurons located in the cerebellum, a region of the brain responsible for the integration of sensory perception and motor control. RyRs are predominantly found in muscle cells and in the brain [Berridge, 1998, Murayama and Ogawa, 1996].

Both IP_3Rs and RyRs are known to co-localize at Ca^{2+} release sites on the ER and SR membranes. For example, in the cortical regions (approximately 6 μm below the plasma membrane) of immature *Xenopus laevis* oocytes, IP_3Rs occur in clusters of 5–50 with inter-cluster spacing on the order of a few microns [Sun et al., 1998]. Similarly, intracellular Ca^{2+} release in skeletal and cardiac myocytes is mediated by clusters

of RyRs that are assembled into clusters of 10-100 cooperatively gating channels [Franzini-Armstrong et al., 1999, Bers, 2002, Wang et al., 2004, Chen-Izu et al., 2006]. The spatial organization of IP$_3$Rs and RyRs is the basis of three distinct modes of Ca^{2+} mobilization that have been observed via confocal microfluorimetry in oocytes, cardiomyocytes, and many other cell types: 1) localized Ca^{2+} elevations due to the activation of single channels that are referred to as Ca^{2+} blips or quarks depending on whether the event is mediated by IP$_3$Rs or RyRs [Niggli, 1999, Bootman et al., 1997], 2) Ca^{2+} puffs and sparks that arise from the activation of multiple channels associated with a single Ca^{2+} release site [Cheng et al., 1993a, Cannell et al., 1995a, Yao et al., 1995, Parker et al., 1996], and 3) global responses such as oscillations and waves that involve multiple release sites [Dupont et al., 1991a, Dupont and Goldbeter, 1992a, Dupont and Goldbeter, 1994, Cheng et al., 1996]. These three modes of Ca^{2+} release have been dubbed fundamental, elementary, and global responses, respectively [Berridge, 1997a].

Global Ca^{2+} signals involve the coordinated activation of many elementary release events. These global responses such as oscillations and waves are important for governing cellular processes [Berridge et al., 2003]. For this reason, accurately capturing the influence of local Ca^{2+} signaling on global Ca^{2+} dynamics is an important aspect to any whole cell model of Ca^{2+} signaling.

1.3 Mathematical modeling of calcium signaling

There is a long history of modeling the activity of ion channels as continuous time discrete state Markov chains [Colquhoun, 1995]. While these channel models can be relatively simple (as few as two states) or complex (hundreds of states), most include only two calcium conductance levels (closed or open). For example, consider the simplest possible single channel model, that is, a two-state model with one closed ($\mathcal{C}$)

and one open ($\mathcal{O}$) state

$$\text{(closed)} \quad \mathcal{C} \quad \underset{k^-}{\overset{k^+ c_{cyt}}{\rightleftharpoons}} \quad \mathcal{O} \quad \text{(open)} \tag{1.1}$$
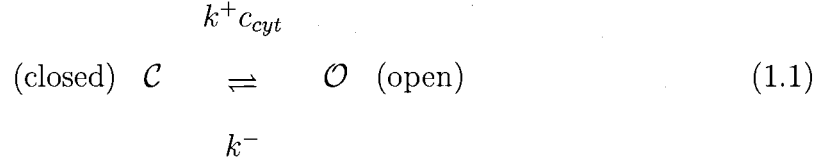
where $k^+ c_{cyt}$ and k^- are transition rates with units of reciprocal time, k^+ is an association rate constant with units of $\text{conc}^{-1}\,\text{time}^{-1}$, and c_{cyt} is the $[\text{Ca}^{2+}]$ experienced by the channel.

If a large number of these two-state Ca^{2+} channels are coupled only via the bulk cytosolic $[\text{Ca}^{2+}]$ the fraction of open channels would solve

$$\frac{d\pi_{\mathcal{O}}}{dt} = k^+ c_{cyt} \pi_{\mathcal{C}} - k^- \pi_{\mathcal{O}} \tag{1.2}$$

where conservation of probability would dictate that $\pi_{\mathcal{C}} = 1 - \pi_{\mathcal{O}}$. By coupling this ordinary differential equation (ODE) for the fraction of open channels to balance equations for the cytosolic and ER calcium concentrations, we may write a simple two-compartment whole cell model as

$$\frac{dc_{cyt}}{dt} = J_{rel} - J_{pump} \tag{1.3}$$

$$\frac{dc_{er}}{dt} = \frac{1}{\lambda_{er}} \left[-J_{rel} + J_{pump} \right] \tag{1.4}$$

where λ_{er} is the ER to cytosolic volume ratio, $J_{rel} = \pi_{\mathcal{O}}(c_{er} - c_{cyt})$ represents the release of calcium through the intracellular Ca^{2+} channels (IP_3R or RyR), and the restorative pump flux (such as the SERCA pump) may be represented by

$$J_{pump} = \frac{v_{pump} c_{cyt}^2}{c_{cyt}^2 + k_{pump}^2}. \tag{1.5}$$

Deterministic models of calcium signaling (such as the simple one presented above)

neglect the stochastic gating of Ca^{2+} channels as well as the important aspects of local Ca^{2+} signaling upon these channels. As the importance of the stochastic gating of ion channels was realized Monte Carlo simulation techniques were implemented to capture local Ca^{2+} signaling phenomena (for review see [Swillens et al., 1998, Stern et al., 1999b, Rice et al., 1999a, Sobie et al., 2002b]). Unfortunately these more realistic Monte Carlo simulations are computationally intensive and impractical, especially when the spatial location of intracellular channels is explicitly represented.

This dissertation focuses on presenting new classes of whole cell models of Ca^{2+} signaling which incorporate the important aspects of localized Ca^{2+} domains and stochastic gating of individual channels. We begin by introducing probability density approaches to modeling Ca^{2+} dynamics in cells with stochastically gating intracellular Ca^{2+} channels. We utilize coupled advection-reaction equations for the time-evolution of the probability density of the $[Ca^{2+}]$ in localized Ca^{2+} domains associated with each channel and conditioned on the channel state. When these equations are coupled to ODEs for the bulk Ca^{2+} concentrations, a realistic but minimal model of whole cell Ca^{2+} dynamics is produced that accurately captures the influence of localized $[Ca^{2+}]$ elevations on channel gating. In Chapter 2 the probability density approach is shown to yield insights into local and global Ca^{2+} signaling in cells with diffusely distributed IP_3Rs. In Chapter 3 we show an application of the probability density approach for cardiac myocytes where calcium-induced calcium release (an important step in cell contraction) is known to occur in restricted spaces located just beneath the plasma membrane.

In Chapter 4 we expand upon the computational advantages of the probability density approaches by introducing a moment closure technique for simulating whole cell models of cardiac myocytes when the dynamics of subspace $[Ca^{2+}]$ are much faster than those of junctional SR $[Ca^{2+}]$. The method begins with the derivation of a system of ODEs describing the time-evolution of the moments of the univariate

9

probability density functions for junctional SR [Ca^{2+}] jointly distributed with CaRU state. This open system of ODEs is then closed using an algebraic relationship that expresses the third moment of junctional SR [Ca^{2+}] in terms of the first and second moments. Finally, Chapter 5 reviews the scientific contributions of this dissertation and suggests areas of future work.

Chapter 2

Modeling local and global intracellular calcium responses mediated by diffusely distributed inositol 1,4,5-trisphosphate receptors

2.1 Summary

Considerable insight into intracellular Ca^{2+} responses has been obtained through the development of whole cell models that are based on molecular mechanisms, e.g., single channel kinetics of the inositol 1,4,5-trisphosphate (IP_3) receptor Ca^{2+} channel. However, a limitation of most whole cell models to date is the assumption that IP_3 receptor Ca^{2+} channels (IP_3Rs) are globally coupled by a "continuously stirred" bulk cytosolic $[Ca^{2+}]$, when in fact open IP_3Rs experience elevated "domain" Ca^{2+} concentrations. Here we present a $2N+2$-compartment whole cell model of local and global

Ca^{2+} responses mediated by $N=100,000$ diffusely distributed IP$_3$Rs, each represented by a four-state Markov chain. Two of these compartments correspond to bulk cytosolic and luminal Ca^{2+} concentrations, and the remaining $2N$ compartments represent time-dependent cytosolic and luminal Ca^{2+} domains associated with each IP$_3$R. Using this Monte Carlo model as a starting point, we present an alternative formulation that solves a system of advection-reaction equations for the probability density of cytosolic and luminal domain [Ca^{2+}] jointly distributed with IP$_3$R state. When these equations are coupled to ODEs for the bulk cytosolic and luminal [Ca^{2+}], a realistic but minimal model of whole cell Ca^{2+} dynamics is produced that accounts for the influence of local Ca^{2+} signaling on channel gating and global Ca^{2+} responses. The probability density approach is benchmarked and validated by comparison to Monte Carlo simulations, and the two methods are shown to agree when the number of Ca^{2+} channels is large (i.e., physiologically realistic). Using the probability density approach, we show that the time scale of Ca^{2+} domain formation and collapse (both cytosolic and luminal) may influence global Ca^{2+} oscillations, and we derive two reduced models of global Ca^{2+} dynamics that account for the influence of local Ca^{2+} signaling on global Ca^{2+} dynamics when there is a separation of time scales between the stochastic gating of IP$_3$Rs and the dynamics of domain Ca^{2+}.

2.2 Introduction

Regenerative Ca^{2+} release from the endoplasmic reticulum (ER) or sarcoplasmic reticulum (SR) is muscle cells is a continuous membrane-delimited intracellular compartment, plays an important role in Ca^{2+} signaling [Berridge, 1993, Berridge, 1997b]. In most cell types, the ER has integrative and regenerative properties analogous to the excitable membranes of neurons [Berridge, 1998, Li et al., 1995, Keizer et al., 1995]. For example, agonist-induced Ca^{2+} signaling in pituitary gonadotrophs is initiated by metabotropic receptors of the plasma membrane that stimulate the production of the intracellular messenger, inositol 1,4,5-trisphosphate (IP_3) [Li and Rinzel, 1994]. IP_3 in turn promotes Ca^{2+} release from intracellular stores by binding and activating IP_3 receptor Ca^{2+} channels (IP_3Rs) located on the ER membrane. In rat basophilic leukemia (RBL) cells, an experimental model for mucosal mast cells, cross-linking the high-affinity immunoglobulin E receptor ($Fc_\epsilon R1$) with multivalent antigen leads to tyrosine kinase-dependent activation of PLC_γ, production of IP_3, release of intracellular Ca^{2+} stores, and a sustained phase of Ca^{2+} influx—events that culminate in the secretion of histamine, serotonin, and other mediators of inflammation [Wilson et al., 1998, Smith, 1996]. In cardiac myocyte excitation-contraction (EC) coupling, membrane depolarization associated with the cardiac action potential causes L-type Ca^{2+} channels to open, and Ca^{2+} influx through these channels activates ryanodine receptors (RyRs) located on the sarcoplasmic reticulum (SR) membrane, a process known as Ca^{2+}-induced Ca^{2+} release (CICR).

Whole cell models of intracellular Ca^{2+} signaling are usually Hodgkin-Huxley-like systems of nonlinear ordinary differential equations (ODEs). Such models have played a role in understanding ER Ca^{2+} excitability and oscillations in gonadotrophs, RBL cells, cardiac myocytes, and other cell types [Dupont et al., 1991b, Dupont and Goldbeter, 1992b, Li et al., 1995, Keizer et al., 1995, Winslow et al., 2000] (see [Smith et al., 2002] for review). For example, two-compartment whole cell models often take

the form

$$\frac{dc_{cyt}}{dt} = J_{rel} + J_{leak} - J_{pump} \tag{2.1}$$

$$\frac{dw}{dt} = \frac{w_{\infty} - w}{\tau_w} \tag{2.2}$$

$$\frac{dc_{er}}{dt} = -\frac{1}{\lambda_{er}} \left[J_{rel} + J_{leak} - J_{pump} \right] \tag{2.3}$$

where λ_{er} is the ER-to-cytosolic effective volume ratio that accounts for the binding capacity of Ca^{2+} buffers. The three fluxes influencing the $[Ca^{2+}]$ in the cytosol (c_{cyt}) and ER (c_{er}) include: Ca^{2+} release via IP_3Rs,

$$J_{rel} = v_{rel} f_{open} \left(c_{er} - c_{cyt} \right), \tag{2.4}$$

a passive leak from the ER to cytosol,

$$J_{leak} = v_{leak} \left(c_{er} - c_{cyt} \right), \tag{2.5}$$

and Ca^{2+} reuptake via SERCA-type Ca^{2+}-ATPases,

$$J_{pump} = \frac{v_{pump} c_{cyt}^2}{c_{cyt}^2 + k_{pump}^2}. \tag{2.6}$$

In this traditional whole cell model, w is a Hodgkin-Huxley-like gating variable satisfying a first order kinetic equation (Eq. 2.2). For example, in the Li-Rinzel reduction of the DeYoung-Keizer IP_3R model [Young and Keizer, 1992, Li and Rinzel, 1994], the variable w represents the fraction of IP_3Rs that are *not* inactivated, $w_{\infty}(c_{cyt})$ and $\tau_w(c_{cyt})$ are both functions of the cytosolic $[Ca^{2+}]$, and $f_{open}(w, c_{cyt})$ is the fraction of open IP_3Rs. By numerically integrating conventional whole cell models such as Eqs. 2.1–2.6, one may simulate Ca^{2+} release and reuptake by IP_3-sensitive intracellular Ca^{2+} stores.

While considerable insight has been obtained through the analogy of plasma mem-

brane electrical excitability and ER Ca^{2+} excitability, the disparity between electrical length scales (100–200 μm) and the range of action of intracellular Ca^{2+} (i.e., a *chemical* length scale of 1–2 μm) suggests that some aspects of the analogy are strained [Neher, 1986, Allbritton et al., 1992, Zador and Koch, 1994, Smith, 1996, Smith et al., 1996, Smith et al., 1998, Neher, 1998b, Neher, 1998a, Naraghi and Neher, 1997, Smith et al., 2001]. In particular, the ODE for the gating variable representing IP_3R inactivation (Eq. 2.2) is an "average rate equation" [Smith, 2002b] that is derived by assuming a large number of intracellular Ca^{2+} channels are globally coupled via bulk cytosolic Ca^{2+} (c_{cyt}). While it is true that plasma membrane ion channels in a small cell experience essentially the same time-course of membrane voltage, intracellular Ca^{2+} channels experience radically different local $[Ca^{2+}]$, even during global Ca^{2+} responses, and clusters of IP_3Rs are in fact only *locally* coupled via the buffered diffusion of intracellular Ca^{2+}. For this reason, the Hodgkin-Huxley-style average rate equation (Eq. 2.2) is not always appropriate.

Indeed, mathematical and computational investigations of excitation-contraction coupling in cardiac myocytes have suggested that whole cell models such as Eqs. 2.1–2.6 are not suitable for simulating CICR release during EC coupling because the release flux is a collection of discrete "Ca^{2+} sparks" evoked by local, rather than global, increases in $[Ca^{2+}]$ [Cheng et al., 1993c]. That is, different groups of RyRs experience different local Ca^{2+} concentrations and stochastically gate in a manner that depends on whether nearby sarcolemmal Ca^{2+} channels have recently been open or closed. One consequence of this "local control" [Stern, 1992b] mechanism of cardiac CICR is that deterministic "common pool" models—whole cell models in which all RyRs in a myocyte experience the same bulk $[Ca^{2+}]$—fail to reproduce several important experimental observations. In particular, the high gain and positive feedback of common pool models ensures that Ca^{2+} is released in an all-or-none fashion [Jafri et al., 1998b, Glukhovsky et al., 1998b, Snyder et al., 2000b, Nordin, 1993b, Tang and

Othmer, 1994b] as opposed to being graded with the amount of Ca^{2+} influx, as observed in numerous experiments [Fabiato, 1985b, Wier et al., 1994b, Cannell et al., 1995c]. More complex and realistic models of EC coupling *are* able to simulate graded Ca^{2+} release mechanistically by treating L-type Ca^{2+} channels and Ca^{2+} release sites as stochastic "Ca^{2+} release units" (CaRUs), each of which is associated with its own diadic subspace [Ca^{2+}]. When activated spontaneously or through membrane depolarization these CaRUs may deplete Ca^{2+} stored in localized regions of junctional SR and, on a slower time scale, interact with one another via diffusion of Ca^{2+} within the network SR and bulk myoplasm [Stern, 1992b, Rice et al., 1999b, Sobie et al., 2002b, Greenstein and Winslow, 2002b, Williams et al., 2007].

Even in cells where intracellular Ca^{2+} channels are not clustered, but rather diffusely distributed, the range of action of intracellular Ca^{2+} may invalidate the conventional whole cell modeling approach (Eqs. 2.1–2.6). Because high concentrations of intraluminal Ca^{2+} can reduce IP_3R activity as measured in planar lipid bilayer experiments [Bezprozvanny and Ehrlich, 1994], it has been suggested that the Ca^{2+} inactivation of open IP_3Rs may be mediated by elevated domain Ca^{2+}, similar to Ca^{2+}-mediated inactivation of voltage-gated plasma membrane Ca^{2+} channels [Sherman et al., 1990a, Smith, 2002b]. In a study of agonist-induced Ca^{2+} oscillations in pituitary gonadotrophs [Li and Rinzel, 1994, Li et al., 1995], investigators were forced to modify Eq. 2.2 in a *post hoc* fashion to account for enhanced IP_3R inactivation (mediated by elevated domain Ca^{2+}) that was required for the persistence of Ca^{2+} oscillations in gonadotrophs at low ER [Ca^{2+}]. Theoretical studies suggest that the dynamics of cytosolic Ca^{2+} domains and luminal depletion domains may significantly affect the stochastic gating of Ca^{2+}-regulated intracellular Ca^{2+} channels [Mazzag et al., 2005b, Huertas and Smith, 2007a]. However, to date there has been little exploration of feasible whole cell modeling approaches that account for the influence of local Ca^{2+} signaling on the stochastic gating of diffusely distributed channels and

resulting global Ca^{2+} responses.

Following prior work on local control of excitation-contraction coupling in cardiac myocytes [Williams et al., 2007], we here present a $2N+2$-compartment whole cell model of local and global Ca^{2+} responses mediated by N=100,000 diffusely distributed IP$_3$Rs, each represented by a four-state Markov chain. Two of these compartments correspond to bulk cytosolic and luminal [Ca^{2+}], and the remaining $2N$ compartments represent time-dependent cytosolic and luminal Ca^{2+} domains associated with each IP$_3$R. Using this Monte Carlo model as a starting point, we present an alternative formulation that solves coupled advection-reaction equations for the probability density of cytosolic and luminal domain [Ca^{2+}] jointly distributed with IP$_3$R state. When these equations are coupled to ODEs for the bulk cytosolic and luminal [Ca^{2+}], a realistic but minimal model of whole cell Ca^{2+} dynamics is produced that accounts for the influence of local Ca^{2+} signaling on channel gating and global Ca^{2+} responses.

The remainder of this paper is organized as follows. In Section 2.3 we describe the formulation of the Monte Carlo and probability density whole cell models that account for the effect of local Ca^{2+} signals on diffusely distributed IP$_3$Rs on global Ca^{2+} dynamics. In Sections 2.4.1–2.4.3 the probability density approach is benchmarked and validated by comparison to traditional Monte Carlo simulations of whole cell Ca^{2+} oscillations, and the two approaches are shown to agree when the number of Ca^{2+} channels is large (i.e., physiologically realistic). Section 2.4.4 uses the probability density approach to show how the time scale of Ca^{2+} domain formation and collapse (both cytosolic and luminal) may influence global Ca^{2+} oscillations. We conclude with a derivation of two reduced models of global Ca^{2+} dynamics that account for the influence of local Ca^{2+} signaling on global Ca^{2+} dynamics when there is a separation of time scales between the stochastic gating of IP$_3$Rs and the dynamics of domain Ca^{2+} (Section 2.4.5).

2.3   Model Formulation

A whole cell model of local and global Ca^{2+} dynamics with luminal and cytosolic Ca^{2+} domains associated with each IP_3R can be simulated using a traditional Monte Carlo approach where the domains and bulk Ca^{2+} concentrations solve a large number of ODEs coupled to a Markov chain representing the stochastically gating channels (see Section 2.3.1). An alternative method is to solve a system of partial differential equations for probability density functions representing the distribution of cytosolic and luminal domain Ca^{2+} concentrations jointly distributed with the state of each channel (see Section 2.3.2). Since many of the equations and parameters are similar for the two formulations, we begin by presenting the traditional Monte Carlo approach.

2.3.1   Whole cell model of local and global calcium signaling — Monte Carlo formulation

Fig. 2.1 shows a diagram of the model with $2N+2$ compartments: the bulk cytosolic compartment, the bulk ER compartment, and $2N$ domains (cytosolic and luminal) associated with each IP_3R. The bulk cytosolic and ER Ca^{2+} concentrations are denoted by c_{cyt} and c_{er}, respectively. Each IP_3R has a corresponding cytosolic Ca^{2+} domain $(c_{cyt}^{d,n})$ and luminal Ca^{2+} domain $(c_{er}^{d,n})$, where the superscript n is an index over all N IP_3Rs.
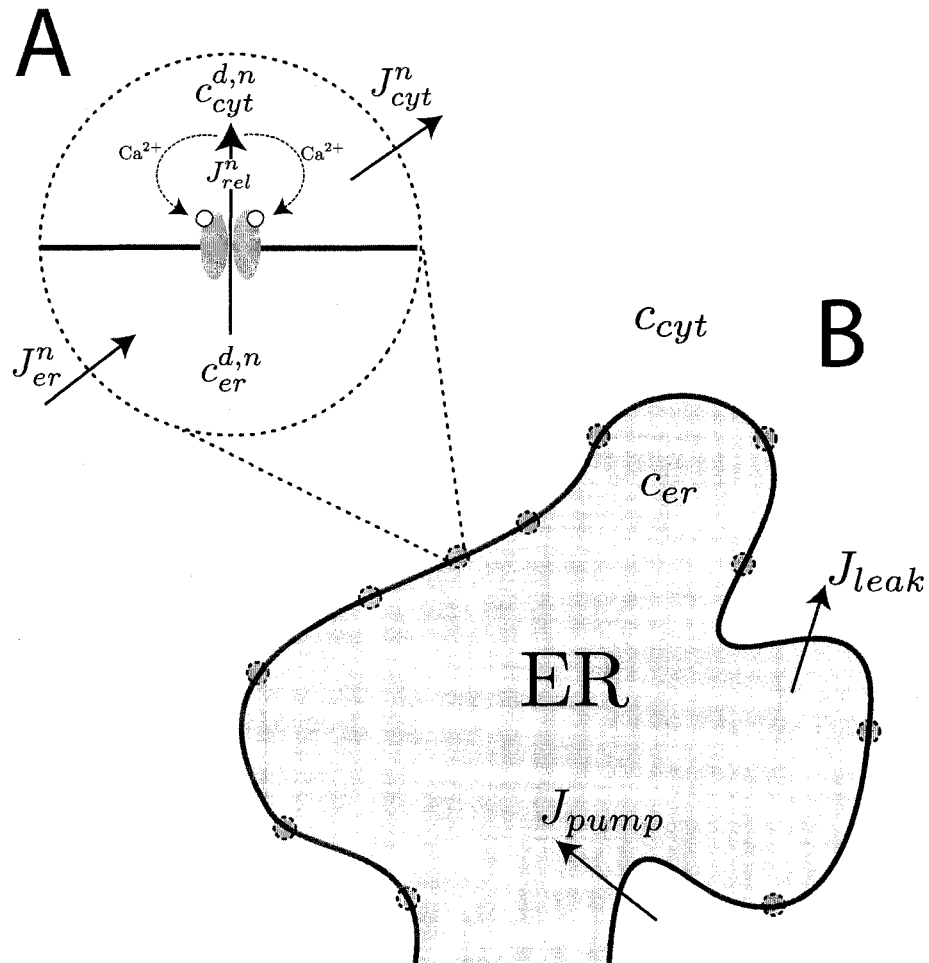
Figure 2.1: Diagram of the $2N+2$-compartment Monte Carlo model. A) Local Ca^{2+} signaling near an individual IP_3R includes the diffusion fluxes (J_{er}^n and J_{cyt}^n) and the release flux (J_{rel}^n) that are functions of the cytosolic and luminal domain $[Ca^{2+}]$ denoted by $c_{cyt}^{d,n}$ and $c_{er}^{d,n}$. B) Section of ER membrane with diffusely distributed IP_3Rs. The restorative flux from SERCA pumps (J_{pump}) and the passive leak from the ER to the cytosol (J_{leak}) are functions of the bulk cytosolic and bulk ER $[Ca^{2+}]$ (c_{cyt} and c_{er}).

2.3.1.1 A four-state IP_3R model

We use a minimal four-state Markov chain model for the stochastically gating IP$_3$Rs given by [Colquhoun and Hawkes, 1995, Smith, 2002a, Nguyen and Jafri, 2005],

$$
\begin{array}{ccccc}
& & k_b^+ (c_{cyt}^d)^\eta & & \\
\text{(open)} \quad \mathcal{O} & \rightleftharpoons & & \mathcal{R}_1 & \text{(refractory)} \\
& k_b^- & & & \\
k_a^+ (c_{cyt}^d)^\eta \ \uparrow\downarrow \ k_a^- & & k_c^- \ \downarrow\uparrow \ k_c^+ (c_{cyt}^d)^\eta & & \hspace{2cm} (2.7) \\
& k_d^- & & & \\
\text{(closed)} \quad \mathcal{C} & \rightleftharpoons & & \mathcal{R}_2 & \text{(refractory)} \\
& k_d^+ (c_{cyt}^d)^\eta & & &
\end{array}
$$
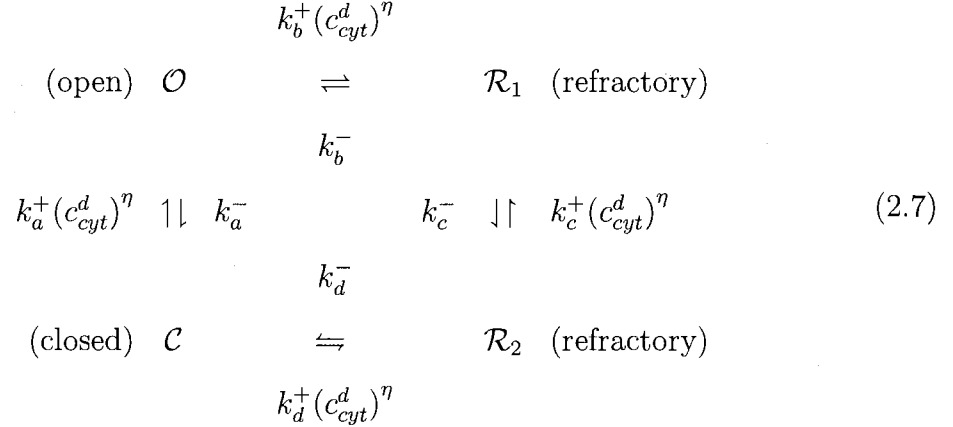
where upward transitions represent Ca^{2+}-mediated activation and rightward transitions represent Ca^{2+}-mediated inactivation (the cooperativity of Ca^{2+} binding is $\eta = 2$). The dynamics of fast Ca^{2+} activation and slower Ca^{2+} inactivation in this model is similar to the well-known DeYoung-Keizer IP$_3$R model, although for simplicity we do not explicitly model IP$_3$ binding or the subunit structure of the tetrameric channel as in [Young and Keizer, 1992]. We denote the state of the nth IP$_3$R at time t by $S^n(t) \in \{\mathcal{C}, \mathcal{O}, \mathcal{R}_1, \mathcal{R}_2\}$ and the number of channels in state i at time t as $N_i(t)$ where $i \in \{\mathcal{C}, \mathcal{O}, \mathcal{R}_1, \mathcal{R}_2\}$.

2.3.1.2 Ca^{2+} concentration balance equations

The time evolution of [Ca^{2+}] in each compartment and domain are modeled by a set of $2N+2$ ordinary differential equations,

$$
\frac{dc_{cyt}}{dt} = J_{cyt}^T + J_{leak} - J_{pump} \tag{2.8}
$$

$$
\frac{dc_{er}}{dt} = \frac{1}{\lambda_{er}} \left(-J_{er}^T - J_{leak} + J_{pump} \right) \tag{2.9}
$$

$$\frac{dc_{cyt}^{d,n}}{dt} = \frac{1}{\lambda_{cyt}^d} \left(J_{rel}^n - J_{cyt}^n \right) \tag{2.10}$$

$$\frac{dc_{er}^{d,n}}{dt} = \frac{1}{\lambda_{er}^d} \left(-J_{rel}^n + J_{er}^n \right), \tag{2.11}$$

where $1 \leq n \leq N$, N is the number of IP$_3$Rs (each with an associated cytosolic and luminal domain), $J_{cyt}^T = \sum_{n=1}^{N} J_{cyt}^n$, and $J_{er}^T = \sum_{n=1}^{N} J_{er}^n$. The effective volume ratios λ_{er}, λ_{cyt}^d, and λ_{er}^d in Eqs. 2.9–2.11 are defined with respect to the bulk cytosolic volume (V_{myo}), that is, $\lambda_{er} = V_{er}/V_{myo}$ and

$$\lambda_{cyt}^d = \frac{V_{cyt}^d}{V_{myo}} \quad \text{and} \quad \lambda_{er}^d = \frac{V_{er}^d}{V_{myo}}$$

where V_{er}, V_{cyt}^d and V_{er}^d are the effective volumes of the bulk ER, an individual cytosolic domain, and an individual luminal domain, respectively. Note that when the total volumes of the cytosolic ($V_{cyt}^{d,T}$) and luminal ($V_{er}^{d,T}$) domains are held constant, for any choice of N we can write $\lambda_{cyt}^d = \Lambda_{cyt}^d/N$ and $\lambda_{er}^d = \Lambda_{er}^d/N$ where

$$\Lambda_{cyt}^d = \frac{V_{cyt}^{d,T}}{V_{myo}} \quad \text{and} \quad \Lambda_{er}^d = \frac{V_{er}^{d,T}}{V_{myo}}. \tag{2.12}$$

Thus, λ_{er}, Λ_{cyt}^d, and Λ_{er}^d are the three effective volume ratios required for the model formulation (see Table 2.1).

2.3.1.3 Description of Ca^{2+} fluxes

The fluxes in Eqs. 2.8–2.11 include the leak from the ER to the bulk cytosol (J_{leak}) and the restorative flux of SR Ca^{2+}-ATPases (J_{pump}) given by

$$J_{leak} = v_{leak} \left(c_{er} - c_{cyt} \right) \tag{2.13}$$

$$J_{pump} = \frac{v_{pump}(c_{cyt})^2}{(k_{pump})^2 + (c_{cyt})^2}. \tag{2.14}$$

The release of Ca^{2+} through IP$_3$Rs (J_{rel}^n) is given by

$$J_{rel}^n = \gamma^n v_{rel} \left(c_{er}^{d,n} - c_{cyt}^{d,n} \right) \tag{2.15}$$

where γ^n indicates whether the nth channel is open ($\gamma^n = 1$ when $S^n \in \{\mathcal{O}\}$) or closed ($\gamma^n = 0$ when $S^n \in \{\mathcal{C}, \mathcal{R}_1, \mathcal{R}_2\}$), the rate v_{rel} is proportional to the IP$_3$R conductance, and the driving force is given by the difference between the luminal ($c_{er}^{d,n}$) and cytosolic ($c_{cyt}^{d,n}$) domain Ca^{2+} concentrations. The domains are coupled to the bulk compartments via the fluxes J_{cyt}^n and J_{er}^n in Eqs. 2.10–2.11 given by

$$J_{cyt}^n = v_{cyt} \left(c_{cyt}^{d,n} - c_{cyt} \right) \tag{2.16}$$

$$J_{er}^n = v_{er} \left(c_{er} - c_{er}^{d,n} \right) \tag{2.17}$$

where v_{cyt}/λ_{cyt}^d is the rate of cytosolic domain collapse and v_{er}/λ_{er}^d is the rate of luminal domain recovery [Huertas and Smith, 2007a]. Note that when Eqs. 2.15–2.17 are substituted into Eqs. 2.10–2.11 one obtains

$$\frac{dc_{cyt}^{d,n}}{dt} = \frac{1}{\lambda_{cyt}^d} \left[\gamma^n v_{rel} \left(c_{er}^{d,n} - c_{cyt}^{d,n} \right) - v_{cyt} \left(c_{cyt}^{d,n} - c_{cyt} \right) \right]$$

$$\frac{dc_{er}^{d,n}}{dt} = \frac{1}{\lambda_{er}^d} \left[-\gamma^n v_{rel} \left(c_{er}^{d,n} - c_{cyt}^{d,n} \right) + v_{er} \left(c_{er} - c_{er}^{d,n} \right) \right].$$

If we multiply and divide the right hand sides of these equations by N we can write

$$\frac{dc_{cyt}^{d,n}}{dt} = \frac{1}{\Lambda_{cyt}^d} \left[\gamma^n v_{rel}^T \left(c_{er}^{d,n} - c_{cyt}^{d,n} \right) - v_{cyt}^T \left(c_{cyt}^{d,n} - c_{cyt} \right) \right]$$

$$\frac{dc_{er}^{d,n}}{dt} = \frac{1}{\Lambda_{er}^d} \left[-\gamma^n v_{rel}^T \left(c_{er}^{d,n} - c_{cyt}^{d,n} \right) + v_{er}^T \left(c_{er} - c_{er}^{d,n} \right) \right],$$

where we use the previously defined aggregate effective volume ratios (Eq. 2.12) as well as the aggregate rates $v_{rel}^T = N v_{rel}$, $v_{cyt}^T = N v_{cyt}$, and $v_{er}^T = N v_{er}$. Thus, we see that concentration balance equations for the Ca^{2+} domains ($c_{cyt}^{d,n}$ and $c_{er}^{d,n}$) do not depend on the number of IP$_3$Rs (N) when fixed aggregate rate constants (v_{rel}^T, v_{cyt}^T, and v_{re}^T) and volume ratios (Λ_{cyt}^d, and Λ_{er}^d) are employed. Nevertheless, the choice of N in simulations of the Monte Carlo model (Eqs. 2.8–2.11) has profound consequences on the dynamics of the bulk Ca^{2+} concentrations c_{cyt} and c_{er} (see below).

2.3.2 Whole cell model of local and global calcium signaling — probability density formulation

The probability density approach is an alternative to Monte Carlo simulation that is valid when the number of IP$_3$Rs (N) is large. We begin by defining continuous multivariate probability density functions for the cytosolic domain [Ca^{2+}] ($\tilde{c}_{cyt}^d$) and luminal domain [Ca^{2+}] ($\tilde{c}_{er}^d$) jointly distributed with IP$_3$R state, $\tilde{S}(t)$ [Mazzag et al., 2005b, Huertas and Smith, 2007a] as

$$
\begin{aligned}
\rho^i(c_{cyt}^d, c_{er}^d, t)\, dc_{cyt}^d\, dc_{er}^d = \mathsf{P}\{ c_{cyt}^d < \tilde{c}_{cyt}^d < c_{cyt}^d + dc_{cyt}^d \\
\text{and } c_{er}^d < \tilde{c}_{er}^d < c_{er}^d + dc_{er}^d \\
\text{and } \tilde{S}(t) = i\}
\end{aligned}
\tag{2.18}
$$

where the index $i \in \{\mathcal{C}, \mathcal{O}, \mathcal{R}_1, \mathcal{R}_2\}$ runs over the four states of the channel (see Eq. 2.7) and in this section the tildes on $\tilde{c}_{cyt}^d(t)$, $\tilde{c}_{er}^d(t)$, and $\tilde{S}(t)$ indicate random quantities. If the meaning of Eq. 2.18 is not obvious, it may be helpful to imagine performing a Monte Carlo simulation as described in the previous section with a very large number of IP$_3$Rs. At any time t one could randomly sample an IP$_3$R from this population to produce an instance of the jointly distributed random variables $\tilde{S}(t)$, $\tilde{c}_{cyt}^d(t)$, and $\tilde{c}_{er}^d(t)$, corresponding to the current state of the sampled IP$_3$R and

the cytosolic and luminal domain Ca^{2+} concentrations associated with this channel. The quantity $\rho^i(c_{cyt}^d, c_{er}^d, t)\, dc_{cyt}^d\, dc_{er}^d$ defined in Eq. 2.18 represents the probability of finding this sampled channel in state i with cytosolic domain $[Ca^{2+}]$ in the range $[c_{cyt}^d, c_{cyt}^d + dc_{cyt}^d]$ and luminal domain $[Ca^{2+}]$ in the range $[c_{er}^d, c_{er}^d + dc_{er}^d]$, provided the total number of IP$_3$Rs in the Monte Carlo simulation is very large.

As discussed in 2.6.1, for the multivariate probability densities of Eq. 2.18 to be consistent with the dynamics of the Monte Carlo model in the previous section, they must satisfy the following system of advection-reaction equations [Mazzag et al., 2005b, Huertas and Smith, 2007a, Gardiner, 2004, Kepler and Elston, 2001]

$$\frac{\partial \rho^{\mathcal{C}}}{\partial t} = -\frac{\partial}{\partial c_{cyt}^d}\left[f_{cyt}^{\mathcal{C}}\rho^{\mathcal{C}}\right] - \frac{\partial}{\partial c_{er}^d}\left[f_{er}^{\mathcal{C}}\rho^{\mathcal{C}}\right] \tag{2.19}$$

$$- k_a^+(c_{cyt}^d)^\eta \rho^{\mathcal{C}} - k_d^+(c_{cyt}^d)^\eta \rho^{\mathcal{C}} + k_a^- \rho^{\mathcal{O}} + k_d^- \rho^{\mathcal{R}_2}$$

$$\frac{\partial \rho^{\mathcal{O}}}{\partial t} = -\frac{\partial}{\partial c_{cyt}^d}\left[f_{cyt}^{\mathcal{O}}\rho^{\mathcal{O}}\right] - \frac{\partial}{\partial c_{er}^d}\left[f_{er}^{\mathcal{O}}\rho^{\mathcal{O}}\right] \tag{2.20}$$

$$+ k_a^+(c_{cyt}^d)^\eta \rho^{\mathcal{C}} - k_a^- \rho^{\mathcal{O}} - k_b^+(c_{cyt}^d)^\eta \rho^{\mathcal{O}} + k_b^- \rho^{\mathcal{R}_1}$$

$$\frac{\partial \rho^{\mathcal{R}_1}}{\partial t} = -\frac{\partial}{\partial c_{cyt}^d}\left[f_{cyt}^{\mathcal{R}_1}\rho^{\mathcal{R}_1}\right] - \frac{\partial}{\partial c_{er}^d}\left[f_{er}^{\mathcal{R}_1}\rho^{\mathcal{R}_1}\right] \tag{2.21}$$

$$+ k_b^+(c_{cyt}^d)^\eta \rho^{\mathcal{O}} - k_b^- \rho^{\mathcal{R}_1} - k_c^- \rho^{\mathcal{R}_1} + k_c^+(c_{cyt}^d)^\eta \rho^{\mathcal{R}_2}$$

$$\frac{\partial \rho^{\mathcal{R}_2}}{\partial t} = -\frac{\partial}{\partial c_{cyt}^d}\left[f_{cyt}^{\mathcal{R}_2}\rho^{\mathcal{R}_2}\right] - \frac{\partial}{\partial c_{er}^d}\left[f_{er}^{\mathcal{R}_2}\rho^{\mathcal{R}_2}\right] \tag{2.22}$$

$$+ k_d^+(c_{cyt}^d)^\eta \rho^{\mathcal{C}} + k_c^- \rho^{\mathcal{R}_1} - k_d^- \rho^{\mathcal{R}_2} - k_c^+(c_{cyt}^d)^\eta \rho^{\mathcal{R}_2}$$

where the advection rates $f_{cyt}^{\mathcal{C}}$, $f_{cyt}^{\mathcal{O}}$, $\cdots$, $f_{er}^{\mathcal{R}_2}$ are functions of c_{cyt}^d and c_{er}^d that can be read off from the ordinary differential equations for the cytosolic and luminal domain $[Ca^{2+}]$. Consistent with Eqs. 2.10 and 2.11 these advection rates are

$$f_{cyt}^i = \frac{1}{\Lambda_{cyt}^d}\left(J_{rel}^T - J_{cyt}^T\right) \tag{2.23}$$

$$f_{er}^i = \frac{1}{\Lambda_{er}^d} \left(J_{er}^T - J_{rel}^T \right) \tag{2.24}$$

where $i \in \{\mathcal{C}, \mathcal{O}, \mathcal{R}_1, \mathcal{R}_2\}$. Equations 2.23 and 2.24 include three fluxes that may influence the cytosolic and luminal $[\text{Ca}^{2+}]$ and, consistent with Eqs. 2.15–2.17, these are given by

$$J_{rel}^T = \gamma^i v_{rel}^T \left[c_{er}^d - c_{cyt}^d \right] \tag{2.25}$$

$$J_{cyt}^T = v_{cyt}^T \left[c_{cyt}^d - c_{cyt}(t) \right] \tag{2.26}$$

$$J_{er}^T = v_{er}^T \left[c_{er}(t) - c_{er}^d \right], \tag{2.27}$$

where γ^i indicates whether the Ca^{2+} channel is closed ($\gamma^{\mathcal{C}} = \gamma^{\mathcal{R}_1} = \gamma^{\mathcal{R}_2} = 0$) or open ($\gamma^{\mathcal{O}} = 1$). Note that the rate constants v_{rel}^T, v_{cyt}^T, and v_{er}^T in Eqs. 2.25–2.27 are aggregate quantities and the parameter N representing the number of IP$_3$Rs does not occur in the probability density formulation. As discussed above, in Monte Carlo simulations with finite N we always choose $v_{rel} = v_{rel}^T/N$, $v_{cyt} = v_{cyt}^T/N$, $v_{er} = v_{er}^T/N$ so that the Monte Carlo simulation converges to the probability density result as N increases (see Section 2.4.2)

The advection terms in Eqs. 2.19–2.22 involving partial derivatives with respect to c_{cyt}^d and c_{er}^d correspond to the deterministic dynamics of the cytosolic and luminal domain Ca^{2+} that depend on IP$_3$R state via γ^i (Eq. 2.15). Conversely, the reaction terms in Eqs. 2.19–2.22 correspond to the stochastic gating of the four-state IP$_3$R model whose transition rates are presented above (Eq. 2.7). That is, IP$_3$R gating moves probability from one joint probability density to another in a manner that may $[k_a^+(c_{cyt}^d)^\eta, \ k_b^+(c_{cyt}^d)^\eta,$ etc.$]$ or may not $[k_a^-, \ k_b^-,$ etc.$]$ depend on the cytosolic domain $[\text{Ca}^{2+}]$.

It is important to note that the functional form of the fluxes J_{cyt}^T and J_{er}^T occurring in Eqs. 2.23 and 2.24 involve the bulk cytosolic and luminal Ca^{2+} concentrations denoted by $c_{cyt}(t)$ and $c_{er}(t)$ in Eqs. 2.26 and 2.27. These bulk Ca^{2+} concentrations

satisfy ODEs that are similar in form to the concentration balance equations used in the Monte Carlo approach (Eqs. 2.8 and 2.9),

$$\frac{dc_{cyt}}{dt} = J^*_{cyt} + J_{leak} - J_{pump} \tag{2.28}$$

$$\frac{dc_{er}}{dt} = \frac{1}{\lambda_{er}} \left(-J^*_{er} - J_{leak} + J_{pump} \right) \tag{2.29}$$

where J_{leak} and J_{pump} are as in Eqs. 2.13 and 2.14, but here J^*_{cyt} and J^*_{er} are functionals of the probability densities $[\rho^i(c^d_{cyt}, c^d_{er}, t)]$ governed by Eqs. 2.19–2.22, that is,

$$J^*_{cyt} = \int_0^\infty \int_0^\infty J^T_{cyt}(c^d_{cyt}, t) \rho^T(c^d_{cyt}, c^d_{er}, t) dc^d_{cyt} dc^d_{er} \tag{2.30}$$

$$J^*_{er} = \int_0^\infty \int_0^\infty J^T_{er}(c^d_{er}, t) \rho^T(c^d_{cyt}, c^d_{er}, t) dc^d_{cyt} dc^d_{er} \tag{2.31}$$

where $\rho^T(c^d_{cyt}, c^d_{er}, t) = \rho^{\mathcal{C}} + \rho^{\mathcal{O}} + \rho^{\mathcal{R}_1} + \rho^{\mathcal{R}_2}$ is the probability distribution of the cytosolic and luminal [Ca^{2+}] irrespective of IP$_3$R state, and the double integrals account for all possible values of domain Ca^{2+}.

2.3.3 Summary of model formulation

The Monte Carlo and probability density formulations of a whole cell model of local and global Ca^{2+} signaling are similar; for example, the equations governing the dynamics of the bulk cytosol and bulk ER are closely related (compare Eqs. 2.8–2.9 to Eqs. 2.28–2.29). However, these two approaches differ greatly in how they represent the cytosolic and luminal Ca^{2+} domains associated with each IP$_3$R. For the traditional Monte Carlo approach each domain is modeled via one ODE resulting in a total of $2N$ ODEs (Eqs. 2.10–2.11), while the probability density approach uses four time-dependent mulitvariate probability densities for the cytosolic and lu-

minal domain $[Ca^{2+}]$ jointly distributed with IP$_3$R state (Eq. 2.18). A set of coupled advection-reaction equations—one for each state of the IP$_3$R—govern the evolution of these densities (Eqs. 2.19–2.22). These advection-reaction equations are solved via a numerical scheme described in Appendix 2.6.6. The probability density approach is, of course, not limited to the four-state channel model (Eq. 2.7) utilized in this paper, but can be generalized to Markov chain models of intracellular Ca^{2+} channels of arbitrary complexity that include cytosolic Ca^{2+} regulation, luminal Ca^{2+} regulation, or both (see Appendix 2.6.5).

Parameter	Definition	Value
λ_{er}	bulk ER effective volume fraction	$1/6$
Λ^d_{er}	total luminal domain effective volume fraction	$1/30$
Λ^d_{cyt}	total cytosolic domain effective volume fraction	$1/30$
k_a^+, k_c^+	IP$_3$R association rate constants	$500\ \mu M^{-1}s^{-1}$
k_b^+, k_d^+	IP$_3$R association rate constants	$4\ \mu M^{-1}s^{-1}$
k_a^-, k_c^-	IP$_3$R dissociation rate constants	$1000\ s^{-1}$
k_b^-, k_d^-	IP$_3$R dissociation rate constants	$0.1\ s^{-1}$
v_{rel}^T	release flux rate	$10\ s^{-1}$
v_{cyt}^T	cytosolic domain collapse rate	$100\ s^{-1}$
v_{er}^T	luminal domain recovery rate	$100\ s^{-1}$
v_{leak}	ER leak rate	$0.01\ s^{-1}$
v_{pump}	maximum pump rate	$0.9\ \mu M s^{-1}$
k_{pump}	dissociation constant of pump	$0.2\ \mu M$

Table 2.1: Standard parameters for the Monte Carlo and probability density models described in Sections 2.3.1 and 2.3.2.

2.4 Results

2.4.1 Representative probability density and Monte Carlo simulations

Figure 2.2 shows representative results from the Monte Carlo (Section 2.3.1) and probability density (Section 2.3.2) approaches to the many-compartment whole cell model that is the focus of this paper. The Monte Carlo calculation (open circles) uses a large but finite number of IP$_3$Rs ($N = 100{,}000$) and is nearly identical to the probability density result (solid line). This agreement validates the formulation of the probability density approach and our implementation of both methods. Parameters are chosen so that whole cell Ca^{2+} oscillations are observed in the range of $c_{cyt} = 0.1$ to 1 μM (top panel). Oscillations in the fraction of non-inactivated IP$_3$Rs ($\pi^C + \pi^O$) are also observed, reflecting cycles of fast Ca^{2+}-mediated activation and slower Ca^{2+}-dependent inactivation of IP$_3$Rs.

Note that while the Ca^{2+} oscillations shown in Fig. 2.2 are qualitatively similar to those exhibited by conventional ODE models of whole cell Ca^{2+} dynamics (Eqs. 2.1–2.6), both the Monte Carlo and probability density simulations include a representation of the influence of local Ca^{2+} signaling on IP$_3$R gating that is lacking in conventional whole cell models. Figure 2.3 shows the distribution of cytosolic and luminal domain [Ca^{2+}] for the simulation shown in Fig. 2.2 at $t = 3$ s. Note the agreement between the histograms and gray circles that correspond to the Monte Carlo simulation, and the solid lines and contour plots that show the probability density result. The four central panels of Fig. 2.3 correspond to the four IP$_3$R states and are arranged in manner consistent with the state-transition diagram (Eq. 2.7). Only a small fraction of the IP$_3$Rs are open at $t = 3$ s ($\pi^O = 0.0013$). This value is calculated
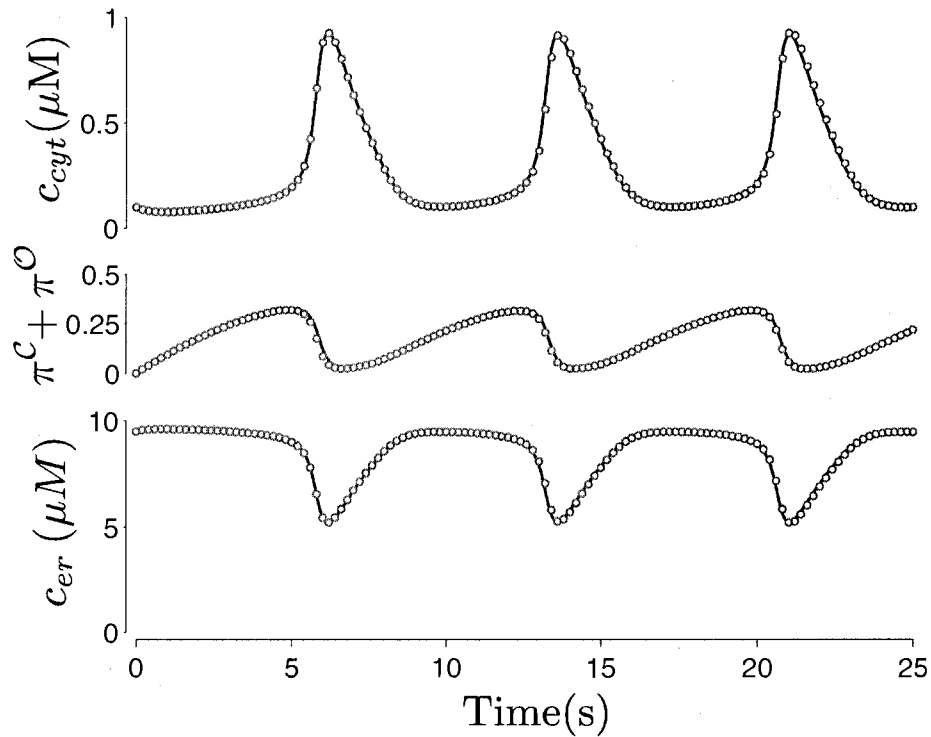
Figure 2.2: Agreement of the Monte Carlo (open circles) and the probability density (solid line) approaches to a whole cell model of local and global Ca^{2+} dynamics that includes luminal and cytosolic Ca^{2+} domains associated with each IP_3R (see Section 2.3). Oscillations of bulk cytoslic $[Ca^{2+}]$ (c_{cyt}, top panel) and the bulk luminal $[Ca^{2+}]$ (c_{er}, bottom panel) are observed with both approaches. In the middle panel, the fraction of non-inactivated channels in the Monte Carlo simulation given by ($N_C + N_O$)/N agrees with the corresponding quantity in the probability density calculation ($\pi^C + \pi^O$). The Monte Carlo simulation uses $N = 100{,}000$ IP_3Rs. Other parameters as in Table 2.1.

by integrating over all possible domain Ca^{2+} concentrations, that is,

$$\pi^i(t) = \int \int \rho^i(c_{cyt}^d, c_{er}^d, t)\, dc_{cyt}^d\, dc_{er}^d \qquad (2.32)$$

where i is the IP_3R state of interest. In the Monte Carlo calculations the fraction of open IP_3Rs at this time is also low ($N_{\mathcal{O}}/N = 0.0014$). But more importantly, in both the Monte Carlo and probability density calculations the few IP_3Rs that are open experience elevated cytosolic and depleted luminal domain Ca^{2+}, that is, $\langle c_{cyt}^d \rangle_{\mathcal{O}} \approx \mathsf{E}_{\mathcal{O}}[c_{cyt}^d] = 0.76\ \mu M$ and $\langle c_{er}^d \rangle_{\mathcal{O}} \approx \mathsf{E}[c_{er}^d] = 8.84\ \mu M$. Here $\langle c_{cyt}^d \rangle_{\mathcal{O}}$ denotes the average cytosolic domain $[Ca^{2+}]$ in the Monte Carlo simulation conditioned on the sampled IP_3R being in the open state, that is,

$$\langle c_{cyt}^d \rangle_{\mathcal{O}}(t) = \frac{1}{N_{\mathcal{O}}} \sum_{n \in n_{\mathcal{O}}} c_{cyt}^{d,n} \qquad (2.33)$$

where $N_{\mathcal{O}}(t)$ is the number of open IP_3Rs and $n_{\mathcal{O}}(t) = \{n : \tilde{S}^n = \mathcal{O}\}$ is the set of indices for IP_3Rs in the open state, while $\mathsf{E}_{\mathcal{O}}[c_{cyt}^d]$ is the corresponding joint expectation of the cytosolic domain $[Ca^{2+}]$ in the probability density calculation,

$$\mathsf{E}_{\mathcal{O}}[c_{cyt}^d](t) = \int \int c_{cyt}^d \rho^{\mathcal{O}}(c_{cyt}^d, c_{er}^d, t)\, dc_{cyt}^d\, dc_{er}^d, \qquad (2.34)$$

with $\langle c_{er}^d \rangle_{\mathcal{O}}$ and $\mathsf{E}_{\mathcal{O}}[c_{er}^d]$ similarly defined. Figure 2.3 shows that at $t = 3$ s those channels that are closed ($\pi^{\mathcal{C}} = 0.24$) or refractory ($\pi^{\mathcal{R}_1} + \pi^{\mathcal{R}_2} = 0.75$) experience cytosolic and luminal domain Ca^{2+} concentrations near the bulk values of $c_{cyt} = 0.1\ \mu M$ and $c_{er} = 9.5\ \mu M$; for example, $\langle c_{cyt}^d \rangle_i \approx \mathsf{E}_i[c_{cyt}^d] \approx 0.1\ \mu M$ where $i \in \{\mathcal{C}, \mathcal{R}_1, \mathcal{R}_2\}$. The dashed lines in the central four panels of Fig. 2.3 are the nullclines for domain Ca^{2+} (Eqs. 2.10–2.11) that take different positions depending on IP_3R state and the current value of the bulk Ca^{2+} concentrations (c_{cyt} and c_{er}).

The solid lines of Fig. 2.3 also show the marginal distributions of cytosolic domain
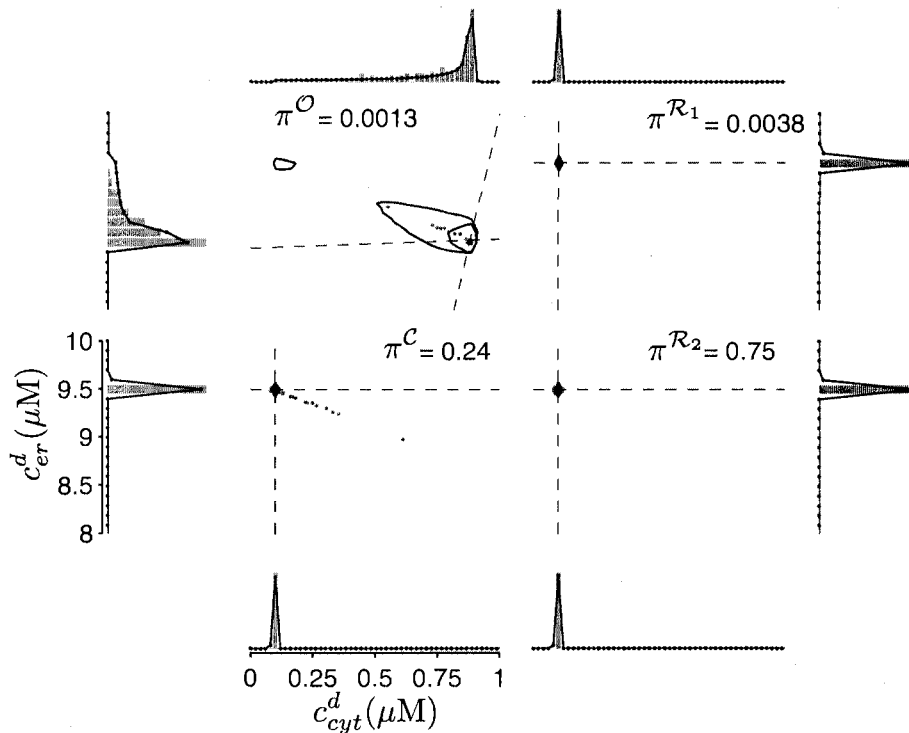
Figure 2.3: Snapshot of the distribution of cytosolic and luminal domain [Ca^{2+}] jointly distributed with IP$_3$R state at $t = 3$ s in Fig. 2.2 (just before the first Ca^{2+} spike) when the bulk cytosolic and luminal Ca^{2+} concentrations are 0.10 and 9.5 μM, respectively. The four central panels are arranged in a manner consistent with the IP$_3$R state-transition diagram (Eq. 2.7) and show the relationship between cytosolic domain [Ca^{2+}] (c_{cyt}^d, horizontal axis) and luminal domain [Ca^{2+}] (c_{er}^d, vertical axis). Note agreement between the Monte Carlo (gray dots) and probability density (solid contour lines) results. Contours are drawn such that 25, 50, and 75% of the density in each panel lies below each line. The uppermost and lowermost panels show the marginal distribution of c_{cyt}^d (Eq. 2.35), while the leftmost and rightmost panels show the marginal distribution of c_{er}^d (Eq. 2.36), and here also there is agreement between the Monte Carlo (gray histograms) and probability density (solid lines) calculations.

[Ca^{2+}] (horizontal) and luminal domain [Ca^{2+}] (vertical) jointly distributed with IP$_3$R state as calculated from the probability density approach, that is,

$$\rho^i_{cyt}(c^d_{cyt}, t) = \int \rho^i(c^d_{cyt}, c^d_{er}, t) \, dc^d_{er} \qquad (2.35)$$

$$\rho^i_{er}(c^d_{er}, t) = \int \rho^i(c^d_{cyt}, c^d_{er}, t) \, dc^d_{cyt} \qquad (2.36)$$

where $\rho^i(c^d_{cyt}, c^d_{er}, t)$ is one of the four bivariate densities (contours of central panels). For comparison, the corresponding marginal distributions of the Monte Carlo simulation are also shown. These marginal distributions indicate the range of elevated cytosolic domain [Ca^{2+}] and depleted luminal domain [Ca^{2+}] experienced by the N = 100,000 IP$_3$Rs. As the first oscillation in Fig. 2.2 begins ($t = 3$ s), the fraction of open IP$_3$Rs is quite small ($\pi^{\mathcal{O}} = 0.0013$, $N_{\mathcal{O}} = 130$) but the range of cytosolic luminal domain Ca^{2+} concentrations is broad compared to closed IP$_3$Rs ($\mathcal{C}$, $\mathcal{R}_1$, $\mathcal{R}_2$).

Figure 2.4 is identical to Fig. 2.3 except that the snapshot is taken at the peak of the first Ca^{2+} oscillation (see Fig. 2.2, $t = 6$ s). Here the fraction of open channels has increased from $\pi^{\mathcal{O}} = 0.0013$ to 0.037 ($N_{\mathcal{O}} = 137$ to 3,733). However, many more channels are now refractory as the [Ca^{2+}] oscillation terminates. In the probability density calculation, the fraction of refractory IP$_3$Rs ($\pi^{\mathcal{R}_1} + \pi^{\mathcal{R}_2}$) has increased from 0.75 to 0.87, while in the Monte Carlo calculation the number of refractory channels ($N_{\mathcal{R}_1} + N_{\mathcal{R}_2}$) has increased from 75,257 to 87,627 (both consistent with $\pi^{\mathcal{C}} + \pi^{\mathcal{O}}$ in Fig. 2.2). When IP$_3$Rs are refractory, the distribution of cytosolic and luminal domain [Ca^{2+}] is focused near the bulk cytosolic and luminal Ca^{2+} concentrations. While this is similar to Fig. 2.3, the bulk cytosolic and luminal Ca^{2+} concentrations have changed significantly ($c_{cyt} = 0.88$ μM and $c_{er} = 5.5$ μM, note shift of axes). The domain Ca^{2+} concentrations for closed IP$_3$Rs are more broadly distributed in Fig. 2.4 than in Fig. 2.3, reflecting the fact that the $\mathcal{C} \to \mathcal{O}$ and $\mathcal{O} \to \mathcal{C}$ probability fluxes given by $k_a^+(c^d_{cyt})^\eta \rho^{\mathcal{C}}$ and $k_a^- \rho^{\mathcal{O}}$ are much larger in Fig. 2.4.
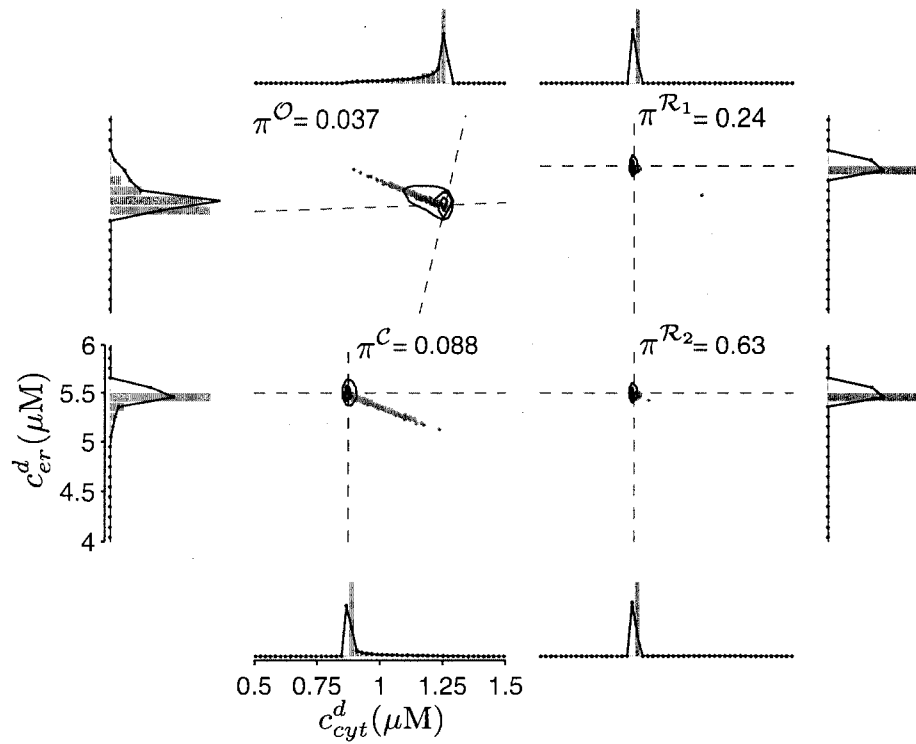
Figure 2.4: Snapshot of the distribution of cytosolic and luminal domain [Ca^{2+}] jointly distributed with IP$_3$R state at $t = 6$ s in Fig. 2.2 (at the peak of the first Ca^{2+} oscillation) when the bulk cytosolic and luminal Ca^{2+} concentrations are 0.88 and 5.5 μM, respectively. See legend of Fig. 2.3.

2.4.2 Monte Carlo simulations converge to the probability density result

Figure 2.5 shows Monte Carlo simulations converging to the probability density result as the number of IP$_3$Rs increases. In each panel, three Monte Carlo results (dotted, dashed, and dot-dashed lines) are shown alongside the probability density calculation (solid line, replotted in each panel). When the Monte Carlo calculation includes relatively few IP$_3$Rs ($N = 100$), the stochastic gating of the channels leads to fluctuations in the oscillatory dynamics of bulk cytosolic [Ca^{2+}] that decrease when N is increased to 1,000. In the Monte Carlo simulation with $N = 10,000$ channels, the dynamics of the bulk cytosolic [Ca^{2+}] is very similar to the probability density result (compare broken and solid lines). Small quantitative differences in the dynamics of bulk cytosolic [Ca^{2+}] are observed in Monte Carlo simulations even when $N = 100,000$ (not shown). These fluctuations are responsible for the minor disparities between the marginal probability distributions and histograms in Fig. 2.4 that are most apparent when IP$_3$Rs are in long-lived refractory states with $c_{cyt}^d \approx c_{cyt}$ and $c_{er}^d \approx c_{er}$. That is, when the calculations shown in Figs. 2.3 and 2.4 are repeated, the marginal distributions of the probability density result are unchanged, while the histograms obtained from the Monte Carlo simulation vary because the average domain Ca^{2+} concentrations ($\langle c_{cyt}^d \rangle_i$ and $\langle c_{er}^d \rangle_i$) are strongly influenced by the bulk Ca^{2+} concentrations (c_{cyt} and c_{er}) that are slightly different for each trial.

2.4.3 Computational efficiency

While Figs. 2.2–2.4 demonstrate the validity of the probability density approach to whole cell modeling of local and global Ca^{2+} dynamics, this section benchmarks the method's computational efficiency. The solid line of Fig. 2.6 shows the 85 minute run time required for the 25 second simulation of Fig. 2.2, using the numerical scheme
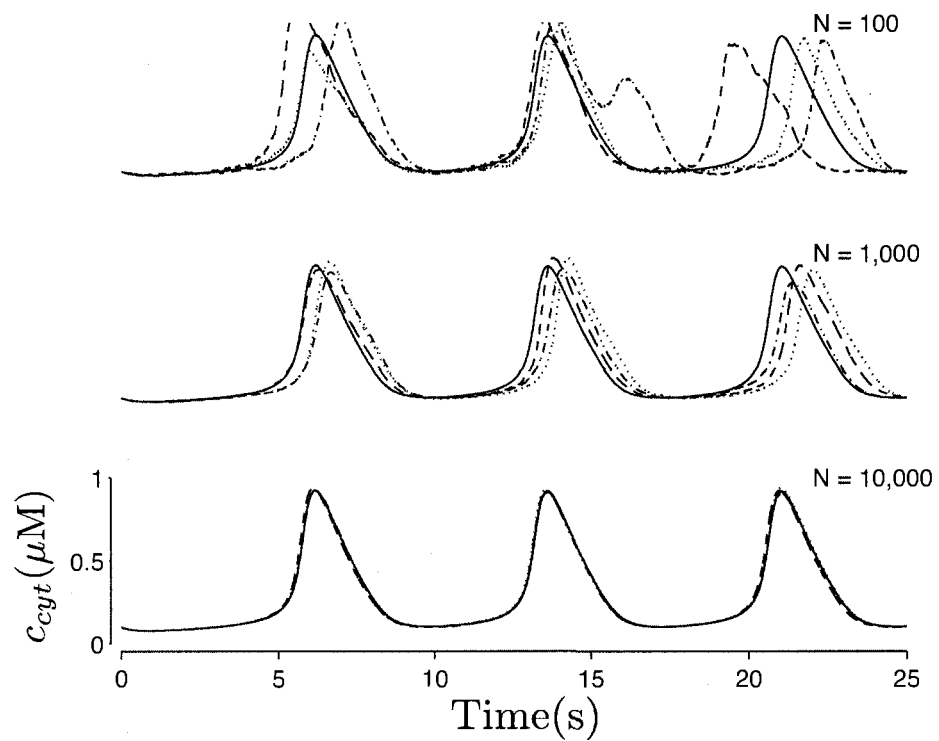
Figure 2.5: Oscillations of bulk cytosolic [Ca^{2+}] (c_{cyt}) for simulations with increasing numbers of IP$_3$Rs (N=100; 1,000; 10,000). The dotted, dashed, and dot-dashed lines correspond to three distinct Monte Carlo simulations. The solid line is the probability density result (replotted in each panel).

presented in Appendix 2.6.6 with an 30×30 mesh for the four probability densities jointly distributed with IP$_3$R state. For comparison, the dotted line of Fig. 2.6 shows the run time required for a corresponding Monte Carlo simulation using $N = 10$ to 100,000 IP$_3$Rs. As expected, the run time of the Monte Carlo calculations are approximately proportional to the number of IP$_3$Rs used (N). Note that the probability density approach becomes computationally more efficient than the Monte Carlo simulation when $N \approx 1,000$, long before a physiologically realistic number of IP$_3$Rs are included.

In Fig. 2.6 the time step used is as large as possible for each method; the average time step of the probability density calculation is 3 ms (constrained by numerical stability of the advection-reaction equations), while in the Monte Carlo calculation $\Delta t = 0.01$ ms (chosen so that the maximum IP$_3$R transition probability per time step is less than 0.05). Of course, the computational advantage of the probability density approach is diminished when this method is arbitrarily forced to use the time step required by the Monte Carlo simulation (not shown). While refining the mesh used in the probability density calculation increases the run time due to a greater number of mesh points and stricter requirements on the time step for numerical stability, meshes 25×25 or larger lead to bulk cytosolic [Ca^{2+}] dynamics that are indistinguishable from Fig. 2.2 where a 100×100 mesh is used.

2.4.4   Influences of domain calcium

Having validated and benchmarked the probability density approach as an alternative to Monte Carlo simulation of the whole cell model that is the focus of this paper, Fig. 2.7 uses this method to highlight the influence of local Ca^{2+} signaling on bulk cytosolic Ca^{2+} oscillations. The solid lines in Fig. 2.7 reproduce the oscillation in bulk cytosolic [Ca^{2+}] of Figs. 2.2–2.5 where the rate of cytosolic domain collapse is $v_{cyt} = 100$ s^{-1}, the rate of luminal domain recovery is $v_{er} = 100$ s^{-1}, and the release
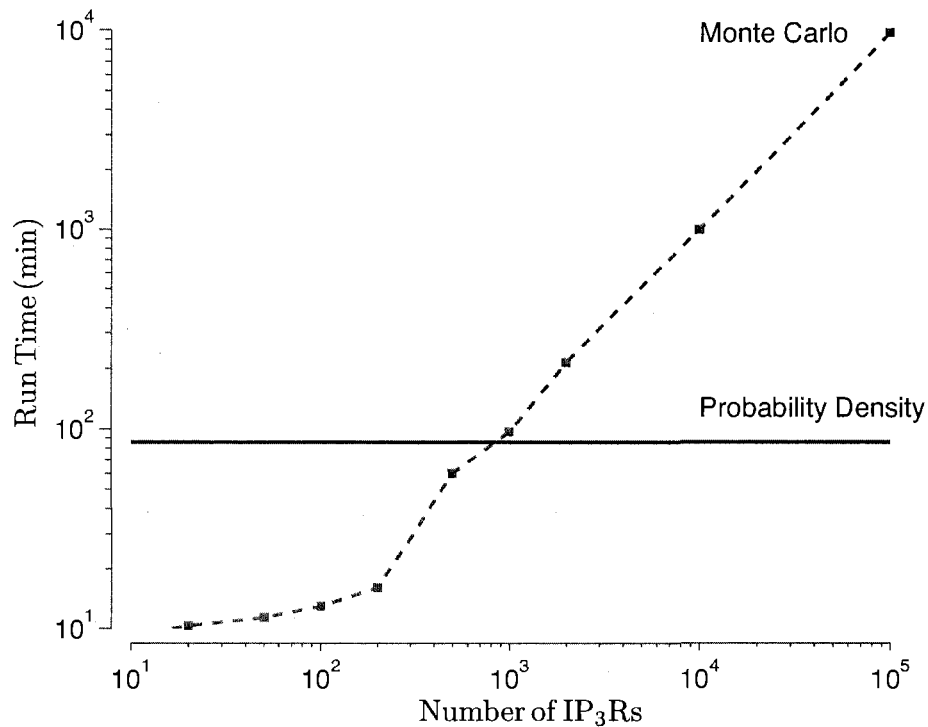
Figure 2.6: Dashed line with filled squares shows the run time of a 25 second Monte Carlo simulation of the whole cell model of local and global Ca^{2+} dynamics presented in Figs. 2.2–2.4 as the number of IP$_3$Rs is increased from $N = 10$ to 100,000 ($\Delta t = 0.01$ ms). Solid line shows the run time of the corresponding mulitvariate probability density simulation (average $\Delta t = 3$ ms). Benchmark calculations computed using a 2.3GHz dual processor Xserve G5 running Mac OS X Server 10.4.9.

rate through open IP$_3$Rs is $v_{rel} = 10$ s^{-1}.

The broken lines in the upper panel of Fig. 2.7 repeat this probability density calculation using slower cytosolic domain collapse rates. When $v_{cyt} = 50$ s^{-1} (dashed line), the amplitude of the [Ca^{2+}] oscillations decreases and their frequency increases. When $v_{cyt} = 25$ s^{-1} (dot-dashed line), the oscillations are no longer observed. Note that decreasing v_{cyt} not only slows domain collapse but also increases the steady-state cytosolic domain [Ca^{2+}] associated with open IP$_3$Rs (see Eq. 2.39). Decreased v_{cyt} may also increase the open probability of non-refractory channels $(\pi^{\mathcal{O}}/(\pi^{\mathcal{O}} + \pi^{\mathcal{C}}))$ as 'residual' [Ca^{2+}] from previous channel openings increases the rate of the Ca^{2+}-mediated $\mathcal{C} \rightarrow \mathcal{O}$ transition [Mazzag et al., 2005b].

The broken lines in the lower panel of Fig. 2.7 show how Ca^{2+} oscillations are modified when the rate of luminal domain recovery is decreased from the standard value of 100 s^{-1} (solid line). When $v_{er} = 10$ and 1 s^{-1} (dashed and dot-dashed lines), both the amplitude and frequency of the [Ca^{2+}] oscillations decreases. When $v_{cyt} = 0.1$ s^{-1} (dotted line), the oscillations are no longer observed. Decreasing v_{er} slows domain recovery, decreases the steady-state cytosolic domain [Ca^{2+}] associated with open IP$_3$Rs (see Eq. 2.39), and decreases the release flux via open IP$_3$Rs [Huertas and Smith, 2007a].

Taken together, the upper and lower panels of Fig. 2.7 demonstrate that the time constants for cytosolic domain collapse and luminal domain refilling can dramatically influence the stochastic gating of IP$_3$Rs and, consequently, the dynamics of bulk cytosolic and luminal [Ca^{2+}]. Figure 2.7 also suggests that whole cell modeling approaches that do not account for the influence of local Ca^{2+} signals on the stochastic gating of intracellular channels may produce inaccurate global Ca^{2+} responses.
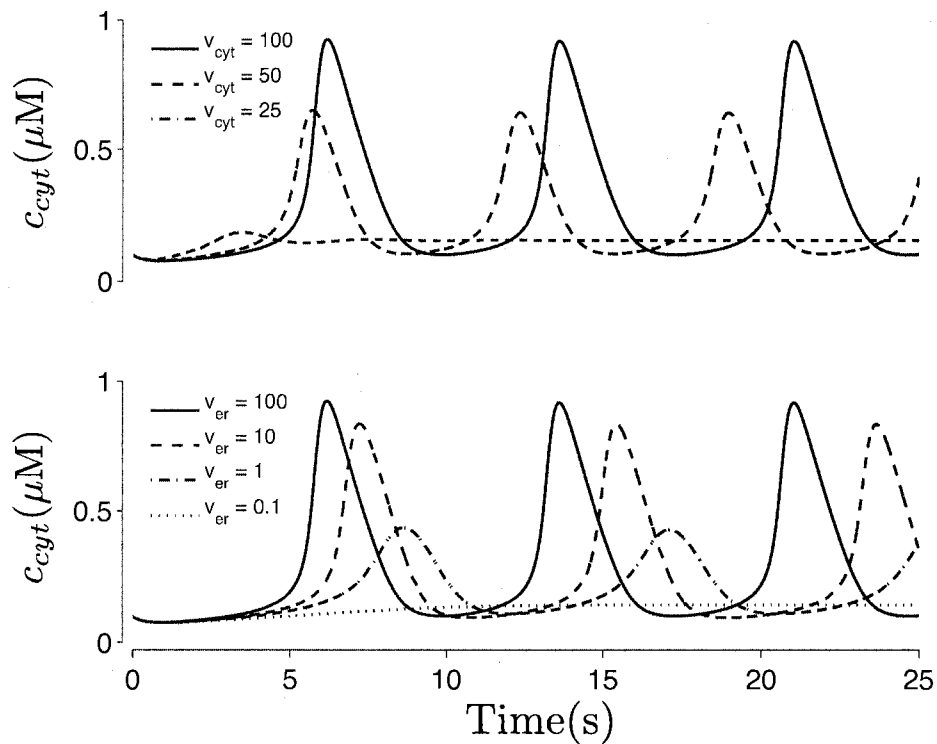
Figure 2.7: Influence of local Ca^{2+} signaling on bulk cytosolic $[Ca^{2+}]$ (c_{cyt}) dynamics as calculated using the probability density approach. The top panel shows the effect of decreasing the cytosolic domain collapse rate (v_{cyt}) from 100 s^{-1} (solid line) to 50 s^{-1}(dashed line) and 25 s^{-1} (dot-dashed line). The bottom panel illustrates the influence of decreasing the luminal domain recovery rate (v_{er}) from 100 s^{-1} (solid line) to 10 s^{-1} (dashed line), 1 s^{-1} (dot-dashed line), and 0.1 s^{-1} (dashed line). Other parameters as in Fig. 2.2 and Table 2.1.

2.4.5   Model reduction based on separation of time scales

While the probability density approach to modeling local and global Ca^{2+} dynamics can be more efficient than traditional Monte Carlo simulation (Section 2.4.3), under certain conditions the advection-reaction equations of the probability density approach (one PDE for each state of the IP_3R) can be reduced to an equivalent number of ODEs, greatly facilitating simulation. As shown schematically in the upper right panels of Fig. 2.8, when the stochastic gating of intracellular Ca^{2+} channels is slow compared to the dynamics of cytosolic and luminal domain Ca^{2+}, the values of $c_{cyt}^{d,n}$ and $c_{er}^{d,n}$ associated with closed channels are well-approximated by the bulk Ca^{2+} concentrations c_{cyt} and c_{er}. On the other hand, the values associated with open channels are well-approximated by the steady-state quantities $c_{cyt}^{d,ss}$ and $c_{er}^{d,ss}$ found by setting the left hand sides of Eqs. 2.10 and 2.11 to zero with $\gamma^n = 1$ in Eq. 2.15 (see Section 2.4.5.1 and Appendix 2.6.2). Conversely, when the stochastic gating of intracellular Ca^{2+} channels is fast compared to the dynamics of domain Ca^{2+} as in the lower right panels of Fig. 2.8, $c_{cyt}^{d,n}$ and $c_{er}^{d,n}$ are well-approximated by $c_{cyt}^{d,*}$ and $c_{er}^{d,*}$, algebraic functions of c_{cyt} and c_{er} that do not depend on channel state (see Section 2.4.5.2 and Appendix 2.6.3). Note that both of these reductions lead to a system of ODEs that includes a representation of the dynamics of local Ca^{2+} signals and, consequently, these reduced models are more realistic than conventional whole cell models.
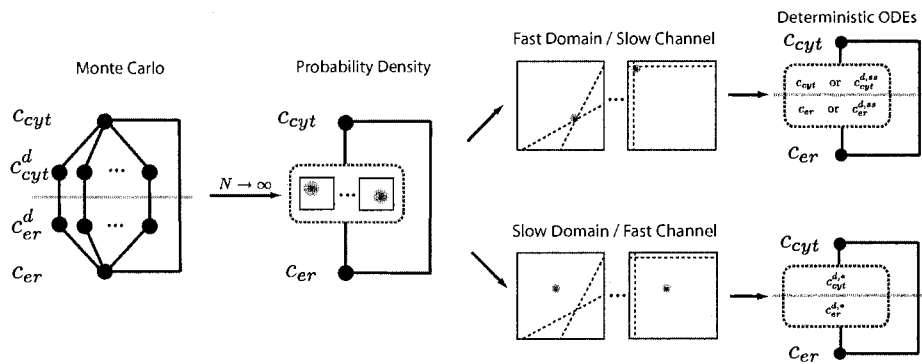
Figure 2.8: Schematic representation of the $2N+2$-compartment Monte Carlo model of local Ca^{2+} signaling where the ellipsis indicate a large number (N) of IP_3Rs with associated cytosolic and luminal Ca^{2+} domains (Section 2.3.1). In the limit of a large number of IP_3Rs $(N \rightarrow \infty)$, an alternative probability density approach (Section 2.3.2) can be used in which cytosolic and luminal domain Ca^{2+} concentrations are represented by multivariate probability density functions (here the ellipsis indicate the number of IP_3R states). When the time scales of channel gating and domain formation are adequately separated, the probability density approach can be reduced to a system of ODEs that account for the influence of local Ca^{2+} signaling on global Ca^{2+} dynamics, i.e., the "fast domain/slow channel" (Section 2.4.5.1) and "slow domain/fast channel" (Section 2.4.5.2) approximations.

2.4.5.1 Fast domain/slow channel approximation

Figure 2.8 (upper right) shows a schematic representation of the probability densities associated with closed and open IP$_3$Rs when the domain Ca^{2+} concentrations are fast compared to channel kinetics. The dashed lines in Fig. 2.8 are the nullclines for domain Ca^{2+} (Eqs. 2.10–2.11) that take different positions depending on IP$_3$R state and the current value of the bulk Ca^{2+} concentrations. When this separation of time scales applies and the IP$_3$R is closed (i.e., in state $i \in \{\mathcal{C}, \mathcal{R}_1, \mathcal{R}_2\}$), the multivariate joint probability densities are well-approximated by

$$\rho^i(c_{cyt}^d, c_{er}^d, t) = \pi^i(t)\delta(c_{cyt}^d - c_{cyt})\delta(c_{er}^d - c_{er}), \qquad (2.37)$$

where $\delta(\cdot)$ is the Dirac delta function, c_{cyt} and c_{er} are the bulk Ca^{2+} concentrations, and $\pi^i(t) = \mathsf{Pr}\{\tilde{S}(t) = i\}$. When the IP$_3$R is open, the multivariate joint probability density is well-approximated by

$$\rho^{\mathcal{O}}(c_{cyt}^d, c_{er}^d, t) = \pi^{\mathcal{O}}(t)\delta(c_{cyt}^d - c_{cyt}^{d,ss})\delta(c_{er}^d - c_{er}^{d,ss}) \qquad (2.38)$$

where the elevated cytosolic $(c_{cyt}^{d,ss})$ and a depleted luminal $(c_{er}^{d,ss})$ domain Ca^{2+} concentrations are found by setting the left hand sides of Eqs. 2.10 and 2.11 to zero with $\gamma^n = 1$, that is,

$$c_{cyt}^{d,ss} = \frac{v_{cyt}}{v_{cyt} + v_{er}'}c_{cyt} + \frac{v_{er}'}{v_{cyt} + v_{er}'}c_{er} \qquad (2.39)$$

$$c_{er}^{d,ss} = \frac{v_{cyt}'}{v_{cyt}' + v_{er}}c_{cyt} + \frac{v_{er}}{v_{cyt}' + v_{er}}c_{er} \qquad (2.40)$$

where

$$v_{cyt}' = \frac{v_{rel}v_{cyt}}{v_{rel} + v_{cyt}} \qquad \text{and} \qquad v_{er}' = \frac{v_{rel}v_{er}}{v_{rel} + v_{er}}.$$

When these assumed forms of the probability densities (Eqs. 2.37–2.38) are substituted into the advection-reaction equations for the probability density approach

(Eqs. 2.19–2.22), the resulting equations can be integrated with respect to cytosolic and luminal domain Ca^{2+} (see Appendix 2.6.4) to obtain a system of ordinary differential equations for the fraction of IP_3Rs in each state,

$$\frac{d\pi^{\mathcal{C}}}{dt} = -k_a^+(c_{cyt})^\eta \pi^{\mathcal{C}} - k_d^+(c_{cyt})^\eta \pi^{\mathcal{C}} + k_a^- \pi^{\mathcal{O}} + k_d^- \pi^{\mathcal{R}_2} \tag{2.41}$$

$$\frac{d\pi^{\mathcal{O}}}{dt} = k_a^+(c_{cyt})^\eta \pi^{\mathcal{C}} - k_a^- \pi^{\mathcal{O}} - k_b^+(c_{cyt}^{d,ss})^\eta \pi^{\mathcal{O}} + k_b^- \pi^{\mathcal{R}_1} \tag{2.42}$$

$$\frac{d\pi^{\mathcal{R}_1}}{dt} = k_b^+(c_{cyt}^{d,ss})^\eta \pi^{\mathcal{O}} - k_b^- \pi^{\mathcal{R}_1} - k_c^- \pi^{\mathcal{R}_1} + k_c^+(c_{cyt})^\eta \pi^{\mathcal{R}_2} \tag{2.43}$$

$$\frac{d\pi^{\mathcal{R}_2}}{dt} = k_d^+(c_{cyt})^\eta \pi^{\mathcal{C}} + k_c^- \pi^{\mathcal{R}_1} - k_d^- \pi^{\mathcal{R}_2} - k_c^+(c_{cyt})^\eta \pi^{\mathcal{R}_2} \tag{2.44}$$

where the cytosolic domain Ca^{2+} concentrations associated with Ca^{2+}-mediated transitions out of closed and open states are c_{cyt} and $c_{cyt}^{d,ss}$, respectively.

To complete the reduced model, we require concentration balance equations that allow us to solve for the bulk concentrations c_{cyt} and c_{er}. When Eqs. 2.28–2.29 are used for this purpose, substitution of Eqs. 2.37–2.38 into Eqs. 2.30–2.31 leads to $J_{cyt}^* = \pi^{\mathcal{O}} v_{cyt}^T \left(c_{cyt}^{d,ss} - c_{cyt} \right)$ for the flux out of the cytosolic domains and $J_{er}^* = \pi^{\mathcal{O}} v_{er}^T \left(c_{er} - c_{er}^{d,ss} \right)$ for the flux into the luminal domains. However, the reduced model given by these fluxes, Eqs. 2.28–2.29, and Eqs. 2.41–2.44 does not conserve the total cell Ca^{2+} defined by

$$c_T = c_{cyt} + \lambda_{er} c_{er} + \Lambda_{cyt}^d \bar{c}_{cyt}^d + \Lambda_{er}^d \bar{c}_{er}^d$$

where Λ_{cyt}^d and Λ_{er}^d (Eq. 2.12) are the relative effective volume of the aggregated cytosolic and luminal domains; and $\bar{c}_{cyt}^d$ and $\bar{c}_{er}^d$ are the average cytosolic and luminal domain concentrations. Note that in the probability density approach these

concentrations are given by

$$\bar{c}_{cyt}^d = \int \int c_{cyt}^d \rho^T \left(c_{cyt}^d, c_{er}^d, t\right) dc_{cyt}^d \, dc_{er}^d \tag{2.45}$$

and similarly for $\bar{c}_{er}^d$. In the fast domain/slow channel limit where the probability densities take the form indicated in Eqs. 2.37 and 2.38, the average cytosolic and luminal domain concentrations are given by

$$\bar{c}_{cyt}^d = \pi^{\mathcal{O}} c_{cyt}^{d,ss} + \left(1 - \pi^{\mathcal{O}}\right) c_{cyt} \tag{2.46}$$

$$\bar{c}_{er}^d = \pi^{\mathcal{O}} c_{er}^{d,ss} + \left(1 - \pi^{\mathcal{O}}\right) c_{er} \tag{2.47}$$

where $1 - \pi^{\mathcal{O}} = \pi^{\mathcal{C}} + \pi^{\mathcal{R}_1} + \pi^{\mathcal{R}_2}$.

In order to derive a reduced model that conserves total calcium, we have found it necessary to use balance equations for the following auxilary concentrations,

$$\hat{c}_{cyt} = c_{cyt} + \Lambda_{cyt}^d \bar{c}_{cyt}^d \tag{2.48}$$

$$\hat{c}_{er} = c_{er} + \frac{\Lambda_{er}^d}{\lambda_{er}} \bar{c}_{er}^d, \tag{2.49}$$

that are obtained by lumping the bulk compartments with their associated domains. To derive concentration balance equations for $\hat{c}_{cyt}$ and $\hat{c}_{er}$, consider the Monte Carlo model with finite N, where the average domain concentrations are given by,

$$\bar{c}_{cyt}^d = \frac{1}{N} \sum_{n=1}^{N} c_{cyt}^{d,n} \qquad \text{and} \qquad \bar{c}_{er}^d = \frac{1}{N} \sum_{n=1}^{N} c_{er}^{d,n}. \tag{2.50}$$

By differentiating these equations,

$$\frac{d\bar{c}_{cyt}^d}{dt} = \frac{1}{N} \sum_{n=1}^{N} \frac{dc_{cyt}^{d,n}}{dt} \qquad \text{and} \qquad \frac{d\bar{c}_{er}^d}{dt} = \frac{1}{N} \sum_{n=1}^{N} \frac{dc_{er}^{d,n}}{dt}, \tag{2.51}$$

45

and substituting into Eqs. 2.8–2.11, it can be shown without approximation that $\hat{c}_{cyt}$ and $\hat{c}_{er}$ solve

$$\frac{d\hat{c}_{cyt}}{dt} = J_{rel}^T + J_{leak} - J_{pump} \qquad (2.52)$$

$$\frac{d\hat{c}_{er}}{dt} = \frac{1}{\lambda_{er}}\left(-J_{rel}^T - J_{leak} + J_{pump}\right) \qquad (2.53)$$

where J_{leak} and J_{pump} are given by Eqs. 2.13 and 2.14 and $J_{rel}^T = \sum_{n=1}^{N} \gamma^n v_{rel}(c_{er}^{d,n} - c_{cyt}^{d,n})$ (Eq. 2.15). However, in the fast domain/slow channel limit where the probability densities take the form Eqs. 2.37–2.38, the total release flux is,

$$J_{rel}^T = \pi^{\mathcal{O}} v_{rel}^T (c_{er}^{d,ss} - c_{cyt}^{d,ss}) \qquad (2.54)$$

because $c_{cyt}^{d,n} \approx c_{cyt}^{d,ss}$ and $c_{er}^{d,n} \approx c_{er}^{d,ss}$ for open IP$_3$Rs. Note that when Eqs. 2.52–2.54 are numerically integrated, the fluxes J_{leak}, J_{pump}, and J_{rel}^T (all functions of c_{cyt} and c_{er} using Eqs. 2.39–2.40) must be evaluated using the current values of $\hat{c}_{cyt}$ and $\hat{c}_{er}$ using Eqs. 2.46–2.49 (see 2.6.2).

The six ODEs (Eqs. 2.41–2.44 and Eqs. 2.52–2.53) and various algebraic relations (Eqs. 2.39–2.40 and Eqs. 2.46–2.47) and fluxes (Eqs. 2.5, 2.6, and 2.54) constitute a whole cell model that represents both local and global Ca^{2+} handling under the assumption of fast Ca^{2+} domains and slow IP$_3$R gating. We will refer to this model below as the "fast domain/slow channel approximation."

2.4.5.2 Slow domain/fast channel approximation

Figure 2.8 (lower right) shows a schematic representation of the probability densities associated with closed and open IP$_3$Rs when the domain Ca^{2+} concentrations are slow compared to channel kinetics. In this case, the multivariate joint probability density functions are well-approximated by

$$\rho^i(c_{cyt}^d, c_{er}^d, t) = \pi^i(t)\delta(c_{cyt}^d - c_{cyt}^{d,*})\delta(c_{er}^d - c_{er}^{d,*}) \qquad (2.55)$$

46
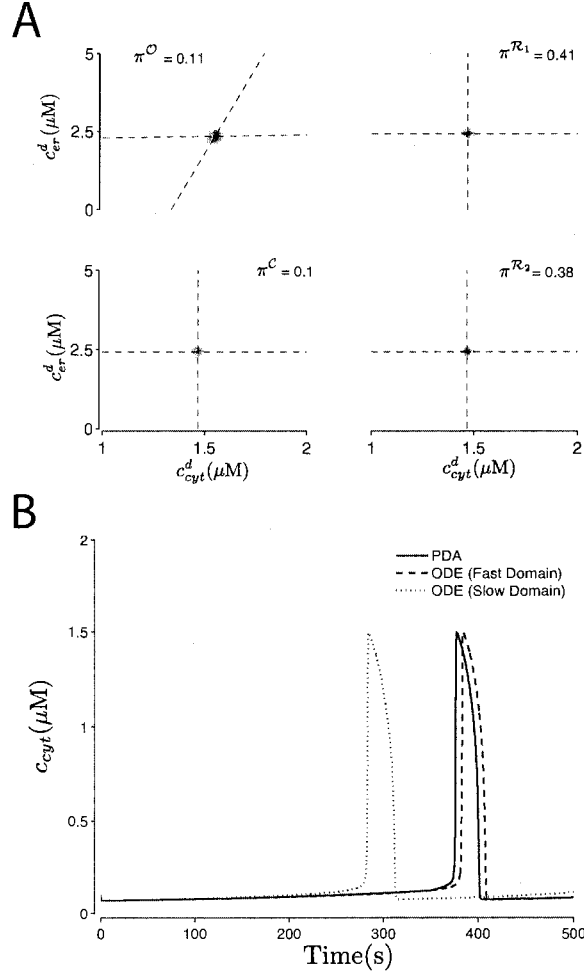
Figure 2.9: A) Snapshot of the distribution of cytosolic and luminal domain [Ca^{2+}] jointly distributed with IP$_3$R state at $t = 380$ s when IP$_3$R kinetics are decreased by a factor of 100 (cf. Table 2.1). The four central panels are arranged in a manner consistent with the IP$_3$R state-transition diagram (Eq. 2.7) and show the relationship between cytosolic (c_{cyt}^d, horizontal axis) and luminal (c_{er}^d, vertical axis) domain Ca^{2+}. Note location of probability mass in agreement with schematic of the fast channel/slow domain approximation shown in Fig. 2.8. B) The probability density calcuation during a 500 s simulation (solid line), the fast domain/slow channel approximation (dashed lines), and the slow domain/fast channel approximation (dotted lines).

where $i \in \{\mathcal{C}, \mathcal{O}, \mathcal{R}_1, \mathcal{R}_2\}$, that is, the probability mass is focused at approximately the same location regardless of IP$_3$R state. In this expression, the quantities $c_{cyt}^{d,*}$ and $c_{er}^{d,*}$ are functions of $\pi^{\mathcal{O}}$, c_{cyt}, and c_{er} that can be found by setting the left hand side of Eqs. 2.10 and 2.11 to zero after replacing γ^n by $\pi^{\mathcal{O}}$ (the open probability of a rapidly gating IP$_3$R), that is,

$$c_{cyt}^{d,*} = \frac{v_{cyt}}{v_{cyt} + v_{er}^*} c_{cyt} + \frac{v_{er}^*}{v_{cyt} + v_{er}^*} c_{er} \tag{2.56}$$

$$c_{er}^{d,*} = \frac{v_{cyt}^*}{v_{cyt}^* + v_{er}} c_{cyt} + \frac{v_{er}}{v_{cyt}^* + v_{er}} c_{er} \tag{2.57}$$

where

$$v_{cyt}^* = \frac{v_{rel}^* v_{cyt}}{v_{rel}^* + v_{cyt}} \qquad v_{er}^* = \frac{v_{rel}^* v_{er}}{v_{rel}^* + v_{er}} \tag{2.58}$$

and $v_{rel}^* = \pi^{\mathcal{O}} v_{rel}$.

When this assumed form of the probability densities (Eq. 2.55) is substituted into the advection-reaction equations for the probability density approach (Eqs. 2.19–2.22), the fraction of IP$_3$Rs in each state are found to solve (see 2.4.5.2),

$$\frac{d\pi^{\mathcal{C}}}{dt} = -k_a^+ (c_{cyt}^{d,*})^\eta \pi^{\mathcal{C}} - k_d^+ (c_{cyt}^{d,*})^\eta \pi^{\mathcal{C}} + k_a^- \pi^{\mathcal{O}} + k_d^- \pi^{\mathcal{R}_2} \tag{2.59}$$

$$\frac{d\pi^{\mathcal{O}}}{dt} = k_a^+ (c_{cyt}^{d,*})^\eta \pi^{\mathcal{C}} - k_a^- \pi^{\mathcal{O}} - k_b^+ (c_{cyt}^{d,*})^\eta \pi^{\mathcal{O}} + k_b^- \pi^{\mathcal{R}_1} \tag{2.60}$$

$$\frac{d\pi^{\mathcal{R}_1}}{dt} = k_b^+ (c_{cyt}^{d,*})^\eta \pi^{\mathcal{O}} - k_b^- \pi^{\mathcal{R}_1} - k_c^- \pi^{\mathcal{R}_1} + k_c^+ (c_{cyt}^{d,*})^\eta \pi^{\mathcal{R}_2} \tag{2.61}$$

$$\frac{d\pi^{\mathcal{R}_2}}{dt} = k_d^+ (c_{cyt}^{d,*})^\eta \pi^{\mathcal{C}} + k_c^- \pi^{\mathcal{R}_1} - k_d^- \pi^{\mathcal{R}_2} - k_c^+ (c_{cyt}^{d,*})^\eta \pi^{\mathcal{R}_2}. \tag{2.62}$$

Note that in the slow domain/fast channel ODEs (Eqs. 2.59–2.62) the cytosolic domain [Ca^{2+}] associated with Ca^{2+}-mediated transitions is given by $c_{cyt}^{d,*}$ regardless of IP$_3$R state, while in the fast domain/slow channel ODEs (Eqs. 2.41–2.44), the cytosolic Ca^{2+}-mediated transitions out of closed and open states involve c_{cyt} and $c_{cyt}^{d,ss}$,

respectively.

The slow domain/fast channel approximation is completed using the balance equations for the auxiliary concentrations $\hat{c}_{cyt}$ and $\hat{c}_{er}$ derived above (Eqs. 2.48–2.49), but in this case the cytosolic and luminal domain Ca^{2+} concentrations are approximated by $c_{cyt}^{d,n} \approx c_{cyt}^{d,*}$ and $c_{er}^{d,n} \approx c_{er}^{d,*}$, so the average domain concentrations (Eq. 2.50) are given by

$$\bar{c}_{cyt}^{d} = c_{cyt}^{d,*} \qquad \text{and} \qquad \bar{c}_{er}^{d} = c_{er}^{d,*} \tag{2.63}$$

while

$$J_{rel}^{T} = \pi^{\mathcal{O}} v_{rel}^{T} (c_{er}^{d,*} - c_{cyt}^{d,*}). \tag{2.64}$$

The six ODEs (Eqs. 2.59–2.62 and Eqs. 2.52–2.53) and various algebraic relations (Eqs. 2.56–2.57 and Eq. 2.63) and fluxes (Eqs. 2.5, 2.6, 2.64) constitute a whole cell model that represents both local and global Ca^{2+} handling under the assumption of slow Ca^{2+} domains and fast IP$_3$R gating. We will refer to this model below as the "slow domain/fast channel approximation."

2.4.6 Validation of reduced whole cell models of local and global calcium dynamics

To validate the fast domain/slow channel approximation of Section 2.4.5.1, the simulation of Figs. 2.2–2.4 was repeated after decreasing the channel rate constants by two orders of magnitude ($k_a^{\pm}$, $k_b^{\pm}$, etc. in Eq. 2.7). Fig. 2.9A shows the multivariate probability densities at the peak of the first Ca^{2+} oscillation that now occurs at $t = 380$ s. Notice that the probability density for cytosolic and luminal domain Ca^{2+} is focused at (c_{cyt}, c_{er}) and ($c_{cyt}^{d,ss}, c_{er}^{d,ss}$) when IP$_3$Rs are closed and open, respectively, consistent with the schematic in Fig. 2.8 (upper right), although this was not the case for $\rho^{\mathcal{C}}$ and $\rho^{\mathcal{O}}$ when the IP$_3$R had faster kinetics (Fig. 2.4). As expected, slowing the IP$_3$R rate constants places the probability density calculation securely in the fast
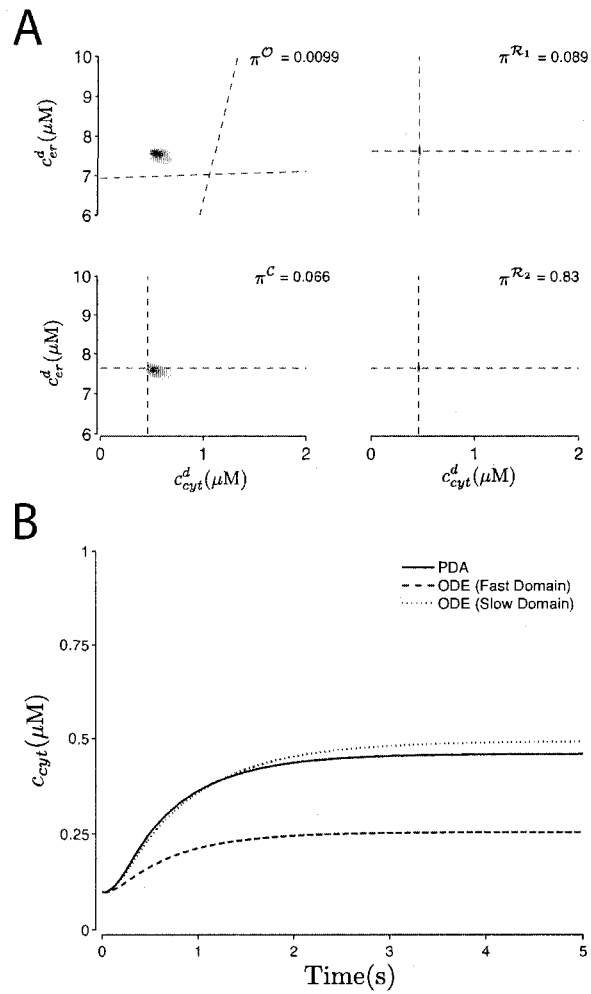
Figure 2.10: A) Snapshot of the distribution of cytosolic and luminal domain [Ca^{2+}] jointly distributed with IP$_3$R state at $t = 5$ s when IP$_3$R kinetics are increased by a factor of 100 (cf. Table 2.1). See legend of Fig. 2.9.

domain/slow channel limit (Section 2.4.5.1). Fig. 2.9B shows the fast domain/slow channel approximation (dashed line) agreeing with the probability density calcuation during a 500 s simulation (the long oscillation period is due to the slow IP$_3$R kinetics). Because the IP$_3$R kinetics are slow compared to the Ca^{2+} domains, the slow domain/fast channel approximation (dotted lines) does not work well.

Conversely, Fig. 2.10A shows the multivariate probability densities at $t = 5$ s when the IP$_3$R rate constants are increased by two orders of magnitude compared to the standard parameters used in Figs. 2.2–2.4. In this case, the cytosolic and luminal domain Ca^{2+} concentrations are positioned at $(c_{cyt}^{d,*}, c_{er}^{d,*})$ regardless of IP$_3$R state, consistent with Fig. 2.8 (lower right). Although increasing the IP$_3$R kinetics to this degree eliminates the Ca^{2+} oscillations, what is more important is that now the slow domain/fast channel approximation (dotted line in Fig. 2.10B) agrees with the probability density calculation (solid line), while the fast domain/slow channel approximation (dashed line) does not work well.

Taken together, Figs. 2.9 and 2.10 validate the two reduced models of global Ca^{2+} dynamics derived in Section 2.4.5 that account for the influence of local Ca^{2+} signaling on global Ca^{2+} dynamics when there is a separation of time scales between the stochastic gating of IP$_3$Rs and the dynamics of domain Ca^{2+}.

2.5 Discussion

While several groups have presented simulations of one or more Ca^{2+} channels stochastically gating under the influence of a time-dependent or time-independent Ca^{2+} domain [Sherman et al., 1990b, Mazzanti et al., 1991, Swillens et al., 1994, Bertram et al., 1999, Rios and Stern, 1997, Swillens and Champeil, 1998, Swillens and Dupont, 1999, Stern et al., 1999a, Shuai and Jung, 2003, Falcke, 2003a, Falcke, 2003b], the whole cell model of local and global Ca^{2+} responses that is the focus of this paper includes

$2N+2$ compartments and N=100,000 diffusely distributed IP_3Rs, each represented by a four-state Markov chain. Two of these compartments correspond to bulk cytosolic and luminal $[Ca^{2+}]$, and the remaining $2N$ compartments represent time-dependent cytosolic and luminal Ca^{2+} domains associated with each IP_3R. This formulation is significantly more complex and realistic than traditional whole cell models such as Eqs. 2.1–2.6 that assume IP_3Rs are globally coupled by a continuously stirred bulk cytosolic $[Ca^{2+}]$, and thereby neglect the influence of local Ca^{2+} signaling on channel dynamics. On the other hand, the Monte Carlo model presented in Section 2.3.1 is simple and convenient compared to a full three dimensional simulations of Ca^{2+} handling [Means et al., 2006].

Using this $2N+2$-compartment Monte Carlo model as a starting point, we present an alternative "probability density" formulation that solves a system of advection-reaction equations for the distribution of cytosolic and luminal domain Ca^{2+} concentrations jointly distributed with IP_3R state (Section 2.3.2). When these equations are coupled to ODEs for the bulk cytosolic and luminal $[Ca^{2+}]$, we obtain a realistic but minimal model of whole cell Ca^{2+} dynamics that accounts for the influence of local Ca^{2+} signaling on channel gating and global Ca^{2+} responses. In Sections 2.4.1–2.4.3 this probability density approach was validated through agreement with the Monte Carlo simulation when the number of IP_3Rs is large (Fig. 2.5), and for $N > 1000$ we find the probability density calculation is computationally more efficient than Monte Carlo (Fig. 2.6).

In Section 2.4.4 the probability density approach was used to demonstrate how the time scale of Ca^{2+} domain formation and collapse (both cytosolic and luminal) may influence the amplitude, frequency, and existence of global Ca^{2+} oscillations. While our prior work has investigated how residual Ca^{2+} from previous channel openings [Mazzag et al., 2005b] and luminal depletion [Huertas and Smith, 2007a] can influence the stochastic gating of Ca^{2+}-regulated channels, Fig. 2.7 demonstrates that the time

52

constants for cytosolic domain collapse (v_{cyt}) and luminal domain refilling (v_{er}) can influence the stochastic gating of IP$_3$Rs and have dramatic consequences on the dynamics of bulk cytosolic and luminal [Ca^{2+}].

So long as the average rate equations such as Eq. 2.2 are interpreted as phenomenological descriptions of the dynamics of Ca^{2+} activation and inactivation of intracellular channels, traditional whole cell models of Ca^{2+} handling such as Eqs. 2.1–2.6 are an appropriately minimal description of global Ca^{2+} responses [Keizer et al., 1995, Li et al., 1995]. But to the extent that whole cell models are modular constructs in which the stochastic gating of Ca^{2+}-regulated channels is constrained by single channel data, the use of an average rate equation that assumes a large number of intracellular Ca^{2+} channels are globally coupled via the bulk cytosolic [Ca^{2+}] (c_{cyt}) is a severe limitation. In the alternative whole cell modeling approach explored here, the advection-reaction equations of the probability density approach represent the dynamics of intracellular channels in a manner that accounts the influence of local Ca^{2+} signaling on the stochastic gating of diffusely distributed channels and resulting global Ca^{2+} responses. As in the traditional formulation, the probability density approach assumes a large number of intracellular channels. However, the probability density approach considers this large N limit while maintaining a description of the cytosolic and luminal Ca^{2+} domains associated with individual IP$_3$Rs. In the trade-off between model complexity and realism in simulations of global Ca^{2+} responses, the probability density approach is an interesting compromise; it is more realistic than traditional whole cell models that neglect the effect of local Ca^{2+} signaling on channel dynamics, but less computationally intensive than explicitly spatial simulations.

The Monte Carlo model of local and global Ca^{2+} signaling that is the starting point for the probability density approach was suggested by our prior work modeling the local control of excitation-contraction coupling in cardiac myocytes. While traditional whole cell models of cardiac myocytes based on realistic Markov chain models of

RyR gating are unable to reproduce Ca^{2+} release that is graded with the amount of Ca^{2+} influx [Stern, 1992b], more complex and realistic models of EC coupling are able to simulate graded Ca^{2+} release by treating L-type Ca^{2+} channels and RyR clusters as stochastic Ca^{2+} release units (CaRUs), each of which is associated with its own diadic subspace and junctional SR $[Ca^{2+}]$. An analogous approach is taken in the Monte Carlo model that is the focus of this paper (Section 2.3.1), that is, each individual $IP_3R$is associated with a restricted cytosolic and luminal compartment and the dynamics of $[Ca^{2+}]$ in these compartments are interpreted as time-dependent Ca^{2+} domains (Eqs. 2.10–2.11). Admittedly, one limitation of this formulation is that there is little evidence for restricted cytosolic and luminal spaces associated with diffusely distributed IP_3Rs. On the other hand, it is not unreasonable to use first order kinetic equations for domain Ca^{2+} as a starting point for the investigation of the impact of local Ca^{2+} signals on global Ca^{2+} oscillations. When the details of the spatio-temporal dynamics of buffered diffusion of intracellular Ca^{2+} near single channels are important, numerical and analytical methods based on the equations for the buffered diffusion of intracellular Ca^{2+} should be employed [Neher, 1986, Smith, 1996, Smith et al., 1996, Smith et al., 1998, Neher, 1998b, Neher, 1998a, Naraghi and Neher, 1997, Smith et al., 2001]. In our opinion, simulation methods that combine the probability density approach to modeling local and global Ca^{2+} responses with more realistic representations of local Ca^{2+} signaling is an important topic for further research.

In Section 2.4.5 the probability density formulation was used to derive two reduced models of global Ca^{2+} dynamics that account for the influence of local Ca^{2+} signaling on global Ca^{2+} dynamics when there is a separation of time scales between the stochastic gating of IP_3Rs and the dynamics of domain Ca^{2+}. These derivations begin by assuming a particular form for the probability densities: Eqs. 2.37–2.38 in the case of the fast domain/slow channel approximation, and Eq. 2.55 in the case

of the slow domain/fast channel approximation. It is important to note that reducing the probability density formulation in this manner is not particularly rigorous, and the discrepancies between the full and reduced models observed in Figs. 2.9 and 2.10 are likely due to the fact that the limiting probability distributions are not delta functions. A more rigorous analysis of the consequences of separation of time scales between channel kinetics and the dynamics of domain Ca^{2+} would involve nondimensionalization, assumptions about the relative size of model parameters, and perturbation methods.

While the probability density approach to modeling local and global Ca^{2+} responses accurately accounts for the dynamics of cytosolic and luminal Ca^{2+} domains associated with a large number of IP_3Rs, it nevertheless assumes continuously stirred bulk cytosolic and ER compartments. In order to investigate the significance of this limitation, the Monte Carlo calculations were extended to include spatially explicit bulk concentrations in a one-dimensional cell (see Fig. 2.11 and Appendix 2.6.7). When the effective diffusion coefficient for Ca^{2+} within the bulk cytosol and ER is in the range 10–100 $\mu m^2/s$, we found that the dynamics of global Ca^{2+} oscillations were very similar to probability density calculations that assume continuously stirred bulk cytosolic and ER compartments (Figs. 2.12–2.15). Thus, it appears that the probability density methodology that is the focus of this paper (Section 2.3.2) need not resolve spatial aspects of global Ca^{2+} signaling in order to accurately represent the effect of heterogeneous local Ca^{2+} on the stochastic dynamics of intracellular Ca^{2+} channels during global Ca^{2+} responses.

A natural question for further research is whether whole cell models based on the probability density approach—with its realistic and compact representation of the dynamics of domain Ca^{2+}—exhibit the same bifurcation structure as conventional whole cell models. Because the answer to this question will depend on the single channel model used, it is important to note that the probability density approach

can be applied to single channel models of arbitrary complexity that include cytosolic Ca^{2+} regulation, luminal regulation, or both (see Appendix 2.6.5). Because it will be significantly more challenging to perform such analysis on whole cell models that utilize advection-reaction equations rather than ODEs to represent the dynamics of intracellular channels, a good starting point for this future work would be a comparison of the bifurcation structure of traditional whole cell models to the reduced models that are applicable when Ca^{2+} domains are either fast or slow compared to channel kinetics (Section 2.4.5) [Smith, 2002a].

Finally, we note that this presentation of the probability density approach to modeling whole cell Ca^{2+} dynamics while accounting for the influence of local Ca^{2+} signaling on channel gating has assumed that IP$_3$Rs are "diffusely distributed," that is, each of of N cytosolic compartments representing cytosolic domains is associated with a Markov chain representing one channel (similarly for the N luminal compartments). There is evidence that IP$_3$Rs are diffusely distributed in some cell types. While canine pulmonary arterial smooth muscle cells exhibit IP$_3$-induced intracellular Ca^{2+} transients, discrete events expected due to the coordinated opening of IP$_3$R clusters (i.e., Ca^{2+} puffs) are not observed, suggesting that IP$_3$Rs are diffusely distributed within the ER membrane [Wilson et al., 2002]. In several cell types IP$_3$Rs are diffusely distributed at rest, but redistribute into clusters after stimulation (e.g., rat basophilic leukemia, rat pancreatoma, and hamster lung broblast cells). [Wilson et al., 1998]. In other cell types, IP$_3$-dependent Ca^{2+} release occurs via Ca^{2+} release sites composed of clusters of IP$_3$Rs (e.g., Xenopus oocytes and oligodendrocyte progenitors) [Mak and Foskett, 1997, Haak et al., 2001].

The functional consequences of IP$_3$R clustering for whole cell responses could be studied using the new class of whole cell models that is the focus of this paper by assuming that the cytosolic Ca^{2+} binding sites of each channel at a release site experience the same local $[Ca^{2+}]$. For example, if M denotes the number of channel

states, S denotes the number of channels per release site, the expanded Markov chain model for the Ca^{2+} release site has $M+S-1$-choose-S distinguishable states [Nguyen et al., 2005]. The resulting model would include one advection-reaction equation for each distinguishable state of the Ca^{2+} release site as well as two ODEs for the bulk cytosolic and ER Ca^{2+} concentrations. Such a model (or the corresponding fast/slow reductions) could be employed to study the effect of clustering of intracellular channels on the dynamics of global Ca^{2+} responses.

2.6 Appendices

2.6.1 Advection-reaction equations for the joint probability densities

Eqs. 2.19–2.22 are a differential Chapman-Kolmogorov equation [Gardiner, 2004] that the multivariate probability densities of Eq. 2.18 must solve in order to be consistent with the dynamics of the Monte Carlo model (Section 2.3.1) in the limit of a large number of IP$_3$Rs ($N \to \infty$). Because the cytosolic and luminal domain Ca^{2+} concentrations evolve deterministically according to Eqs. 2.10–2.11, the only stochasticity is due to the gating of the IP$_3$Rs, and the resulting master equation is given by Eqs. 2.19–2.22. To see this, consider the simpler situation where a continuous random variable X evolves according to

$$\frac{dX}{dt} = f_{\mathcal{C}/\mathcal{O}} \qquad \text{when} \qquad S(t) = \mathcal{C}/\mathcal{O} \tag{2.1}$$

where $S(t) \in \{\mathcal{C}, \mathcal{O}\}$ is a two-state continous-time telegraph process with transition rates $k_{\mathcal{C}\mathcal{O}}$ and $k_{\mathcal{O}\mathcal{C}}$. In this case the time-dependent joint probability densities $\rho_{\mathcal{C}}(x, t)$

and $\rho_{\mathcal{O}}(x, t)$ defined by [Mazzag et al., 2005b]

$$\rho_{\mathcal{C}/\mathcal{O}}(x, t)dx = \mathsf{Pr}\left\{x < X < x + dx \text{ and } S(t) = \mathcal{C}/\mathcal{O}\right\} \qquad (2.2)$$

solve

$$\frac{\partial \rho_C}{\partial t} = -\frac{\partial}{\partial x}\left[f_C \rho_C\right] - k_{\mathcal{CO}}\rho_C + k_{\mathcal{OC}}\rho_{\mathcal{O}} \qquad (2.3)$$

$$\frac{\partial \rho_{\mathcal{O}}}{\partial t} = -\frac{\partial}{\partial x}\left[f_{\mathcal{O}}\rho_{\mathcal{O}}\right] + k_{\mathcal{CO}}\rho_C - k_{\mathcal{OC}}\rho_{\mathcal{O}}. \qquad (2.4)$$

Eqs. 2.3 and 2.4 represent a conservation law indicating that the probability density can only change due to the impact of the distinct deterministic dynamics of X (the advection terms) or the stochastic dynamics of S (the reaction terms). Advection-reaction equations for the joint probability densities (Eqs. 2.19–2.22) are a generalization of this result to include the deterministic dynamics of two domain concentrations (resulting in advection terms with partial derivatives with respect to both c_{cyt}^d and c_{er}^d) and the stochastic dynamics of an IP$_3$R with four states and Ca^{2+}-dependent transition rates (resulting in four equations with more complicated reaction terms). Note that if Ca^{2+} fluxes were modeled in a discrete and stochastic fashion (i.e., movement of individual ions), in an appropriate limit a master equation can be obtained that is similar to Eqs. 2.19–2.22 but includes a diffusion term in each equation [Kepler and Elston, 2001].

2.6.2 Fast domain/slow channel approximation

In the fast domain/slow channel approximation the assumed form of the probability densities (Eqs. 2.37 and 2.38) are substituted into the advection-reaction equations for the probability density approach (Eqs. 2.19–2.22) to obtain a system of ordinary differential equations for the fraction of IP$_3$Rs in each state (Eqs. 2.41–2.44). Here we show that substituting Eq. 2.38 into Eq. 2.20 and integrating the resulting equations

with respect to cytosolic and luminal domain [Ca^{2+}] leads term by term to Eq. 2.42. The left hand side of Eq. 2.20 becomes

$$\int_0^\infty \int_0^\infty \frac{\partial \rho^{\mathcal{O}}}{\partial t} \, dc_{cyt}^d \, dc_{er}^d =$$

$$\int_0^\infty \int_0^\infty \frac{\partial}{\partial t} \left[\pi^{\mathcal{O}} \delta(c_{cyt}^d - c_{cyt}^{d,ss}) \delta(c_{er}^d - c_{er}^{d,ss}) \right] dc_{cyt}^d \, dc_{er}^d =$$

$$\frac{d\pi^{\mathcal{O}}}{dt} \int_0^\infty \int_0^\infty \delta(c_{cyt}^d - c_{cyt}^{d,ss}) \delta(c_{er}^d - c_{er}^{d,ss}) \, dc_{cyt}^d \, dc_{er}^d$$

which due to the properties of the Dirac delta function is equal to $d\pi^{\mathcal{O}}/dt$, the left hand side of Eq. 2.42. The first term on the right hand side of Eq. 2.20 involving the partial derivative with respect to c_{cyt}^d disappears after integrating with respect to cytosolic and luminal domain Ca^{2+}, because

$$-\int_0^\infty \frac{\partial}{\partial c_{cyt}^d} \left[f_{cyt}^{\mathcal{O}} \rho^{\mathcal{O}} \right] dc_{cyt}^d = - \left. f_{cyt}^{\mathcal{O}} \rho^{\mathcal{O}} \right|_0^\infty = 0,$$

a consequence of the fact that the probability density $\rho^{\mathcal{O}}(c_{cyt}^d, c_{er}^d, t)$ evaluates to zero at the minimum and maximum physical values for the domain [Ca^{2+}]. Similarly, the second term on the right hand side of Eq. 2.20 involving the partial derivative with respect to c_{er}^d disappears,

$$-\int_0^\infty \frac{\partial}{\partial c_{er}^d} \left[f_{er}^{\mathcal{O}} \rho^{\mathcal{O}} \right] dc_{er}^d = - \left. f_{er}^{\mathcal{O}} \rho^{\mathcal{O}} \right|_0^\infty = 0.$$

Finally, each reaction term in Eq. 2.20 also reduces to the corresponding term in Eq. 2.42. For example,

$$k_b^+ \int_0^\infty \int_0^\infty (c_{cyt}^d)^\eta \rho^{\mathcal{O}} \, dc_{cyt}^d dc_{er}^d =$$

$$k_b^+ \int\limits_0^\infty \int\limits_0^\infty \left[(c_{cyt}^d)^\eta \pi^{\mathcal{O}} \delta(c_{cyt}^d - c_{cyt}^{d,ss}) \delta(c_{er}^d - c_{er}^{d,ss}) \right] dc_{cyt}^d dc_{er}^d =$$

$$k_b^+ (c_{cyt}^{d,ss})^\eta \pi^{\mathcal{O}} \int\limits_0^\infty \delta(c_{er}^d - c_{er}^{d,ss}) \, dc_{er}^d = k_b^+ (c_{cyt}^{d,ss})^\eta \pi^{\mathcal{O}}.$$

Note that due to the sifting property of the Dirac delta function, c_{cyt}^d becomes $c_{cyt}^{d,ss}$ for Ca^{2+}-mediated transitions out of open states ($\mathcal{O}$), while c_{cyt}^d becomes c_{cyt} for Ca^{2+}-mediated transitions out of closed states ($\mathcal{C}, \mathcal{R}_1, \mathcal{R}_2$; not shown).

As mentioned in Section 2.4.5.1, the fluxes J_{leak}, J_{pump}, and J_{rel}^T that occur in Eqs. 2.52–2.53 are functions of c_{cyt} and c_{er} that must be evaluated using the values of $\hat{c}_{cyt}$ and $\hat{c}_{er}$ found by integrating Eqs. 2.48 and 2.49. From Eqs. 2.39–2.40 we see that $c_{cyt}^{d,ss}$ and $c_{er}^{d,ss}$ are both functions of c_{cyt} and c_{er} that take the form

$$c_{cyt}^{d,ss} = \chi_{cyt}^1 c_{cyt} + \chi_{er}^1 c_{er}$$

$$c_{er}^{d,ss} = \chi_{cyt}^2 c_{cyt} + \chi_{er}^2 c_{er}$$

where $\chi_{cyt}^1 = v_{cyt}/(v_{cyt} + v_{er}')$, etc. Using these expressions and the values of the average domain Ca^{2+} concentrations ($\bar{c}_{cyt}^d$ and $\bar{c}_{er}^d$) given by Eqs. 2.46–2.47, we must solve

$$\hat{c}_{cyt} = c_{cyt} + \Lambda_{cyt}^d \left[\pi^{\mathcal{O}} \left(\chi_{cyt}^1 c_{cyt} + \chi_{er}^1 c_{er} \right) + \left(1 - \pi^{\mathcal{O}} \right) c_{cyt} \right]$$

$$\hat{c}_{er} = c_{er} + \frac{\Lambda_{er}^d}{\lambda_{er}} \left[\pi^{\mathcal{O}} \left(\chi_{cyt}^2 c_{cyt} + \chi_{er}^2 c_{er} \right) + \left(1 - \pi^{\mathcal{O}} \right) c_{er} \right]$$

simultaneously for c_{cyt} and c_{er}. Rearranging terms gives

$$\hat{c}_{cyt} = a_{11} c_{cyt} + a_{12} c_{er}$$

$$\hat{c}_{er} = a_{21} c_{cyt} + a_{22} c_{er}$$

where

$$a_{11} = 1 + \Lambda_{cyt}^d \left[\pi^{\mathcal{O}} \chi_{cyt}^1 + \left(1 - \pi^{\mathcal{O}}\right) \right]$$

$$a_{12} = \Lambda_{cyt}^d \pi^{\mathcal{O}} \chi_{er}^1$$

$$a_{21} = \Lambda_{er}^d \pi^{\mathcal{O}} \chi_{cyt}^2 / \lambda_{er}$$

$$a_{22} = 1 + \Lambda_{er}^d \left[\pi^{\mathcal{O}} \chi_{er}^2 + \left(1 - \pi^{\mathcal{O}}\right) \right] / \lambda_{er}.$$

From Cramer's rule we find

$$c_{cyt} = \frac{a_{22} \hat{c}_{cyt} - a_{12} \hat{c}_{er}}{D} \qquad c_{er} = \frac{a_{11} \hat{c}_{er} - a_{21} \hat{c}_{cyt}}{D} \tag{2.1}$$

where $D = a_{11}a_{22} - a_{12}a_{21}$. During numerical integration of Eqs. 2.52–2.53 these values of c_{cyt} and c_{er} back-calculated from $\hat{c}_{cyt}$ and $\hat{c}_{er}$ can be used to evaluate the fluxes J_{leak}, J_{pump}, and J_{rel}^T.

2.6.3 Slow domain/fast channel approximation

The derivation of the ODEs for the slow domain/fast channel approximation (Eqs. 2.59–2.62) begins with substitution of Eq. 2.55 into the advection-reaction equations of the multivariate probability density formulation (Eqs. 2.19–2.22), a procedure similar to that employed in the fast domain/slow channel case (Appendix 2.6.2). However, in the case of the slow domain/fast channel approximation, the reaction terms of the advection-reaction equations involving Ca^{2+} lead to terms in the ODE model that involve $c_{cyt}^{d,*}$ regardless of IP$_3$R state. For example, after substitution of Eq. 2.55 and integration, the first term on the right hand side of Eq. 2.19 given by $-k_a^+ \left(c_{cyt}^d\right)^\eta \rho^{\mathcal{C}}$ becomes $-k_a^+ (c_{cyt}^{d,*})^\eta \pi^{\mathcal{C}}$, as opposed to $-k_a^+ c_{cyt} \pi^{\mathcal{C}}$ in the fast domain/slow channel case.

In the slow domain/fast channel approximation, evaluating the fluxes J_{leak}, J_{pump}, and J_{rel}^T that occur in Eqs. 2.52–2.53 is similar to the fast domain/slow channel case.

From Eqs. 2.56–2.57 we see that $c_{cyt}^{d,ss}$ and $c_{er}^{d,ss}$ take the form

$$c_{cyt}^{d,*} = \chi_{cyt}^1 c_{cyt} + \chi_{er}^1 c_{er}$$

$$c_{er}^{d,*} = \chi_{cyt}^2 c_{cyt} + \chi_{er}^2 c_{er}$$

where $\chi_{cyt}^1 = v_{cyt}/(v_{cyt} + v_{er}^*)$, etc. Using these expressions and average domain Ca^{2+} concentrations given by Eq. 2.63, we see that in order to evaluate J_{leak}, J_{pump}, and J_{rel}^T, we must solve

$$\hat{c}_{cyt} = c_{cyt} + \Lambda_{cyt}^d \left[\chi_{cyt}^1 c_{cyt} + \chi_{er}^1 c_{er} \right]$$

$$\hat{c}_{er} = c_{er} + \frac{\Lambda_{er}^d}{\lambda_{er}} \left[\chi_{cyt}^2 c_{cyt} + \chi_{er}^2 c_{er} \right]$$

simultaneously for c_{cyt} and c_{er}. Ultimately we find an expression of the form of Eq. 2.1, but in this case $a_{11} = 1 + \Lambda_{cyt}^d \chi_{cyt}^1$, $a_{12} = \Lambda_{cyt}^d \chi_{er}^1$, $a_{21} = \Lambda_{er}^d \chi_{cyt}^2 / \lambda_{er}$, and $a_{22} = 1 + \Lambda_{er}^d \chi_{er}^2 / \lambda_{er}$.

2.6.4 Fast/slow reduction of the advection-reaction equations for the joint probability densities

While the reduced models presented in Section 2.4.5 are applicable when Ca^{2+} domains are either fast or slow compared to channel kinetics, it is interesting to note that the advection-reaction equations for the joint probability densities (Eqs. 2.19–2.22) can be reduced when some (but not necessarily all) transition rates in the single channel model are fast compared to the dynamics of Ca^{2+} domains. For example, consider the case of a four-state IP$_3$R model (Eq. 2.7) in which the process of Ca^{2+} activation (but not necessarily Ca^{2+} inactivation) is faster than Ca^{2+} domain formation and collapse. In this case, a Li-Rinzel-type reduction of the IP$_3$R model can be performed by assuming quasi-static equilibrium of the subset of channel transitions that are fast [Li and Rinzel, 1994]. To see this, define $\rho^W = \rho^C + \rho^O$ and sum Eqs. 2.19 and 2.20 to

obtain,

$$\frac{\partial \rho^{\mathcal{W}}}{\partial t} = -\frac{\partial}{\partial c_{cyt}^d} \left[f_{cyt}^{\mathcal{C}} \rho^{\mathcal{C}} + f_{cyt}^{\mathcal{O}} \rho^{\mathcal{O}} \right] - \frac{\partial}{\partial c_{er}^d} \left[f_{er}^{\mathcal{C}} \rho^{\mathcal{C}} + f_{er}^{\mathcal{O}} \rho^{\mathcal{O}} \right] \qquad (2.1)$$

$$- k_d^+ (c_{cyt}^d)^\eta \rho^{\mathcal{C}} - k_b^+ (c_{cyt}^d)^\eta \rho^{\mathcal{O}} + k_d^- \rho^{\mathcal{R}_2} + k_b^- \rho^{\mathcal{R}_1}.$$

Similarly, define $\rho^{\mathcal{V}} = \rho^{\mathcal{R}_1} + \rho^{\mathcal{R}_2}$ and sum Eqs. 2.21 and 2.22 to obtain,

$$\frac{\partial \rho^{\mathcal{V}}}{\partial t} = -\frac{\partial}{\partial c_{cyt}^d} \left[f_{cyt}^{\mathcal{R}_1} \rho^{\mathcal{R}_1} + f_{cyt}^{\mathcal{R}_2} \rho^{\mathcal{R}_2} \right] - \frac{\partial}{\partial c_{er}^d} \left[f_{er}^{\mathcal{R}_1} \rho^{\mathcal{R}_1} + f_{er}^{\mathcal{R}_2} \rho^{\mathcal{R}_2} \right] \qquad (2.2)$$

$$+ k_d^+ (c_{cyt}^d)^\eta \rho^{\mathcal{C}} + k_b^+ (c_{cyt}^d)^\eta \rho^{\mathcal{O}} - k_d^- \rho^{\mathcal{R}_2} - k_b^- \rho^{\mathcal{R}_1}.$$

Now under the assumption that $\mathcal{C} \leftrightarrow \mathcal{O}$ and $\mathcal{R}_1 \leftrightarrow \mathcal{R}_2$ transitions are much faster than the domain dynamics, we have

$$\rho^{\mathcal{C}} = \frac{K_a^\eta}{K_a^\eta + (c_{cyt}^d)^\eta} \rho^{\mathcal{W}} \qquad \rho^{\mathcal{O}} = \frac{(c_{cyt}^d)^\eta}{K_a^\eta + (c_{cyt}^d)^\eta} \rho^{\mathcal{W}}$$

$$\rho^{\mathcal{R}_2} = \frac{K_c^\eta}{K_c^\eta + (c_{cyt}^d)^\eta} \rho^{\mathcal{V}} \qquad \rho^{\mathcal{R}_1} = \frac{(c_{cyt}^d)^\eta}{K_c^\eta + (c_{cyt}^d)^\eta} \rho^{\mathcal{V}}$$

where $K_i^\eta = k_i^- / k_i^+$ for $i \in \{a, c\}$. Upon substitution into Eqs. 2.1 and 2.2 these relations yield

$$\frac{\partial \rho^{\mathcal{W}}}{\partial t} = -\frac{\partial}{\partial c_{cyt}^d} \left[\frac{f_{cyt}^{\mathcal{C}} K_a^\eta + f_{cyt}^{\mathcal{O}} (c_{cyt}^d)^\eta}{K_a^\eta + (c_{cyt}^d)^\eta} \rho^{\mathcal{W}} \right] - \frac{\partial}{\partial c_{er}^d} \left[\frac{f_{er}^{\mathcal{C}} K_a^\eta + f_{er}^{\mathcal{O}} (c_{cyt}^d)^\eta}{K_a^\eta + (c_{cyt}^d)^\eta} \rho^{\mathcal{W}} \right] + Z \quad (2.3)$$

$$\frac{\partial \rho^{\mathcal{V}}}{\partial t} = -\frac{\partial}{\partial c_{cyt}^d} \left[\frac{f_{cyt}^{\mathcal{R}_2} K_c^\eta + f_{cyt}^{\mathcal{R}_1} (c_{cyt}^d)^\eta}{K_c^\eta + (c_{cyt}^d)^\eta} \rho^{\mathcal{V}} \right] - \frac{\partial}{\partial c_{er}^d} \left[\frac{f_{er}^{\mathcal{R}_2} K_c^\eta + f_{er}^{\mathcal{R}_1} (c_{cyt}^d)^\eta}{K_c^\eta + (c_{cyt}^d)^\eta} \rho^{\mathcal{V}} \right] - Z$$

$$(2.4)$$

where the reaction terms are

$$Z = -\frac{k_d^+ K_a^\eta + k_b^+ (c_{cyt}^d)^\eta}{K_a^\eta + (c_{cyt}^d)^\eta} (c_{cyt}^d)^\eta \rho^{\mathcal{W}} + \frac{k_d^- K_c^\eta + k_b^- (c_{cyt}^d)^\eta}{K_c^\eta + (c_{cyt}^d)^\eta} \rho^{\mathcal{V}}. \qquad (2.5)$$

63

Thus, the original four advection-reaction equations (Eqs. 2.19–2.22) can be replaced by two (Eqs. 2.3–2.5). Note that the fraction of channels in the lumped states $\mathcal{W}$ and $\mathcal{V}$ sum to one (i.e., $\pi^{\mathcal{W}} + \pi^{\mathcal{V}} = 1$, where these quantities are found by integrating over the probability densities as in Eq. 2.32), but this fact cannot be used to eliminate Eq. 2.4 as occurs when the Li-Rinzel reduction applied to a conventional whole cell model to yield Eq. 2.2.

2.6.5 Generalization of the probability density approach

The probability density approach can be applied to single channel models of arbitrary complexity that include cytosolic Ca^{2+} regulation, luminal regulation, or both. Let $S(t) = i \in \{1, ..., M\}$ be the state of the single channel model and let the $M \times M$ matrix $Q(c_{cyt}^d, c_{er}^d)$ denote its infinitesimal generator matrix whose elements are transition rates that may be constant or functions of the cytosolic and luminal domain Ca^{2+} concentrations so that $\sum_i q_{ij} = 0$ and $q_{ij} \geq 0$ for $i \neq j$. Let us also rewrite the multivariate probability density functions defined in Eq. 2.18 using slightly more compact notation,

$$\rho^i(\boldsymbol{c}, t) \, d\boldsymbol{c} = \mathsf{P}\{\boldsymbol{c} < \tilde{\boldsymbol{c}}(t) < \boldsymbol{c} + d\boldsymbol{c} \text{ and } \tilde{S}(t) = i\},$$

where $\boldsymbol{c} = (c_{cyt}^d, c_{er}^d)$ is a vector including both the cytosolic and luminal domain Ca^{2+} concentrations and the probability of finding the randomly sampled IP$_3$R in state i is

$$\pi^i(t) = \mathsf{P}\{\tilde{S}(t) = i\} = \int \rho^i(\boldsymbol{c}, t) d\boldsymbol{c}$$

where $d\boldsymbol{c} = dc_{cyt}^d \, dc_{er}^d$.

Using this notation, the advection-reaction equations (Eqs. 2.19–2.22) for the probability density of cytosolic and luminal domain $[Ca^{2+}]$ jointly distributed with

64

the state of the IP$_3$R can be written compactly as

$$\frac{\partial \rho^i}{\partial t} = -\frac{\partial}{\partial c_{cyt}^d}[f_{cyt}^i \, \rho^i] - \frac{\partial}{\partial c_{er}^d}[f_{er}^i \, \rho^i] + [\boldsymbol{\rho}Q]^i \qquad (2.1)$$

where $\boldsymbol{\rho}$ is the row vector $\boldsymbol{\rho} = (\rho^1, \rho^2, ..., \rho^M)$ in which each element ρ^i is a function of c_{cyt}^d and c_{er}^d; and $[\boldsymbol{\rho}Q]^i$ is the ith element of the row vector resulting from a vector-matrix product of $\boldsymbol{\rho}$ and Q.

2.6.6 Numerical scheme for the multivariate probability density approach

The probability density approach is implemented by numerically solving the time-dependent system of advection-reaction equations given by Eq. 3.49,

$$\frac{\partial \rho^k}{\partial t} = -\frac{\partial \phi_{cyt}^k}{\partial c_{cyt}^d} - \frac{\partial \phi_{er}^k}{\partial c_{er}^d} + [\boldsymbol{\rho}Q]^k \qquad (2.1)$$

where the probability fluxes $\phi_{cyt}^k = f_{cyt}^k \rho^k$ and $\phi_{cyt}^k = f_{er}^k \rho^k$ are made explicit. We solve Eq. 2.1 on a uniform two-dimensional mesh with $I \times J$ points located at the domain concentrations

$$[(c_{cyt}^d)_i, (c_{er}^d)_j] = [c_{cyt}^{d,min} + i\Delta c_{cyt}^d, c_{er}^{d,min} + j\Delta c_{er}^d]$$

where $1 \leq i \leq I$, $1 \leq j \leq J$ and Δc_{cyt}^d and Δc_{er}^d are chosen so that $c_{cyt}^{d,max} = c_{cyt}^{d,min} + I\Delta c_{cyt}^d$ and $c_{er}^{d,max} = c_{er}^{d,min} + J\Delta c_{er}^d$. We use upwinded first order accurate finite difference approximations to the spatial derivatives in Eq. 2.1,

$$\left.\frac{\partial \phi_{cyt}}{\partial c_{cyt}^d}\right|_{i,j} \approx \begin{cases} \dfrac{(\phi_{cyt})_{i+1,j} - (\phi_{cyt})_{i,j}}{\Delta c_{cyt}^d} & \text{for} \quad (\phi_{cyt})_{i,j} < 0 \\[2ex] \dfrac{(\phi_{cyt})_{i,j} - (\phi_{cyt})_{i-1,j}}{\Delta c_{cyt}^d} & \text{for} \quad (\phi_{cyt})_{i,j} \geq 0 \end{cases}$$

65

$$
\left. \frac{\partial \phi_{er}}{\partial c_{er}^d} \right|_{i,j} \approx \begin{cases} \dfrac{(\phi_{er})_{i,j+1} - (\phi_{er})_{i,j}}{\Delta c_{er}^d} & \text{for} \quad (\phi_{er})_{i,j} < 0 \\[3mm] \dfrac{(\phi_{er})_{i,j} - (\phi_{er})_{i,j-1}}{\Delta c_{er}^d} & \text{for} \quad (\phi_{er})_{i,j} \geq 0 \end{cases}
$$

where we have dropped the index k (channel state) for clarity. Because the $\rho_{i,j}$ are non-negative, we can define $g_{i,j}^- = \min\left[0, (f_{cyt})_{i,j}\right]$, $g_{i,j}^+ = \max\left[0, (f_{cyt})_{i,j}\right]$, $h_{i,j}^- = \min\left[0, (f_{er})_{i,j}\right]$, $h_{i,j}^+ = \max\left[0, (f_{er})_{i,j}\right]$, and rewrite the previous equations as

$$
\begin{aligned}
\left. \frac{\partial \phi_{cyt}}{\partial c_{cyt}^d} \right|_{i,j} &\approx \frac{1}{\Delta c_{cyt}^d} \Big[g_{i+1,j}^- \rho_{i+1,j} \\
&\quad + \left(g_{i,j}^+ - g_{i,j}^- \right) \rho_{i,j} - g_{i-1,j}^+ \rho_{i-1,j} \Big] \\
\left. \frac{\partial \phi_{er}}{\partial c_{er}^d} \right|_{i,j} &\approx \frac{1}{\Delta c_{er}^d} \Big[h_{i,j+1}^- \rho_{i,j+1} \\
&\quad + \left(h_{i,j}^+ - h_{i,j}^- \right) \rho_{i,j} - h_{i,j-1}^+ \rho_{i,j-1} \Big].
\end{aligned}
$$

Combining these finite difference approximations with a backwards Euler time step

$$
\left. \frac{\partial \rho}{\partial t} \right|_n \approx \frac{\rho^{n+1} - \rho^n}{\Delta t} \tag{2.2}
$$

and substituting these expressions into Eq. 2.1, leads to the following numerical scheme

$$
\begin{aligned}
\frac{\rho_{i,j}^{k,n+1} - \rho_{i,j}^{k,n}}{\Delta t} &+ \frac{1}{\Delta c_{cyt}^d} \Big[g_{i+1,j}^- \rho_{i+1,j} + \left(g_{i,j}^+ - g_{i,j}^- \right) \rho_{i,j} \\
&- g_{i-1,j}^+ \rho_{i-1,j} \Big]^{k,n+1} \\
&+ \frac{1}{\Delta c_{er}^d} \Big[h_{i,j+1}^- \rho_{i,j+1} + \left(h_{i,j}^+ - h_{i,j}^- \right) \rho_{i,j} \\
&- h_{i,j-1}^+ \rho_{i,j-1} \Big]^{k,n+1} = R_{i,j}^{k,n+1}
\end{aligned} \tag{2.3}
$$

where we reintroduce the index k. In this expression, the reaction terms $R_{i,j}^{k,n+1}$ are a function of the densities $\rho_{i,j}^{1,n+1}, \rho_{i,j}^{2,n+1}, \cdots, \rho_{i,j}^{M,n+1}$ given by

$$R_{i,j}^{k,n+1} = \sum_{\hat{k}=1}^{M} \rho_{i,j}^{\hat{k},n+1} Q_{i,j}^{\hat{k},k} \tag{2.4}$$

$$= \sum_{\hat{k}=1}^{M} K_{\hat{k},k}^{-} \rho_{i,j}^{\hat{k},n+1} + (c_{cyt}^{d})_i^{\eta} \sum_{\hat{k}=1}^{M} K_{\hat{k},k}^{+} \rho_{i,j}^{\hat{k},n+1}$$

where $Q_{i,j}^{\hat{k},k}$ is the $\hat{k} \to k$ transition rate in the IP$_3$R model that may (or may not) depend on cytosolic domain Ca^{2+} through $(c_{cyt}^{d})_i^{\eta}$, and $Q = K^{-} + (c_{cyt}^{d})^{\eta} K^{+}$. Combining Eq. 2.3 and 2.4 leads to the following sparse linear system

$$\left\{ 1 + \bar{g}_{i,j}^{+} - \bar{g}_{i,j}^{-} + \bar{h}_{i,j}^{+} - \bar{h}_{i,j}^{-} - \bar{K}_{k,k}^{-} - \bar{K}_{k,k}^{+} \right\} \rho_{i,j}^{k,n+1}$$

$$- \bar{g}_{i-1,j}^{+} \, \rho_{i-1,j}^{k,n+1} + \bar{g}_{i+1,j}^{-} \, \rho_{i+1,j}^{k,n+1}$$

$$- \bar{h}_{i,j-1}^{+} \, \rho_{i,j-1}^{k,n+1} + \bar{h}_{i,j+1}^{-} \, \rho_{i,j+1}^{k,n+1} \tag{2.5}$$

$$- \sum_{\hat{k} \neq k} \bar{K}_{\hat{k},k}^{-} \rho_{i,j}^{\hat{k},n+1} - (c_{cyt}^{d})_i^{\eta} \sum_{\hat{k} \neq k} \bar{K}_{\hat{k},k}^{+} \rho_{i,j}^{\hat{k},n+1} = \rho_{i,j}^{k,n}$$

where the $\bar{g}^{\pm} = g^{\pm} \Delta t / \Delta c_{cyt}^{d}$ and $\bar{h}^{\pm} = h^{\pm} \Delta t / \Delta c_{er}^{d}$, and $\bar{K}^{\pm} = \Delta t K^{\pm}$. In each time step, this equation was solved to find $\rho_{i,j}^{k,n+1}$ from $\rho_{i,j}^{k,n}$ given the current value of $\bar{g}_{i,j}^{+}$, $\bar{g}_{i,j}^{-}$, $\bar{h}_{i,j}^{+}$, and $\bar{h}_{i,j}^{-}$, each of which depends on the current cytosolic and luminal bulk [Ca^{2+}] (c_{cyt} and c_{er}). Euler's method was then used to update c_{cyt} and c_{er} according to Eqs. 2.28 and 2.29 where the functionals defining J_{cyt}^{*} and J_{er}^{*} (Eqs. 2.30 and 2.31) are numerically evaluated at each time step.

Note that Eq. 2.5 can be used as written on the interior of the two-dimensional mesh ($1 < i < I$, $1 < j < J$), but when the indices i and j are at extreme values, the coefficients with indexes that are out of bounds are defined as zero, that is, $\bar{g}_{0,j}^{\pm} = \bar{g}_{I+1,j}^{\pm} = 0$ for all j and $\bar{h}_{i,0}^{\pm} = \bar{h}_{i,J+1}^{\pm} = 0$ for all i. Initial conditions for the discretized densities ($\rho_{i,j}^{k,n}$ for $n = 0$) were chosen so that the sum over indexes i, j, and k was

unity. We initially set $\rho_{i,j}^{k,0} = 0$ for any mesh point outside of the quadrilateral defined by superimposing the (four distinct) nullclines associated with domain Ca^{2+} dynamics (two for closed IP$_3$Rs, two for open IP$_3$Rs). It is also important to ensure there is always at least one mesh point between the outermost extent of the quadrilateral defined by these moving nullclines and the domain Ca^{2+} concentrations that bound the simulation ($c_{cyt}^{d,min}$, $c_{cyt}^{d,max}$, $c_{er}^{d,min}$, $c_{er}^{d,max}$), for example, if $c_{cyt}^{d,min} = 0$ then I and $c_{cyt}^{d,max}$ must be chosen so that $\Delta c_{cyt}^d < c_{cyt}$.

2.6.7 Spatial influences on global calcium dynamics

While the probability density approach to modeling local and global Ca^{2+} responses accurately accounts for the dynamics of cytosolic and luminal Ca^{2+} domains associated with a large number of IP$_3$Rs, it nevertheless assumes a continuously stirred bulk cytosolic and ER compartments. In order to investigate the significance of this limitation, the compartmental structure of the original Monte Carlo model presented in Section 2.3.1 that includes N IP$_3$Rs, $2N$ domains, and two bulk concentrations (shown schematically in Fig. 2.11A) is replicated at L mesh points located along the length of a one dimensional cell (Fig. 2.11B). That is, the concentration balance equations for bulk cytosolic and luminal Ca^{2+} originally given by Eqs. 2.8–2.11 are now explicitly spatial and include lateral diffusion with diffusion coefficient D_{er} and D_{cyt}), respectively,

$$\frac{dc_{cyt}^\ell}{dt} = D_{cyt}\frac{\partial^2 c_{cyt}^\ell}{\partial x^2} + J_{cyt}^{T,\ell} + J_{leak}^\ell - J_{pump}^\ell \tag{2.6}$$

$$\frac{dc_{er}^\ell}{dt} = D_{er}\frac{\partial^2 c_{er}^\ell}{\partial x^2} + \frac{1}{\lambda_{er}}\left(-J_{er}^{T,\ell} - J_{leak}^\ell + J_{pump}^\ell\right) \tag{2.7}$$

where $1 \leq \ell \leq L$. Associated with each mesh point are $2N$ time-dependent domains,

$$\frac{d(c_{cyt}^d)^{\ell,n}}{dt} = \frac{1}{\lambda_{cyt}^d}\left(J_{rel}^{\ell,n} - J_{cyt}^{\ell,n}\right) \tag{2.8}$$

$$\frac{d(c_{er}^d)^{\ell,n}}{dt} = \frac{1}{\lambda_{er}^d}\left(-J_{rel}^{\ell,n} + J_{er}^{\ell,n}\right) \qquad (2.9)$$

where $1 \leq n \leq N$, for a total of NL channels in the spatial model. The total efflux and refill fluxes from all the relevant Ca^{2+} domains are given by $J_{cyt}^{T,\ell} = \sum_{n=1}^{N} J_{cyt}^{\ell,n}$ and $J_{er}^{T,\ell} = \sum_{n=1}^{N} J_{er}^{\ell,n}$ and the fluxes $(J_{cyt}^{\ell,n}, J_{er}^{\ell,n}, J_{leak}^{\ell}, J_{pump}^{\ell})$ and effective volume ratios $(\lambda, \lambda_{cyt}^d$ and $\lambda_{er}^d)$ are as defined in Eqs. 2.15–2.17 and Eqs. 2.13–2.14. For example, the release of Ca^{2+} through the channel n at the ℓth mesh point is given by

$$J_{rel}^{\ell,n} = \gamma^{\ell,n} v_{rel}\left[(c_{cyt}^d)^{\ell,n} - (c_{er}^d)^{\ell,n}\right] \qquad (2.10)$$

where $\gamma^{\ell,n} = 0$ or 1. Simulations of the spatial model were performed by numerically solving Eqs. 2.6–2.9 using an explicit method with a forward first difference in time and a centered second difference in space.
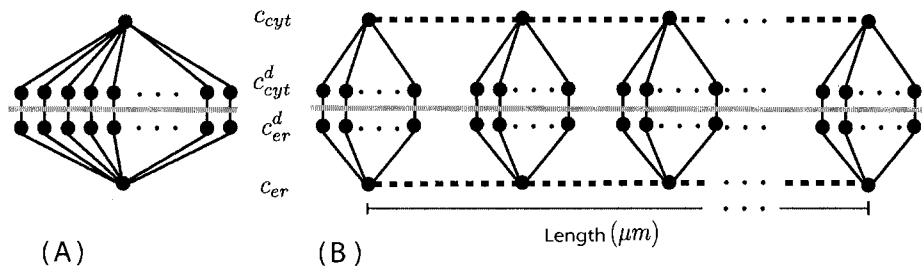
Figure 2.11: A) Schematic diagram of the original Monte Carlo model of Section 2.3.1. B) Diagram of spatially extended Monte Carlo model of Appendix E in which compartmental structure of panel A is replicated at L mesh points located along the length of a one dimensional cell with lateral diffusion between bulk cytosolic and luminal compartments (dashed lines).

Figure 2.12 shows the one-dimensional Monte Carlo results converging to the non-spatial probability density result as the diffusion coefficient for bulk cytosolic and ER Ca^{2+} is increased ($D = D_{cyt} = D_{er}$). In each panel the solid line is the bulk $[Ca^{2+}]$ (c_{cyt}) as calculated using the non-spatial probability density approach (Section 2.3.2), while the broken lines show the spatially averaged bulk $[Ca^{2+}]$ defined by

$$\langle c_{cyt} \rangle(t) = \frac{1}{L} \sum_{\ell=1}^{L} c_{cyt}^{\ell}.$$

for three Monte Carlo trials. When $D = 0.1$ $\mu m^2/s$ (upper panel of Fig. 2.12), the spatially averaged bulk Ca^{2+} concentrations in the one-dimensional Monte Carlo simulations are significantly different than the non-spatial probability density result. When D is in the more physiological range of 10–100 $\mu m^2/s$ (middle and bottom panels), the spatial and non-spatial calculations are very similar.
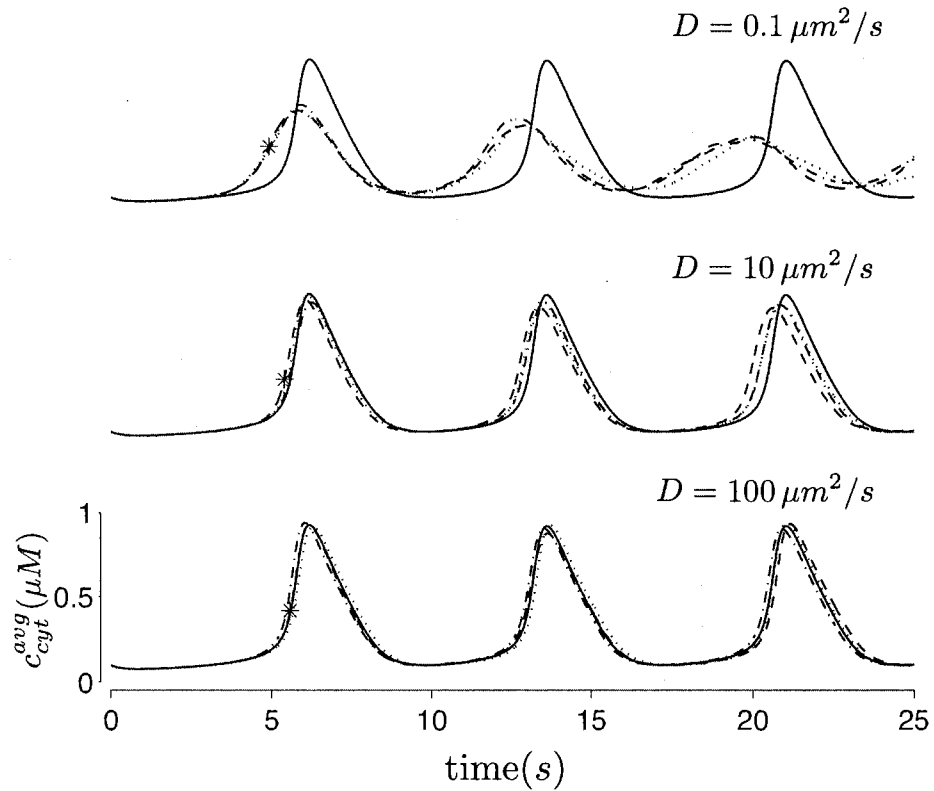
Figure 2.12: The average bulk Ca^{2+} concentration $\langle c_{cyt} \rangle$ as a function of time in the spatially extended Monte Carlo model. In each panel, the solid line is the non-spatial probability density calculation, while the dotted, dashed and dot-dashed lines show three Monte Carlo trials. In the top, middle, and bottom panels, the diffusion coefficient for bulk cytosolic and luminal Ca^{2+} ($D = D_{cyt} = D_{er}$) is increased from 0.1 to 100 $\mu m^2/s$. Asterisk indicates the time at which $\langle c_{cyt} \rangle =$ reaches 0.4 μM for one of the Monte Carlo trials.
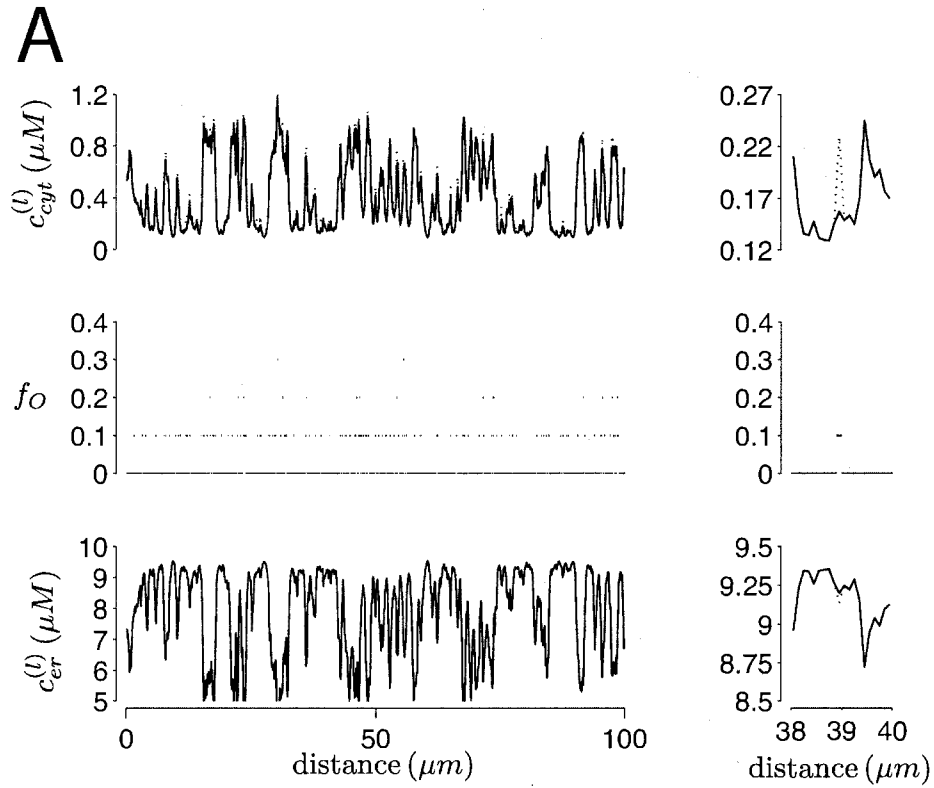
Figure 2.13: A) Concentration profiles at $t = 4.9$ s for spatial Monte Carlo simulation using $D = 0.1$ $\mu m^2/s$ (corresponding to asterisk in upper panel of Fig. 2.12). The top and bottom panels show the bulk cytosolic and luminal Ca^{2+} concentrations (solid lines) as well as the cytosolic and luminal domain Ca^{2+} concentrations (dotted lines). The middle panel shows the fraction of the N IP_3Rs channels at each mesh point that are open (f_O). Insets show results on different scales.
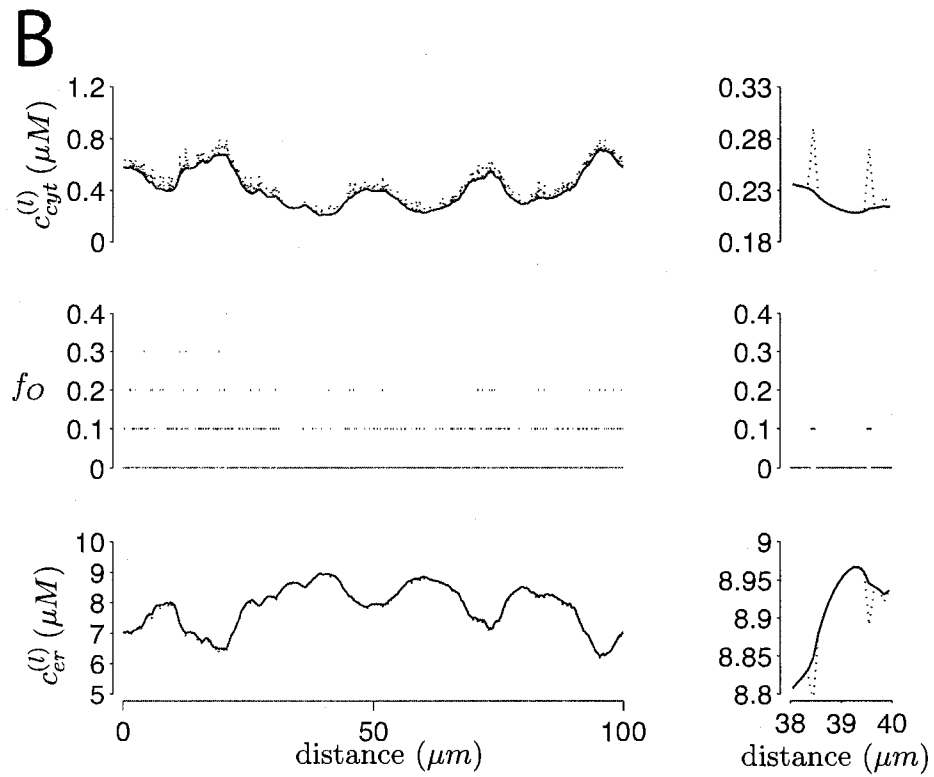
Figure 2.14: B) Concentration profiles at $t = 5.40$ s for spatial Monte Carlo simulation using $D = 10$ $\mu m^2/s$ (middle panel of Fig. 2.12). See legend of Fig. 2.13.

Figures 2.13 – 2.15 show the spatial profiles of the one dimensional Monte Carlo calculation for $D = 0.1$, 10 and 100 $\mu m^2/s$ at the times indicated by the asterisks in Fig. 2.12 when $\langle c_{cyt} \rangle$=0.4 μM. These concentration profiles show how the bulk and domain [Ca^{2+}] (both cytosolic and luminal) vary with spatial position. During these cell-wide global Ca^{2+} oscillations, the cytosolic and luminal bulk [Ca^{2+}] become more spatially uniform as D is increased. On the other hand, the insets in Figs. 2.13– 2.15 show that domain [Ca^{2+}] in the spatial model does not become less variable or equivalent to the bulk Ca^{2+} concentrations as D is increased. Rather, the cytosolic domain [Ca^{2+}] (dotted lines) is always greater than or equal to the cytosolic bulk [Ca^{2+}] (solid lines), and bulk Ca^{2+} is more likely to be in equilibrium with domain Ca^{2+} when the bulk Ca^{2+} diffusion coefficient (D) is small.

As physiologically realistic values for the diffusion coefficients are in the range 10–100 $\mu m^2/s$ [Allbritton et al., 1992, Hille, 2001], Figs. 2.12–2.15 together indicate that the assumption of continuously stirred bulk cytosolic and ER compartments is not a major limitation of the probability density approach to modeling the effect of local Ca^{2+} signals on global Ca^{2+} responses such as oscillations.
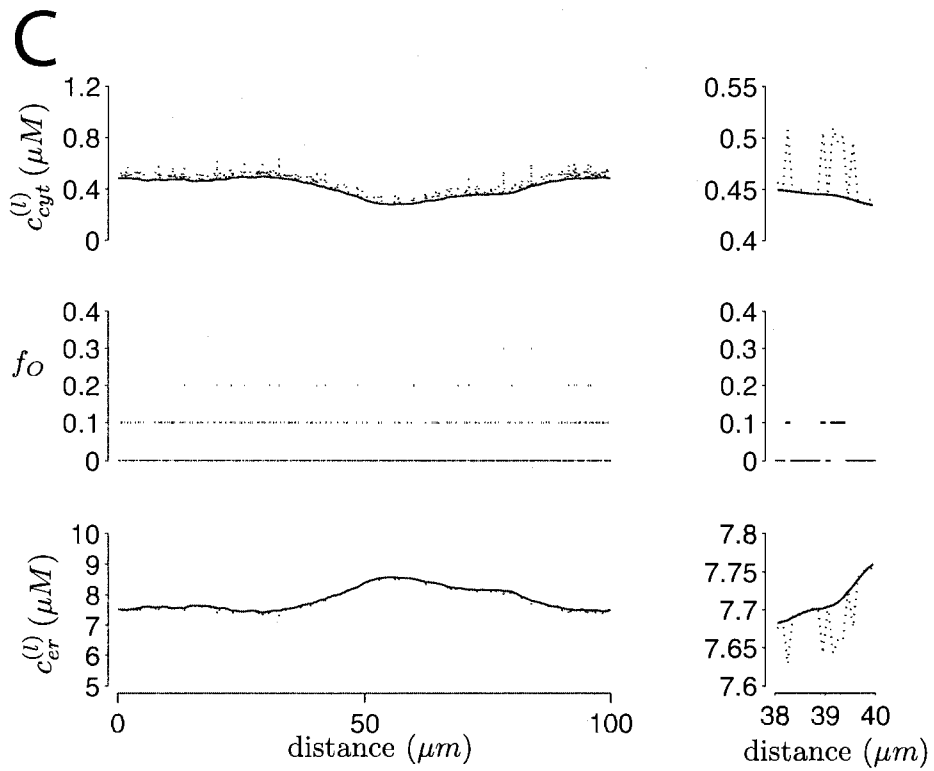
Figure 2.15: C) Concentration profiles at $t = 5.57$ s for spatial Monte Carlo simulation using $D = 100$ $\mu m^2/s$ (bottom panel of Fig. 2.12). See legend of Fig. 2.13.

Chapter 3

A probability density approach to modeling local control of calcium-induced calcium release in cardiac myocytes

3.1 Summary

We present a probability density approach to modeling localized Ca^{2+} influx via L-type Ca^{2+} channels and Ca^{2+}-induced Ca^{2+} release mediated by clusters of ryanodine receptors during excitation-contraction coupling in cardiac myocytes. Coupled advection-reaction equations are derived relating the time-dependent probability density of subsarcolemmal subspace and junctional sarcoplasmic reticulum $[Ca^{2+}]$ conditioned on "Ca^{2+} release unit" state. When these equations are solved numerically using a high-resolution finite difference scheme and the resulting probability densities are coupled to ordinary differential equations for the bulk myoplasmic and sarcoplasmic reticulum $[Ca^{2+}]$, a realistic but minimal model of cardiac excitation-contraction

coupling is produced. Modeling Ca^{2+} release unit activity using this probability density approach avoids the computationally demanding task of resolving spatial aspects of global Ca^{2+} signaling, while accurately representing heterogeneous local Ca^{2+} signals in a population of diadic subspaces and junctional sarcoplasmic reticulum depletion domains. The probability density approach is validated for a physiologically realistic number of Ca^{2+} release units and benchmarked for computational efficiency by comparison to traditional Monte Carlo simulations. In simulated voltage-clamp protocols, both the probability density and Monte Carlo approaches to modeling local control of excitation-contraction coupling produce high-gain Ca^{2+} release that is graded with changes in membrane potential, a phenomenon not exhibited by so-called "common pool" models. However, a probability density calculation can be significantly faster than the corresponding Monte Carlo simulation, especially when cellular parameters are such that diadic subspace $[Ca^{2+}]$ is in quasi-static equilibrium with junctional sarcoplasmic reticulum $[Ca^{2+}]$ and, consequently, univariate rather than multivariate probability densities may be employed.

The contents of this chapter were presented as "A probability density approach to modeling local control of calcium-induced calcium release in cardiac myocytes" in *Biophysical Journal* [George S. B. Williams, Marco A. Huertas, Eric A. Sobie, M. Saleet Jafri, and Gregory D. Smith, 92(7):2311–28, 2007]. The author gratefully acknowledges numerous discussions with Eric Sobie and Saleet Jafri who contributed significantly to the design and parameters of the Monte Carlo model. Some of these results have also appeared in poster form at the 2006 Biophysical Society Annual Meeting in Salt Lake City, UT.

3.2 Introduction

The mechanical function of the heart depends on complex bi-directional interactions between electrical and calcium (Ca^{2+}) signaling systems. Each time the heart beats, current flowing through the ion channels in the plasma membrane (sarcolemma) causes a characteristic change in membrane voltage known as an action potential (AP). Membrane depolarization during the AP causes L-type Ca^{2+} channels to open, and Ca^{2+} current through these channels causes the release of a larger amount of Ca^{2+} from the sarcoplasmic reticulum, a process known as Ca^{2+}-induced Ca^{2+} release (CICR). This leads to a large, transient increase in $[Ca^{2+}]$ in each heart cell, and contraction occurs when these Ca^{2+} ions bind to myofilaments, a sequence of events known as excitation-contraction (EC) coupling. In addition, intracellular $[Ca^{2+}]$ feeds back upon and changes the cell's membrane potential through the Ca^{2+}-dependence of several ion channels and membrane transporters.

Mathematical and computational modeling has proved to be an important tool for understanding cardiac electrophysiology and EC coupling. Computer simulations have been used to test hypotheses about heart cell function and predict underlying mechanisms [DiFrancesco and Noble, 1985, Nordin, 1993a, Jafri et al., 1998a, Luo and Rudy, 1994]. Most investigations have employed deterministic models that ignore molecular fluctuations and assume an isopotential cell, an approach that is valid for simulating current flowing through a large population of voltage-gated ion channels. Even though the individual channels open and close stochastically, each channel experiences the same voltage, so identical rate constants apply to each channel and only average behavior needs to be considered. However, this approach is not suitable for simulating CICR release during EC coupling because the overall release flux represents a collection of discrete events, known as Ca^{2+} sparks, evoked by local—rather than global—increases in Ca^{2+} concentration [Cheng et al., 1993b]. That is, each spark reflects Ca^{2+} release from a cluster of Ca^{2+}-regulated intracellular Ca^{2+} chan-

nels known as ryanodine receptors (RyRs) that is triggered by entry of Ca^{2+} through nearby L-type Ca^{2+} channels [Cannell et al., 1995b]. Thus, different groups of RyRs experience different local Ca^{2+} concentrations and stochastically gate in a manner that depends on whether nearby sarcolemmal Ca^{2+} channels have recently been open or closed. One consequence of this "local control" [Stern, 1992a] mechanism of cardiac CICR is that deterministic "common pool" models—whole cell models in which all RyR clusters in a myocyte experience the same $[Ca^{2+}]$—fail to reproduce several important experimental observations. In particular, the high gain and positive feedback of common pool models ensures that Ca^{2+} is released in an all-or-none fashion [Jafri et al., 1998a, Glukhovsky et al., 1998a, Snyder et al., 2000a, Nordin, 1993a, Tang and Othmer, 1994a] as opposed to being graded with the amount of Ca^{2+} influx, as observed in numerous experiments [Fabiato, 1985a, Wier et al., 1994a, Cannell et al., 1995b]. Deterministic common pool models of cardiac CICR during EC coupling that have been able to reproduced graded release have done so in an ad hoc fashion [Bondarenko et al., 2004, Luo and Rudy, 1994, Wong et al., 1992, Hilgemann and Noble, 1987, Shiferaw et al., 2003].

Models of EC coupling are able to simulate graded Ca^{2+} release mechanistically by treating L-type Ca^{2+} channels and juxtaposed Ca^{2+} release sites as stochastic "Ca^{2+} release units" (CaRUs), each of which is associated with its own diadic subspace Ca^{2+} concentration. When activated spontaneously or through membrane depolarization these CaRUs may deplete Ca^{2+} stored in localized regions of junctional SR and, on a slower time scale, interact with one another via diffusion of Ca^{2+} within the network SR and bulk myoplasm. This approach, however, requires relatively large computational resources to perform Monte-Carlo simulations of stochastic Ca^{2+} release from a large population of CaRUs. Indeed, the number of simulated CaRUs is often reduced to unphysiological values in such models to obtain shorter run times [Stern, 1992a, Rice et al., 1999a, Sobie et al., 2002a, Greenstein and Winslow, 2002a].

Two recent deterministic models have used a minimal Ca^{2+} release unit formulation of interactions between L-type channels and RyR clusters to produce graded release [Hinch, 2004, Greenstein et al., 2006]. In these models ordinary differential equations for the fraction of Ca^{2+} release units in each of a small number of states are solved under the assumption that subspace $[Ca^{2+}]$ is an algebraic function of the bulk myoplasmic and network SR $[Ca^{2+}]$. This function depends on Ca^{2+} release unit state and is determined by balancing the Ca^{2+} fluxes into and out of the diadic subspace. While the large number of Ca^{2+} release units in cardiac myocytes—estimated in the range of 10,000–20,000 via both structural [Chen-Izu et al., 2006] and functional [Cleemann et al., 1998] observations—does indeed suggest that it should be possible to produce deterministic local control models of EC coupling, the assumption that diadic subspace $[Ca^{2+}]$ is in quasi-static equilibrium with bulk myoplasmic and network SR Ca^{2+} may be overly restrictive. Indeed, this modeling approach is only valid when the dynamics of subspace $[Ca^{2+}]$ are very fast compared to stochastic Ca^{2+} release unit transition rates. Moreover, $[Ca^{2+}]$ in a particular subspace is likely to depend on the local "junctional" SR $[Ca^{2+}]$ rather than the bulk or network SR $[Ca^{2+}]$, especially if junctional SR depletion influences RyR gating, as suggested by both simulations [Sobie et al., 2002a] and recent experiments [Terentyev et al., 2002a, Brochet et al., 2005].

Here we present an alternative deterministic formalism for modeling local control of CICR during cardiac EC coupling that captures the collective behavior of a large population of Ca^{2+} release units without this restrictive assumption. We utilize the fact that the number of Ca^{2+} release units is large (similar to references [Hinch, 2004] and [Greenstein et al., 2006]), but we do *not* assume a simple algebraic relationship between the local diadic subspace $[Ca^{2+}]$ associated with each Ca^{2+} release unit and the bulk Ca^{2+} concentrations. Instead, we define a set of multivariate continuous probability density functions for the diadic subspace and junctional SR $[Ca^{2+}]$

conditioned on CaRU state [Mazzag et al., 2005a, Huertas and Smith, 2006a]. As described below, these probability density functions solve a system of advection-reaction equations that are derived from the stochastic ordinary differential equations used in Monte Carlo simulations of local control. These equations are solved numerically using a high-resolution finite difference scheme while coupled to ordinary differential equations for the bulk myoplasmic and network SR $[Ca^{2+}]$. This produces a minimal model of cardiac EC coupling that avoids computationally demanding Monte Carlo simulation while accurately representing heterogeneous local Ca^{2+} signals; in particular, the statistical recruitment of CaRUs and the dynamics of junctional SR depletion, spark termination, and junctional SR refilling.

3.3 Model Formulation

The minimal whole cell model of cardiac EC coupling that is the focus of this paper can be formulated as a traditional Monte Carlo calculation in which heterogeneous local Ca^{2+} signals associated with a large number of Ca^{2+} release units (CaRUs) are simulated. In this Monte Carlo formulation, a diadic subspace and junctional SR compartment is associated with each CaRU and the $[Ca^{2+}]$ in these compartments is found by solving a large number of ordinary differential equations. Alternatively, these heterogeneous local Ca^{2+} signals can be simulated using a novel probability density approach that represents the distribution of diadic subspace and junctional SR Ca^{2+} concentrations with a system of partial differential equations (see below). Because many of the equations and parameters of the whole cell model of EC coupling are identical in the two formulations, we begin by presenting the Monte Carlo formulation.

3.3.1 Whole cell model of EC coupling — Monte Carlo formulation

Figure 4.1 shows a diagram of the components and fluxes of the model of local Ca^{2+} signaling and CaRU activity during cardiac EC coupling that is the focus of this paper. As illustrated in Fig. 4.1A, each Ca^{2+} release unit includes two restricted compartments (the diadic subspace and junctional SR) with $[Ca^{2+}]$ denoted by c_{ds}^n and c_{jsr}^n, respectively, where the superscripted n is an index over a total number of Ca^{2+} release units (denoted by N). Each Ca^{2+} release unit includes an L-type Ca^{2+} channel (DHPR) and a minimal representation of a cluster of RyRs that is either fully closed or fully open. The fluxes J_{dhpr}^n and J_{ryr}^n indicate Ca^{2+} entry into a subspace via the DHPR or RyR cluster, respectively. Diffusion of Ca^{2+} between the nth diadic subspace and bulk myoplasm (c_{myo}) is indicated by J_{efflux}^n. Similarly, J_{refill}^n indicates diffusion between the network SR (c_{nsr}) and junctional SR compartment associated with the nth Ca^{2+} release unit.

Figure 4.1B illustrates how the bulk myoplasm and network SR Ca^{2+} concentrations in the model are coupled via the diffusion fluxes (J_{efflux}^n and J_{refill}^n) to a large number of Ca^{2+} release units (for clarity only four are shown). Importantly, each of the N Ca^{2+} release units may have a different diadic subspace (c_{ds}^n) and junctional SR (c_{jsr}^n) Ca^{2+} concentration. Four additional fluxes directly influence the bulk myoplasm: a background Ca^{2+} influx denoted by J_{in}, extrusion of Ca^{2+} via the Na^+-Ca^{2+} exchanger (J_{ncx}), SR Ca^{2+}-ATPase (SERCA) pumps (J_{serca}) that resequester Ca^{2+} into the network SR, and a passive leak out of the network SR to the bulk myoplasm (J_{leak}).

A complete description of CICR would include stochastic gating of roughly N = 20,000 CaRUs, each of which would contain multiple L-type Ca^{2+} channels (1–10) [Bers and Stiffel, 1993] and RyRs (30–300) [Franzini-Armstrong, 1999], with each individual channel described by a Markov chain that consists of two to several tens of

83
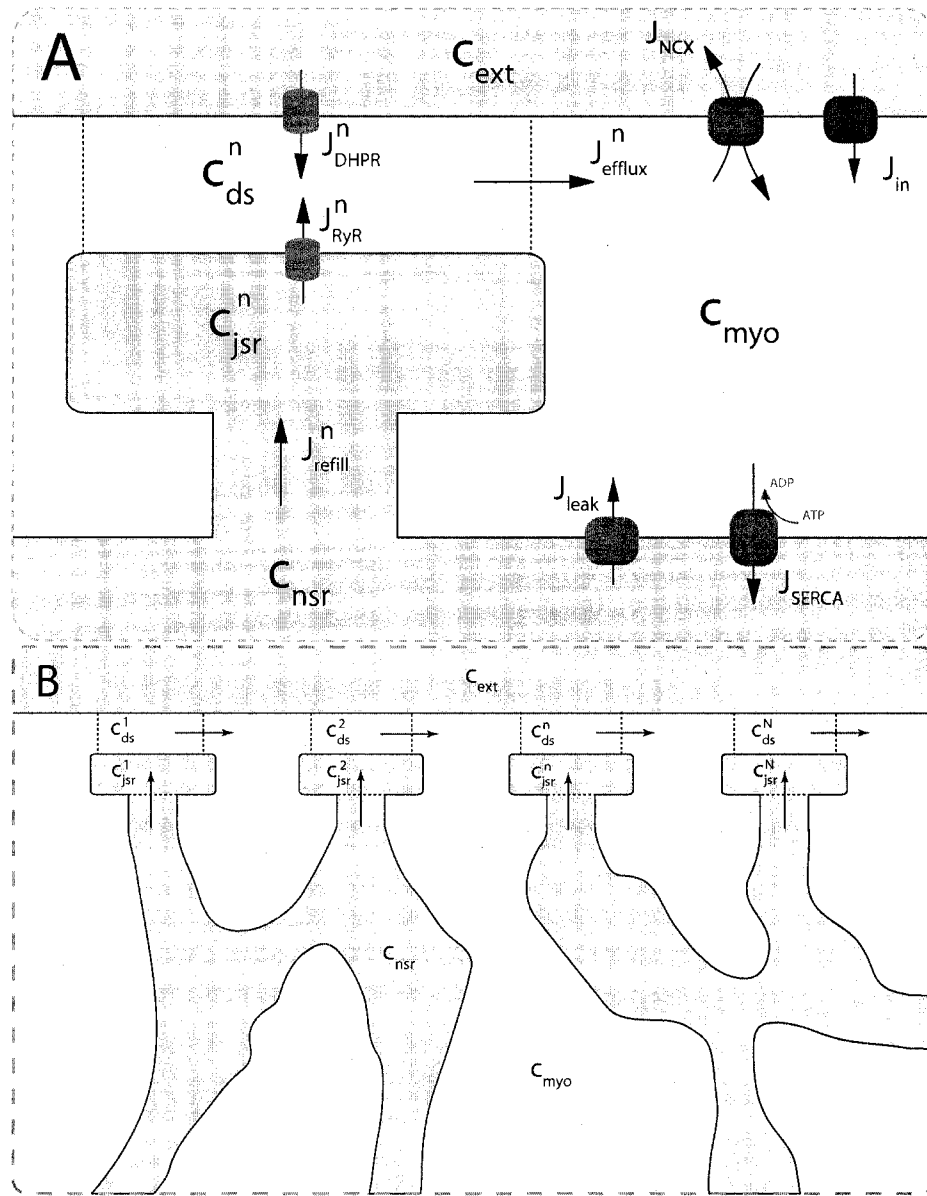
Figure 3.1: Diagrams of model components and fluxes. A: Each Ca^{2+} release unit consists of two restricted compartments (the diadic subspace and junctional SR with $[Ca^{2+}]$ denoted by c_{ds} and c_{jsr}, respectively), a two-state L-type Ca^{2+} channel (DHPR), and a two-state Ca^{2+} release site (a RyR "megachannel" [Sobie et al., 2002a]). The t-tubular $[Ca^{2+}]$ is denoted by c_{ext} and the fluxes J_{dhpr}^{n}, J_{ryr}^{n}, J_{efflux}^{n}, J_{refill}^{n}, J_{in}, J_{ncx}, J_{serca}, and J_{leak} are described in the text. B: The bulk myoplasm (c_{myo}) and network SR (c_{nsr}) Ca^{2+} concentrations in the model are coupled via J_{efflux}^{n} and J_{refill}^{n} to a large number of Ca^{2+} release units (for clarity only four are shown), each with different diadic subspace (c_{ds}^{n}) and junctional SR (c_{jsr}^{n}) Ca^{2+} concentration.

states. However, previous Monte Carlo simulations of EC coupling focusing on local control have often used Markov models of reduced complexity [Stern, 1992a, Sobie et al., 2002a, Hinch, 2004]. Because such minimal models capture the essential characteristics of EC coupling gain and gradedness in simulated whole cell voltage clamp protocols, this level of resolution will suffice for our main purpose, which is to introduce the probability density approach as an alternative to Monte Carlo simulation.

3.3.1.1 A minimal four-state calcium release unit model

Previous modeling studies indicate that the gating of the cluster of RyRs associated with each CaRU is all-or-none [Stern, 1992a, Rice et al., 1999a, Sobie et al., 2002a] and this suggests the following minimal two-state model of an RyR "megachannel,"

$$
[\text{closed}] \; \mathcal{C} \quad \underset{k_{ryr}^{-}}{\overset{k_{ryr}^{+}\left(c_{ds}^{n}, c_{jsr}^{n}\right)}{\rightleftharpoons}} \quad \mathcal{O} \; [\text{open}] \tag{3.1}
$$
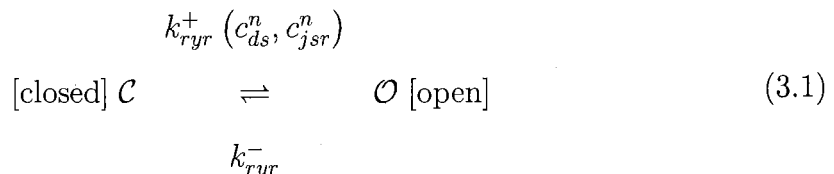
where the Ca^{2+} activation of the cluster of RyRs is a sigmoidal function of the diadic subspace $[Ca^{2+}]$ [Sobie et al., 2002a],

$$
k_{ryr}^{+} = \bar{k}_{ryr}^{+} \frac{(c_{ds}^{n})^4}{(K_{ryr})^4 + (c_{ds}^{n})^4},
$$

and the influence of junctional SR $[Ca^{2+}]$ on RyR gating is included by making the half-maximal activation of the RyR megachannel (K_{ryr}) a decreasing function of c_{jsr}^{n},

$$
K_{ryr} = K_{ryr}^{max} - \alpha_{ryr} \, c_{jsr}^{n},
$$

so that depletion of the junctional SR will render CaRUs refractory to activation after release terminates [Sobie et al., 2002a].

Similarly, to illustrate and validate the probability density approach it is sufficient

to consider a two-state model of the L-type Ca^{2+} channel (DHPR),

$$[\text{closed}]\ \mathcal{C} \underset{k_{dhpr}^{-}}{\overset{k_{dhpr}^{+}(V)}{\rightleftharpoons}} \mathcal{O}\ [\text{open}] \tag{3.2}$$
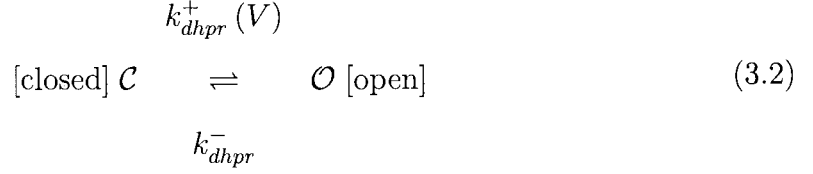
with a voltage-dependent activation rate k_{dhpr}^{+} given by [Luo and Rudy, 1994]

$$k_{dhpr}^{+} = \bar{k}_{dhpr}^{+} \frac{e^{(V-V_{dhpr}^{\theta})/\sigma_{dhpr}}}{1 + e^{(V-V_{dhpr}^{\theta})/\sigma_{dhpr}}}$$

and constant de-activation rate k_{dhpr}^{-} that sets the mean open time (0.2 ms) and maximum open probability (0.1) of the channel. Although this two-state DHPR model ignores voltage- and Ca^{2+}-dependent inactivation of L-type Ca^{2+} channels, these processes do not significantly influence the triggering of CICR during the whole-cell voltage clamp protocols that are the focus of this paper (cf. [Hinch, 2004]).

When the kinetic schemes of the RyR megachannel and DHPR (Eq. 3.1 and Eq. 3.2) are combined we obtain the following minimal four-state model of a Ca^{2+} release unit,

$$
\begin{array}{ccc}
[\text{both closed}]\ \mathcal{CC} & \underset{k_{ryr}^{-}}{\overset{k_{ryr}^{+}\left(c_{ds}^{n},c_{jsr}^{n}\right)}{\rightleftharpoons}} & \mathcal{CO}\ [\text{RyRs open}] \\
k_{dhpr}^{+}(V)\ \downarrow\uparrow\ k_{dhpr}^{-} & & k_{dhpr}^{-}\ \uparrow\downarrow\ k_{dhpr}^{+}(V) \\
[\text{DHPR open}]\ \mathcal{OC} & \underset{k_{ryr}^{+}\left(c_{ds}^{n},c_{jsr}^{n}\right)}{\overset{k_{ryr}^{-}}{\rightleftharpoons}} & \mathcal{OO}\ [\text{both open}]
\end{array}
\tag{3.3}
$$
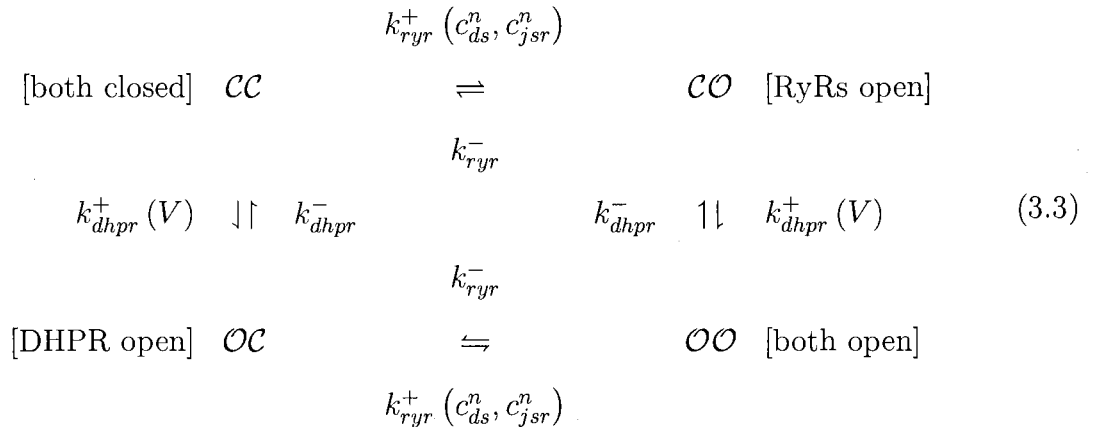
where the horizontal transitions represent RyR opening and closing while vertical transitions represent DHPR gating.

3.3.1.2 Concentration balance equations

In the Monte Carlo formulation of the minimal whole cell model of EC coupling there are $2 + 2N$ ordinary differential equations representing Ca^{2+} concentration balance for the bulk myoplasm, network SR, N diadic subspaces, and N junctional SRs. Consistent with Fig. 4.1 these equations are

$$\frac{dc_{myo}}{dt} = J_{leak} + J_{efflux}^T - J_{ncx} - J_{serca} + J_{in} \tag{3.4}$$

$$\frac{dc_{ds}^n}{dt} = \frac{1}{\lambda_{ds}} \left(J_{dhpr}^n + J_{ryr}^n - J_{efflux}^n \right) \tag{3.5}$$

$$\frac{dc_{jsr}^n}{dt} = \frac{1}{\lambda_{jsr}} \left(J_{refill}^n - J_{ryr}^n \right) \tag{3.6}$$

$$\frac{dc_{nsr}}{dt} = \frac{1}{\lambda_{nsr}} \left(J_{serca} - J_{refill}^T - J_{leak} \right) \tag{3.7}$$

where $1 \leq n \leq N$ in Eqs. 3.5 and 3.6 and the total efflux and refill fluxes occurring in Eqs. 3.4 and 3.7 include a contribution from each CaRU and thus are given by $J_{refill}^T = \sum_{n=1}^N J_{refill}^n$ and $J_{efflux}^T = \sum_{n=1}^N J_{efflux}^n$. Similarly, the total (trigger) flux via dihydropiridine receptor (DHPR) channels and the total release flux via RyR megachannels throughout the whole cell model are given by

$$J_{dhpr}^T = \sum_{n=1}^N J_{dhpr}^n \quad \text{and} \quad J_{ryr}^T = \sum_{n=1}^N J_{ryr}^n. \tag{3.8}$$

The effective volume ratios λ_{nsr}, λ_{ds}, and λ_{jsr} in Eqs. 3.7–3.6 are defined with respect to the physical volume (V_{myo}) and include a constant-fraction Ca^{2+} buffer capacity for the myoplasm (β_{myo}). For example, the effective volume ratio associated with the network SR is

$$\lambda_{nsr} = \frac{\hat{V}_{nsr}}{\hat{V}_{myo}} = \frac{V_{nsr}/\beta_{nsr}}{V_{myo}/\beta_{myo}}$$

with effective volumes defined by $\hat{V}_{nsr} = V_{nsr}/\beta_{nsr}$ and $\hat{V}_{myo} = V_{myo}/\beta_{myo}$. Because each individual diadic subspace is assumed to have the same physical volume (V_{ds})

and buffering capacity (β_{ds}), the effective volume ratio that occurs in Eq. 3.5 is

$$\lambda_{ds} = \frac{\hat{V}_{ds}}{\hat{V}_{myo}} = \frac{V_{ds}/\beta_{ds}}{V_{myo}/\beta_{myo}} = \frac{1}{N}\left(\frac{V_{ds}^T/\beta_{ds}}{V_{myo}/\beta_{myo}}\right) \tag{3.9}$$

where the second expression defines λ_{ds} in terms of the total physical volume of all the diadic subspaces in aggregate ($V_{ds}^T = NV_{ds}$). Similar assumptions and equations apply for the junctional SR so that the definition of λ_{jsr} follows Eq. 3.9.

We also define an overall myoplasmic [Ca^{2+}] that includes contributions from the bulk myoplasm and each of the N diadic spaces (scaled by their effective volumes),

$$\hat{c}_{myo\&ds} = \frac{\hat{V}_{myo}\,c_{myo} + \hat{V}_{ds}\sum_{n=1}^{N} c_{ds}^n}{\hat{V}_{myo} + N\hat{V}_{ds}} = \frac{\hat{V}_{myo}\,c_{myo} + \hat{V}_{ds}^T c_{ds}^{avg}}{\hat{V}_{myo} + \hat{V}_{ds}^T}, \tag{3.10}$$

where the second equality uses natural definitions for the total effective diadic subspace volume, $\hat{V}_{ds}^T = N\hat{V}_{ds}$, and the average diadic subspace [Ca^{2+}],

$$c_{ds}^{avg} = \frac{1}{N}\sum_{n=1}^{N} c_{ds}^n. \tag{3.11}$$

Similarly, the overall SR [Ca^{2+}] involves both the junctional and network SR,

$$\hat{c}_{nsr\&jsr} = \frac{\hat{V}_{nsr}c_{nsr} + \hat{V}_{jsr}\sum_{n=1}^{N} c_{jsr}^n}{\hat{V}_{nsr} + N\hat{V}_{jsr}} = \frac{\hat{V}_{nsr}c_{nsr} + \hat{V}_{jsr}^T c_{jsr}^{avg}}{\hat{V}_{nsr} + \hat{V}_{jsr}^T} \tag{3.12}$$

where $\hat{V}_{jsr} = V_{jsr}/\beta_{jsr}$, $\hat{V}_{jsr}^T = N\hat{V}_{jsr}$, and the average junctional SR [Ca^{2+}] is defined as $c_{jsr}^{avg} = N^{-1}\sum_{n=1}^{N} c_{jsr}^n$.

3.3.1.3 Description of fluxes

The trigger Ca^{2+} flux into each of the N diadic spaces through DHPR channels (J_{dhpr}^n in Eq. 3.5) is given by

$$J_{dhpr}^n = -\frac{A_m}{zF}I_{dhpr}^n \tag{3.13}$$

88

where $A_m = C_m \beta_{myo}/V_{myo}$. The inward Ca^{2+} current ($I_{dhpr}^n \leq 0$) is given by

$$I_{dhpr}^n = \gamma_{dhpr}^n \frac{P_{dhpr}^T}{N} \left(\frac{zFV}{V_\theta} \right) \left(\frac{c_{ds}^n e^{V/V_\theta} - c_{ext}}{e^{V/V_\theta} - 1} \right) \tag{3.14}$$

where $V_\theta = RT/zF$, P_{dhpr}^T is the total (whole cell) permeability of the L-type Ca^{2+} channels, and γ_{dhpr}^n is a random variable that is 0 when the L-type Ca^{2+} channel associated with the nth CaRU is closed and 1 when this channel is open (Eqs. 3.2 and 3.3).

Similarly, the flux through the RyR megachannel associated with the nth CaRU (J_{ryr}^n) is given by

$$J_{ryr}^n = \gamma_{ryr}^n \frac{v_{ryr}^T}{N} (c_{jsr}^n - c_{ds}^n) \tag{3.15}$$

where $\gamma_{ryr}^n = 0$ or 1 when the release site is closed or open, respectively (Eqs. 3.1 and 3.3). Diffusion from each subspace into the bulk myoplasm is given by

$$J_{efflux}^n = \frac{v_{efflux}^T}{N} (c_{ds}^n - c_{myo}) \tag{3.16}$$

and, similarly, diffusion from the network SR to each junctional SR compartment is given by

$$J_{refill}^n = \frac{v_{refill}^T}{N} (c_{nsr} - c_{jsr}^n). \tag{3.17}$$

The remaining four fluxes that appear in Eqs. 3.4–3.6 include J_{in} (background Ca^{2+} influx), J_{ncx} (Na$^+$-Ca^{2+} exchange), J_{serca} (SR Ca^{2+}-ATPases), and J_{leak} (the network SR leak). The functional form of these four fluxes that directly influence the bulk myoplasmic [Ca^{2+}] follows previous work [Jafri et al., 1998a, Rice et al., 2000, Shannon et al., 2000] (see Appendix 3.6.1).

3.3.2 Whole cell model of EC coupling — probability density formulation

The probability density approach to modeling local Ca^{2+} signaling and CaRU activity during cardiac EC coupling is an alternative to Monte Carlo simulation that is valid when the number of Ca^{2+} release units is large. We begin by defining continuous multivariate probability density functions for the diadic subspace ($\tilde{c}_{ds}$) and junctional SR ($\tilde{c}_{jsr}$) Ca^{2+} concentrations jointly distributed with the state of the Ca^{2+} release unit ($\tilde{S}$) [Bertram and Sherman, 1998, Nykamp and Tranchina, 2000, Mazzag et al., 2005a], that is,

$$
\begin{aligned}
\rho^i(c_{ds}, c_{jsr}, t) \, dc_{ds} dc_{jsr} = \ & \mathsf{Pr}\{c_{ds} < \tilde{c}_{ds}(t) < c_{ds} + dc_{ds} \text{ and} \\
& c_{jsr} < \tilde{c}_{jsr}(t) < c_{jsr} + dc_{jsr} \text{ and } \tilde{S}(t) = i\} \quad (3.18)
\end{aligned}
$$

where the index $i \in \{\mathcal{CC}, \mathcal{CO}, \mathcal{OC}, \mathcal{OO}\}$ runs over the four Ca^{2+} release unit states (see Eq. 3.3) and the tildes on $\tilde{c}_{ds}(t)$, $\tilde{c}_{jsr}(t)$, and $\tilde{S}(t)$ indicate random quantities. If the meaning of Eq. 3.18 is not obvious, it may be helpful to imagine performing a Monte Carlo simulation as described in the previous section with a very large number of CaRUs. At any time t one could randomly sample one CaRU from this population to produce an instance of the random variables $\tilde{S}(t)$, $\tilde{c}_{ds}(t)$, and $\tilde{c}_{jsr}(t)$, corresponding to the current state of the sampled L-type channel and RyR cluster and the diadic subspace and junctional SR [Ca^{2+}] associated with this CaRU. The quantity $\rho^i(c_{ds}, c_{jsr}, t)$ defined in Eq. 3.18 simply indicates the probability with which you would find this sampled CaRU in state i with diadic subspace [Ca^{2+}] in the range $[c_{ds}, c_{ds} + dc_{ds}]$ and junctional SR [Ca^{2+}] in the range $[c_{jsr}, c_{jsr} + dc_{jsr}]$ provided the total number of CaRUs is very large.

For the multivariate probability densities defined by Eq. 3.18 to be consistent with the dynamics of the Monte Carlo model of cardiac EC coupling described in

the previous section, they must satisfy the following system of advection-reaction equations [Mazzag et al., 2005a, Huertas and Smith, 2006a],

$$\frac{\partial \rho^{CC}}{\partial t} = -\frac{\partial}{\partial c_{ds}}\left[f_{ds}^{CC}\rho^{CC}\right] - \frac{\partial}{\partial c_{jsr}}\left[f_{jsr}^{CC}\rho^{CC}\right] - \left(k_{ryr}^{+} + k_{dhpr}^{+}\right)\rho^{CC} + k_{ryr}^{-}\rho^{CO} + k_{dhpr}^{-}\rho^{OC}$$

$$\tag{3.19}$$

$$\frac{\partial \rho^{CO}}{\partial t} = -\frac{\partial}{\partial c_{ds}}\left[f_{ds}^{CO}\rho^{CO}\right] - \frac{\partial}{\partial c_{jsr}}\left[f_{jsr}^{CO}\rho^{CO}\right] - \left(k_{ryr}^{-} + k_{dhpr}^{+}\right)\rho^{CO} + k_{ryr}^{+}\rho^{CC} + k_{dhpr}^{-}\rho^{OO}$$

$$\tag{3.20}$$

$$\frac{\partial \rho^{OC}}{\partial t} = -\frac{\partial}{\partial c_{ds}}\left[f_{ds}^{OC}\rho^{OC}\right] - \frac{\partial}{\partial c_{jsr}}\left[f_{jsr}^{OC}\rho^{OC}\right] - \left(k_{ryr}^{+} + k_{dhpr}^{-}\right)\rho^{OC} + k_{ryr}^{-}\rho^{OO} + k_{dhpr}^{+}\rho^{CC}$$

$$\tag{3.21}$$

$$\frac{\partial \rho^{OO}}{\partial t} = -\frac{\partial}{\partial c_{ds}}\left[f_{ds}^{OO}\rho^{OO}\right] - \frac{\partial}{\partial c_{jsr}}\left[f_{jsr}^{OO}\rho^{OO}\right] - \left(k_{ryr}^{-} + k_{dhpr}^{-}\right)\rho^{OO} + k_{ryr}^{+}\rho^{OC} + k_{dhpr}^{+}\rho^{CO}$$

$$\tag{3.22}$$

where the advection rates f_{ds}^{CC}, f_{ds}^{CO}, $\cdots$, f_{jsr}^{OO} are functions of c_{ds} and c_{jsr} that can be read off the ordinary differential equations for the evolution the diadic subspace and junctional SR [Ca^{2+}]. Consistent with Eqs. 3.5 and 3.6 we have

$$f_{ds}^{i} = \frac{1}{\lambda_{ds}^{T}}\left(\gamma_{dhpr}^{i}J_{dhpr}^{T} + \gamma_{ryr}^{i}J_{ryr}^{T} - J_{efflux}^{T}\right) \tag{3.23}$$

$$f_{jsr}^{i} = \frac{1}{\lambda_{jsr}^{T}}\left(J_{refill}^{T} - \gamma_{ryr}^{i}J_{ryr}^{T}\right) \tag{3.24}$$

where γ_{dhpr}^{i} indicates whether or not the L-type Ca^{2+} channel is open ($\gamma_{dhpr}^{CC} = \gamma_{dhpr}^{CO} = 0$, $\gamma_{dhpr}^{OC} = \gamma_{dhpr}^{OO} = 1$) and, similarly, γ_{ryr}^{i} indicates whether or not the RyR channel cluster is open ($\gamma_{ryr}^{CC} = \gamma_{ryr}^{CO} = 0$, $\gamma_{ryr}^{OC} = \gamma_{ryr}^{OO} = 1$). Eqs. 3.23 and 3.24 include four fluxes that may influence the diadic subspace and junctional SR [Ca^{2+}] and consistent

91

with Eqs. 3.13–4.5 these are given by

$$J_{ryr}^T = v_{ryr}^T \left(c_{jsr} - c_{ds} \right) \tag{3.25}$$

$$J_{efflux}^T = v_{efflux}^T \left[c_{ds} - c_{myo}(t) \right] \tag{3.26}$$

$$J_{refill}^T = v_{refill}^T \left[c_{nsr}(t) - c_{jsr} \right] \tag{3.27}$$

$$J_{dhpr}^T = -A_m P_{dhpr}^T \frac{V}{V_\theta} \left(\frac{c_{ds}^n e^{V/V_\theta} - c_{ext}}{e^{V/V_\theta} - 1} \right). \tag{3.28}$$

The advection terms in Eqs. 3.19–3.22 involving partial derivatives with respect to c_{ds} and c_{jsr} correspond to the deterministic dynamics of diadic subspace and junctional SR Ca^{2+} that depend on Ca^{2+} release unit state via γ_{dhpr}^i and γ_{ryr}^i (Eqs. 3.5–3.6). Conversely, the reaction terms in Eqs. 3.19 and 3.22 correspond to the stochastic gating of the four-state Ca^{2+} release unit model whose transition rates are presented above (Eqs. 3.1–3.3). That is, Ca^{2+} release unit state changes move probability from one joint probability density to another in a manner that may $[k_{ryr}^+ (c_{ds}, c_{jsr})]$ or may not $[k_{dhpr}^+ (V), \ k_{dhpr}^-, \ \text{and} \ k_{ryr}^-]$ depend on the diadic subspace and junctional SR $[Ca^{2+}]$.

It is important to note that the functional form of the fluxes J_{efflux}^T and J_{refill}^T occurring in Eqs. 3.23 and 3.24 involve the bulk myoplasmic and network SR Ca^{2+} concentrations $[c_{myo}(t)$ and $c_{nsr}(t)$ in Eqs. 3.26 and 3.27]. These bulk Ca^{2+} concentrations satisfy ODEs that are similar in form to the concentration balance equations used in the Monte Carlo approach (Eqs. 3.4 and 3.7),

$$\frac{dc_{myo}}{dt} = J_{leak} + J_{efflux}^* - J_{ncx} - J_{serca} + J_{in} \tag{3.29}$$

$$\frac{dc_{nsr}}{dt} = \frac{1}{\lambda_{nsr}} \left(J_{serca} - J_{refill}^* - J_{leak} \right) \tag{3.30}$$

where J_{leak}, J_{ncx}, J_{serca}, and J_{in} are defined as in the Monte Carlo approach (see Appendix A), but J_{efflux}^* and J_{refill}^* are functionals of the probability densities $[\rho^i(c_{ds}, c_{jsr}, t)]$

governed by Eqs. 3.19–3.22, that is,

$$J_{efflux}^* = \int_0^\infty \int_0^\infty v_{efflux}^T \left[c_{ds} - c_{myo}(t)\right] \rho^T (c_{ds}, c_{jsr}, t) dc_{ds} dc_{jsr} \qquad (3.31)$$

$$J_{refill}^* = \int_0^\infty \int_0^\infty v_{refill}^T \left[c_{nsr}(t) - c_{jsr}\right] \rho^T (c_{ds}, c_{jsr}, t) dc_{ds} dc_{jsr} \qquad (3.32)$$

where $\rho^T (c_{ds}, c_{jsr}, t) = \rho^{CC} + \rho^{CO} + \rho^{OC} + \rho^{OO}$ is the total probability distribution of the diadic subspace and junctional SR $[Ca^{2+}]$ irrespective of the state of a randomly sampled CaRU, and the double integrals account for all possible values of diadic and junctional SR $[Ca^{2+}]$.

3.3.3 Summary of model formulation

The probability density and Monte Carlo formulations of the minimal model of EC coupling presented above have much in common. For example, the dynamics of the bulk myoplasmic and network SR $[Ca^{2+}]$ take similar forms (compare Eqs. 3.29–3.30 to Eqs. 3.4 and 3.7). However, the two approaches differ fundamentally in how the heterogeneous localized Ca^{2+} concentrations associated with a large number of Ca^{2+} release units are represented. In the traditional Monte Carlo simulation, $2N$ ordinary differential equations are solved to determine the dynamics of $[Ca^{2+}]$ in the diadic subspace and junctional SR compartments associated with N Ca^{2+} release units (Eqs. 3.5 and 3.6). In the probability density formulation, time-dependent multivariate probability densities for the diadic subspace and junctional SR $[Ca^{2+}]$ jointly distributed with CaRU state are updated by solving four coupled advection-reaction equations (Eqs. 3.19–3.22), one for each state of the chosen CaRU model (Eq. 3.3). Further details of the probability density approach presented in Appendices 3.6.2 – 3.6.4.

Parameter	Definition	Value
N	number of diadic subspaces	50–20000
V_{nsr}	network SR volume	3.15×10^{-7} μL
V_{myo}	myoplasmic volume	2.15×10^{-5} μL
$V_{ds}^T = NV_{ds}$	total diadic subspace volume	2×10^{-8} μL
$V_{jsr}^T = NV_{jsr}$	total junctional SR volume	3.5×10^{-8} μL
C_m	capacative membrane area	1.534×10^{-4} μF
β_{ds}	subspace buffering factor	0.5
β_{jsr}	junctional SR buffering factor	0.05
β_{nsr}	network SR buffering factor	1.0
β_{myo}	myoplasmic buffering factor	0.05
$v_{refill}^T = \lambda_{jsr}^T / \tau_{refill}$	junctional SR refilling rate	0.018 s^{-1}
$v_{efflux}^T = \lambda_{ds}^T / \tau_{efflux}$	diadic subspace efflux rate	5.2 s^{-1}
F	Faraday's constant	96480 coul mol^{-1}
R	gas constant	8314 mJ mol^{-1} K^{-1}
T	absolute temperature	$310K$
c_{ext}	extracellular Ca^{2+} concentration	1.8 mM
$[Na^+]_{ext}$	extracellular Na$^+$ concentration	140 mM
$[Na^+]_{myo}$	intracellular Na$^+$ concentration	10.2 mM

Table 3.1: Model parameters: volume fractions, Ca^{2+} buffering, and exchange between restricted domains and the bulk, physical constants, and fixed ion concentrations.

Parameter	Definition	Value
$v_{ryr}^T = N v_{ryr}$	total RyR cluster release rate	0.9 s^{-1}
$P_{dhpr}^T = N P_{dhpr}$	total DHPR permeability	3.5×10^{-5} cm s^{-1}
V_{dhpr}^θ	DHPR activation threshold	-10 mV
σ_{dhpr}	DHPR activation parameter	6.24 mV
$\bar{k}_{dhpr}^+$	maximum rate of DHPR opening	556 s^{-1}
k_{dhpr}^-	rate of DHPR closing	5000 s^{-1}
$\bar{k}_{ryr}^+$	maximum rate of RyR opening	2000 s^{-1}
k_{ryr}^-	rate of RyR closing	100 s^{-1}
K_{ryr}^{max}	maximum binding constant for RyR	7.4 μM
α_{ryr}	coefficient of RyR luminal regulation	0.0024

Table 3.2: Ca^{2+} release unit parameters (L-type Ca^{2+} channel and RyR cluster).

Parameter	Definition	Value
K_{fs}	forward half-saturation constant for SERCA pump	$0.17~\mu M$
K_{rs}	reverse half-saturation constant	$1702~\mu M$
η_{fs}	forward cooperativity constant	0.75
η_{rs}	reverse cooperativity constant	0.75
v_{serca}	maximum SERCA pump rate	$8.6~\mu M~s^{-1}$
I^o_{ncx}	magnitude of Na^+-Ca^{2+} exchange current	$150~\mu A~\mu F^{-1}$
$K_{ncx,n}$	Na^+ half saturation constant	$87.5 \times 10^3 \mu M$
$K_{ncx,c}$	Ca^{2+} half saturation constant	$1.38 \times 10^3 \mu M$
k^{sat}_{ncx}	saturation factor	0.1
η_{ncx}	voltage dependence of Na^+-Ca^{2+} exchange	0.35
v_{leak}	SR Ca^{2+} leak rate constant	$2.4 \times 10^{-6}~s^{-1}$
g_{in}	maximum conductance of background Ca^{2+} influx	$1.5 \times 10^{-4}~mS~\mu F^{-1}$

Table 3.3: Model parameters: Na^+-Ca^{2+} exchange current, SERCA pumps, and background Ca^{2+} influx.

3.4 Results

In the following sections, traditional Monte Carlo simulations of voltage-clamp protocols using the minimal whole cell model of EC coupling presented above are shown to produce high-gain Ca^{2+} release that is graded with changes in membrane potential, a phenomenon not exhibited by so-called "common pool" models of excitation-contraction coupling. Analysis of these Monte Carlo results suggests a simplification of the advection-reaction equations that form the basis of the probability density approach. This reduced probability density formulation is subsequently validated against, and benchmarked for computational efficiency by comparison to, traditional Monte Carlo simulations.

3.4.1 Representative Monte Carlo simulations

Figures 3.2A shows representative Monte Carlo simulations of the minimal whole cell model of EC coupling presented above (Eqs. 3.1–4.5 and Appendix 3.6.1). In this simulated voltage-clamp protocol, the holding potential of -80 mV is followed by a 20 ms duration test potential to -30, -20, and -10 mV (*dotted, dot-dashed,* and *solid lines,* respectively). Because these simulations involve a large but finite number of Ca^{2+} release units ($N = 5000$), the resulting Ca^{2+} influx through L-type Ca^{2+} channels (J_{dhpr}^T), elevation in the average diadic subspace concentration (c_{ds}^{avg}), and the induced Ca^{2+} release flux (J_{ryr}^T) are erratic functions of time. As expected, the test potential of -10 mV leads to greater Ca^{2+} influx, higher diadic subspace $[Ca^{2+}]$, and more Ca^{2+} release than the test potentials of -30 and -20 mV. When the test potential is -10 mV a 30X "gain" is observed, here defined here as the ratio $\bar{J}_{ryr}^T / \bar{J}_{dhpr}^T$ where the overbar indicates an average over the duration of the pulse. Importantly, Ca^{2+} release exhibited by this Monte Carlo model is graded with changes in membrane potential (compare traces) and depolarization duration (not shown), phenomena that
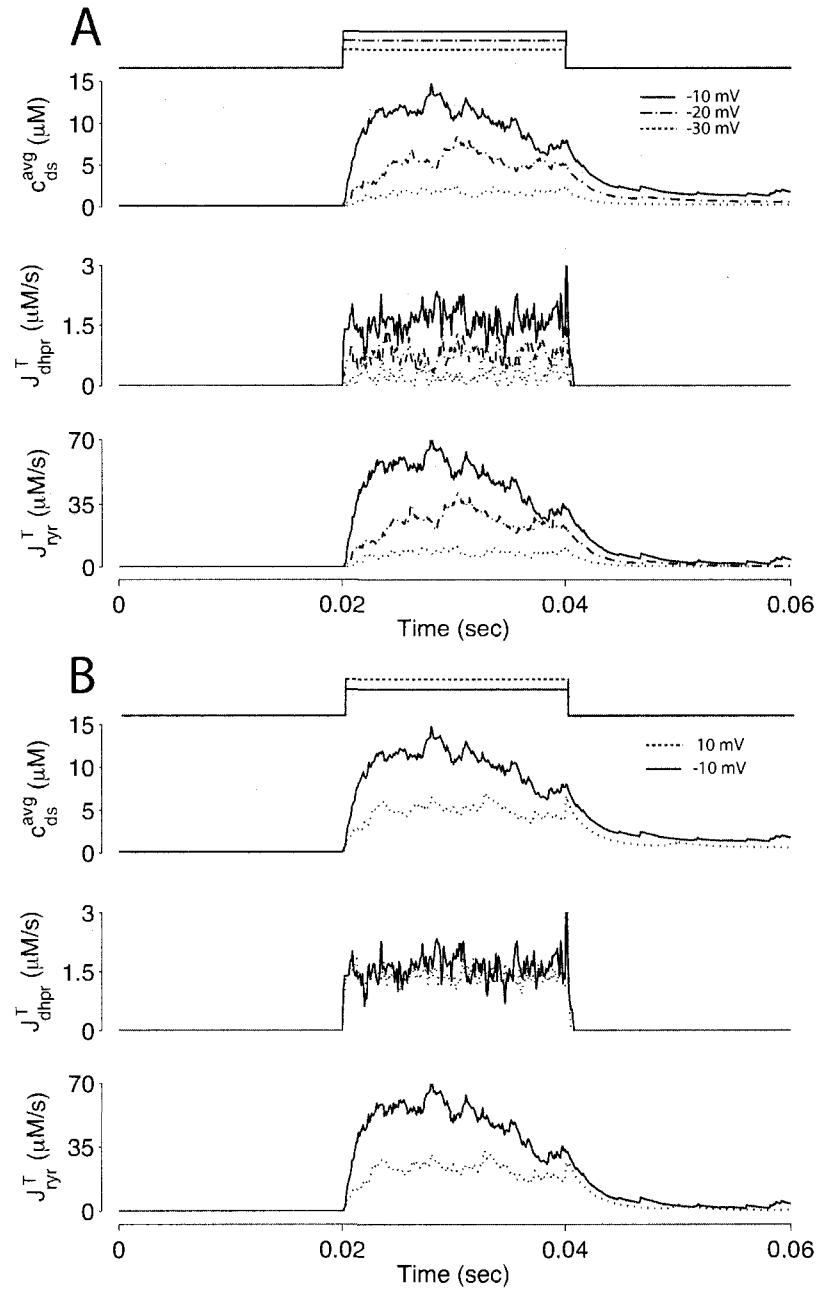
Figure 3.2: A: Monte Carlo simulation of the whole cell model exhibits graded release during step depolarization from a holding potential of -80 mV to -30, -20 and -10 mV (*dotted, dot-dashed,* and *solid lines,* respectively). From top to bottom: command voltage, average diadic subspace $[Ca^{2+}]$ (c_{ds}^{avg}, Eq. 3.11), total Ca^{2+} flux via L-type PM Ca^{2+} channels (J_{dhpr}^{T}, Eqs. 3.8, 3.13, 3.14), and total Ca^{2+}-induced Ca^{2+} release flux (J_{ryr}^{T}, Eqs. 3.8 and 3.15). The simulation used $N = 5000$ Ca^{2+} release units. B: Monte Carlo simulations similar to panel A except that the step potential is -10 (*solid lines*) and $+10$ mV (*dotted lines*), respectively. Here and below parameters are as in Tables 3.1 – 3.3.

are not exhibited by common pool models of excitation-contraction coupling.

Figures 3.2B shows a direct comparison between test potentials of -10 and 10 mV. These test potentials result in nearly identical whole cell Ca^{2+} currents (averaged over the duration of the pulse, $\bar{J}^T_{dhpr} = 1.6$ and 1.4 $\mu M/s$, respectively). In spite of this, the induced Ca^{2+} release flux is significantly greater when the test potential is -10 mV ($\bar{J}^T_{ryr} = 47$ $\mu M/s$) as opposed to 10 mV (21 $\mu M/s$). This phenomenon occurs because the L-type channel open probability is greater at 10 mV than -10 mV (Eq. 3.2), while the driving force for Ca^{2+} ions is reduced (Eqs. 3.14 and 3.14). Although the overall trigger Ca^{2+} flux is nearly the same at these two test potentials, Ca^{2+} release is more effectively induced when the trigger Ca^{2+} is apportioned in larger quantities among a smaller number of diadic subspaces, because the influx that does occur is then more likely to trigger Ca^{2+} sparks. This physiologically realistic aspect of local control during EC coupling is observed in Monte Carlo simulations (see also [Greenstein and Winslow, 2002a, Greenstein et al., 2006]), but can not be reproduced by common pool models [Stern, 1992a], nor is it seen in models in which SR Ca^{2+} release depends explicitly on whole-cell Ca^{2+} current (e.g., [Shiferaw et al., 2003]).

The *solid lines* of Fig. 3.3 show $[Ca^{2+}]$ in the bulk myoplasm (c_{myo}) and network SR (c_{nsr}) during and after the -10 mV voltage pulse (note change in time scale). Approximately 400 ms is required for the bulk myoplasm and network SR concentrations to return to resting levels. Note that although the voltage pulse ends at $t = 30$ ms, the bulk myoplasmic $[Ca^{2+}]$ continues to increase for approximately 20 ms. Similarly, the network SR $[Ca^{2+}]$ concentration continues to decrease until $t = 80$ ms.

The *dashed line* of Figure 3.3 shows that the total SR $[Ca^{2+}]$ including both network and junctional SR (Eq. 3.12) is transiently *less than* the network SR $[Ca^{2+}]$ ($\hat{c}_{nsr\&jsr} < c_{nsr}$), reflecting the fact that for several hundred milliseconds after the voltage pulse junctional SR Ca^{2+} is depleted. While the ratio between the total junctional SR effective volume and the network SR effective volume is $\hat{V}^T_{jsr}/\hat{V}_{nsr} \approx 2$,
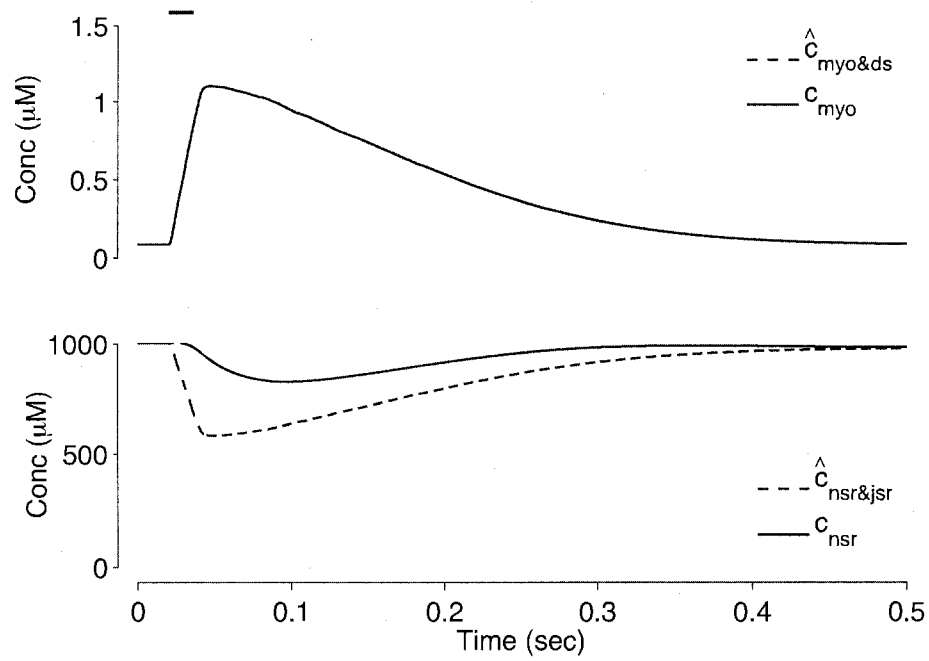
Figure 3.3: *Solid lines* show the dynamics of bulk myoplasmic (c_{myo}) and network SR (c_{nsr}) [Ca^{2+}] in the whole cell voltage clamp protocol of Fig. 3.2 with step potential of -10 mV (note longer time scale). *Dashed lines* show the overall myoplasmic ($\hat{c}_{myo\&ds}$, Eq. 3.10) and network SR ($\hat{c}_{nsr\&jsr}$, Eq. 3.12) [Ca^{2+}] that include contributions from diadic subspaces and junctional SR, respectively. Note that $\hat{c}_{myo\&ds}$ is only slightly greater than c_{myo} and the two traces are not distinguishable.

the corresponding ratio between the total diadic subspace volume and the myoplasmic volume is much smaller $(\hat{V}_{ds}^T / \hat{V}_{myo} \approx 10^{-4})$. Consequently, the elevated average diadic subspace $[\text{Ca}^{2+}]$ during the depolarizing voltage step $(c_{ds}^{avg} \approx 10 \ \mu\text{M}$ as shown in Fig. 3.2) does not significantly increase the overall myoplasmic $[\text{Ca}^{2+}]$ $(\hat{c}_{myo\&ds} \approx c_{myo}$ and the two traces overlap in Fig. 3.3). On the other hand, depleted junctional SR Ca^{2+} during and after the voltage pulse $(c_{jsr}^{avg} \approx 500 \ \mu\text{M}$, not shown) represents a significant depletion of the overall SR Ca^{2+} content $(\hat{c}_{nsr\&jsr} < c_{nsr}$ in Fig. 3.3). While junctional SR depletion develops rapidly after the initiation of the voltage pulse, refilling of these compartments via diffusion of Ca^{2+} from the network SR $(J_{refill}^n$ in Eq. 3.6) is not complete until approximately 400 ms after the termination of the voltage pulse (compare *solid* and *dashed lines*).

Dynamics of a representative calcium release unit

Figure 3.4 shows the dynamics of an individual Ca^{2+} release unit from the Monte Carlo simulations above (test potential of -10 mV, *solid line* of Fig. 3.2). Figure 3.4A shows the state of this representative Ca^{2+} release unit and the associated diadic subspace and junctional SR Ca^{2+} concentrations. When the DHPR initially opens (transition from state $\mathcal{CC}$ to $\mathcal{OC}$ in Eq. 3.3) an influx of trigger Ca^{2+} leads to $\sim 7 \ \mu\text{M}$ increase in diadic subspace $[\text{Ca}^{2+}]$ and causes the RyR cluster to open $(\mathcal{OC} \rightarrow \mathcal{OO}$ transition). The resulting Ca^{2+}-induced Ca^{2+} release quickly drives the diadic subspace $[\text{Ca}^{2+}]$ to $\sim 150 \ \mu\text{M}$ but over the next 10 ms the resulting decrease in junctional SR $[\text{Ca}^{2+}]$ leads to decreasing diadic subspace $[\text{Ca}^{2+}]$. Note that junctional SR depletion is nearly complete in Fig. 3.4 before the $\mathcal{CO}$ to $\mathcal{CC}$ transition that ends Ca^{2+} release; however, this example is not representative in this regard as most sparks terminate via stochastic attrition while depletion is only partial. Superimposed on the gradual decrease in diadic subspace $[\text{Ca}^{2+}]$ are square pulses of increased $[\text{Ca}^{2+}]$ $(\pm 7 \ \mu\text{M})$ due to the stochastic openings of the L-type Ca^{2+} channel associated with this CaRU

$(\mathcal{CO} \leftrightarrows \mathcal{OO}$ transitions).

The observation that diadic subspace [Ca^{2+}] decreases during the voltage-pulse suggests that its dynamics are fast compared to the time-evolution of junctional SR [Ca^{2+}]. In fact, for the physiologically realistic parameters used in Figs. 3.2–3.4, the diadic subspace [Ca^{2+}] (c_{ds}^n) is well-approximated by assuming quasi-static equilibrium with the junctional SR (c_{jsr}^n), bulk myoplasmic (c_{myo}), and network SR (c_{nsr}) Ca^{2+} concentrations. Setting the $dc_{ds}^n/dt = 0$ in Eq. 3.5 and solving for c_{ds}^n we find that

$$c_{ds}^n \approx \frac{\gamma_{dhpr}^i J_{dhpr}^0 + v_{efflux}^T c_{myo} + \gamma_{ryr}^i v_{ryr}^T c_{jsr}^n}{\gamma_{ryr}^i v_{ryr}^T + v_{efflux}^T - \gamma_{dhpr}^i J_{dhpr}^1} \qquad (3.33)$$

where γ_{dhpr}^i and γ_{ryr}^i depend on Ca^{2+} release unit state and J_{dhpr}^0 and J_{dhpr}^1 are functions of plasma membrane voltage defined by $J_{dhpr}^T = J_{dhpr}^0 + c_{ds} J_{dhpr}^1$ with J_{dhpr}^T as in Eq. 4.4.

Figure 3.4B replots the dynamics of the diadic subspace and junctional SR [Ca^{2+}] shown in Fig. 3.4A in the (c_{ds}, c_{jsr})-plane. The *black arrows* indicate the direction of the trajectories and color of the *solid lines* indicates CaRU state ($\mathcal{CC}$ black, $\mathcal{OC}$ green, $\mathcal{OO}$ red, $\mathcal{CO}$ blue). The diagonal trajectory is one consequence of diadic subspace [Ca^{2+}] being "slaved" to junctional SR [Ca^{2+}] as the junctional SR depletes. The four colored *dotted lines* correspond to the four functional relationships between c_{ds}^n and c_{jsr}^n given by Eq. 3.33 (one for each CaRU state). The dynamics of diadic subspace [Ca^{2+}] (*solid lines*) are well-approximated by these *dotted lines* (save for short time intervals immediately following CaRU state transitions), demonstrating the validity of the quasi-static approximation leading to Eq. 3.33.

3.4.2 Dynamics of the population of calcium release units

Figure 3.4 shows the dynamics of the diadic subspace and junctional SR [Ca^{2+}] associated with a single Ca^{2+} release unit during a voltage clamp step (Figs. 3.2 and 3.3).
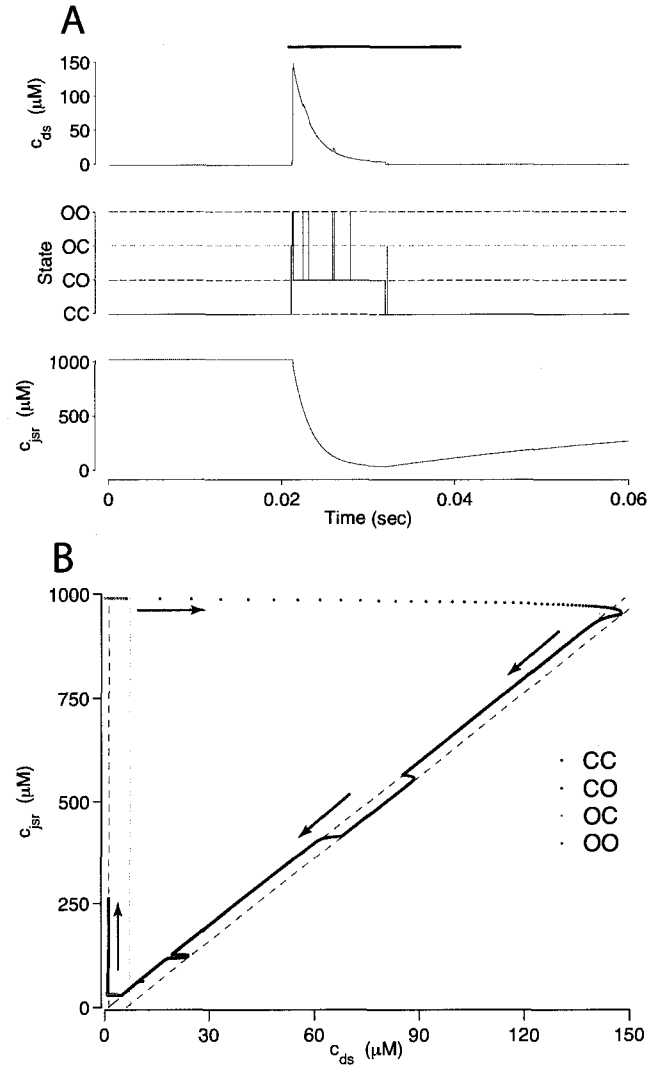
Figure 3.4: A: Dynamics of the diadic subspace (c_{ds}^n) and junctional SR (c_{jsr}^n) Ca^{2+} concentrations associated with a single Ca^{2+} release unit during the voltage clamp protocol of Figs. 3.2 and 3.3. B: The dynamics of these local Ca^{2+} concentrations in the (c_{ds}, c_{jsr})-plane. Trajectory color indicates CaRU state: both the L-type channel and the RyR cluster closed ($\mathcal{CC}$, *black*); L-type channel open and RyR cluster closed ($\mathcal{OC}$, *green*); L-type channel closed and RyR cluster open ($\mathcal{CO}$, *blue*); both the L-type channel and the RyR cluster open ($\mathcal{OO}$, *red*). *Colored dashed lines* correspond to estimates of diadic subspace [Ca^{2+}] given by Eq. 3.33.
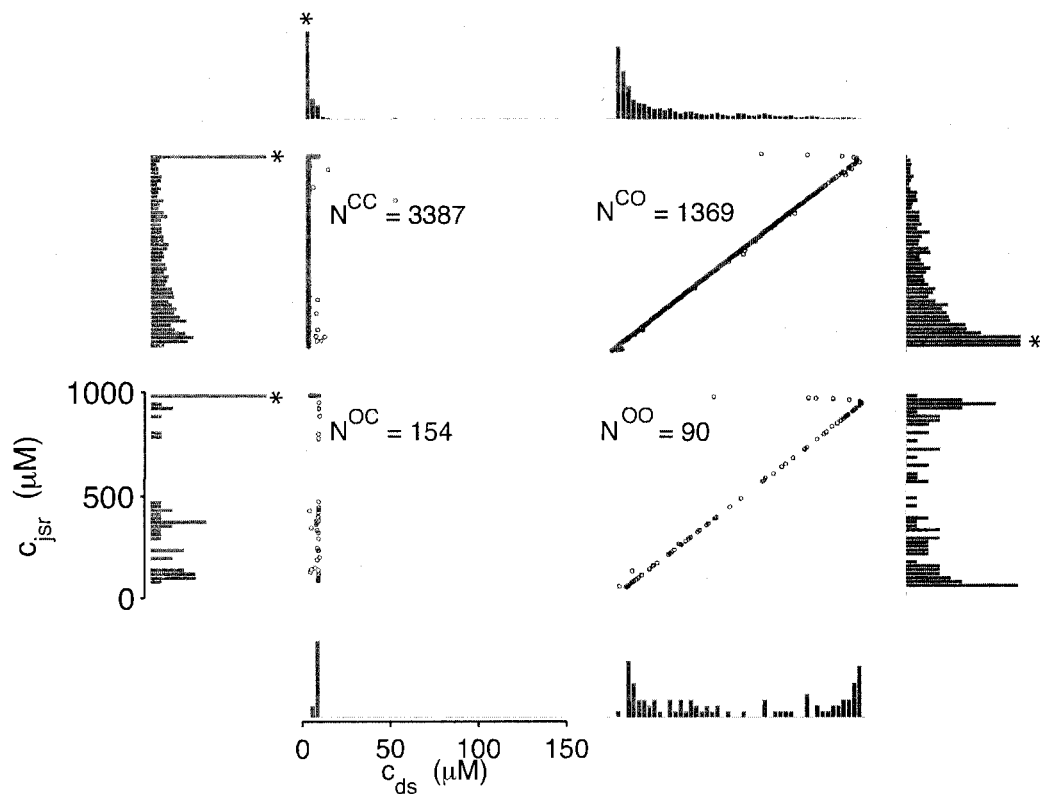
Figure 3.5: The *open circles* are a snapshot at $t = 30$ ms of the diadic subspace (c_{ds}^n) and junctional SR (c_{jsr}^n) Ca^{2+} concentrations in the Monte Carlo simulation of Fig. 3.2. Each of the four central panels corresponds to a particular Ca^{2+} release unit state and size of each subpopulation at this moment is indicated by N^{CC} through N^{OO}. The horizontally (vertically) oriented histograms give the marginal distribution of diadic subspace (junctional SR) [Ca^{2+}] conditioned on CaRU state. Histograms are scaled for clarity and in some cases also truncated (*asterisks*).

Conversely, Fig. 3.5 presents the state of each of the 5000 CaRUs at a particular moment in time ($t = 30$ ms, halfway through the test potential of -10 mV). To interpret this figure, it is important to understand that the four central panels of Fig. 3.5 correspond to the four CaRU states and are arranged in a manner corresponding to the transition state diagram of Eq. 3.3. At this moment during the simulation, approximately 5% of the Ca^{2+} release units have open L-type channels ($N^{\mathcal{OC}} + N^{\mathcal{OO}} = 244$) while approximately 30% have an open RyR cluster ($N^{\mathcal{CO}} + N^{\mathcal{OO}} = 1459$). Note that for each of the four subpopulations of CaRUs there is a linear relationship between c_{ds} and c_{jsr}, that is, the *open circles* tend to be arranged in lines, the position of which depends on CaRU state (and the slope of which depends on whether or not the RyR cluster is open). Thus, Fig. 3.5 demonstrates that across the entire population of Ca^{2+} release units, the observed diadic subspace [Ca^{2+}] is well approximated by the quasi-static approximation given by Eq. 3.33.

Figure 3.5 also shows histograms of the observed distribution of diadic subspace [Ca^{2+}] (horizontal) and junctional SR [Ca^{2+}] (vertical). The histograms associated with CaRU state $\mathcal{CC}$ clearly indicate that most of these 3387 CaRUs have replete junctional SR ($c_{jsr}^n \approx 1000$ μM), something that is not obvious from the *open circles* in the (c_{ds}, c_{jsr})-plane. Similarly, most of the 154 CaRUs in state $\mathcal{OC}$ are associated with replete junctional SR. Conversely, the junctional SR [Ca^{2+}] for the 1369 CaRUs in state $\mathcal{CO}$ is broadly distributed with the "average" junctional SR severely depleted ($\sim$100 μM). At $t = 30$ ms only 90 CaRUs are in state $\mathcal{OO}$ and the distributions of junctional SR [Ca^{2+}] and diadic subspace [Ca^{2+}] associated with this state are bimodal.

3.4.3 A univariate probability density formulation for junctional SR calcium concentration

It is important to note that the Monte Carlo simulations presented in Fig. 3.5 are only a snapshot of the population of 5000 Ca^{2+} release units. As the simulation progresses, imagine the *open circles* moving around in these four (c_{ds}, c_{jsr})-planes consistent with Eqs. 3.5 and 3.6 with occasional jumps from one plane to another when a CaRU changes state. These four planes are analogous to the four time-dependent joint probability densities that form the basis of the probability density approach presented above (Eq. 3.18).

The observation that the diadic subspace $[Ca^{2+}]$ is well approximated by Eq. 3.33 across the entire population of Ca^{2+} release units (Fig. 3.5) suggests that the multivariate joint probability density functions defined in Eq. 3.18 will be well approximated by

$$\rho^i(c_{ds}, c_{jsr}, t) = \rho^i_{jsr}(c_{jsr}, t)\delta(c_{ds} - \bar{c}^i_{ds}) \qquad (3.34)$$

where $\bar{c}^i_{ds}$ is a function of CaRU state and the junctional SR, bulk myoplasmic, and network SR $[Ca^{2+}]$ analogous to Eq. 3.33,

$$\bar{c}^i_{ds} = \frac{\gamma^i_{dhpr} J^0_{dhpr} + v^T_{efflux} c_{myo} + \gamma^i_{ryr} v^T_{ryr} c_{jsr}}{\gamma^i_{ryr} v^T_{ryr} + v^T_{efflux} - \gamma^i_{dhpr} J^1_{dhpr}} \qquad (3.35)$$

where γ^i_{dhpr}, γ^i_{ryr}, J^0_{dhpr} and J^1_{dhpr} are as defined in the previous section. The univariate probability density $\rho^i_{jsr}(c_{jsr}, t)$ that appears in Eq. 3.34 is the marginal density of the junctional SR $[Ca^{2+}]$ jointly distributed with CaRU state defined by

$$\rho^i_{jsr}(c_{jsr}, t)\, dc_{jsr} = \mathsf{Pr}\{c_{jsr} < \tilde{c}_{jsr}(t) < c_{jsr} + dc_{jsr} \text{ and } \tilde{S}(t) = i\}. \qquad (3.36)$$

That is, when the observed form of the joint multivariate probability densities (Eq. 3.34)

is integrated with respect to diadic subspace [Ca^{2+}] we obtain

$$\int_0^\infty \rho^i(c_{ds}, c_{jsr}, t) dc_{ds} = \int_0^\infty \rho^i_{jsr}(c_{jsr}, t) \delta(c_{ds} - \bar{c}^i_{ds}) dc_{ds}$$

$$= \rho^i_{jsr}(c_{jsr}, t) \int_0^\infty \delta(c_{ds} - \bar{c}^i_{ds}) dc_{ds} = \rho^i_{jsr}(c_{jsr}, t) \quad (3.37)$$

where the last equality uses the unit mass of the delta function, $\int_0^\infty \delta(c_{ds} - \bar{c}^i_{ds}) dc_{ds} = 1$.

As shown in Appendix 3.6.3, the observed form of the multivariate probability densities (Eq. 3.34) and the definition of the marginal density (first equality in Eq. 3.37) can be used to reduce Eqs. 3.19–3.22 into a univariate version of the probability density formulation that focuses on the dynamics of the marginal densities for the junctional SR [Ca^{2+}] jointly distributed with CaRU state [$\rho^i_{jsr}(c_{jsr}, t)$]. The resulting advection-reaction equations are [Mazzag et al., 2005a, Huertas and Smith, 2006a],

$$\frac{\partial \rho^{CC}_{jsr}}{\partial t} = -\frac{\partial}{\partial c_{jsr}} \left[\bar{f}^{CC}_{jsr} \rho^{CC}_{jsr} \right] - \left(k^+_{ryr} + k^+_{dhpr} \right) \rho^{CC}_{jsr} + k^-_{ryr} \rho^{CO}_{jsr} + k^-_{dhpr} \rho^{OC}_{jsr} \quad (3.38)$$

$$\frac{\partial \rho^{CO}_{jsr}}{\partial t} = -\frac{\partial}{\partial c_{jsr}} \left[\bar{f}^{CO}_{jsr} \rho^{CO}_{jsr} \right] - \left(k^-_{ryr} + k^+_{dhpr} \right) \rho^{CO}_{jsr} + k^+_{ryr} \rho^{CC}_{jsr} + k^-_{dhpr} \rho^{OO}_{jsr} \quad (3.39)$$

$$\frac{\partial \rho^{OC}_{jsr}}{\partial t} = -\frac{\partial}{\partial c_{jsr}} \left[\bar{f}^{OC}_{jsr} \rho^{OC}_{jsr} \right] - \left(k^+_{ryr} + k^-_{dhpr} \right) \rho^{OC}_{jsr} + k^-_{ryr} \rho^{OO}_{jsr} + k^+_{dhpr} \rho^{CC}_{jsr} \quad (3.40)$$

$$\frac{\partial \rho^{OO}_{jsr}}{\partial t} = -\frac{\partial}{\partial c_{jsr}} \left[\bar{f}^{OO}_{jsr} \rho^{OO}_{jsr} \right] - \left(k^-_{ryr} + k^-_{dhpr} \right) \rho^{OO}_{jsr} + k^+_{ryr} \rho^{OC}_{jsr} + k^+_{dhpr} \rho^{CO}_{jsr} \quad (3.41)$$

where the advection rates $\bar{f}^{CC}_{jsr}$, $\bar{f}^{CO}_{jsr}$, $\bar{f}^{OC}_{jsr}$, and $\bar{f}^{OO}_{jsr}$ are given by Eq. 3.24 with the substitution of $\bar{c}^i_{ds}$ for c_{ds}, that is,

$$\bar{f}^i_{jsr} = \frac{1}{\lambda^T_{jsr}} \left(J^T_{refill} - \gamma^i_{ryr} J^T_{ryr} \right) \quad (3.42)$$

$$= \frac{1}{\lambda^T_{jsr}} \left\{ v^T_{refill} \left[c_{nsr}(t) - c_{jsr} \right] - \gamma^i_{ryr} v^T_{ryr} \left[c_{jsr} - \bar{c}^i_{ds}(t) \right] \right\} \quad (3.43)$$

where $\bar{c}^i_{ds}(t)$ is the function of $c_{myo}(t)$, c_{jsr}, and CaRU state (i) given by Eq. 3.35.

In this univariate probability density formulation, the bulk myoplasmic and network SR [Ca^{2+}] are still given by Eqs. 3.29 and 3.30, but J_{efflux}^* and J_{refill}^* are now functionals of the joint marginal probability densities $[\rho_{jsr}^i(c_{jsr}, t)]$,

$$J_{efflux}^* = \sum_{i=1}^{M} \int_0^\infty v_{efflux}^T \left[\bar{c}_{ds}^i - c_{myo}(t)\right] \rho_{jsr}^i(c_{jsr}, t) dc_{jsr} \qquad (3.44)$$

$$J_{refill}^* = \sum_{i=1}^{M} \int_0^\infty v_{refill}^T \left[c_{nsr}(t) - c_{jsr}\right] \rho_{jsr}^i(c_{jsr}, t) dc_{jsr} \qquad (3.45)$$

3.4.4 Comparison of probability density and Monte Carlo results

The four histograms presented in Fig. 3.6A–D show the marginal distributions of junctional SR [Ca^{2+}] observed in Fig. 3.5 on identical scales. When presented in this fashion it becomes apparent that at $t = 30$ ms only a small fraction ($\sim5\%$) of the Ca^{2+} release units have open L-type Ca^{2+} channels (states $\mathcal{OC}$ and $\mathcal{OO}$), while approximately 30% contain open RyR clusters ($\mathcal{CO}$ and $\mathcal{OO}$). Note that the *asterisk* in Fig. 3.6A indicates that the histogram bin representing Ca^{2+} release units with closed L-type Ca^{2+} channel, closed RyR cluster and replete junctional SR is truncated; in fact, $\sim80\%$ of CaRUs in state $\mathcal{CC}$ have $c_{jsr}^n \approx c_{nsr}$. With this understanding, a comparison of Fig. 3.6A and B shows that CaRUs with open RyR clusters are more likely to be depleted than CaRUs with closed RyR clusters, but CaRUs with closed RyR clusters are not necessarily replete, because recovery of junctional SR [Ca^{2+}] is not complete until approximately 400 ms after RyR closure (cf. Fig. 3.3).

The *solid lines* of Fig. 3.6A–D show snapshots of the four joint probability densities $\rho_{jsr}^{\mathcal{CC}}(c_{jsr}, t)$, $\rho_{jsr}^{\mathcal{CO}}(c_{jsr}, t)$, $\rho_{jsr}^{\mathcal{OC}}(c_{jsr}, t)$, and $\rho_{jsr}^{\mathcal{OO}}(c_{jsr}, t)$ as calculated using the probability density approach ($t = 30$ ms). These results were obtained by numerically solving Eqs. 3.29, 3.30, and 3.38–3.45 using the numerical scheme presented in Appendix 3.6.4 (parameters as in Figs. 3.2–3.5). Importantly, the entire distribution of junctional SR
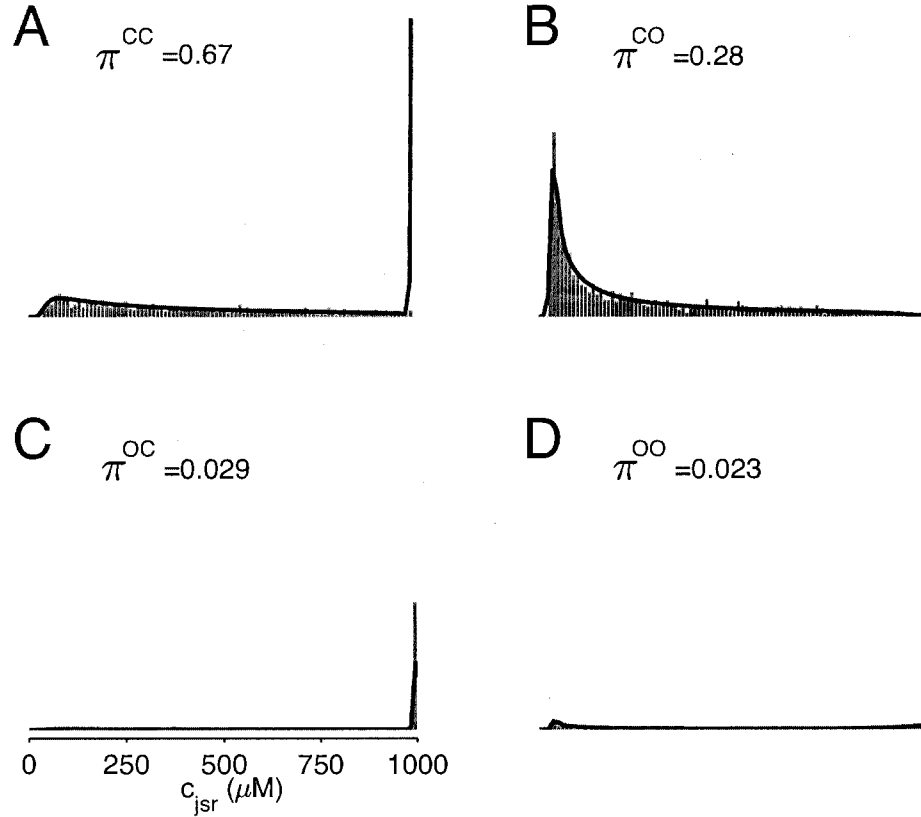
Figure 3.6: Histograms of the junctional SR Ca^{2+} concentrations (c_{jsr}^n) at $t = 30$ ms in the Monte Carlo simulation of Figs. 3.2–3.5 jointly distributed with CaRU state. These histograms are plotted on the same scale, but one is truncated for clarity (*asterisk*). For comparison, the *solid lines* show the four joint probability densities $\rho_{jsr}^{CC}(c_{jsr}, t)$, $\rho_{jsr}^{CO}(c_{jsr}, t)$, $\rho_{jsr}^{OC}(c_{jsr}, t)$, and $\rho_{jsr}^{OO}(c_{jsr}, t)$ for junctional SR $[Ca^{2+}]$ (Eq. 3.34) calculated via numerical solution of Eqs. 3.29, 3.30, and 3.38–3.45. The probability density calculation of the fraction of subunits in each of the four states is denoted by π^i (Eq. 3.46).

Ca^{2+} concentrations observed for each CaRU state in the probability density calculation (*solid lines*) agrees with the corresponding Monte Carlo result (*histograms*), thereby validating the probability density methodology and our implementation of both approaches. In particular, notice that the fraction of CaRUs in each state given by

$$\pi^i(t) = \mathsf{Pr}\left\{\tilde{S}(t) = i\right\} = \int_0^\infty \rho^i_{jsr}(c_{jsr}, t)dc_{jsr} \tag{3.46}$$

in the probability density calculation is consistent with the Monte Carlo simulation Fig. 3.5, for example, in Fig. 3.6A $\pi^{CC} = 0.67$ and this corresponds to $N^{CC}/N = 3387/5000$ in Fig. 3.5A.

While Fig. 3.6 shows the four marginal probability densities $[\rho^i_{jsr}(c_{jsr}, t)]$ for the junctional SR [Ca^{2+}] jointly distributed with CaRU state at a particular moment in time, Fig. 3.7 shows the total probability density

$$\rho^T_{jsr}(c_{jsr}, t) = \rho^{CC}_{jsr} + \rho^{CO}_{jsr} + \rho^{OC}_{jsr} + \rho^{OO}_{jsr} \tag{3.47}$$

evolving over time. Initially the mass of this probability density is concentrated at $c_{jsr} \approx 1000$ μM (label "a" in Fig. 3.7). During the 20 ms voltage pulse, a significant fraction of the probability density (about 65%) moves to junctional SR Ca^{2+} concentrations that are more that half depleted (label "b"), while approximately 35% remains above 500 μM. Interestingly, the probability density remains bimodal for approximately 200 ms after the voltage pulse ends ("c" and "d"). During this time, the probability mass that corresponds to depleted junctional SR ("c") gradually moves to higher values of c_{jsr} as these junctional SR compartments are refilled via Ca^{2+} transport from the network SR. At the same time, the probability mass that corresponds to replete junctional SR compartments ("d") follows the network SR [Ca^{2+}] that decreases from $t = 30$–100 ms and increases again when $t > 100$ ms (recall the *solid line* in Fig. 3.3). Perhaps most importantly, Fig. 3.7 shows that the shape and

temporal evolution of the distributions that form the basis of the probability density approach can be quite complicated.

3.4.5 Monte Carlo simulations converge to the probability density result

The coupled system of advection-reaction equations used in the univariate probability density approach (Eqs. 3.38–3.41) are the master equations for the marginal probability densities for junctional SR [Ca^{2+}] jointly distributed with the Ca^{2+} release unit state (Eq. 3.36). Solving these partial differential equations is equivalent to performing Monte Carlo simulation of diadic subspace [Ca^{2+}], junctional SR [Ca^{2+}], and CaRU state provided that 1) diadic subspace [Ca^{2+}] is a fast dynamic variable in quasi-static equilibrium with junctional SR [Ca^{2+}] and 2) the number of Ca^{2+} release units (N) is large enough. Figure 3.6 demonstrates agreement between probability density simulations of a minimal whole cell model of EC coupling and corresponding Monte Carlo simulations using $N = 5000$ CaRUs. Because this agreement will only improve when the number of CaRUs is increased to physiologically realistic values (N = 20,000), the probability density approach is clearly a viable method of modeling heterogeneous diadic subspace and junctional SR [Ca^{2+}] during EC coupling.

Figure 3.8 clarifies this point by showing how the total release flux (J_{ryr}^{T}, *open squares*) observed in Monte Carlo simulation converges to the probability density result (*solid lines*) as the number of Ca^{2+} release units is increased from $N = 50$ to 20,000. Each panel shows a representative Monte Carlo simulation with voltage step to -10 mV (*solid grey line*) as well as the mean and standard deviation of 10 trials (*open squares* and *error bars*). As expected, the fluctuations in the total release flux decrease in magnitude as the number of CaRUs used in the Monte Carlo calculation increases. Similarly, Fig. 3.9 shows histograms of the junctional SR [Ca^{2+}] (irrespective of CaRU state) at $t = 30$ ms in Monte Carlo simulations performed with
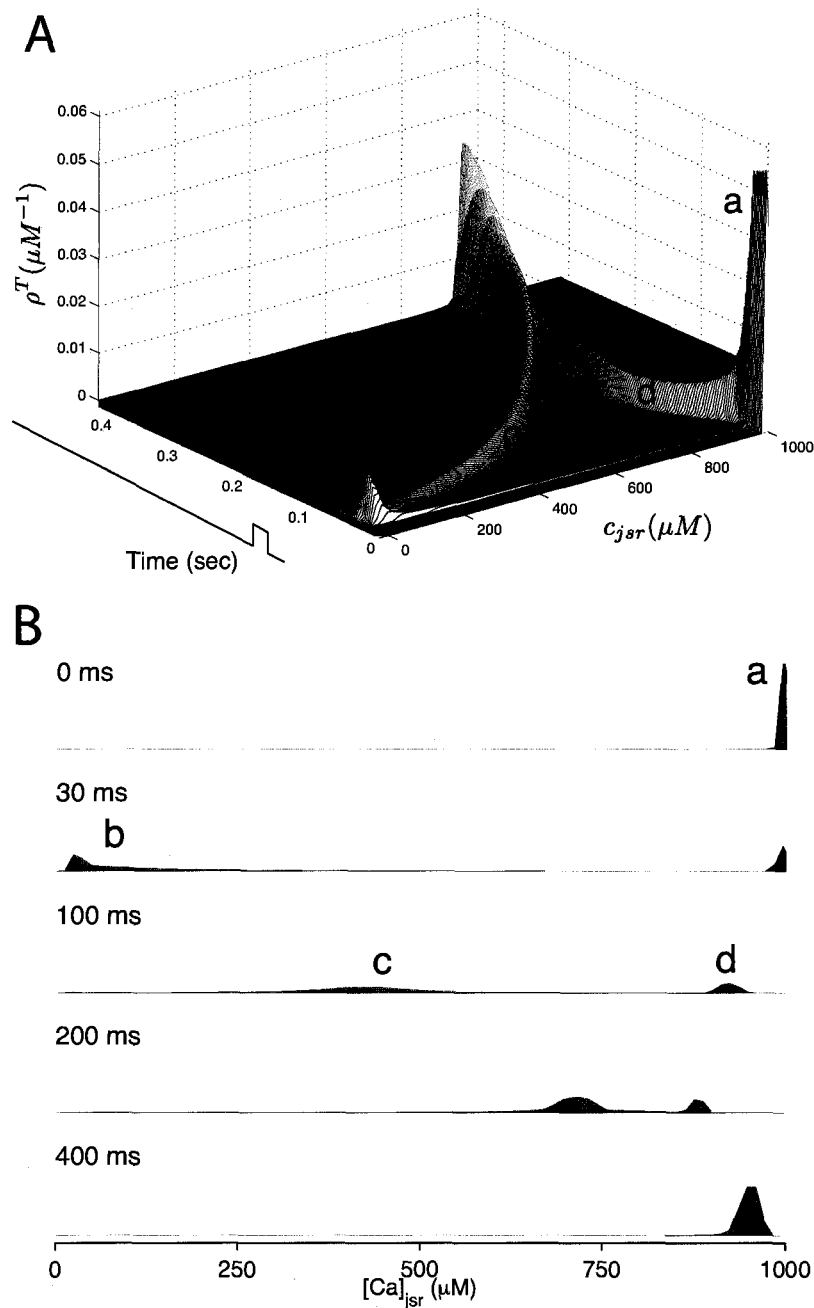
Figure 3.7: Waterfall plot (A) and snapshots (B) of the time-evolution of the total probability density for the junctional SR [Ca^{2+}] [$\rho^T(c_{jsr}, t)$ given by Eq. 3.47] calculated via numerical solution of Eqs. 3.29, 3.30, and 3.38–3.45. The *solid black lines* show the 20 ms voltage step to -10 mV. See text for description of labels "a"–"d".
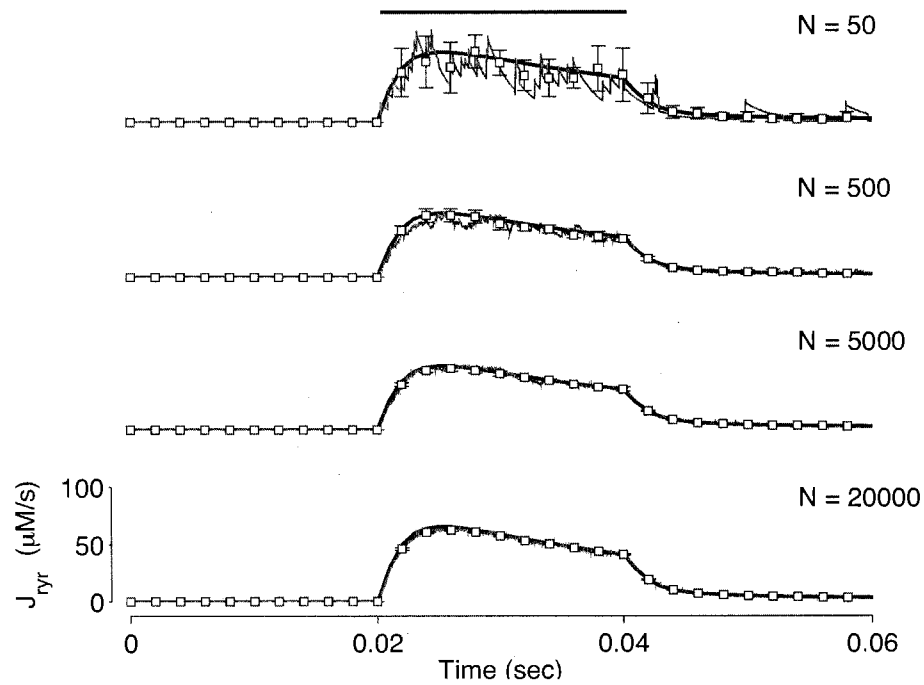
Figure 3.8: Total Ca^{2+} release flux (J_{ryr}^T) in Monte Carlo simulations utilizing increasing numbers of Ca^{2+} release units ($N = 50$, 500, 5000, and 20000, respectively). Each panel shows a representative Monte Carlo simulation (*solid grey line*) and the mean and standard deviation of 10 trials (*open squares* and *error bars*). The *solid lines* show the corresponding probability density result (same in each panel).

a greater or lesser number of CaRUs. Notice that the probability density function $\rho^T(c_{jsr}, t)$ (Eq. 3.47) accurately represents the distribution of junctional SR $[Ca^{2+}]$ so long as the number of CaRUs is 5000 or more. Indeed, in both Figs. 3.8 and 3.9 the Monte Carlo simulations are converging to the probability density result *well before* the Monte Carlo calculations include a physiological number of Ca^{2+} release units ($N = 20,000$). This indicates that the probability density approach to modeling local Ca^{2+} signaling and Ca^{2+} release unit activity in cardiac myocytes is a viable alternative to Monte Carlo simulation.

3.4.6 The probability density calculation exhibits gain and gradedness

To further compare of the probability density and Monte Carlo approaches, Fig. 3.10A summarizes a large number of simulated whole cell voltage clamp protocols such as those presented in Fig. 3.2. The *open circles* and *error bars* of Fig. 3.10A show the trigger Ca^{2+} influx via L-type Ca^{2+} channels integrated over the 20 ms voltage step to test potentials in the range -40 to 40 mV (mean $\pm$ SD for 10 Monte Carlo simulations using 10,000 CaRUs). For comparison, the *solid lines* of Fig. 3.10A show that the trigger Ca^{2+} influx in the probability density calculation agrees with the Monte Carlo simulations. Similarly, the *open squares* of Fig. 3.10A show the voltage-dependence of the Ca^{2+} release flux plotted in a manner that illustrates the pronounced EC coupling gain in the Monte Carlo calculations, while the *dashed lines* of Fig. 3.10A show that the Ca^{2+} release flux observed in the corresponding probability density calculations also exhibits high gain. When these trigger and release fluxes are normalized and replotted in Fig. 3.10B, the gradedness of Ca^{2+} release with respect to membrane potential and Ca^{2+} influx is highlighted. In particular, we note that both the Monte Carlo and probability density calculations exhibit graded Ca^{2+} release and that the voltage-dependence of the EC coupling gain is nearly identical in the two formulations
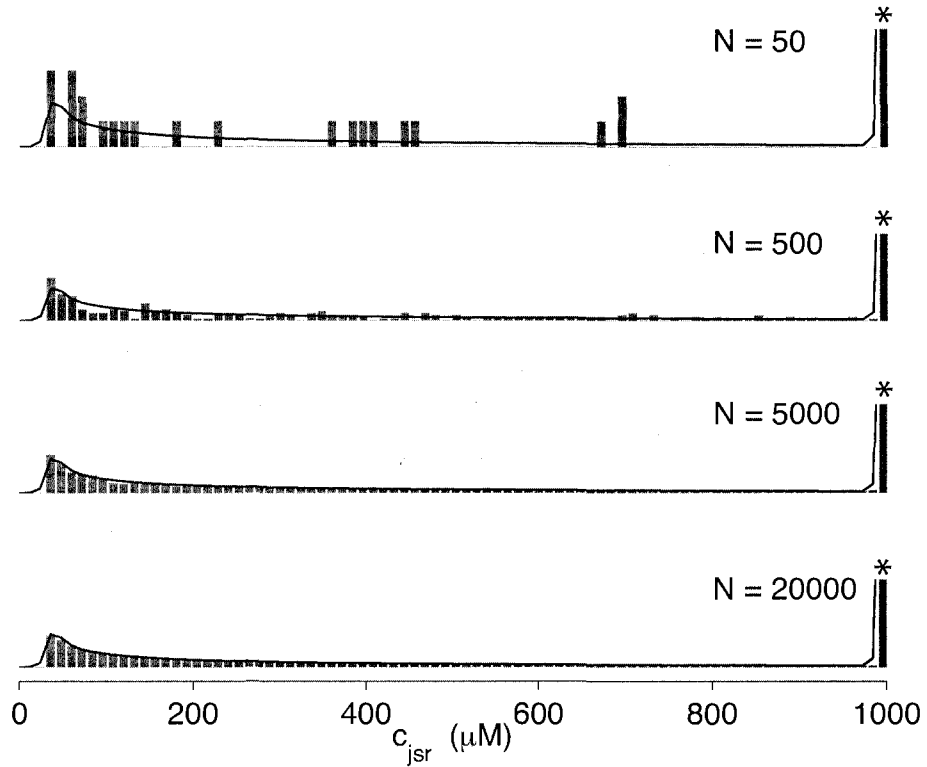
Figure 3.9: Histograms of junctional SR [Ca^{2+}] (c_{jsr}^n) at $t = 30$ ms in the Monte Carlo simulations similar to Fig. 3.5 but with increasing numbers of Ca^{2+} release units (N = 50, 500, 5000, and 20000, respectively) One bin representing $\sim$57% probability of a replete junctional SR is truncated for clarity (*asterisk*). The *solid lines* show the probability density calculation of $\rho^T(c_{jsr}, t)$ (Eq. 3.47), the distribution of the total probability density for the junctional SR [Ca^{2+}] (same in each panel).

(see Fig. 3.10C).

3.4.7 Computational efficiency of the probability density approach

The convergence between the Monte Carlo and probability density calculations presented above indicates that the probability density approach is a viable alternative to Monte Carlo simulations of heterogeneous local $[Ca^{2+}]$ and Ca^{2+} release unit activity in cardiac myocytes. In fact, as shown in Fig. 3.10, the probability density approach leads to EC coupling dynamics that are nearly identical to Monte Carlo calculations so long as these Monte Carlo simulations involve a realistic number of Ca^{2+} release units ($N > 5000$).

Because the probability density and Monte Carlo calculations are essentially equivalent in terms of the cellular responses they predict, it is of interest to explore the computational efficiency of the two approaches. The *filled squares* of Fig. 3.11 show the run time required to perform a simulated whole cell voltage clamp protocol such as those presented in Fig. 3.2 using traditional Monte Carlo simulation methods. As expected, the run time increases with the number of Ca^{2+} release units used and this run time scales linearly with the number of CaRUs when N is large. For comparison, the *thick dashed line* of Fig. 3.11 shows the 2.1 minute run time required for the univariate probability density approach, that is, numerical solution of Eqs. 3.29, 3.30, and 3.38–3.45 (see Appendix 3.6.4). Notice that the intersection of the *filled squares* and the *thick dashed line* in Fig. 3.11 shows that a Monte Carlo simulation using about 500 CaRUs leads to the same run time as the probability density approach. Not only is this smaller than the true number of CaRUs in a ventricular myocyte, but in practice multiple Monte Carlo runs would have to be performed and averaged to obtain a definitive result. For example, if 10 trials are to be averaged as in Fig. 3.8, then the appropriate comparison is given by the *open squares* and the *thick dashed*
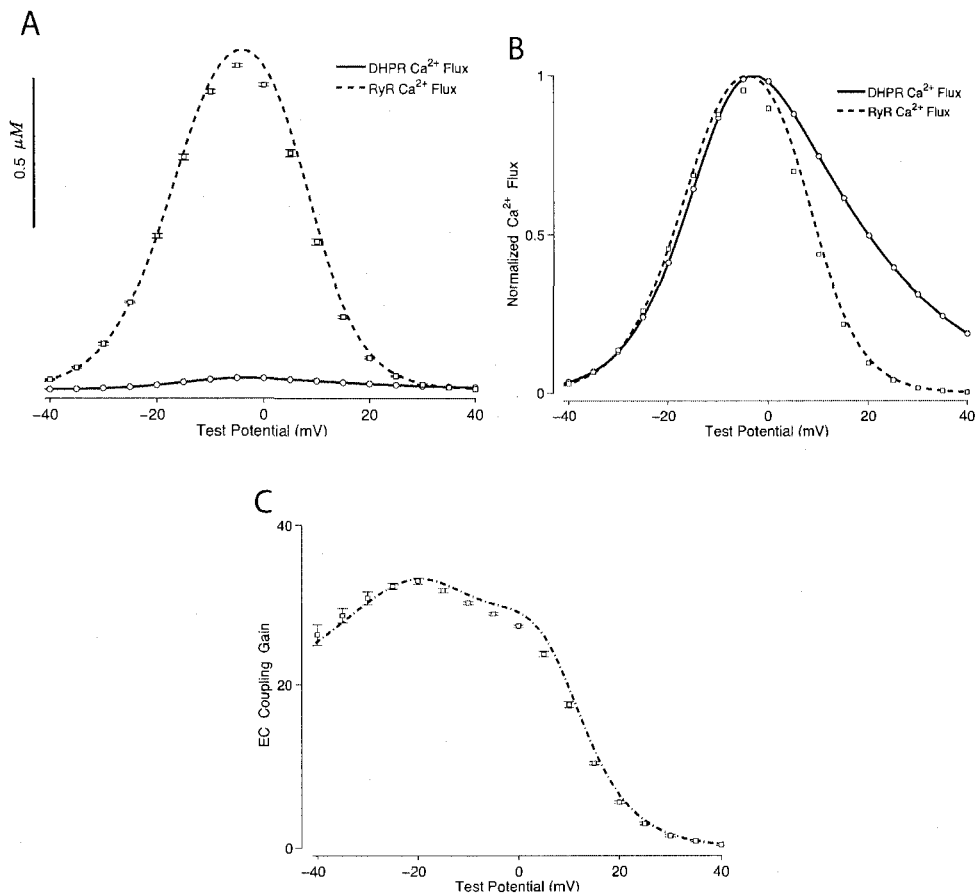
Figure 3.10: Summary of simulated whole cell voltage clamp protocols such as those presented in Fig. 3.2 using both the Monte Carlo and probability density formulations. A: *Open circles* and *error bars* show trigger Ca^{2+} influx via L-type Ca^{2+} channels integrated over the 20 ms voltage step to test potentials in the range -40 to 40 mV (mean $\pm$ SD for 10 Monte Carlo simulations using 10,000 CaRUs). *Open squares* and *error bars* show the voltage-dependence of the resulting Ca^{2+} release. The *solid* and *dashed lines* of Fig. 3.10A show that the trigger and release fluxes as calculated using the probability density approach agrees with these Monte Carlo simulations. B: Results from panel A normalized and replotted to emphasize gradedness of Ca^{2+} release with respect to membrane potential and Ca^{2+} influx. C: EC coupling gain as a function of membrane potential for Monte Carlo (*open squares* and *error bars*) and probability density (*solid line*) calculations.
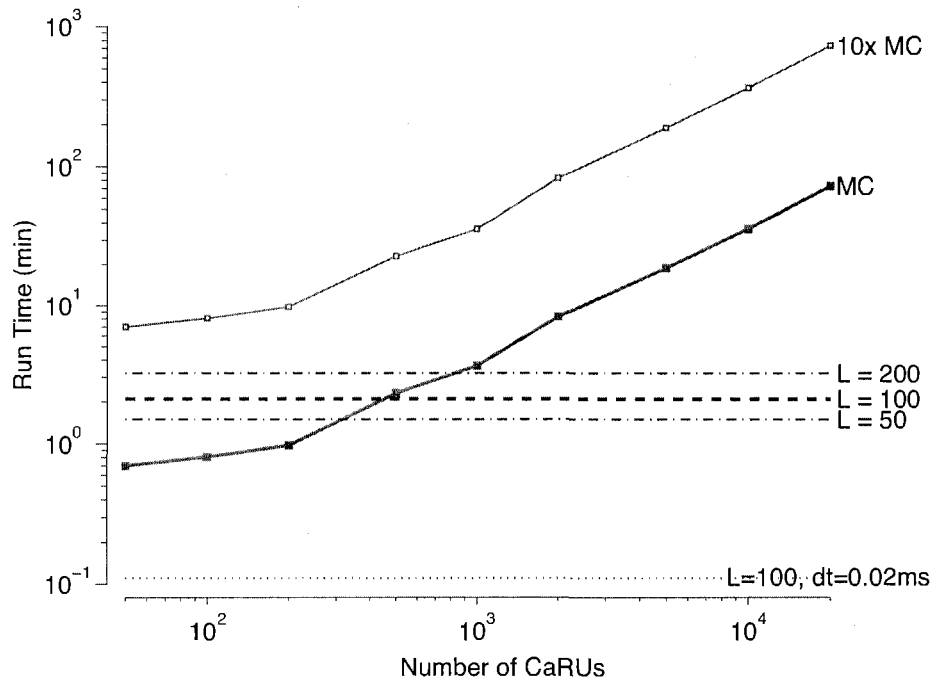
Figure 3.11: *Filled squares* show the run time required to perform a simulated whole cell voltage clamp protocol such as those presented in Fig. 3.2 using traditional Monte Carlo simulation methods when the number of Ca^{2+} release units is increased from $N = 50$ to 20000. *Open squares* show 10 times the Monte Carlo run time to account for averaging multiple trials as in Fig. 3.8. The *thick dashed line* and *thin dot-dashed lines* show the run time required for the univariate probability density approach using mesh sizes of $L = 50$, 100, and 200 and a time step of 1 μs. The *thin dotted line* shows the univariate probability density approach run time using mesh sizes of $L = 100$ and a time step of 0.02 ms (see Discussion and Appendix 3.6.4). Total simulation time is 60 ms.

line and these show that the probability density approach requires less run time than ten Monte Carlo simulations with 50 CaRUs. Intriguingly, and perhaps most importantly, when the traditional Monte Carlo simulations use a physiologically realistic number of CaRUs, the probability density approach is approximately 35 times faster than Monte Carlo (73 vs. 2.1 minutes). While the computational efficiency of the probability density approach as compared to Monte Carlo simulation may be model dependent, in the context of this whole cell model an additional 20X acceleration is easily obtained (see *thin dotted line* in Fig. 3.8 and Discussion). For this reason we suggests that the probability density approach be further investigated and developed as a computationally efficient alternative to Monte Carlo simulations of the local control of EC coupling in cardiac myocytes.

3.5 Discussion

In this paper we have introduced, validated and benchmarked a novel probability density approach to modeling localized Ca^{2+} influx via L-type Ca^{2+} channels and Ca^{2+}-induced Ca^{2+} release mediated by clusters of RyRs during excitation-contraction coupling in cardiac myocytes. To illustrate the approach we have focused on a minimal whole cell model of cardiac EC coupling that includes a four-state Ca^{2+} release unit representing voltage-dependent activation of an L-type Ca^{2+} channels as well as Ca^{2+}-induced Ca^{2+} release mediated by a two-state RyR cluster that includes regulation by both diadic subspace and junctional SR Ca^{2+}. However, it is important to note that the probability density formulation does not require a minimal Ca^{2+} release unit model; in fact, the approach is fully generalizable to CaRUs with an arbitrary number of states (see Appendix 3.6.4).

As illustrated by leftmost schematic in Fig. 3.12, the Monte Carlo formulation of the minimal whole cell model of EC coupling that is the focus of this paper includes 2+

$2N$ ordinary differential equations representing [Ca^{2+}] balance for the bulk myoplasm, network SR, N diadic subspaces, and N junctional SRs. Alternatively, the probability density formulation represents the dynamics of these heterogeneous local Ca^{2+} signals using a system of advection-reaction equations for the time-dependent probability density of diadic subspace and junctional SR [Ca^{2+}] conditioned on Ca^{2+} release unit state. In this formulation, the number of equations (M) is equal the number of unique states that define the gating behavior of the CaRU. As originally derived, these joint probability densities are two-dimensional, that is, at a specified time they are functions of both c_{ds} and c_{jsr}. The system of advection-reaction equations satisfied by these multivariate probability densities is the "master equation" for diadic subspace and junctional SR [Ca^{2+}] jointly distributed with the Ca^{2+} release unit state. The only approximation used in the derivation of these equations is that the number of CaRUs units is very large ($N \rightarrow \infty$).

In the Monte Carlo simulations of the whole cell model of cardiac EC coupling we observed that diadic subspace [Ca^{2+}] was in quasi-static equilibrium with junctional SR [Ca^{2+}]. Figure 3.12 illustrates this feature of the simulations with two *thick gray lines* in two (c_{ds};c_{jsr})-planes labeled *slaved diadic subspace* (the lines have different slopes as in Fig. 3.5). In this situation the multivariate probability density functions defined in Eq. 3.18 are well approximated by univariate (marginal) probability densities representing the time-dependent probability density of junctional sarcoplasmic reticulum [Ca^{2+}] jointly distributed with CaRU state. These marginal probability densities are one-dimensional, that is, at a specified time they are functions of c_{jsr} (illustrated by *narrow rectangles* in Fig. 3.12). When the system of advection-reaction equations satisfied by these marginal probability densities was solved numerically using a high-resolution finite difference scheme (see Appendix 3.6.4), a realistic but minimal model of cardiac excitation-contraction coupling is produced that includes a novel representation of heterogeneous junctional SR [Ca^{2+}].

Importantly, we have validated this novel probability density approach to modeling local control of Ca^{2+} release against traditional Monte Carlo simulations with a physiologically realistic number of CaRUs. In simulated voltage-clamp protocols, the univariate probability density formulation of our whole cell model of cardiac EC coupling produced high-gain Ca^{2+} release that was graded with changes in membrane potential. Indeed, the voltage-dependence of trigger Ca^{2+} influx via L-type Ca^{2+} channels, the resulting Ca^{2+} release via RyR clusters, and the observed EC coupling gain obtained using the univariate probability density formulation are nearly identical to that seen in corresponding Monte Carlo calculations. This agreement validates the conceptually novel aspects of the probability density formulation as well as our implementation of both approaches.
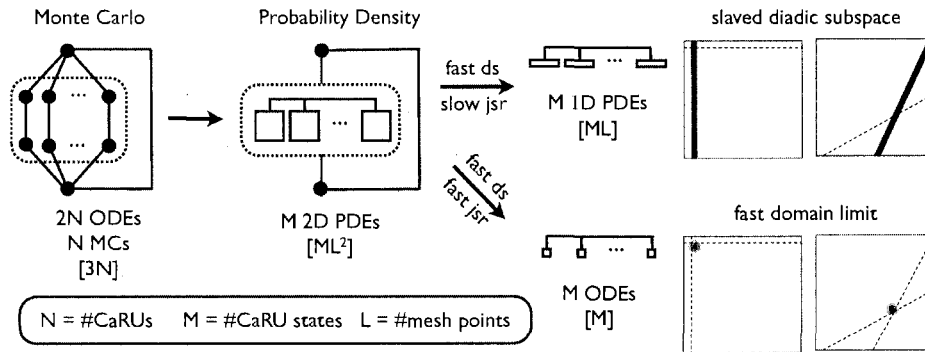
Figure 3.12: From left to right: Schematic representation of the $(2N+2)$-compartment *Monte Carlo* model of the local control of EC coupling that is the starting point of this paper. Schematic representation of the multivariate *Probability Density* formulation that can be reduced to the univariate probability density formulation when diadic subspace Ca^{2+} is in quasi-static equilibrium with junctional SR Ca^{2+} (*slaved diadic subspace*). An alternative reduction is possible if diadic subspace and junctional SR Ca^{2+} are both fast dynamic variables (*fast domain limit*). The *large open squares* represent the (c_{ds}, c_{jsr})-plane of the probability density approach and the *dotted lines* represent the c_{ds} and c_{jsr} nullclines. Values in brackets show how run times of each method scale with increasing number of Ca^{2+} release units (N), number of Ca^{2+} release unit states (M), and the number of mesh points used in the probability density approach (L).

3.5.1 Relationship to other simplified models of EC coupling

It is instructive to compare and contrast the probability density approach introduced in this paper to models of the local control of EC coupling that have previously appeared. As shown diagrammatically in Fig. 3.12, the Monte Carlo local control model of EC coupling that is our starting point includes $2N + 2$ compartments, similar to the functional organization of some previously published Monte Carlo models of local control [Greenstein and Winslow, 2002a], but distinct from two recently published simplified models [Hinch, 2004, Greenstein et al., 2006] that do not make a distinction between junctional and network SR.

The one requirement for the validity of the multivariate probability density approach is that the number of CaRUs units is very large (denoted by $N \rightarrow \infty$ in Fig. 3.12). While previously published models of local control also assume that the number of CaRUs is very large [Hinch, 2004, Greenstein et al., 2006], the multivariate probability density approach represents this "large system size" limit in a manner that accounts for the heterogeneous diadic subspace and junctional SR Ca^{2+} concentrations.

Similar to previously published simplified models of local control [Hinch, 2004, Greenstein et al., 2006], we make use of the fact that diadic subspace Ca^{2+} is a fast dynamic variable. Because references [Hinch, 2004] and [Greenstein et al., 2006] do not distinguish junctional and network SR, the assumption of fast diadic subspace Ca^{2+} immediately leads to a simplified local control model involving M ODEs (one for each CaRU state). Conversely, in this paper the observation that diadic subspace Ca^{2+} is in quasi-static equilibrium with junctional SR Ca^{2+} allows us to reduce the multivariate probability density formulation to a univariate form that still accounts for the dynamics of junctional SR depletion. This reduction from the multivariate to univariate probability density approach is denoted by the *arrow* labeled *fast ds/slow jsr* in Fig. 3.12.

Note that if diadic subspace and junctional SR [Ca^{2+}] changes were both fast compared to the stochastic gating of Ca^{2+} release units, the Monte Carlo simulations of Fig. 3.2 would have revealed delta function-like probability densities. That is, rather than observing the linear relationship between diadic subspace and junctional SR [Ca^{2+}] in each (c_{ds},c_{jsr})-plane that suggested Eq. 3.34, we would instead have observed that the probability density in each plane was well approximated by

$$\rho^i(c_{ds}, c_{jsr}, t) = \pi^i(t)\delta(c_{ds} - \bar{c}^i_{ds})\delta(c_{jsr} - \bar{c}^i_{jsr})$$

where $1 \leq i \leq M$ is the index over CaRU states and $\bar{c}^i_{ds}$ and $\bar{c}^i_{jsr}$ are functions of c_{myo} and c_{nsr} found by simultaneously solving Eqs. 3.5 and 3.6 with the left hand sides equal to zero. Although this *fast domain limit* was not observed in our Monte Carlo simulations, for completeness it is denoted in Fig. 3.12 by the *arrow* labeled *fast ds/fast jsr*. If the simplified models of local control that have prevously appeared [Hinch, 2004, Greenstein et al., 2006] were generalized to account for heterogeneous junctional SR [Ca^{2+}], they would correspond to the *fast domain limit* of the multivariate probability density approach presented here.

3.5.2 Computational efficiency of the probability density approach

While the probability density and Monte Carlo calculations are essentially equivalent in terms of the dynamics cellular responses they predict, the probability density approach can be significantly faster than Monte Carlo simulation (Fig. 3.11). Indeed, when both methods are applied using the same (non-adaptive) time step, our current implementation of the univariate probability density approach is approximately 35 times faster than Monte Carlo simulations that employ a physiologically realistic number of CaRUs. Intriguingly, when this comparison is made using time steps that

are distinct and as large as possible while ensuring numerical stability and accuracy of each calculation, we find that the univariate probability density approach can be up to 650 times faster than the corresponding Monte Carlo simulations. For example, the *thin dotted line* of Fig. 3.11 indicates a 6.6 second run time for the probability density approach with a time step of 0.02 ms. This suggests that the probability density approach could be further investigated and developed as a computationally efficient alternative to Monte Carlo simulations of the local control of EC coupling in cardiac myocytes.

Although the computational efficiency of the probability density approach is intriguing, it is important to note that the relative merits of Monte Carlo and probability density simulation methods are in general model dependent. For example, the time required for the Monte Carlo simulation of the whole cell voltage clamp protocols such as those presented in Fig. 3.2 is, at least ultimately, a linear function of the number of CaRUs (i.e., the limiting slope of the *filled squares* of Fig. 3.10 is one). Similarly, we have observed that the computational efficiency of the univariate probability density calculation presented in Figs. 3.6 and 3.7 scales linearly with the number of Ca^{2+} release unit states (M) and the number of mesh points used to discretize the junctional SR $[Ca^{2+}]$ (L) (not shown). Indeed, the *thin dotted lines* of Fig. 3.11 show the run time of the probability density approach decreasing or increasing by a factor of two when the standard number of mesh points ($L = 100$) is decreased or increased to 50 or 200, respectively. Of course, the standard value of $L = 100$ was chosen because further refinement resulted in a negligible change in the probability density result. However, we expect that the number of mesh points required for an accurate probability density calculation will generally depend on the details of the chosen Ca^{2+} release unit model. In the same way, increasing the number M of CaRU states will lead to a less efficient probability density calculation.

Indeed, the relative merits of the probability density and Monte Carlo simulation

methods can be clarified if we assume that the computational effort involved in updating one mesh point of the probability density calculation is equivalent to Monte Carlo simulation of one Ca^{2+} release unit. If we let N denote number of Ca^{2+} release units, M the number of states of the CaRU model, and L the number of mesh points used in the probability density calculation, then in a traditional Monte Carlo calculation, there are $2N$ ODEs to integrate for the local Ca^{2+} concentrations as well as N Markov chains to update at each time step, for a (very roughly calculated) computational effort of $3N$. Conversely, in the univariate probability density approach, there are M PDEs to solve with L mesh points each, for a computational effort of ML. Given the fact that the physiologically realistic number of CaRUs is $N = 20,000$ and the observed number of mesh points required in our probability density calculations is $L = 100$, we might have expected the univariate probability density approach to be approximately 150 times computationally more efficient than Monte Carlo for the minimal $M = 4$ state CaRU model used here (consistent with the observed values of 35–700 in Fig. 3.11). Continuing this reasoning, we might expect the univariate probability density approach to outperform Monte Carlo calculations for any CaRU model with fewer than 600 states ($M \leq 3N/L$).

On the other hand, if model parameters were such that it was not a good approximation to assume that in each CaRU diadic subspace $[Ca^{2+}]$ is in quasi-static equilibrium with junctional SR $[Ca^{2+}]$, then the appropriate probability density alternative to Monte Carlo simulation would be multivariate. In this case each of the M joint probability densities would require a two-dimensional $L \times L$ mesh that discretizes both the diadic subspace and junctional SR $[Ca^{2+}]$. If we presume that the computational effort of the multivariate probability density approach scales as ML^2, then we would expect it to be superior to Monte Carlo calculations involving $N = 20,000$ CaRUs when the chosen CaRU model has fewer than 6 states ($M \leq 3N/L^2$). Consistent with this back-of-the-envelope estimate, when we do not assume fast diadic subspace

[Ca^{2+}] but instead numerically solve the 2D system of advection-reaction equations given by Eqs. 3.19–3.22, we find the multivariate probability density approach is only marginally faster than Monte Carlo simulation (not shown). However, these estimates and preliminary benchmarks fail to account for accelerations of the multivariate probability density approach that could be obtained by using more sophisticated numerical schemes (e.g., a nonuniform or adaptive mesh) and model reduction techniques applicable to the probability density but not the Monte Carlo formulation. For this reason we recommend the probability density approach for further development as a computationally efficient alternative to Monte Carlo simulations of the local control of EC coupling in cardiac myocytes.

3.6   Appendices

3.6.1   Description of fluxes influencing bulk myoplasmic and network SR calcium concentration

The whole cell model of EC coupling that is the focus of this paper includes several fluxes that directly influence the dynamics of the bulk myoplasmic and network SR [Ca^{2+}]. For example, the Na^+-Ca^{2+} exchanger current that appears in Eq. 3.29 takes the form [Luo and Rudy, 1994, Jafri et al., 1998a, Rice et al., 2000],

$$J_{ncx} = -\frac{A_m}{F} I_{ncx}$$

where

$$I_{ncx} = I_{ncx}^o \frac{[\text{Na}^+]_{myo}^3 c_{ext} e^{\eta_{ncx} FV/RT} - [\text{Na}^+]_{ext}^3 c_{myo} e^{(\eta_{ncx}-1)FV/RT}}{\left(K_{ncx,n}^3 + [\text{Na}^+]_{ext}^3\right)\left(K_{ncx,c} + c_{ext}\right)\left(1 + k_{ncx}^{sat} e^{(\eta_{ncx}-1)FV/RT}\right)},$$

$A_m = C_m \beta_{myo}/V_{myo}$, c_{ext} is the extracellular Ca^{2+} concentration, and $[Na^+]_{myo}$ and $[Na^+]_{ext}$ are the intracellular and extracellular sodium concentrations, respectively (for parameters see Tables 3.1 – 3.3).

The SERCA-type Ca-ATPase flux that appears in Eqs. 3.29 and 3.30 includes both forward and reverse modes [Shannon et al., 2000] and is given by

$$J_{serca} = v_{serca} \frac{\left(\dfrac{c_{myo}}{K_{fs}}\right)^{\eta_{fs}} - \left(\dfrac{c_{nsr}}{K_{rs}}\right)^{\eta_{rs}}}{1 + \left(\dfrac{c_{myo}}{K_{fs}}\right)^{\eta_{fs}} + \left(\dfrac{c_{nsr}}{K_{rs}}\right)^{\eta_{rs}}} \tag{3.48}$$

with parameters as in Table 3.3. In addition, Eqs. 3.29 and 3.30 include a leakage Ca^{2+} flux given by

$$J_{leak} = v_{leak}(c_{nsr} - c_{myo}).$$

Following [Rice et al., 2000], Eq. 3.29 includes a constant background Ca^{2+} influx that takes the form,

$$J_{in} = -\frac{A_m}{zF} I_{in}$$

where $I_{in} = g_{in}(V - E_{Ca})$ and $E_{Ca} = (RT/2F)\ln(c_{ext}/c_{myo})$.

3.6.2   Generalization of the probability density approach

The probability density approach is completely general and in principle the methodology can be applied to Ca^{2+} release unit models of arbitrary complexity. Let $S(t) = i \in \{1, ..., M\}$ be the state of a continuous time discrete state Markov Chain model of an individual Ca^{2+} release unit and let the $M \times M$ matrix Q be the infinitesimal generator matrix for this stochastic process composed of rates that may be constant or, alternatively, arbitrary functions of voltage, diadic subspace $[Ca^{2+}]$, or junctional SR $[Ca^{2+}]$. Let us also rewrite the multivariate probability density

functions defined in Eq. 3.18 using slightly more compact notation,

$$\rho^i(\boldsymbol{c}, t)\, d\boldsymbol{c} = \Pr\{\boldsymbol{c} < \tilde{\boldsymbol{c}}(t) < \boldsymbol{c} + d\boldsymbol{c} \text{ and } \tilde{S}(t) = i\},$$

where $\boldsymbol{c}$ is a vector including both the diadic subspace and junctional SR Ca^{2+} concentrations. Using Bayes' formula these joint probability densities can be related to the probability densities for diadic subspace and junctional SR $[Ca^{2+}]$ *conditioned* on the the state of the channel,

$$\Pr\{\boldsymbol{c} < \tilde{\boldsymbol{c}}(t) < \boldsymbol{c} + d\boldsymbol{c} \mid \tilde{S}(t) = i\} = \frac{\Pr\{\boldsymbol{c} < \tilde{\boldsymbol{c}}(t) < \boldsymbol{c} + d\boldsymbol{c} \text{ and } \tilde{S}(t) = i\}}{\Pr\left\{\tilde{S}(t) = i\right\}}.$$

That is, if the probability density $\rho^i(\boldsymbol{c}, t)$ is integrated over all possible diadic subspace and junctional SR Ca^{2+} concentrations, the probability π^i of finding the randomly sampled Ca^{2+} release unit in state i is obtained,

$$\pi^i = \Pr\left\{\tilde{S}(t) = i\right\} = \int \rho^i(\boldsymbol{c}, t) d\boldsymbol{c}$$

where $d\boldsymbol{c} = dc_{ds}\, dc_{jsr}$.

Using this notation, the advection-reaction equations (Eqs. 3.19–3.22) for the probability density of diadic subspace and junctional SR $[Ca^{2+}]$ jointly distributed with the state of the Ca^{2+} release unit become,

$$\frac{\partial \rho^i}{\partial t} = -\frac{\partial}{\partial c_{ds}}[f_{ds}^i\, \rho^i] - \frac{\partial}{\partial c_{jsr}}[f_{jsr}^i\, \rho^i] + [\rho Q]^i \tag{3.49}$$

where $\boldsymbol{\rho}$ is a row vector given by $\boldsymbol{\rho} = (\rho^1, \rho^2, ..., \rho^M)$ in which each element ρ^i is a function of c_{ds} and c_{jsr}; and $[\rho Q]^i$ is the ith element of the row vector resulting from a vector-matrix product of $\boldsymbol{\rho}$ and Q.

3.6.3 Derivation of the univariate probability density approach

Using Eqs. 3.34–3.37 the advection-reaction equations of the multivariate probability density formulation (Eqs. 3.19–3.22) can be reduced to the univariate version (Eqs. 3.38–3.41). For example, here we show that making the substitution given by Eq. 3.34 in Eq. 3.22 and integrating the resulting equations with respect to diadic subspace [Ca^{2+}] leads term by term to Eq. 3.41. The first term of the left hand side of Eq. 3.22 involving the partial derivative with respect to time becomes

$$\int_0^\infty \frac{\partial \rho^{\mathcal{OO}}}{\partial t} \, dc_{ds} = \int_0^\infty \frac{\partial}{\partial t} \left[\rho_{jsr}^{\mathcal{OO}} \delta(c_{ds} - \bar{c}_{ds}^{\mathcal{OO}}) \right] \, dc_{ds} = \frac{\partial \rho_{jsr}^{\mathcal{OO}}}{\partial t} \int_0^\infty \delta(c_{ds} - \bar{c}_{ds}^{\mathcal{OO}}) \, dc_{ds} = \frac{\partial \rho_{jsr}^{\mathcal{OO}}}{\partial t},$$

i.e., the first term of Eq. 3.41. The first term on the right hand side of Eq. 3.22 involving the partial derivative with respect to c_{ds} is disappears, that is,

$$-\int_0^\infty \frac{\partial}{\partial c_{ds}} \left[f_{ds}^{\mathcal{OO}} \rho^{\mathcal{OO}} \right] \, dc_{ds} = - \left. f_{ds}^{\mathcal{OO}} \rho^{\mathcal{OO}} \right|_0^\infty = 0,$$

because the probability density $\rho^{\mathcal{OO}}(c_{ds}, c_{jsr}, t)$ evaluates to zero at the minimum and maximum physical values for diadic subspace [Ca^{2+}]. The second term on the right hand side of Eq. 3.22 involving the partial derivative with respect to c_{jsr} becomes

$$
\begin{aligned}
-\int_0^\infty \frac{\partial}{\partial c_{jsr}} \left[f_{jsr}^{\mathcal{OO}} \rho^{\mathcal{OO}} \right] \, dc_{ds} &= -\int_0^\infty \frac{\partial}{\partial c_{jsr}} \left[f_{jsr}^{\mathcal{OO}} \rho_{jsr}^{\mathcal{OO}} \delta(c_{ds} - \bar{c}_{ds}^{\mathcal{OO}}) \right] \, dc_{ds} \\
&= -\frac{\partial}{\partial c_{jsr}} \left\{ \left[\int_0^\infty f_{jsr}^{\mathcal{OO}} \delta(c_{ds} - \bar{c}_{ds}^{\mathcal{OO}}) \, dc_{ds} \right] \rho_{jsr}^{\mathcal{OO}} \right\} \\
&= -\frac{\partial}{\partial c_{jsr}} \left[\bar{f}_{jsr}^{\mathcal{OO}} \rho_{jsr}^{\mathcal{OO}} \right]
\end{aligned}
$$

where $\bar{f}_{jsr}^{\mathcal{OO}} = f_{jsr}^{\mathcal{OO}}(\bar{c}_{ds}^{\mathcal{OO}}, c_{jsr})$ due to the sifting property of the delta function, in agreement with Eqs. 3.41 and 3.43. Finally, the three reaction terms in Eq. 3.22

130

reduce as required because

$$k^i \int_0^\infty \rho^i \, dc_{ds} = k^i \int_0^\infty \rho^i_{jsr} \delta(c_{ds} - \bar{c}^i_{ds}) \, dc_{ds} = k^i \rho^i_{jsr} \int_0^\infty \delta(c_{ds} - \bar{c}^i_{ds}) \, dc_{ds} = k^i \rho^i_{jsr}$$

where $i = \mathcal{OO}, \mathcal{OC}$, and $\mathcal{CO}$; $k^{\mathcal{OO}} = -\left(k^-_{ryr} + k^-_{dhpr}\right)$, $k^{\mathcal{OC}} = k^+_{ryr}$, and $k^{\mathcal{CO}} = k^+_{dhpr}$.

3.6.4 Numerical scheme for the univariate probability density approach

In the notation of Appendix 3.6.2, the advection-reaction equations (Eqs. 3.38–3.41) used in the univariate probability density approach take the form,

$$\frac{\partial \rho^i}{\partial t} = -\frac{\partial}{\partial c_{jsr}}[\bar{f}^i_{jsr} \rho^i] + [\rho Q]^i. \tag{3.50}$$

Numerical solution of these equations was performed using a total variation diminishing scheme following [Casti et al., 2002, Huertas and Smith, 2006b]. Briefly, we discretize junctional SR [Ca^{2+}] according to $c_{jsr,\ell} = \ell \Delta c_{jsr} + c^{min}_{jsr}$ where $\ell = 0, 1, \cdots, L$ and $\Delta c_{jsr} = (c^{max}_{jsr} - c^{min}_{jsr})/L$. With these preliminaries, the numerical scheme can be written as

$$\frac{d\rho^i_\ell}{dt} = -\frac{1}{\Delta c_{jsr}} \left[g^i_\ell - g^i_{\ell-1}\right] + \sum_{m=1}^M \rho^m_\ell q^{mi}_\ell$$

where q^{mi}_ℓ is the transition rate in the mth row and ith column of Q evaluated at a junctional SR [Ca^{2+}] of $c_{jsr,\ell}$. In this expression, g^i_ℓ and $g^i_{\ell-1}$ are given by

$$g_\ell = \phi^*_{\ell+\frac{1}{2}} + \frac{1}{2}\psi^+_{\ell-\frac{1}{2}}(\phi_\ell - \phi^*_{\ell-\frac{1}{2}}) + \psi^-_{\ell+\frac{3}{2}}(\phi_{\ell+1} - \phi^*_{\ell+\frac{3}{2}}) \tag{3.51}$$

where we have dropped the superscripted i, $\phi_\ell = \bar{f}_\ell \rho_\ell$, and $\phi^*_{\ell+\frac{1}{2}}$ is the first-order Roe flux defined by [Casti et al., 2002, Hundsdorfer and Verwer, 2003]

$$\phi^*_{\ell+\frac{1}{2}} = \frac{1}{2}(\phi_\ell + \phi_{\ell+1}) - \frac{1}{4}\left|\bar{f}_\ell + \bar{f}_{\ell+1}\right|(\rho_{\ell+1} - \rho_\ell)$$

where $\bar{f}_\ell = \bar{f}^i_{jsr,\ell}$ is the discretized advection rate appearing in Eq. 3.50. The quantities ψ^+ and ψ^- occurring in Eq. 3.51 are flux limiters given by

$$\psi^+_{\ell-\frac{1}{2}} = \psi\left[\frac{f_{\ell+1} - f^*_{\ell+\frac{1}{2}}}{f_\ell - f^*_{\ell-\frac{1}{2}}}\right] \qquad \psi^-_{\ell+\frac{3}{2}} = \psi\left[\frac{f_\ell - f^*_{\ell+\frac{1}{2}}}{f_{\ell+1} - f^*_{\ell+\frac{3}{2}}}\right]$$

where

$$\psi[r] = \max\left[0, \min(2r, 1), \min(r, 2)\right].$$

The ordinary differential equations in the univariate model (Eqs. 3.29–3.30) were intregrated using Euler's method with a time step of 1 μs. The efflux and refill fluxes of Eqs. 3.31 and 3.32 were approximated by

$$J^*_{efflux} = v^T_{efflux}\Delta c_{jsr}\sum_{i=1}^{M}\sum_{\ell=0}^{L}\rho^i_\ell\left[\bar{c}^i_{ds,\ell} - c_{myo}(t)\right]$$

$$J^*_{refill} = v^T_{refill}\Delta c_{jsr}\sum_{i=1}^{M}\sum_{\ell=0}^{L}\rho^i_\ell\left[c_{nsr}(t) - c_{jsr,\ell}\right]$$

where $\bar{c}^i_{ds,\ell}$ is given by Eq. 3.35 with the junctional SR [Ca^{2+}] evaluated at $c_{jsr,\ell}$.

Chapter 4

Moment closure for local control models of calcium-induced calcium release in cardiac myocytes

4.1 Summary

In prior work we introduced a probability density approach to modeling local control of Ca^{2+}-induced Ca^{2+} release in cardiac myocytes [Williams et al., Biophys. J. 92(7):2311–28, 2007] where we derived coupled advection-reaction equations for the time-dependent bivariate probability density of subsarcolemmal subspace and junctional sarcoplasmic reticulum (SR) $[Ca^{2+}]$ conditioned on Ca^{2+} release unit (CaRU) state. When coupled to ODEs for the bulk myoplasmic and network SR $[Ca^{2+}]$, a realistic but minimal model of cardiac excitation-contraction coupling was produced that avoids the computationally demanding task of resolving spatial aspects of global Ca^{2+} signaling, while accurately representing heterogeneous local Ca^{2+} signals in a population of diadic subspaces and junctional SR depletion domains. Here we introduce a computationally efficient method for simulating such whole cell models

when the dynamics of subspace $[Ca^{2+}]$ are much faster than those of junctional SR $[Ca^{2+}]$. The method begins with the derivation of a system of ODEs describing the time-evolution of the moments of the univariate probability density functions for junctional SR $[Ca^{2+}]$ jointly distributed with CaRU state. This open system of ODEs is then closed using an algebraic relationship that expresses the third moment of junctional SR $[Ca^{2+}]$ in terms of the first and second moments. In simulated voltage-clamp protocols using 12-state CaRUs that respond to the dynamics of both subspace and junctional SR $[Ca^{2+}]$, this moment closure approach to simulating local control of excitation-contraction coupling produces high-gain Ca^{2+} release that is graded with changes in membrane potential, a phenomenon not exhibited by common pool models. Benchmark simulations indicate that the moment closure approach is nearly 10,000-times more computationally efficient than corresponding Monte Carlo simulations while leading to nearly identical results. We conclude by applying the moment closure approach to study the restitution of Ca^{2+}-induced Ca^{2+} release during simulated two-pulse voltage-clamp protocols.

The contents of this chapter are under review as "Moment closure for local control models of calcium-induced calcium release in cardiac myocytes" in *Biophysical Journal* [George S. B. Williams, Marco A. Huertas, Eric A. Sobie, M. Saleet Jafri, and Gregory D. Smith]. The author gratefully acknowledges Marco Huertas' contribution to the development of the moment closure technique. Some of these results have also appeared in poster form at the 2008 Biophysical Society Annual Meeting in Long Beach, CA.

4.2 Introduction

The key step linking electrical excitation to contraction in cardiac myocytes is Ca^{2+}-induced Ca^{2+} release (CICR), in which Ca^{2+} current flowing across the cell mem-

brane triggers the release of additional Ca^{2+} from the sarcoplasmic reticulum (SR). In ventricular cells, CICR occurs as a set of discrete microscopic events known as Ca^{2+} sparks [Cheng et al., 1993b], with each spark triggered by local, rather than cell-wide, increases in myoplasmic $[Ca^{2+}]$. As a consequence of this "local control" mechanism of CICR, the cellular SR Ca^{2+} release flux is not a function of a single quantity, such as spatially-averaged intracellular $[Ca^{2+}]$, but instead depends on thousands of different local Ca^{2+} concentrations, each of which can fluctuate with stochastic openings and closings of nearby Ca^{2+} channels in the sarcolemmal and SR membranes. The picture is further complicated by the fact that dynamic changes in local SR $[Ca^{2+}]$, which are also spatially heterogeneous, are thought to influence the gating of SR Ca^{2+} release channels known as ryanodine receptors (RyRs).

Computational models have been developed in which SR Ca^{2+} release depends directly on the average myoplasmic $[Ca^{2+}]$ [Jafri et al., 1998a, Glukhovsky et al., 1998a, Snyder et al., 2000a]. These so-called "common pool" models [Stern, 1992a] display SR Ca^{2+} release that occurs in an "all-or-none" fashion, contrary to experiments showing that release is smoothly graded with changes in Ca^{2+} influx [Fabiato, 1985a, Wier et al., 1994a, Cannell et al., 1995b]. On the other hand, several published models achieve graded Ca^{2+} release using non-mechanistic formulations, such as having SR Ca^{2+} release depend explicitly on Ca^{2+} currents rather than on local $[Ca^{2+}]$ [Bondarenko et al., 2004, Luo and Rudy, 1994, Wong et al., 1992, Hilgemann and Noble, 1987, Shiferaw et al., 2003].

Models of EC coupling are able to reproduce graded Ca^{2+} release mechanistically by simulating the stochastic gating of channels in Ca^{2+} release sites using Monte Carlo methods. In these approaches, one or more L-type Ca^{2+} channels interact with a cluster of RyRs through changes in $[Ca^{2+}]$ in a small "diadic subspace" between the sarcolemmal and SR membranes. These models also generally consider local changes in junctional SR $[Ca^{2+}]$, because these changes are thought to be important for Ca^{2+}

spark termination and refractoriness [Stern et al., 1999c, Rice et al., 1999a, Sobie et al., 2002a]. Realistic cellular SR Ca^{2+} release can be simulated by computing the stochastic triggering of sparks from hundreds to thousands of such "Ca^{2+} release units" (CaRUs) [Stern, 1992a, Rice et al., 1999a, Sobie et al., 2002a, Greenstein and Winslow, 2002a]. However, Monte Carlo simulations of local control of EC coupling can be computationally demanding, making it difficult to augment these models with representations of the ionic currents responsible for action potentials, and impractical to use this approach for simulations of phenomena occurring over the course of many heartbeats.

We recently demonstrated that an alternative "probability density approach" can be used to simulate graded, locally controlled SR Ca^{2+} release mechanistically [Williams et al., 2007]. In this prior work, coupled advection-reaction equations were derived relating the time-dependent probability density of subsarcolemmal subspace and junctional SR $[Ca^{2+}]$ conditioned on CaRU state. By numerically solving these equations using a high-resolution finite difference scheme and coupling the resulting probability densities to ordinary differential equations (ODEs) for the bulk myoplasmic and sarcoplasmic reticulum $[Ca^{2+}]$, a realistic but minimal model of cardiac excitation-contraction coupling was produced. This new approach to modeling local control of EC coupling is often computationally more efficient than Monte Carlo simulation, particularly if the dynamics of subspace $[Ca^{2+}]$ are much faster that those of junctional SR $[Ca^{2+}]$, allowing the bivariate probability density functions for subspace and junctional SR $[Ca^{2+}]$ to be replaced with univariate densities for junctional SR $[Ca^{2+}]$. However, the probability density approach can lose its computational advantage when the number of states in the CaRU model is large or the dynamics of local $[Ca^{2+}]$ are such that numerical stability requires a refined mesh for solving the advection-reaction equations.

We therefore aimed to develop methods for improving upon the probability den-

sity approach, and in this study we describe for the first time a "moment closure" technique that leads to significant computational advantages. After briefly reviewing the Monte Carlo and probability density approaches to modeling local control of EC coupling in cardiac myocytes, the new methodology begins with a derivation of a system of ODEs describing the time-evolution of the moments of the univariate probability density functions for junctional SR $[Ca^{2+}]$ jointly distributed with CaRU state. This open system of ODEs is then closed using an algebraic relationship that expresses the third moment of junctional SR $[Ca^{2+}]$ in terms of the first and second moments. In this manner, the partial differential equations describing the univariate probability densities of junctional SR $[Ca^{2+}]$ jointly distributed with CaRU state are replaced with ODEs describing the time-evolution of the moments of these distributions. In simulated voltage-clamp protocols using 12-state CaRUs that respond to the dynamics of both subspace and junctional SR $[Ca^{2+}]$, this moment closure approach to simulating local control of EC coupling produces high-gain Ca^{2+} release that is graded with changes in membrane potential, a phenomenon not exhibited by common pool models. Benchmark simulations indicate that this moment closure technique for local control models of CICR in cardiac myocytes is nearly 10,000-times more computationally efficient than corresponding Monte Carlo simulations, while leading to nearly identical results. We conclude by applying the moment closure approach to study the restitution of Ca^{2+}-induced Ca^{2+} release during simulated two-pulse voltage-clamp protocols.

4.3 Model Formulation

The focus of this manuscript is a novel moment closure technique to modeling local control of CICR in cardiac myocytes. The whole cell model of EC coupling that will be used to demonstrate the method closely follows our prior work in which we

presented traditional Monte Carlo simulations of graded, locally controlled SR Ca^{2+} release to validate a novel probability density approach that represents the distribution of diadic subspace and junctional SR Ca^{2+} concentrations with a system of partial differential equations [Williams et al., 2007]. Below we briefly review the Monte Carlo and probability density formulations, emphasizing minor adjustments that were required to implement the moment closure technique. The Results section begins with the derivation of the moment closure equations and follows with the validation and benchmarking of the moment closure technique for local control models of CICR in cardiac myocytes by comparison to Monte Carlo simulation.

4.3.1   Monte Carlo formulation

The Monte Carlo model of local control of CICR in cardiac myocytes describes the dynamics of bulk myoplasmic $[Ca^{2+}]$, network SR $[Ca^{2+}]$, N diadic subspace Ca^{2+} concentrations and N junctional SR domain Ca^{2+} concentrations through a system of ODEs that are coupled to N Markov chains representing the stochastic gating of each CaRU that consists of one L-type Ca^{2+} channel (DHPR) and one RyR "megachannel" coupled through the local diadic subspace (c_{ds}) $[Ca^{2+}]$. While a complete description of CICR would include stochastic gating of roughly $N = 10{,}000$ CaRUs, each containing multiple L-type Ca^{2+} channels (1–10) [Bers and Stiffel, 1993] and RyRs (30–300) [Franzini-Armstrong, 1999], Monte Carlo simulations of EC coupling focusing on local control have often used Markov models of reduced complexity [Stern, 1992a, Sobie et al., 2002a, Hinch, 2004], and this level of resolution will suffice to introduce the moment closure technique.

4.3.1.1   Concentration balance equations

The Monte Carlo model consists of $N+2$ ODEs representing the time-evolution of $[Ca^{2+}]$ in the bulk myoplasm (c_{myo}), network SR (c_{nsr}), and N junctional SRs (c_{jsr}^n)
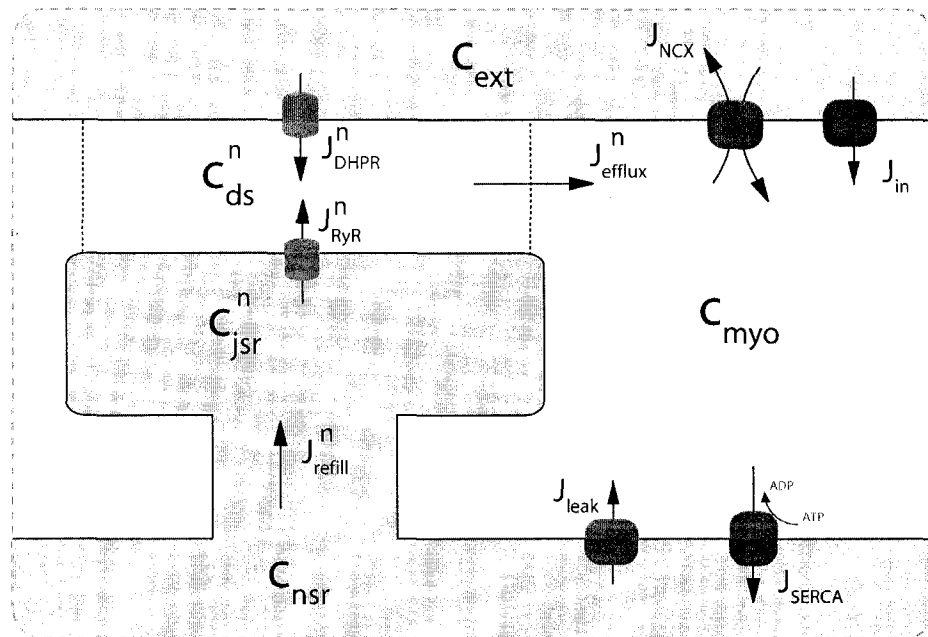
Figure 4.1: Diagram of model components and fluxes. Each Ca^{2+} release unit consists of two restricted compartments (the diadic subspace and junctional SR with $[Ca^{2+}]$ denoted by c_{ds} and c_{jsr}, respectively), a two-state L-type Ca^{2+} channel (DHPR), and a 6-state Ca^{2+} release site. The t-tubular $[Ca^{2+}]$ is denoted by c_{ext} and the fluxes J_{dhpr}^n, J_{ryr}^n, J_{efflux}^n, J_{refill}^n, J_{in}, J_{ncx}, J_{serca}, and J_{leak} are described in the text and Appendix A.

compartments. Consistent with Fig. 4.1, the concentration balance equations for these compartments are

$$\frac{dc_{myo}}{dt} = J_{leak} + J^T_{efflux} - J_{ncx} - J_{serca} + J_{in} \tag{4.1}$$

$$\frac{dc_{nsr}}{dt} = \frac{1}{\lambda_{nsr}} \left(J_{serca} - J^T_{refill} - J_{leak} \right) \tag{4.2}$$

$$\frac{dc^n_{jsr}}{dt} = \frac{1}{\lambda_{jsr}} \left(J^n_{refill} - J^n_{ryr} \right) \tag{4.3}$$

where $1 \leq n \leq N$ and λ_{nsr} and λ_{jsr} are volume fractions (see Appendix 4.6.1). The flux through the RyR megachannel associated with the nth CaRU (J^n_{ryr}) is given by

$$J^n_{ryr} = \gamma^n_{ryr} \frac{v^T_{ryr}}{N} (c^n_{jsr} - \bar{c}^n_{ds}) \tag{4.4}$$

where γ^n_{ryr} is a stochastic variable that takes the value 1 or 0 depending on whether the nth RyR megachannel is open or closed, and $\bar{c}^n_{ds}$ is the associated diadic subspace concentration defined below (Eq. 4.9). Similarly, diffusion from the network SR to each junctional SR compartment is given by

$$J^n_{refill} = \frac{v^T_{refill}}{N} (c_{nsr} - c^n_{jsr}). \tag{4.5}$$

The total refill flux occurring in Eq. 4.2 includes the contribution from each CaRU and is given by

$$J^T_{refill} = \sum_{n=1}^{N} J^n_{refill} \tag{4.6}$$

while the total flux out of the N diadic subspaces is given by

$$J^T_{efflux} = \sum_{n=1}^{N} J^n_{efflux} = \sum_{n=1}^{N} \frac{v^T_{efflux}}{N} (\bar{c}^n_{ds} - c_{myo}). \tag{4.7}$$

140

The remaining four fluxes that appear in Eqs. 4.1–4.3 and Fig. 4.1 include J_{dhpr}^n (influx into the diadic subspaces via L-type Ca^{2+} channels that is a function of the random variable γ_{dhpr}^n), J_{in} (background Ca^{2+} influx), J_{ncx} (Na^+-Ca^{2+} exchange), J_{serca} (SR Ca^{2+}-ATPases), and J_{leak} (the network SR leak). The functional form of these four fluxes can be found in Appendix 4.6.1.

4.3.1.2   Diadic subspace calcium concentration

Note that a concentration balance equation is not included for diadic subspace $[Ca^{2+}]$, because in our previous study we observed that model parameters lead to rapid equilibrium of the diadic subspace $[Ca^{2+}]$ with the $[Ca^{2+}]$ in the juctional SR and bulk myoplasm [Williams et al., 2007]. Thus, in each diadic subspace we assume a $[Ca^{2+}]$ ($\bar{c}_{ds}^n$) that balances the fluxes in and out of that compartment,

$$0 = \frac{1}{\lambda_{ds}} \left(J_{dhpr}^n + J_{ryr}^n - J_{efflux}^n \right), \tag{4.8}$$

that is,

$$\bar{c}_{ds}^n = \bar{c}_{ds,0}^n + \bar{c}_{ds,1}^n \, c_{jsr} \tag{4.9}$$

where $1 \leq n \leq N$ and

$$\bar{c}_{ds,0}^n = \frac{\gamma_{dhpr}^n J_{dhpr}^0 + v_{efflux} c_{myo}}{\gamma_{ryr}^n v_{ryr} + v_{efflux} - \gamma_{dhpr}^n J_{dhpr}^1} \tag{4.10}$$

$$\bar{c}_{ds,1}^n = \frac{\gamma_{ryr}^n v_{ryr}}{\gamma_{ryr}^n v_{ryr} + v_{efflux} - \gamma_{dhpr}^n J_{dhpr}^1}. \tag{4.11}$$

In these expressions, the quanties γ_{dhpr}^n and γ_{ryr}^n indicate whether the channel is open or closed, $v_{ryr} = v_{ryr}^T/N$, $v_{efflux} = v_{efflux}^T/N$, and J_{dhpr}^0 and J_{dhpr}^1 are functions of plasma membrane voltage defined by

$$J_{dhpr}^n = \gamma_{dhpr}^n \left(J_{dhpr}^0 + \bar{c}_{ds}^n J_{dhpr}^1 \right) \tag{4.12}$$

where the L-type Ca^{2+} channel flux, J_{dhpr}^n is given by Eq. 4.2 (see Appendix 4.6.1).

4.3.1.3 Twelve-state CaRU model

The RyR model used here is similar to the two-state minimal model of an RyR "megachannel" used in prior work [Williams et al., 2007]. Consistent with several studies indicating that the gating of the RyR cluster associated with each CaRU is essentially all-or-none [Stern, 1992a, Rice et al., 1999a, Sobie et al., 2002a], the two-state RyR megachannel model used in [Williams et al., 2007] included transition rates that were nonlinear functions of diadic subspace (c_{ds}) and junctional SR (c_{jsr}) [Ca^{2+}], thereby allowing for Ca^{2+}-dependent activation of RyR gating as well as spark termination facilitated by localized depletion of junctional SR [Ca^{2+}]. Because the moment closure approach is most easily presented when all Ca^{2+}-mediated transitions in the CaRU model are bimolecular association reactions, the six-state RyR megachannel model used here employs sequential binding of diadic subspace Ca^{2+} ions to achieve highly cooperative Ca^{2+}-dependent opening of the RyR megachannel. Similarly, an explicit junctional SR Ca^{2+}-dependent transition is included so that depletion of luminal Ca^{2+} decreases the open probability of the megachannel,

$$
\mathcal{C}_1 \underset{\beta^3 k_{ryr}^-}{\overset{4k_{ryr}^+ c_{ds}}{\rightleftharpoons}} \mathcal{C}_2 \underset{2\beta^2 k_{ryr}^-}{\overset{3\alpha k_{ryr}^+ c_{ds}}{\rightleftharpoons}} \mathcal{C}_3 \underset{3\beta k_{ryr}^-}{\overset{2\alpha^2 k_{ryr}^+ c_{ds}}{\rightleftharpoons}} \mathcal{C}_4 \underset{4k_{ryr}^-}{\overset{\alpha^3 k_{ryr}^+ c_{ds}}{\rightleftharpoons}} \mathcal{C}_5 \underset{k_{ryr,*}^-}{\overset{k_{ryr,*}^+ c_{jsr}}{\rightleftharpoons}} \mathcal{O} .
$$

$$(4.13)$$
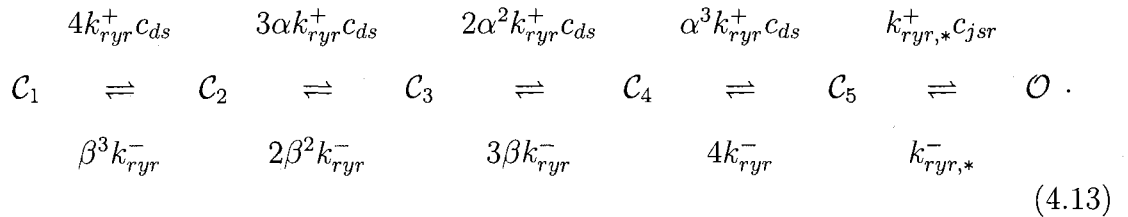
Parameters were chosen (see Table 4.2) so that the behavior of this minimal six-state RyR megachannel model approximated the above-mentioned two-state model.

As in prior work [Williams et al., 2007], we use a two-state model of the L-type

Ca^{2+} channel (DHPR),

$$\mathcal{C} \underset{k_{dhpr}^{-}}{\overset{k_{dhpr}^{+}(V)}{\rightleftharpoons}} \mathcal{O}\,, \qquad\qquad (4.14)$$

where $\mathcal{C}$ and $\mathcal{O}$ represent closed and open states, k_{dhpr}^{+} is the voltage-dependent activation rate [Luo and Rudy, 1994] given by

$$k_{dhpr}^{+} = \bar{k}_{dhpr}^{+} \frac{e^{(V-V_{dhpr}^{\theta})/\sigma_{dhpr}}}{1 + e^{(V-V_{dhpr}^{\theta})/\sigma_{dhpr}}}, \qquad\qquad (4.15)$$

and k_{dhpr}^{-} is the constant de-activation rate that sets the mean open time (0.2 ms) and maximum open probability (0.1) of the channel. Although this two-state DHPR model ignores voltage- and Ca^{2+}-dependent inactivation of L-type Ca^{2+} channels, these processes do not significantly influence the triggering of CICR during the whole-cell voltage clamp protocols that are used in this paper to validate the moment closure technique.

Combining the six-state RyR megachannel model with the two-state L-type channel model yields a twelve-state CaRU model that takes the form,

$$
\begin{array}{ccccccccccc}
\mathcal{CC}_1 & \rightleftharpoons & \mathcal{CC}_2 & \rightleftharpoons & \mathcal{CC}_3 & \rightleftharpoons & \mathcal{CC}_4 & \rightleftharpoons & \mathcal{CC}_5 & \rightleftharpoons & \mathcal{CO} \\
\updownarrow & & \updownarrow & & \updownarrow & & \updownarrow & & \updownarrow & & \updownarrow \\
\mathcal{OC}_1 & \rightleftharpoons & \mathcal{OC}_2 & \rightleftharpoons & \mathcal{OC}_3 & \rightleftharpoons & \mathcal{OC}_4 & \rightleftharpoons & \mathcal{OC}_5 & \rightleftharpoons & \mathcal{OO}
\end{array}
\qquad (4.16)
$$
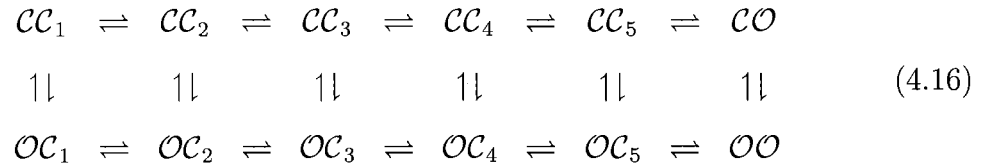
where horizontal and vertical transitions are governed by Eqs. 4.13 and 4.14, respectively, and the first character ($\mathcal{C}$ or $\mathcal{O}$) indicates the state of the DHPR while the second character ($\mathcal{C}_1, \mathcal{C}_2, \mathcal{C}_3, \mathcal{C}_4, \mathcal{C}_5$, or $\mathcal{O}$) refers to the state of the RyR megachannel.

Note that the 12-by-12 infinitesimal generator matrix (sometimes called the Q-matrix) that collects the rate constants of the CaRU model (Eq. 4.16) can be written

compactly in the form,

$$Q = K_\phi(V) + c_{ds}\,K_{ds} + c_{jsr}\,K_{jsr} \tag{4.17}$$

where the elements of $K_\phi(V)$ are the Ca^{2+}-independent transitions (both voltage-dependent and voltage-independent with units of $time^{-1}$), and the elements of K_{ds} and K_{jsr} are the association rate constants for the transitions mediated by diadic subspace (c_{ds}) and junctional SR (c_{jsr}) $[Ca^{2+}]$, respectively (with units of $concentration^{-1}$ $time^{-1}$). Although non-cooperative binding of Ca^{2+} is not a formal requirement for the application of the moment closure technique, for simplicity we will assume the CaRU model is written in the form of Eq. 4.17.

4.3.1.4 Univariate probability density model

The moment closure technique begins with the equations for a univariate probability density model of local control of Ca^{2+}-induced Ca^{2+} release in cardiac myocytes [Williams et al., 2007]. We write $\rho^i(c_{jsr}, t)$ to denote probability density functions for the distribution of $[Ca^{2+}]$ in a large number of junctional SR compartments jointly distributed with CaRU state, that is,

$$
\begin{aligned}
\rho^i_{jsr}(c_{jsr}, t)\,dc_{jsr} \;&=\; \mathsf{Pr}\{c_{jsr} < \tilde{c}_{jsr}(t) < c_{jsr} + dc_{jsr} \\
&\quad \text{and } \tilde{S}(t) = i\}
\end{aligned}
\tag{4.18}
$$

where i is an index over CaRU state, and the tilde in $\tilde{c}_{jsr}$ and $\tilde{S}$ indicate random quantities. For these densities to be consistent with the dynamics of the Monte Carlo model of cardiac EC coupling as $N \to \infty$, they must satisfy a system of advection-reaction equations of the form [Williams et al., 2007, Mazzag et al., 2005a, Huertas

and Smith, 2007b],

$$\frac{\partial \rho^i}{\partial t} = -\frac{\partial}{\partial c_{jsr}} [f^i_{jsr} \rho^i] + [\rho Q]^i, \qquad (4.19)$$

where $1 \le i \le M$, M=12 is the number of states in the CaRU model, Q is the $M \times M$ generator matrix (Eq. 4.17), the row-vector $\boldsymbol{\rho}(c_{jsr}, t) = (\rho^1, \rho^2, \cdots, \rho^M)$ collects the time-dependent probability densities for the junctional SR [Ca^{2+}] jointly distributed with CaRU state (Eq. 4.18), and $[\boldsymbol{\rho} Q]^i$ is the ith element of the vector-matrix product $\boldsymbol{\rho} Q$.

Note that the factor $f^i_{jsr}(c_{jsr})$ in Eq. 4.19 describes the deterministic aspect of the time-evolution of c_{jsr} when the CaRU is in state i. That is, consistent with Eq. 4.3 we have

$$
\begin{aligned}
f^i_{jsr} &= \frac{1}{\lambda^T_{jsr}} \left(J^T_{refill} - \gamma^i_{ryr} J^T_{ryr} \right) \\
&= \frac{1}{\lambda^T_{jsr}} \left(v^T_{refill} \left[c_{nsr} - c_{jsr} \right] - \gamma^i_{ryr} v^T_{ryr} \left[c_{jsr} - \bar{c}^i_{ds} \right] \right)
\end{aligned} \qquad (4.20)
$$

where $1 \le i \le M$ and $\bar{c}^i_{ds}$ is a function of CaRU state, the local junctional SR [Ca^{2+}], and the bulk myoplasmic [Ca^{2+}] analogous to Eqs. 4.9–4.11,

$$\bar{c}^i_{ds} = \bar{c}^i_{ds,0} + \bar{c}^i_{ds,1} \, c_{jsr} \qquad (4.21)$$

where

$$\bar{c}^i_{ds,0} = \frac{\gamma^i_{dhpr} J^{T,0}_{dhpr} + v^T_{efflux} c_{myo}}{\gamma^i_{ryr} v^T_{ryr} + v^T_{efflux} - \gamma^i_{dhpr} J^{T,1}_{dhpr}} \qquad (4.22)$$

$$\bar{c}^i_{ds,1} = \frac{\gamma^i_{ryr} v^T_{ryr}}{\gamma^i_{ryr} v^T_{ryr} + v^T_{efflux} - \gamma^i_{dhpr} J^{T,1}_{dhpr}} . \qquad (4.23)$$

In these expressions, the quanties γ^i_{dhpr} and γ^i_{ryr} take values of 0 or 1 depending on whether the respective component of the CaRU model is closed or open, and $J^{T,0}_{dhpr}$

and $J_{dhpr}^{T,1}$ are functions of plasma membrane voltage defined by

$$J_{dhpr}^T = \sum_{i=1}^{M} \gamma_{dhpr}^i \left(J_{dhpr}^{T,0} + \bar{c}_{ds}^i J_{dhpr}^{T,1} \right) \qquad (4.24)$$

where J_{dhpr}^T is the total flux through the L-type Ca^{2+} channels (Eq. 4.4).

Conversely, the reaction terms ($[\boldsymbol{\rho}Q]^i$) on the right hand side of Eq. 4.19 correspond to the stochastic aspect of the CaRU dynamics (i.e., changes in probability due to the stochastic gating of the RyR megachannel and DHPRs). This term involves processes that may depend on the junctional SR $[Ca^{2+}]$ directly (as in the transition $\mathcal{CC}_5 \to \mathcal{CO}$) or indirectly (as in the transition $\mathcal{CC}_4 \to \mathcal{CC}_5$), as well as terms dependent on the membrane voltage (such as the transition $\mathcal{CC}_1 \to \mathcal{OC}_1$). Using the decomposition of Q given by Eq. 4.17, one can see that $[\boldsymbol{\rho}Q]^i$ is a function of V and c_{jsr} given by

$$
\begin{aligned}
[\boldsymbol{\rho}Q]^i &= \sum_{j=1}^{M} \rho^j \left[K_\phi^{j,i} + \bar{c}_{ds}^j K_{ds}^{j,i} + c_{jsr} K_{jsr}^{j,i} \right] \qquad (4.25) \\
&= \sum_{j=1}^{M} \rho^j \left[K_\phi^{j,i} + \bar{c}_{ds,0}^j K_{ds}^{j,i} + c_{jsr} \left(\bar{c}_{ds,1}^j K_{ds}^{j,i} + K_{jsr}^{j,i} \right) \right]
\end{aligned}
$$

where $K_\phi(V)$ provides the voltage-dependence, the superscripts of $K_\phi^{j,i}$, $K_{ds}^{j,i}$, and $K_{jsr}^{j,i}$ indicate row and column indices of these matrices, $\rho^j(c_{jsr}, t)$ is the probability density for state j, and $\bar{c}_{ds,0}^j$ and $\bar{c}_{ds,1}^j$ are given by Eqs. 4.21–4.23.

The concentration balance equations governing the bulk myoplasmic (c_{myo}) and network SR (c_{nsr}) $[Ca^{2+}]$ in the probability density formulation are identical to those used in the Monte Carlo approach (Eqs. 4.1–4.2), except that the fluxes J_{refill}^T and

J^T_{efflux} are dependent on the densities (ρ^i_{jsr}), that is,

$$J^T_{refill} = \sum_{i=1}^{M} \int_0^{\infty} v^T_{refill} \left[c_{nsr} - c_{jsr}\right] \rho^i_{jsr}(c_{jsr}, t)\, dc_{jsr} \qquad (4.26)$$

$$J^T_{efflux} = \sum_{i=1}^{M} \int_0^{\infty} v^T_{efflux} \left[\bar{c}^i_{ds} - c_{myo}\right] \rho^i_{jsr}(c_{jsr}, t)\, dc_{jsr} \qquad (4.27)$$

where $\bar{c}^i_{ds}$ is a function of c_{jsr} (Eq. 4.21).

Parameter	Definition	Value
N	number of diadic subspaces	50–20000
V_{nsr}	network SR volume	3.15×10^{-7} μL
V_{myo}	myoplasmic volume	2.15×10^{-5} μL
$V_{ds}^T = N V_{ds}$	total diadic subspace volume	2×10^{-8} μL
$V_{jsr}^T = N V_{jsr}$	total junctional SR volume	2.45×10^{-8} μL
C_m	capacative membrane area	1.534×10^{-4} μF
β_{ds}	subspace buffering factor	0.5
β_{jsr}	junctional SR buffering factor	0.065
β_{nsr}	network SR buffering factor	1.0
β_{myo}	myoplasmic buffering factor	0.05
$v_{refill}^T = \lambda_{jsr}^T / \tau_{refill}$	junctional SR refilling rate	0.018 s^{-1}
$v_{efflux}^T = \lambda_{ds}^T / \tau_{efflux}$	diadic subspace efflux rate	5.2 s^{-1}
F	Faraday's constant	96480 coul mol^{-1}
R	gas constant	8314 mJ mol^{-1} K^{-1}
T	absolute temperature	$310K$
c_{ext}	extracellular Ca^{2+} concentration	1.8 mM
$[\text{Na}^+]_{ext}$	extracellular Na$^+$ concentration	140 mM
$[\text{Na}^+]_{myo}$	intracellular Na$^+$ concentration	10.2 mM

Table 4.1: Model parameters: volume fractions, Ca^{2+} buffering, and exchange between restricted domains and the bulk, physical constants, and fixed ion concentrations.

Parameter	Definition	Value
$v_{ryr}^{T} = N v_{ryr}$	total RyR cluster release rate	0.9 s^{-1}
$P_{dhpr}^{T} = N P_{dhpr}$	total DHPR permeability	$3.5 \times 10^{-5} \text{ cm s}^{-1}$
V_{dhpr}^{θ}	DHPR activation threshold	-10 mV
σ_{dhpr}	DHPR activation parameter	6.24 mV
$\bar{k}_{dhpr}^{+}$	maximum rate of DHPR opening	556 s^{-1}
k_{dhpr}^{-}	closing rate of DHPR opening	5000 s^{-1}
k_{dhpr}^{-}	rate of DHPR closing	5000 s^{-1}
k_{ryr}^{+}	rate of RyR activation	$2000 \ \mu M^{-1} \text{s}^{-1}$
k_{ryr}^{-}	rate of RyR deactivation	1600 s^{-1}
$k_{ryr,*}^{+}$	rate of RyR opening	$40 \ \mu M^{-1} \text{s}^{-1}$
$k_{ryr,*}^{-}$	rate of RyR closing	500 s^{-1}
α	cooperativity factor	2
β	cooperativity factor	2

Table 4.2: Ca^{2+} release unit parameters (L-type Ca^{2+} channel and RyR cluster).

Parameter	Definition	Value
K_{fs}	forward half-saturation constant for SERCA pump	0.17 μM
K_{rs}	reverse half-saturation constant	1702 μM
η_{fs}	forward cooperativity constant	0.75
η_{rs}	reverse cooperativity constant	0.75
v_{serca}	maximum SERCA pump rate	8.6 μM s^{-1}
I^o_{ncx}	magnitude of Na$^+$-Ca^{2+} exchange current	150 μA μF^{-1}
$K_{ncx,n}$	Na$^+$ half saturation constant	$87.5 \times 10^3 \mu$M
$K_{ncx,c}$	Ca^{2+} half saturation constant	$1.38 \times 10^3 \mu$M
k^{sat}_{ncx}	saturation factor	0.1
η_{ncx}	voltage dependence of Na$^+$-Ca^{2+} exchange	0.35
v_{leak}	SR Ca^{2+} leak rate constant	2.4×10^{-6} s^{-1}
g_{in}	maximum conductance of background Ca^{2+} influx	9.6×10^{-5} mS μF^{-1}

Table 4.3: Model parameters: Na$^+$-Ca^{2+} exchange current, SERCA pumps, and background Ca^{2+} influx.

4.4   Results

4.4.1   Moments of junctional SR calcium concentration

The application of the moment closure technique to the local control model of Ca^{2+}-induced Ca^{2+} release (CICR) in cardiac myocytes presented above begins by writing the q-th moment of the univariate probability density function, $\rho^i(c_{jsr}, t)$, as

$$\mu_q^i(t) = \int (c_{jsr})^q \, \rho^i(c_{jsr}, t) \, dc_{jsr} \qquad (4.28)$$

where the non-negative integer q indicates the moment degree in μ_q^i and is an exponent in $(c_{jsr})^q$. As defined in Eq. 4.18, $\rho^i(c_{jsr}, t)$ is the distribution of $[Ca^{2+}]$ in a large number of junctional SR compartments jointly distributed with CaRU state. Thus, the zeroth moment μ_0^i corresponds to the probability—denoted as $\pi^i(t)$ in [Williams et al., 2007]—that a randomly sampled CaRU is in state i, that is,

$$\pi^i(t) = \mu_0^i(t) = \int \rho^i(c_{jsr}, t) dc_{jsr} = \Pr\{\tilde{S}(t) = i\}$$

where conservation of probability implies $\sum_i \pi^i = 1$. Because the joint probability densities do not individually integrate to unity, the first moment,

$$\mu_1^i(t) = \int c_{jsr} \, \rho^i(c_{jsr}, t) dc_{jsr},$$

is related to the expected value of the junctional SR $[Ca^{2+}]$ conditioned on CaRU state through

$$E^i[\tilde{c}_{jsr}] = \frac{\mu_1^i}{\mu_0^i}, \qquad (4.29)$$

while the conditional variance of the junctional SR $[Ca^{2+}]$ is

$$Var^i[\tilde{c}_{jsr}] = \frac{\mu_2^i}{\mu_0^i} - \left(\frac{\mu_1^i}{\mu_0^i}\right)^2. \qquad (4.30)$$

151

4.4.2 Expressing fluxes in terms of moments

Considering Eqs. 4.1 and 4.2 and Eqs. 4.26–4.27, one sees that the fluxes J_{efflux}^T and J_{refill}^T mediate the influence of the distribution of diadic subspace and junctional SR $[Ca^{2+}]$ on the dynamics of the bulk myoplasmic $[Ca^{2+}]$ (c_{myo}) and the network SR $[Ca^{2+}]$ (c_{nsr}). Using the definition of the moments of junctional SR $[Ca^{2+}]$ (Eq. 4.28), these fluxes become functions of the zeroth and first moments,

$$J_{refill}^T = \sum_{i=1}^{M} v_{refill}^T \left(c_{nsr}\mu_0^i - \mu_1^i \right)$$

$$J_{efflux}^T = \sum_{i=1}^{M} v_{efflux}^T \left(\bar{c}_{ds,0}^i - c_{myo} \right) \mu_0^i + v_{efflux}^T \bar{c}_{ds,1}^i \mu_1^i. \tag{4.31}$$

Similarly, the total flux through all the L-type Ca^{2+} channels (J_{dhpr}^T, Eq. 4.24) and the RyR Ca^{2+} channels (J_{ryr}^T) become,

$$J_{dhpr}^T = \sum_{i=1}^{M} \gamma_{dhpr}^i \left[J_{dhpr}^0 \mu_0^i + J_{dhpr}^1 \left(\bar{c}_{ds,0}^i \mu_0^i + \bar{c}_{ds,1}^i \mu_1^i \right) \right] \tag{4.32}$$

and

$$J_{ryr}^T = \sum_{i=1}^{M} \gamma_{ryr}^i \left(\mu_1^i - \bar{c}_{ds,1}^i \mu_1^i - \bar{c}_{ds,0}^i \mu_0^i \right). \tag{4.33}$$

Note that the average diadic subspace and junctional SR Ca^{2+} concentrations can also be written in terms of the moments,

$$c_{ds}^{avg} = \mathsf{E}[\tilde{c}_{ds}] = \sum_{i=1}^{M} \pi^i \mathsf{E}^i[\bar{c}_{ds,0}^i + \bar{c}_{ds,1}^i \tilde{c}_{jsr}] = \sum_{i=1}^{M} \left(\bar{c}_{ds,0}^i \mu_0^i + \bar{c}_{ds,1}^i \mu_1^i \right) \tag{4.34}$$

$$c_{jsr}^{avg} = \mathsf{E}[\tilde{c}_{jsr}] = \sum_{i=1}^{M} \pi^i \mathsf{E}^i[\tilde{c}_{jsr}] = \sum_{i=1}^{M} \mu_1^i, \tag{4.35}$$

and $J_{efflux}^T = v_{efflux}^T \left[c_{ds}^{avg} - c_{myo} \right]$ and $J_{refill}^T = v_{refill}^T \left[c_{nsr} - c_{jsr}^{avg} \right]$ when expressed in terms using these quantities.

4.4.3 Derivation of moment equations

Differentiating Eq. 4.28 with respect to time and using the equations of the univariate probability density approach (Eqs. 4.19–4.25), we obtain a system of ODEs that describe the time-evolution of these moments defined in Eq. 4.28,

$$
\begin{aligned}
\frac{d\mu_q^i}{dt} =\;& \frac{q\mu_{q-1}^i}{\lambda_{jsr}^T} \left(v_{refill}^T\, c_{nsr} + \gamma_{ryr}^i\, \bar{c}_{ds,0}^i \right) \\
&+ \frac{q\mu_q^i}{\lambda_{jsr}^T} \left(\gamma_{ryr}^i\, v_{ryr}^T\, \bar{c}_{ds,1}^i - v_{refill}^T - \gamma_{ryr}^i\, v_{ryr}^T \right) \\
&+ \sum_{j=1}^{M} \mu_q^j \left(K_\phi^{j,i} + \bar{c}_{ds,0}^j\, K_{ds}^{j,i} \right) \\
&+ \sum_{j=1}^{M} \mu_{q+1}^j \left(\bar{c}_{ds,1}^i\, K_{ds}^{j,i} + K_{jsr}^{j,i} \right)
\end{aligned}
\tag{4.36}
$$

where $M = 12$, $1 \leq i \leq M$, $q = 0, 1, 2, ...$, $\bar{c}_{ds,0}^j$ and $\bar{c}_{ds,1}^j$ are given by Eqs. 4.22 and 4.23. In this expression the CaRU model is specified by the $M \times M$ matrices K_ϕ, K_{ds}, and K_{jsr} defined in Eq. 4.17, and the superscripts in $K_\phi^{j,i}$, $K_{ds}^{j,i}$, and $K_{jsr}^{j,i}$ indicate the transition rate or bimolecular rate constant in the jth row and ith column of these matrices. Note that in the M equations for the zeroth moments (μ_0^i) the first two terms evaluate to zero because $q = 0$. When $q \geq 1$ the first term depends on both the network SR [Ca^{2+}] (c_{nsr}) and the bulk myoplasmic [Ca^{2+}] (c_{myo}) through $\bar{c}_{ds,0}^j$. The terms in the first summation have a similar dependence on c_{myo} and this can affect transitions mediated by diadic subspace Ca^{2+} ($K_{ds}^{j,i}$), and the magnitude of these terms depends also on voltage through $K_\phi^{j,i}(V)$. Perhaps most importantly, the presence of diadic subspace and junction SR Ca^{2+}mediated transitions in the CaRU model implies that $d\mu_q^j/dt$ is a function of $\mu_{q+1}^1, \mu_{q+1}^2, \cdots, \mu_{q+1}^M$ whenever $K_{ds}^{j,i}$ or $K_{jsr}^{j,i}$

is nonzero. That is, Eq. 4.36 is an open system of the form

$$\frac{d\mu_0^i}{dt} = f_0^i \left(\{\mu_0^i\}, \{\mu_1^i\} \right) \tag{4.37}$$

$$\frac{d\mu_q^i}{dt} = f_q^i \left(\{\mu_{q-1}^i\}, \{\mu_q^i\}, \{\mu_{q+1}^i\} \right) \qquad q = 1, 2, 3, \cdots \tag{4.38}$$

where we write $\{\mu_q^i\}$ as a shorthand for $\mu_q^1, \mu_q^2, \cdots, \mu_q^M$. Consequently, Eq. 4.36 is unusable in its current form, because in order to determine the time-evolution of the q-th moments one needs to know the value of the $(q+1)$-th moments.

4.4.4 Moment closure

To utilize Eq. 4.36, we truncate the open system at the second moment ($q = 2$) and close the system of ODEs by assuming that the third moment can be expressed as an algebraic function ϕ of the lower moments $(\mu_0^i, \mu_1^i, \mu_2^i)$, that is,

$$\frac{d\mu_0^i}{dt} = f_0^i \left(\{\mu_0^i\}, \{\mu_1^i\} \right) \tag{4.39}$$

$$\frac{d\mu_1^i}{dt} = f_1^i \left(\{\mu_0^i\}, \{\mu_1^i\}, \{\mu_2^i\} \right) \tag{4.40}$$

$$\frac{d\mu_2^i}{dt} = f_2^i \left(\{\mu_1^i\}, \{\mu_2^i\}, \{\phi(\mu_0^i, \mu_1^i, \mu_2^i)\} \right). \tag{4.41}$$

The remainder of this section derives the required expression of the form $\mu_3^i = \phi(\mu_0^i, \mu_1^i, \mu_2^i)$ (Eqs. 4.48–4.53). This is accomplished by specifying the function ϕ in a manner that would be strictly correct if the probability density functions were scaled Beta distributions. Note that choosing this form of ϕ to perform the moment closure given by Eqs. 4.39–4.41 is not equivalent to assuming that the probability density functions are well approximated by Beta distributions. What we are assuming is that the relationship between μ_3^i and the lower moments $(\mu_0^i, \mu_1^i, \mu_2^i)$ is similar to the relationship observed in the Beta distribution. This assumption is validated *a posteriori* by evaluating the accuracy of results obtained using this approach (see

Figs. 4.2–4.6).

The derivation begins by considering a random variable $0 \le \tilde{x} \le 1$ that is functionally dependent on $\tilde{c}_{jsr}$ through

$$\tilde{x} = \frac{\tilde{c}_{jsr} - c_{jsr}^{min}}{\delta c_{jsr}} \qquad \text{where} \qquad \delta c_{jsr} = c_{jsr}^{max} - c_{jsr}^{min}. \qquad (4.42)$$

In this expression, the minimum and maximum values of junctional SR [Ca^{2+}] are given by $c_{jsr}^{min} = \min_i \bar{c}_{jsr}^i$ and $c_{jsr}^{max} = \max_i \bar{c}_{jsr}^i$ where $\bar{c}_{jsr}^i$ are the steady-state values of c_{jsr} found by setting $f_{jsr}^i = 0$ in Eq. 4.20,

$$\bar{c}_{jsr}^i = \frac{\gamma_{ryr}^i v_{ryr}^T \bar{c}_{ds,0}^i + v_{refill}^T c_{nsr}}{v_{refill}^T + \gamma_{ryr}^i v_{ryr}^T (1 - \bar{c}_{ds,1}^i)}$$

where $\bar{c}_{ds,0}^i$ and $\bar{c}_{ds,1}^i$ are given by Eqs. 4.22 and 4.23. In this way, the maximum and minimum junctional SR Ca^{2+} concentrations are determined to be

$$c_{jsr}^{max} = c_{nsr} \qquad (4.43)$$

$$c_{jsr}^{min} = \frac{v_*^T}{v_*^T + v_{refill}^T} c_{myo} + \frac{v_{refill}^T}{v_*^T + v_{refill}^T} c_{nsr} \qquad (4.44)$$

where $v_*^T = v_{ryr}^T v_{efflux}^T / \left(v_{ryr}^T + v_{efflux}^T \right)$. If the probability density for $\tilde{x}$ conditioned on CaRU state i were Beta distributed, then

$$\Pr\{x < \tilde{x} < x + dx | \tilde{S} = i\} = \frac{x^{\alpha^i - 1} (1 - x)^{\beta^i - 1} \, dx}{B(\alpha^i, \beta^i)} \qquad (4.45)$$

where the beta function $B(\alpha^i, \beta^i)$ appears as a normalization constant and $\tilde{x}(t)$, $\tilde{S}(t)$, $\alpha^i(t)$, and $\beta^i(t)$ are all functions of time. Under this assumption, the first several

conditional moments of $\tilde{x}$ would be

$$E^i[\tilde{x}] = \frac{\alpha^i}{\alpha^i + \beta^i} \tag{4.46}$$

$$E^i[\tilde{x}^2] = \frac{\alpha^i\left(\alpha^i + 1\right)}{\left(\alpha^i + \beta^i\right)\left(\alpha^i + \beta^i + 1\right)} \tag{4.47}$$

and inverting these expressions gives

$$\alpha^i = \frac{E^i[\tilde{x}]\left(E^i[\tilde{x}] - E^i[\tilde{x}^2]\right)}{E^i[\tilde{x}^2] - \left(E^i[\tilde{x}]\right)^2} \tag{4.48}$$

$$\beta^i = \alpha^i\left(\frac{1 - E^i[\tilde{x}]}{E^i[\tilde{x}]}\right). \tag{4.49}$$

Note that Eq. 4.42 implies the following relationship between the conditional moments of $\tilde{x}$ and $\tilde{c}_{jsr}$,

$$E^i[\tilde{x}] = \frac{1}{\delta c_{jsr}}\left(\frac{\mu_1^i}{\mu_0^i} - c_{jsr}^{min}\right) \tag{4.50}$$

$$E^i[\tilde{x}^2] = \frac{1}{\left(\delta c_{jsr}\right)^2}\left(\frac{\mu_2^i}{\mu_0^i} - 2c_{jsr}^{min}\frac{\mu_1^i}{\mu_0^i} + \left(c_{jsr}^{min}\right)^2\right), \tag{4.51}$$

where we have used $\mu_q^i = \mu_0^i E^i[(\hat{c}_{jsr})^q]$ for $q = 0, 1$, and 2; consequently, α^i and β^i can be found as a function of μ_0^i, μ_1^i, and μ_2^i. These parameters allow us to approximate the third conditional moment of $\tilde{x}$,

$$E^i[\tilde{x}^3] = \frac{\alpha^i\left(\alpha^i + 1\right)\left(\alpha^i + 2\right)}{\left(\alpha^i + \beta^i\right)\left(\alpha^i + \beta^i + 1\right)\left(\alpha^i + \beta^i + 2\right)}, \tag{4.52}$$

which in turn allows us to approximate the third conditional moment of junctional SR [Ca^{2+}] given by $\mu_3^i = \mu_0^i E^i[(\tilde{c}_{jsr})^3]$ where

$$E^i[(\tilde{c}_{jsr})^3] = E^i\left[\left(\delta c_{jsr}\tilde{x} + c_{jsr}^{min}\right)^3\right]$$

$$= (\delta c_{jsr})^3 E^i[\tilde{x}^3] + 3(\delta c_{jsr})^2 c_{jsr}^{min} E^i[\tilde{x}^2] - 3\delta c_{jsr}\left(c_{jsr}^{min}\right)^2 E^i[\tilde{x}] + \left(c_{jsr}^{min}\right)^3.$$

After some simplification one obtains

$$\mu_3^i = \mu_0^i (\delta c_{jsr})^3 \mathsf{E}^i[\tilde{x}^3] + 3c_{jsr}^{min} \mu_2^i - 3\left(c_{jsr}^{min}\right)^2 \mu_1^i + \mu_0^i (c_{jsr}^{min})^3, \qquad (4.53)$$

which is an expression that takes the form $\mu_3^i = \phi(\mu_0^i, \mu_1^i, \mu_2^i)$ as required by Eq. 4.41, because $\mathsf{E}^i[\tilde{x}^3]$ is a function of μ_0^i, μ_1^i, and μ_2^i given by Eqs. 4.48–4.52.

Note that the expression $\mu_3^i = \phi(\mu_0^i, \mu_1^i, \mu_2^i)$ derived above is one of several possibilities that we tested, but the only one that could be validated. For example, when ϕ was chosen in a manner that would be strictly correct if the probability densities were scaled normal or log-normal distributions, the resulting moment closure did not perform well (not shown). Using the Beta distribution to derive ϕ makes sense because it is a continuous distribution defined on a finite interval. In addition, for particular values of α^i and β^i the Beta distribution (while remaining integrable) diverges at the boundaries ($\tilde{x} = 0$ or 1). Similarly, prior work has established that the densities $\rho^i(c_{jsr}, t)$ can accumulate probability at the minimum and maximum junctional SR Ca^{2+} concentrations (Eqs. 4.43 and 4.44) and diverge as $c_{jsr} \to c_{jsr}^{min}$ or c_{jsr}^{max} [Mazzag et al., 2005a,Williams et al., 2007]. As mentioned above, the use of the Beta distribution to derive ϕ is ultimately validated by evaluating the accuracy of results obtained using this approach (see Figs. 4.2–4.6).

4.4.5 Representative Monte Carlo and moment closure results

Figure 4.2 shows representative results from the minimal whole cell model of EC coupling described above. In this simulated voltage-clamp protocol, the holding potential of -80 mV is followed by a 20 ms duration test potential to -10 mV. The Monte Carlo result (*grey line*) which involves a large but finite number of Ca^{2+} release units ($N = 1000$) can be easily spotted by the fluctuations due to the stochastic gating
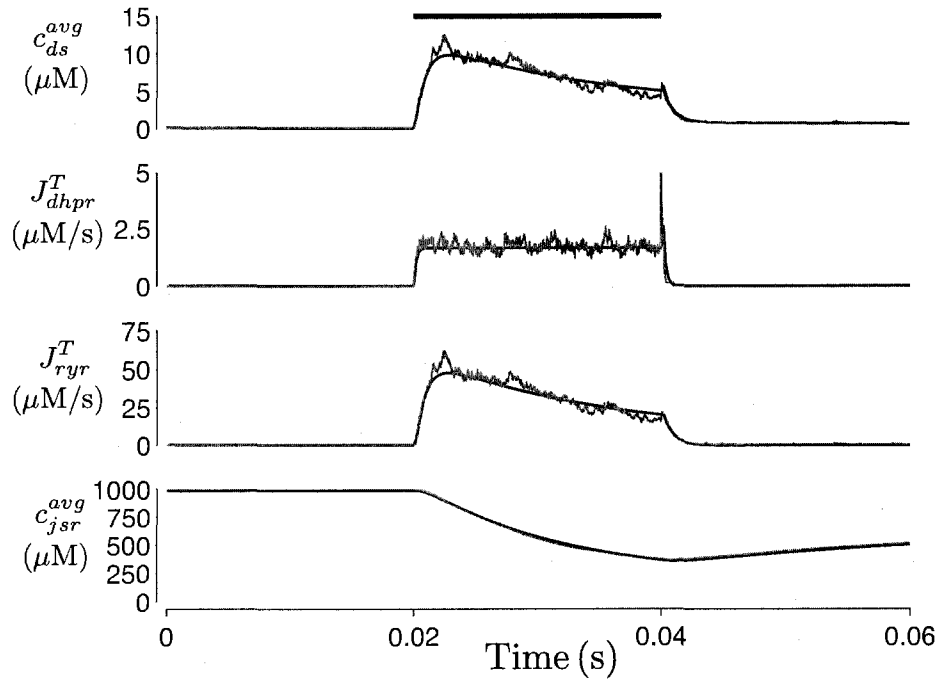
Figure 4.2: The response of the whole cell model during a 20 ms step depolarization from a holding potential of -80 mV to -10 mV (*bar*) with the Monte Carlo and moment closure results indicated as a *grey line* and *black line*, respectively. From top to bottom: average diadic subspace $[Ca^{2+}]$ (c_{ds}^{avg}), total Ca^{2+} flux via the DHPR Ca^{2+} channels (J_{dhpr}^{T}), total Ca^{2+}-induced Ca^{2+} release flux (J_{ryr}^{T}), and average junctional SR $[Ca^{2+}]$ (c_{jsr}^{avg}). The Monte Carlo simulation used $N = 1000$ Ca^{2+} release units and parameters as in Tables 4.1–4.3.

of the CaRUs. The moment closure result (*black line*) that assumes $N \to \infty$ lacks these fluctuations. The top and bottom panels of Fig. 4.2 show the average diadic subspace ($c_{ds}^{\text{avg}} = N^{-1} \sum_{n=1}^{N} c_{ds}^n$) and junctional SR ($c_{jsr}^{\text{avg}} = N^{-1} \sum_{n=1}^{N} c_{jsr}^n$) Ca^{2+} concentrations in the Monte Carlo calculation (*grey lines*) as well as the corresponding quantities from the moment closure calculation (*black lines*, Eqs. 4.34 and 4.35). The middle two panels of Fig. 4.2 show the total Ca^{2+} influx through L-type Ca^{2+} channels ($J_{dhpr}^T = \sum_{n=1}^{N} J_{dhpr}^n$) and the total Ca^{2+} release from the RyR Ca^{2+} channels ($J_{ryr}^T = \sum_{n=1}^{N} J_{ryr}^n$) for the Monte Carlo calculation (*grey lines*) as well as the corresponding quantities for the moment closure result (*black lines*, Eqs. 4.32 and 4.33). In both the Monte Carlo and moment closure calculations, the test potential of -10 mV leads to 16X "gain," here defined as the ratio $\bar{J}_{ryr}^T / \bar{J}_{dhpr}^T$ where the overbar indicates an average over the duration of the pulse.

Fig. 4.3 shows [Ca^{2+}] in the bulk myoplasm (c_{myo}) and network SR (c_{nsr}) before, during, and after the -10 mV voltage pulse (note change in time scale). In both cases the moment closure result is shown as a *solid black line* while the Monte Carlo is displayed as a *dashed grey line* (note agreement). While junctional SR depletion develops rapidly after the initiation of the voltage pulse (not shown), refilling the junctional SR compartments via diffusion of Ca^{2+} from the network SR (J_{refill}^n in Eq. 4.2) depletes this compartment (c_{nsr}), which does not fully recover until approximately 300 ms after the termination of the voltage pulse.

Taken together, Figs. 4.2 and 4.3 validate our implementation of both the Monte Carlo and moment closure approaches. Also note that the similarity of these results to Figs. 2 and 3 in [Williams et al., 2007] indicates that the six-state RyR megachannel model (Eq. 4.13)—used here because it takes the form of Eq. 4.17—has behavior similar to the two-state model of [Williams et al., 2007].
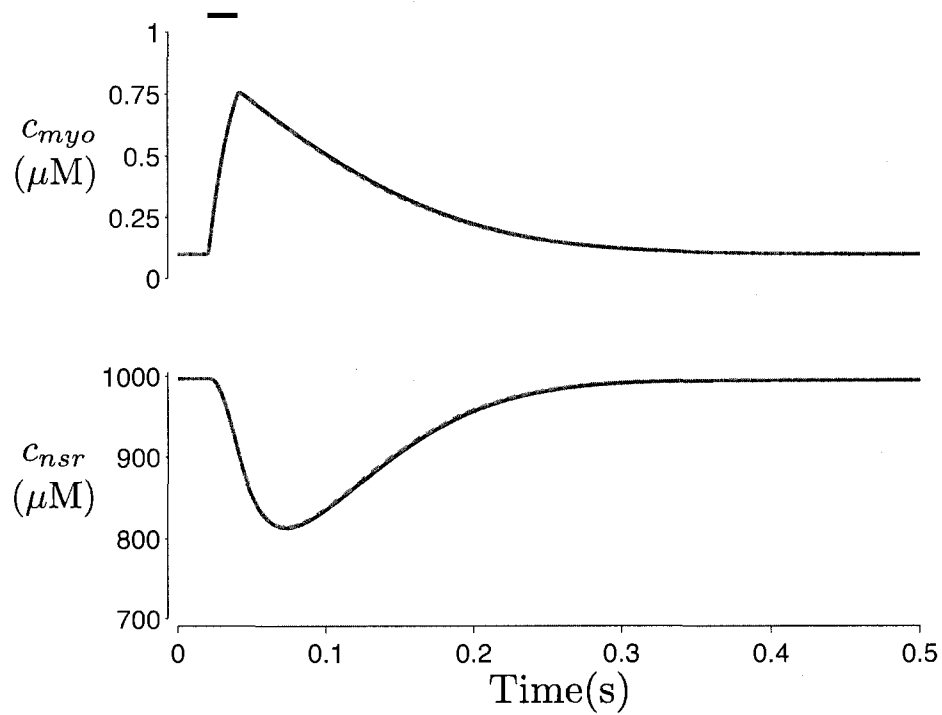
Figure 4.3: Solid lines show the dynamics of bulk myoplasmic (c_{myo}) and network SR (c_{nsr}) [Ca^{2+}] in the whole cell voltage clamp protocol of Fig. 4.2 with step potential of -10 mV (note longer time scale). The *dashed* and *solid lines* are the Monte Carlo and moment closure results, respectively.

4.4.6 Dynamics of the moments of junctional SR calcium concentration

The top row of Fig. 4.4 shows the time evolution of the probability of three selected CaRU states during the simulated voltage-clamp protocol of Figs. 4.2 and 4.3, as calculated using both the Monte Carlo (*grey lines*) and moment closure (*black lines*) methods. Before the voltage pulse, the probability of state $\mathcal{CC}_1$ (DHPR in state $\mathcal{C}$ and RyR in state $\mathcal{C}_1$, see Eqs. 4.13–4.16) is approximately 1, but during the voltage pulse to -10 mV this probability drops to approximately 0.78 (20–40 ms). Conversely, the probability of CaRU state $\mathcal{OO}$ (DHPR open and RyR open) and $\mathcal{CO}$ (DHPR closed and RyR open) both increase during the voltage pulse. The dynamics of voltage-dependent activation of DHPRs and subsequent triggering the opening of RyR megachannels is similar in both the Monte Carlo (*grey lines*) and moment closure (black lines) calculations.

The second row of Fig. 4.4 shows the mean junctional SR $[Ca^{2+}]$ conditioned on CaRU state for the Monte Carlo (*grey line*) and the moment closure (*black line*) techniques. In the Monte Carlo calculation this conditional mean is given by

$$\langle c_{jsr} \rangle^i(t) = \frac{1}{N^i} \sum_{n \in n^i} c_{jsr}^n \tag{4.54}$$

where $N^i(t)$ is the number of CaRUs in state i at time t and $n^i(t) = \{n : \tilde{S}^n = i\}$ so that the sum includes only those CaRUs in state i. The corresponding quantity in the moment closure technique is the conditional expectation $\mathsf{E}^i[c_{jsr}] = \mu_1^i / \mu_0^i$ (Eq. 4.29). Note that before the voltage pulse the expectation of SR $[Ca^{2+}]$ is approximately 1000 μM when conditioning on CaRU state $\mathcal{CC}_1$, 851 μM when conditioning on CaRU state $\mathcal{OO}$, and 306 μM when conditioning on CaRU state $\mathcal{CO}$. That is, at the holding potential of -80 mV, the stochastic gating of CaRUs leads to depletion of junctional SR $[Ca^{2+}]$ associated with release sites with open RyR megachannels (more pronounced

161
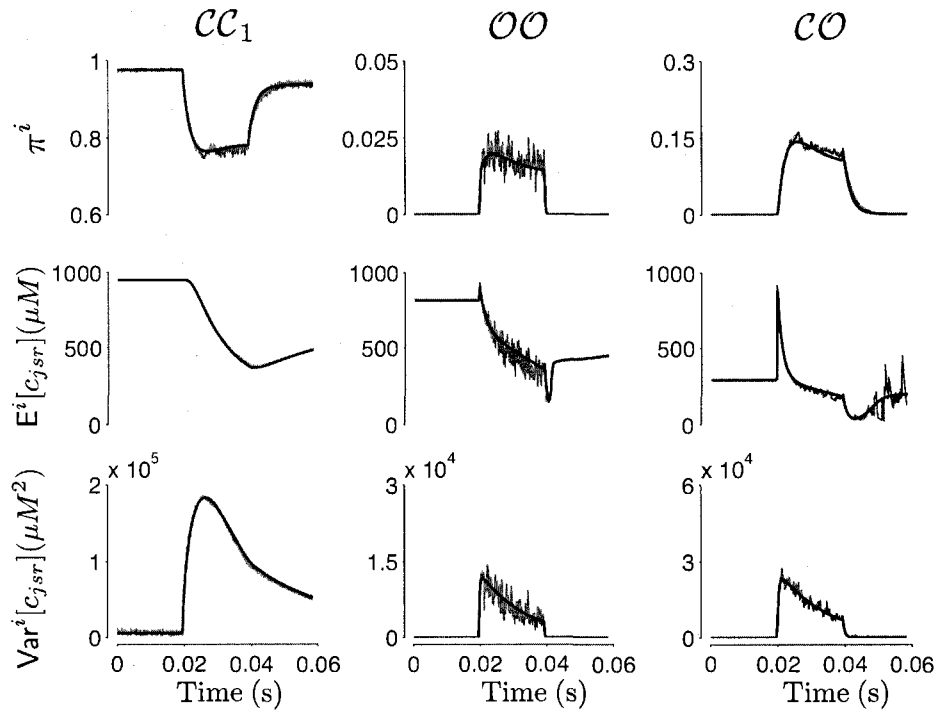
Figure 4.4: Comparison between results obtained from Monte Carlo (*grey line*) simulations and moment closure approach (*black line*) for the probability (π^i), the conditional expectation of c_{jsr} ($\mathsf{E}^i[\tilde{c}_{jsr}]$) and the conditional variance of c_{jsr} ($\mathsf{Var}^i[\tilde{c}_{jsr}]$), for three selected CaRU states, $\mathcal{CC}_1$ (left column), $\mathcal{CO}$ (middle column) and $\mathcal{OO}$ (right column). The Monte Carlo simulation used $N = 2000$ Ca^{2+} release units.

in $\mathcal{CO}$ than $\mathcal{OO}$ because the former state is longer lived). However, the probability of CaRU states $\mathcal{OO}$ and $\mathcal{CO}$ is very low at -80 mV and, consequently, the expectation of junctional SR [Ca^{2+}] irrespective of CaRU state given by the weighted average

$$\langle c_{jsr} \rangle(t) = \frac{1}{N} \sum_{i=1}^{M} N^i \langle c_{jsr} \rangle^i$$

in the Monte Carlo model and

$$\mathsf{E}[\tilde{c}_{jsr}] = \sum_{i=1}^{M} \pi^i \mathsf{E}^i[\tilde{c}_{jsr}] = \sum_{i=1}^{M} \mu_1^i$$

in the moment closure calculation is approximately 1000 μM, consistent with Fig. 4.2. Also note that during the voltage pulse the conditional expectation of junctional SR [Ca^{2+}] decreases for CaRU states $\mathcal{CC}_1$ and $\mathcal{OO}$, but first increases and then decreases for CaRU state $\mathcal{CO}$, presumably because the increasing probability of state $\mathcal{CO}$ during the pulse is due to CaRU transitions into this state from others (such as $\mathcal{CC}_1$) that have higher resting junctional SR [Ca^{2+}].

The third row of Fig. 4.4 shows the variance of the junctional SR [Ca^{2+}] conditioned upon the CaRU state for the Monte Carlo (*grey line*) and the moment closure (*black line*) techniques. For the Monte Carlo calculation

$$\left\langle \left(c_{jsr}^n - \langle c_{jsr} \rangle^i \right)^2 \right\rangle^i = \frac{1}{N^i} \sum_{n \in n^i} \left(c_{jsr}^n - \langle c_{jsr} \rangle^i \right)^2$$

where N^i and $n^i(t)$ are defined as in Eq. 4.54, while the corresponding conditional variance of the junctional SR [Ca^{2+}] in the moment closure calculation is $\mathsf{Var}^i[\tilde{c}_{jsr}] = \mu_2^i/\mu_0^i - (\mu_1^i/\mu_0^i)^2$ (Eq. 4.30). Note that during the voltage pulse the conditional variance of c_{jsr} increases, as the dynamics of EC coupling lead to increased heterogeneity of junctional SR [Ca^{2+}], and that the moment closure technique accurately accounts for this heterogeneity (compare *grey* and *black lines*).

4.4.7 The distribution of junctional SR calcium concentration conditioned on CaRU state

Figure 4.5 shows a snapshot of the distribution of junctional SR [Ca^{2+}] (c_{jsr}) conditioned upon the state of the Ca^{2+} release unit at $t = 30$ ms, midway through the voltage pulse protocol of Figs. 4.2–4.4. For clarity, the five closed states of the RyR megachannel ($\mathcal{C}_1, \mathcal{C}_2, \cdots, \mathcal{C}_5$ in Eq. 4.13) have been lumped resulting in a contracted presentation with four CaRU states: $\mathcal{CC}$, $\mathcal{CO}$, $\mathcal{OC}$, and $\mathcal{OO}$, where $\mathcal{CC} = \mathcal{CC}_1 \cdots \mathcal{CC}_5$ and $\mathcal{OC} = \mathcal{OC}_1 \cdots \mathcal{OC}_5$ (Eq. 4.16). Thus, the two histograms on the bottom of Fig. 4.5 indicate the distribution of JSR [Ca^{2+}] when the DHPR is open ($\pi^{\mathcal{OC}} + \pi^{\mathcal{OO}} = 0.05$), while the two histograms on the right of Fig. 4.5 indicate the distribution of JSR [Ca^{2+}] when the RyR megachannel is open ($\pi^{\mathcal{CO}} + \pi^{\mathcal{OO}} = 0.16$).

Figure 4.5 shows a broad range of junctional SR [Ca^{2+}] regardless of CaRU state, consistent with the high variances at $t = 30$ ms in Fig. 4.4. For example, when the RyR megachannel is closed ($\mathcal{CC}$ and $\mathcal{OC}$, left panels), a randomly sampled junctional SR is likely to be replete, as indicated by the large vertical bar at $c_{jsr} \approx 1000 \ \mu M$. However, one can also find depleted junctional SR [Ca^{2+}] associated with closed RyR megachannels, where RyRs have recently opened and the junctional SR has not had time to refill. Conversely, when the RyR is open ($\mathcal{CO}$ and $\mathcal{OO}$, right panels), the probability mass has shifted to lower junctional SR [Ca^{2+}].

The *diamonds* of Fig. 4.5 show Beta distributions with the same mean and variance as the histograms obtained from Monte Carlo simulation. While the agreement is noteworthy, this correspondence is not required for the moment closure technique to work well. What is required is that the relationship between the third (μ_3^i) and lower ($\mu_0^i, \mu_1^i, \mu_2^i$) moments in the histograms is similar to that observed in the Beta distribution. For example, the histogram junctional SR [Ca^{2+}] for CaRU state $\mathcal{CO}$ at $t = 30$ ms has moments of $\mu_0^{\mathcal{CO}} = 0.14$, $\mu_1^{\mathcal{CO}} = 35.3 \ \mu M$, $\mu_2^{\mathcal{CO}} = 1.59 \times 10^4 \ \mu M^2$, and $\mu_3^{\mathcal{CO}} = 9.17 \times 10^6 \ \mu M^3$. When moments zero through two are used to estimate the

$$\pi^{CC} = 0.81 \qquad \pi^{CO} = 0.14$$

$$\pi^{OC} = 0.03 \qquad \pi^{OO} = 0.02$$
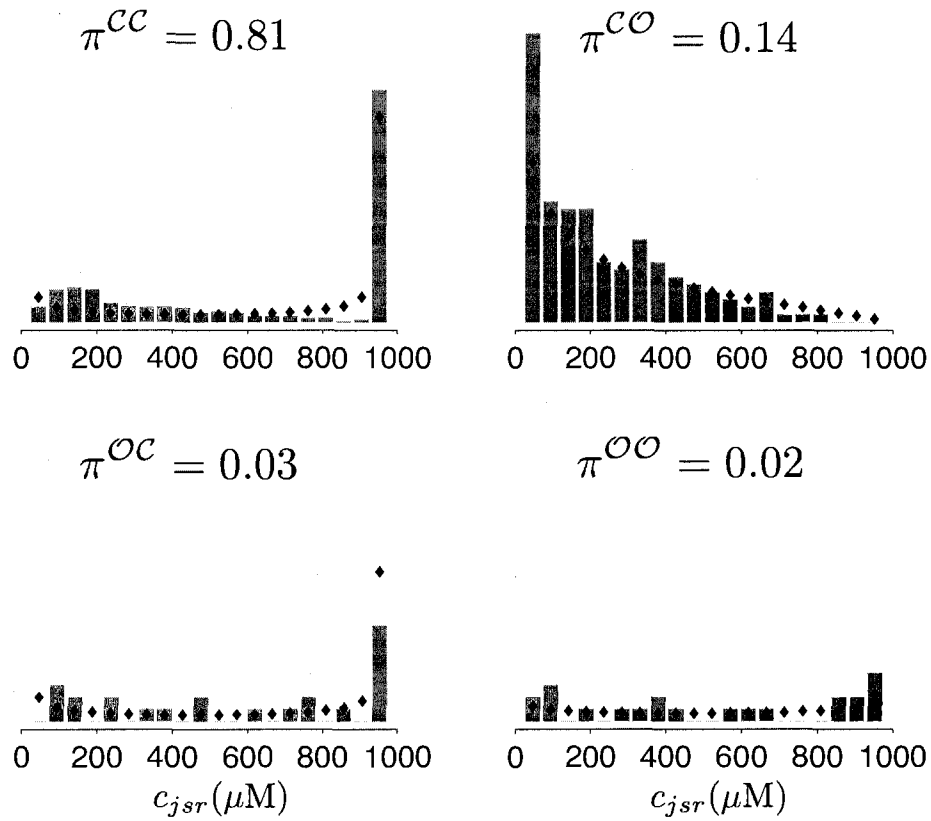
Figure 4.5: Histograms of junctional SR [Ca^{2+}] conditioned on CaRU state obtained by Monte Carlo simulation ($t = 30$ ms in Fig. 4.2). *Filled diamonds* show Beta distributions with same mean and variance. Each panel corresponds to one of four agglomerated states of the CaRU: CC, DHPR and RyR megachannel both closed; OC, DHPR open and RyR megachannel closed; CO, DHPR closed and RyR megachannel open; OO, DHPR and RyR megachannel both open.

third moment using Eq. 4.53 with $c_{jsr}^{min} = 22$ and $c_{jsr}^{max} = 981$ (Eqs. 4.43 and 4.44), one obtains $\mu_3^{CO} = 9.18 \times 10^6 \ \mu M^3$, for a relative error of only 0.1%. It is this low error that is responsible for the excellent agreement between the moment closure result and the Monte Carlo calculation observed in Figs. 4.2–4.4.

4.4.8 The model displays gain and gradedness

To further validate the moment closure approach by comparison to Monte Carlo simulation, Fig. 4.6 summarizes a large number of simulated whole cell voltage clamp protocols such as those presented in Figs. 4.2–4.4. The *open circles* of Fig. 4.6 show the trigger Ca^{2+} influx via L-type Ca^{2+} channels integrated over the 20 ms voltage step to test potentials in the range -40 to 40 mV using 1,000 CaRUs (the plot is normalized to maximum value of $\bar{J}_{dhpr}^T = 0.038 \ \mu M$). The *dotted line* of Fig. 4.6 shows that the trigger Ca^{2+} influx in the moment closure calculation agrees with the Monte Carlo simulations. Similarly, the *open squares* of Fig. 4.6 show the voltage-dependence of the Ca^{2+} release flux (normalized to maximum value of $\bar{J}_{ryr}^T = 0.678 \ \mu M$), while the *dashed lines* of Fig. 4.6 show that the Ca^{2+} release flux observed in the moment closure calculation agrees with the Monte Carlo simulations. Note that the Monte Carlo and moment closure calculations exhibit graded Ca^{2+} release. Furthermore, the EC coupling gain $(\bar{J}_{ryr}^T / \bar{J}_{dhpr}^T)$ is a decreasing function of voltage, is in the range of 32 to 15X for test potentials between -40 and 0 mV. Most importantly, the Monte Carlo and moment closure calculations are nearly identical (compare *open diamonds* and *solid line*).
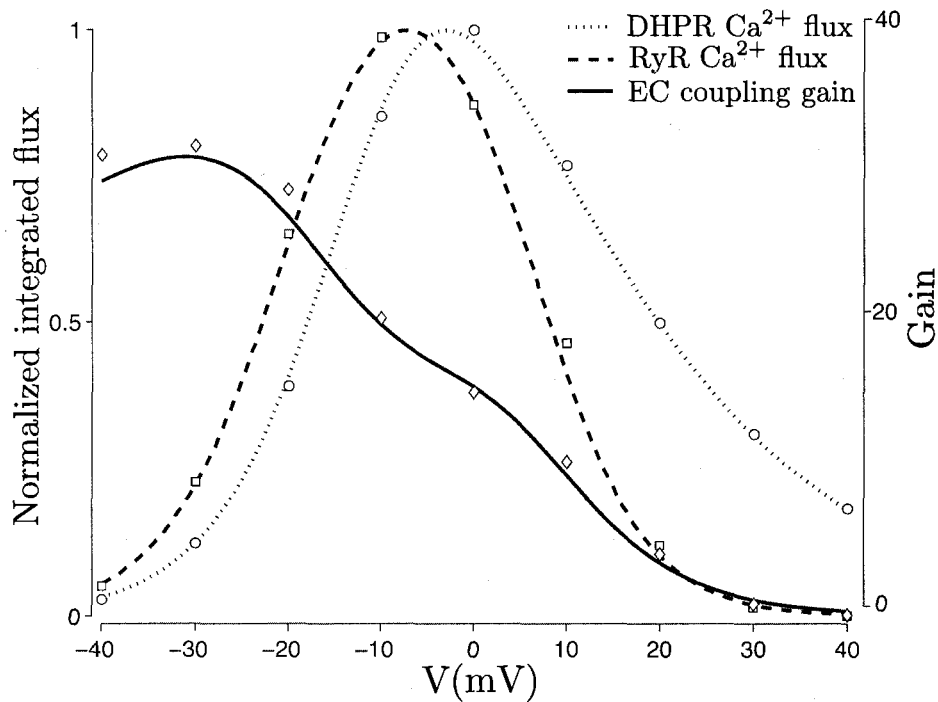
Figure 4.6: Summary of whole cell voltage clamp simulations such as those presented in Figs. 4.2–4.4 normalized to emphasize gradedness of Ca^{2+} release with respect to membrane potential and Ca^{2+} influx. Moment closure results (*solid* and *broken lines*) agree with Monte Carlo calculations (*open symbols*) for a range of test potentials. Integrated Ca^{2+} influx via L-type channels ($\bar{J}_{dhpr}^{T}$) is shown as *open cirlces* (Monte Carlo) and *dotted line* (moment closure). Integrated RyR flux ($\bar{J}_{ryr}^{T}$) is shown as *open squares* (Monte Carlo) and *dashed line* (moment closure). EC coupling gain ($\bar{J}_{ryr}^{T}/\bar{J}_{dhpr}^{T}$, right axis) is shown as *open diamonds* (Monte Carlo) and *solid line* (moment closure).

4.4.9 Computational efficiency of the moment closure approach

While the previous sections have shown that the moment closure and Monte Carlo calculations are essentially equivalent in terms of the dynamic cellular responses they predict, it is important to note that the moment closure approach is significantly faster than Monte Carlo simulation. The Monte Carlo simulations presented above are performed using $\Delta t = 0.01$ μs a value chosen so the probability of transition occurring in each CaRU is less than 5% per time step. Table 4.4 shows that the run time for these 60 ms simulations increases approximately linearly with the number of CaRU units, for example, an $N = 10,000$ simulation takes about 11 times longer than a $N = 1000$ simulation. When our current implementation of the moment closure method is employed using a non-adaptive time step of $\Delta t = 0.01$ μs, the run time is 95 min, which is about 100 times faster than Monte Carlo simualations with a physiologically realistic number of CaRUs (e.g., $N = 10,000$). However, a time step of 0.01 μs is much smaller than required for integrating the moment closure ODEs. When this artificial constraint is removed and the moment closure approach is benchmarked using a non-adaptive time step as large as numerical stability will allow, the calculations are $8755/0.9 = 9728$ times faster than Monte Carlo simulations containing $N = 10,000$ CaRUs. That is, the computational efficiency of the moment closure approach is nearly four orders of magnitude superior to physiologically realistic Monte Carlo simulations, while leading to nearly identical results (see Figs. 4.2–4.4, and 4.6). Furthermore, integration methods that utilize adaptive time-steping are likely to further enhance the computational advantage of the moment closure approach to modeling local control of EC coupling.

	Δt (μs)	N	Time (min)
	0.01	100	50
Monte Carlo	0.01	1,000	794
	0.01	10,000	8755
Moment closure	0.01	-	95
	1	-	0.9

Table 4.4: Run times required for a 60 ms simulation such as that presented in Fig. 4.2 using both Monte Carlo and moment closure approaches.

4.4.10 Restitution of CICR studied using moment closure approach

To show how the computational efficiency of the moment closure approach facilitates studies that can provide biophysical insight, we present a study of the restitution of Ca^{2+}-induced Ca^{2+} release during simulated two-pulse voltage-clamp protocols (cf. [Szentesi et al., 2004]). As diagrammed in the inset, Fig. 4.7A plots the ratio of the integrated release during the two pulses $(\bar{J}_{ryr}^{T(2)}/\bar{J}_{ryr}^{T(1)})$ as a function of time between the end of the first pulse and beginning of the second (denoted by τ). Using the standard value for the maximum reuptake flux $(v_{serca}^{T} = 8.6 \ \mu M^{-1}s^{-1})$, the time constant for recovery of CICR is approximately 93 ms. Increasing or decreasing v_{serca}^{T} by 20% (dashed and dotted lines) leads to a time constant for CICR recovery of 80 ms and 120 ms, respectively. This result is qualitatively consistent with the results of [Szentesi et al., 2004], and the hypothesis that restitution of calcium release depends primarily on refilling of local SR calcium stores [Szentesi et al., 2004, Terentyev et al., 2002b, Sobie et al., 2005].

The filled symbols in the four panels of Fig. 4.7B show that in each of these three cases the expected value of the junctional SR $[Ca^{2+}]$ at the beginning of the second pulse is an increasing function of the inter-pulse interval τ. Also shown are the distributions of junctional SR $[Ca^{2+}]$ consistent with the conditional expectations and variances observed in the moment closure model at the time of the second pulse begins when $\tau = 0.02, 0.06, 0.1$, and 0.2 s. Note that the rightmost extent of these distributions indicates the network SR $[Ca^{2+}]$ in the corresponding simulation $(c_{jsr} \leq c_{nsr})$, and the fully recovered distribution (dotted lines) has an expectation of approximately 1000 μM (open triangle). Note that the variance of the junctional SR $[Ca^{2+}]$ decreases as a function of the inter-pulse interval τ (compare widths of distributions).

Fig. 4.8 shows the recovery of the network SR $[Ca^{2+}]$ (dotted line), the junctional
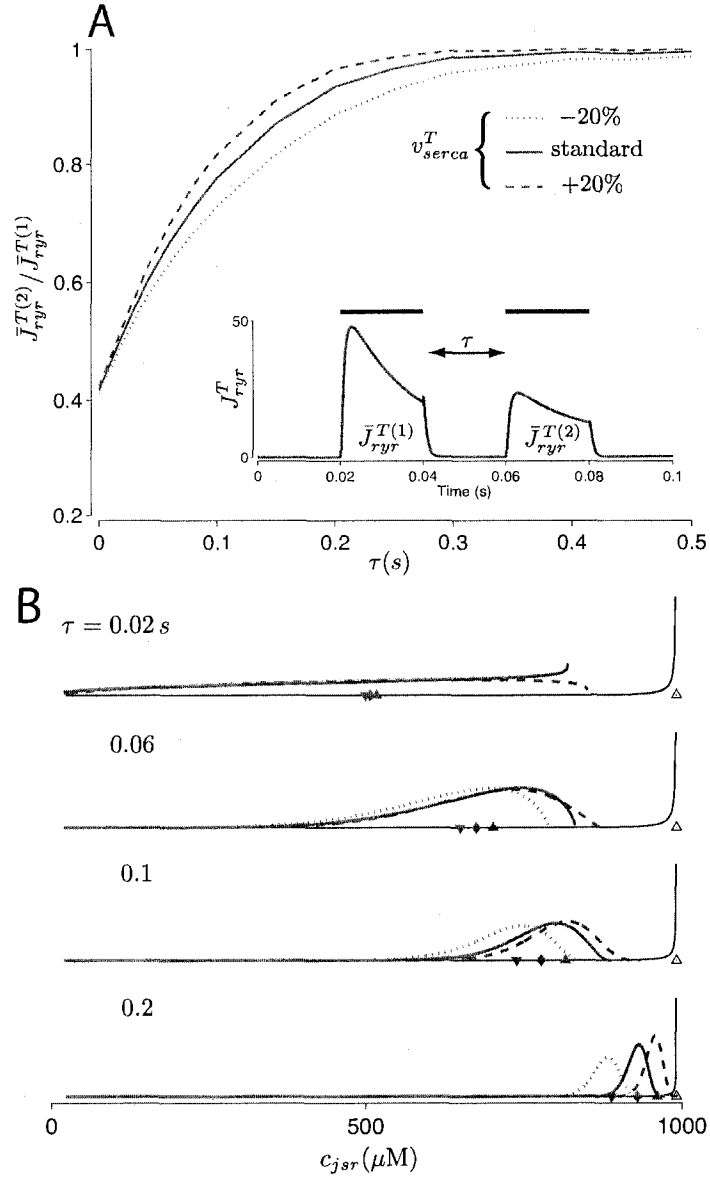
Figure 4.7: CICR restitution study using a simulated two-pulse voltage clamp protocol and different values of the maximum reuptake flux v^T_{serca}. A: Ratio of the integrated release during the two pulses $(\bar{J}^{T(2)}_{ryr}/\bar{J}^{T(1)}_{ryr})$ as a function of time between the end of the second pulse and beginning of the first (τ). Parameters: $v^T_{serca} = 6.88$ (dotted line), 8.60 (solid line), and $10.32\ \mu M^{-1}s^{-1}$ (dashed line) and as in Tables 4.1–4.3. Inset: timing of voltage pulses from -80 to -10 mV. B: Distributions of junctional SR [Ca^{2+}] consistent with the conditional expectations and variances observed in the moment closure model at the beginning of the second pulse when $\tau = 0.02, 0.06, 0.1$, and 0.2 s. Dotted, solid, and dashed lines indicate value of v^T_{serca} as in panel A. Filled symbols indicate the expected value of junctional SR [Ca^{2+}] given by $E[\tilde{c}_{jsr}] = \sum_i \pi^i E^i[\tilde{c}_{jsr}]$ and Eq. 4.29. The solid line and open triangles correspond to the initial (and fully recovered) distribution.
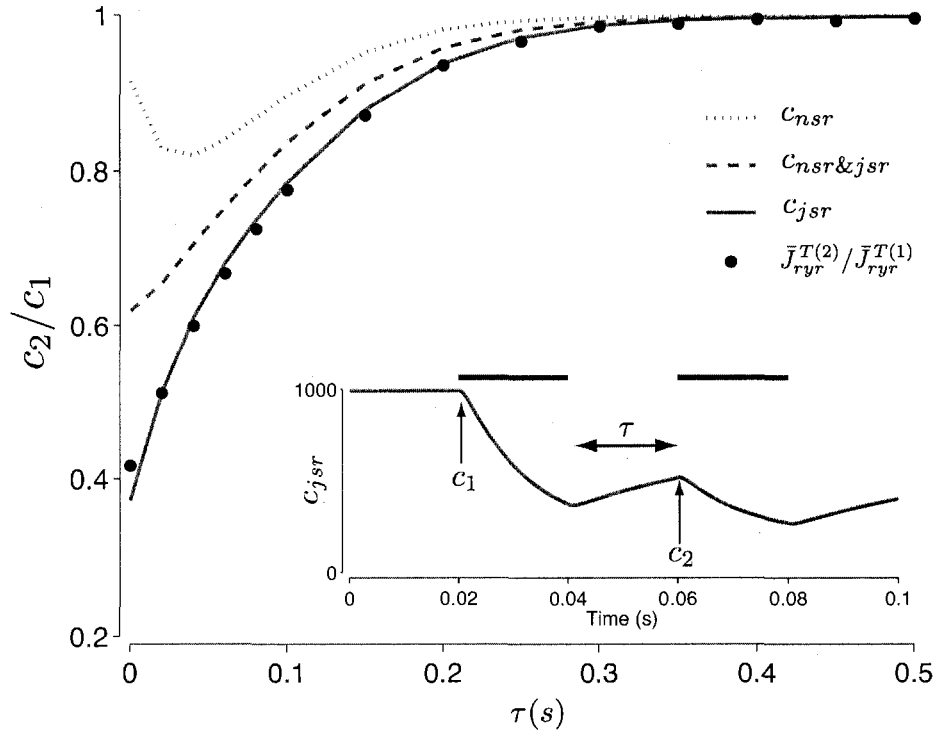
Figure 4.8: Recovery of the network SR [Ca^{2+}] (c_{jsr}, dotted line), the junctional SR [Ca^{2+}] (c_{nsr}, solid line), and the average concentration when the two compartments are aggregated according to their effective volumes ($c_{nsr\&jsr}$, dashed line). Inset: timing of voltage pulses from -80 to -10 mV and representative c_{jsr} trace. Filled circles show CICR restitution observed in Fig. 4.7A. Standard value of $v_{serca}^T = 8.60$ $\mu M^{-1} s^{-1}$ used.

SR [Ca^{2+}] (solid line), and the average concentration when the two compartments are aggregated according to their effective volumes (dashed line). This last measure represents the total SR content as would be assessed experimentally via the rapid application of caffeine. Importantly, the restitution of CICR as probed by the ratio of the integrated release ($\bar{J}_{ryr}^{T(2)}/\bar{J}_{ryr}^{T(1)}$, filled circles) is consistent with the recovery of the junctional SR [Ca^{2+}], but not consistent with recovery of the network SR [Ca^{2+}] or the aggregate concentration.

Fig. 4.9A is similar to Fig. 4.7A except that in this case the rate of calcium diffusion from network SR to junctional SR (v_{refill}^{T}) is modified from the standard value of $v_{refill}^{T} = 0.018 \ \mu M^{-1}s^{-1}$. In spite of the fact that the restitution of CICR follows the recovery of junctional SR [Ca^{2+}] (see Fig. 4.8), the time constant of CICR restitution is less sensitive to the junctional SR refill rate (v_{refill}^{T}) than the maximum SERCA pump rate (v_{serca}^{T}). For example, increasing or decreasing v_{refill}^{T} by a factor of 2 (dashed and dotted lines) leads to a time constant for CICR recovery of 91 and 105 ms (similar to the standard value of 93 ms). Conversely, the extent of junctional SR depletion at the end of the first pulse ranges from 51–65% in Fig. 4.9A and 58–59% in Fig. 4.7 and thus appears to be more sensitive to the value of v_{refill}^{T} than v_{serca}^{T} (a range proportional to the parameter variation in Fig. 4.9A the former range would span 2.5 rather than 14%).

Consistent with these observations, Fig. 4.9B shows that the expected value of junctional SR [Ca^{2+}] increases with increasing inter-pulse interval τ and that decreased values of v_{refill}^{T} lead to increased depletion (compare filled triangles). Comparison of the reconstructed distributions indicates that decreased v_{refill}^{T} slows the recovery of junctional SR [Ca^{2+}] and leads to increased heterogeneity, i.e., higher variance in junctional SR [Ca^{2+}] (compare dotted and solid lines).
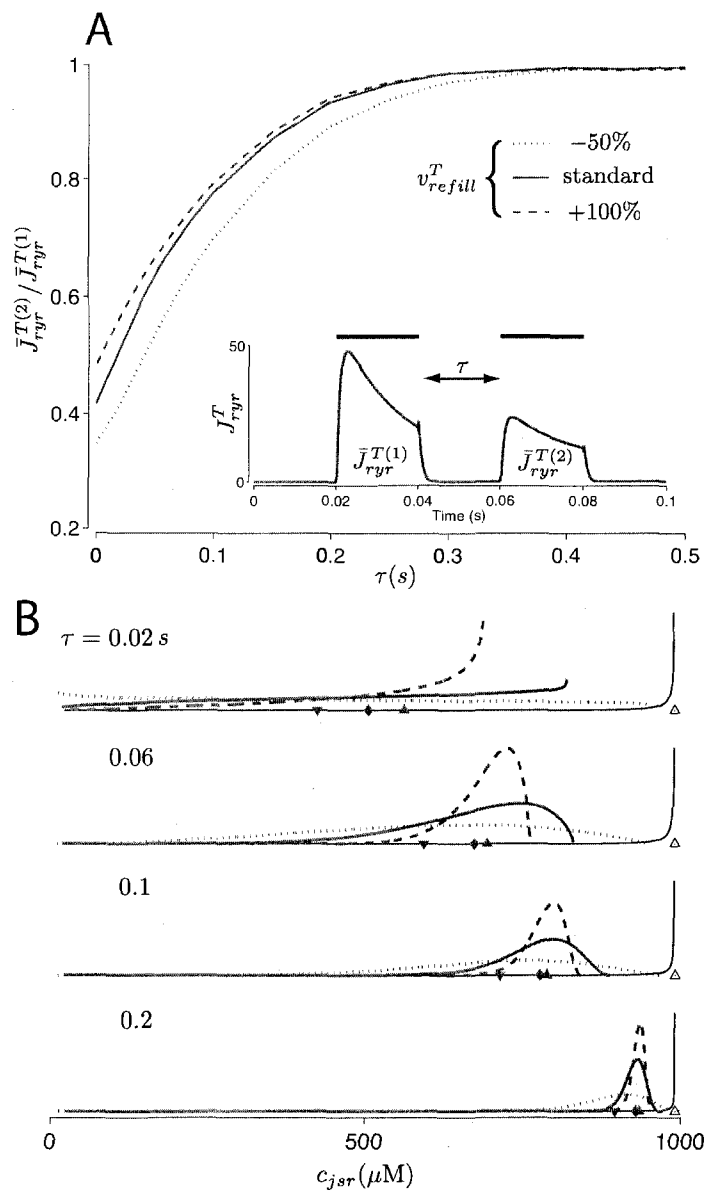
Figure 4.9: Summary of CICR restitution study using a simulated two-pulse voltage clamp protocol and different values of the junctional SR refill rate given by $v_{refill}^T = 0.009$ (dotted line), 0.018 (solid line), and 0.036 $\mu M^{-1}s^{-1}$ (dashed line). Standard value of $v_{serca}^T = 8.60$ $\mu M^{-1}s^{-1}$ used. See legend to Fig. 4.7.

4.5 Discussion

In previous work [Williams et al., 2007] we showed that the probability density approach to modeling local control of Ca^{2+} release in cardiac myocytes can be 30–650 times faster than traditional Monte Carlo simulations when the probability densities are univariate (i.e., functions of the junctional SR $[Ca^{2+}]$ but not explicitly functions of diadic subspace $[Ca^{2+}]$). The derivation of the moment closure technique presented in this manuscript begins with a univariate probability density formulation, but the resulting simulations are nearly 10,000 times faster than Monte Carlo (see Table 4.4). For the whole cell model that is the focus of this manuscript, the moment closure technique is thus significantly more efficient that our previously presented univariate probability density method [Williams et al., 2007].

Although the computational efficiency of the moment closure technique in this local control context is exciting, it is important to note that the relative merits of Monte Carlo, probability density, and moment closure methods are in general model dependent. For example, the run time required for the Monte Carlo simulations such as Fig. 4.2 is, at least ultimately, an almost linear function of the number of CaRUs (see Table 4.4). Similarly, we have observed that the computational efficiency of the univariate probability density calculation presented in [Williams et al., 2007] scales linearly with the number of Ca^{2+} release unit states (M) and the number of mesh points used to discretize the junctional SR $[Ca^{2+}]$. Because the moment closure approach results in $2 + 3M$ ODEs (bulk myoplasmic $[Ca^{2+}]$, network SR $[Ca^{2+}]$, and μ_0^i, μ_1^i, and μ_2^i for each CaRU state), the computational demand of the moment closure approach is expected to scale linearly with M. That is, increasing the number of CaRU states could reduce the computational advantage of the moment closure approach relative to Monte Carlo.

While the CaRU model used here to introduce and validate the moment closure approach includes a two-state DHPR model and a six-state RyR megachannel

(Eq. 4.16), the success of the moment equations (Eq. 4.36 and Eqs. 4.39–4.41) and moment closure using $\mu_3^i = \phi(\mu_0^i, \mu_1^i, \mu_2^i)$ given by Eqs. 4.48–4.53 does not depend on the CaRU model; rather, any CaRU that takes the form of Eq. 4.17 could be employed. For example, a more realistic DHPR model that includes voltage and Ca^{2+}-dependent inactivation would allow integration of the moment closure approach to modeling local control of CICR and action potentials modeled using Hodgkin-Huxley-style membrane currents. Similarly, a more realistic CaRU model could be constructed as the composition of multiple RyR single channel models. This approach will therefore allow for the development of mechanistic, local control models that can examine phenomena such as stochastic SR calcium leak and bidirectional interactions between calcium transients and action potential morphology. However, to maintain the computational advantage of the moment closure approach relative to Monte Carlo, the state-space explosion that inevitably occurs in compositional models is an important practical consideration. For example, one 12-state L-type channel and twelve 4-state RyRs leads to a CaRU model with $M = 5460$ distinguishable states and thus over sixteen thousand ODEs, a value approaching the 20,000 ODEs required in a 10,000 CaRU Monte Carlo simulation.

The moment closure approach presented here begins with a univariate probability density approach to modeling heterogeneous junctional SR $[Ca^{2+}]$. This was motivated by our previous work in which we observed that model parameters lead to rapid equilibrium of the diadic subspace $[Ca^{2+}]$ with the $[Ca^{2+}]$ in the juctional SR and bulk myoplasm [Williams et al., 2007]. When junctional SR $[Ca^{2+}]$ was also assumed to be rapidly equilibrated with the bulk myoplasmic and network SR Ca^{2+} concentrations so that these local Ca^{2+} concentrations could be expressed as algebraic functions of c_{myo}, c_{nsr}, and CaRU state [Hinch, 2004, Greenstein et al., 2006], the resulting model did not exhibit high gain Ca^{2+} release that is graded with membrane potential (not shown). That is, the assumption that both diadic subspace $[Ca^{2+}]$ and junctional SR

[Ca^{2+}] are in quasi-static equilibrium with bulk myoplasmic and network SR Ca^{2+} leads to unacceptable errors and cannot be employed to accelerate this particular whole cell model. This approximation has, however, been successfully employed in previous studies of cardiac CICR [Hinch, 2004, Greenstein et al., 2006]. It therefore seems likely that the model simplifications that can be employed depend on the details of both RyR gating and local concentration changes, issues that are currently being extensively studied.

In situations where rapid equilibration of diadic subspace [Ca^{2+}] does not occur, the appropriate starting point for the moment closure approach is a bivariate probability density model [Williams et al., 2007]. While it is straight forward to derive the open system of ODEs analogous to Eq. 4.36 for the time-evolution of the moments of a bivariate probability densities $\rho^i(c_{ds}, c_{jsr}, t)$ defined by,

$$\mu_{p,q}^i(t) = \int \int \rho^i\left(c_{ds}, c_{jsr}, t\right) \left(c_{ds}\right)^p \left(c_{jsr}\right)^q dc_{ds}\, dc_{jsr},$$

we have yet to find a moment closure method that works well in the bivariate case. This would be an important further development of the moment closure approach as a computationally efficient alternative to Monte Carlo simulations of the local control of EC coupling in cardiac myocytes.

4.6 Appendices

4.6.1 Whole cell model of EC coupling: fluxes and volume ratios

The whole cell model of EC coupling that is the focus of this paper includes several fluxes that directly influence the dynamics of the bulk myoplasmic and network SR [Ca^{2+}]. For example, the Na$^+$-Ca^{2+} exchanger current that appears in Eqs. 4.1 and 4.2

identical in the Monte Carlo, probability density, and moment closure formulations and takes the form $J_{ncx} = -A_m I_{ncx}/F$ where [Jafri et al., 1998a, Luo and Rudy, 1994, Rice et al., 2000]

$$I_{ncx} = I_{ncx}^o \frac{[\text{Na}^+]_{myo}^3 c_{ext} e^{\eta_{ncx} FV/RT} - [\text{Na}^+]_{ext}^3 c_{myo} e^{(\eta_{ncx}-1)FV/RT}}{\left(K_{ncx,n}^3 + [\text{Na}^+]_{ext}^3\right)\left(K_{ncx,c} + c_{ext}\right)\left(1 + k_{ncx}^{sat} e^{(\eta_{ncx}-1)FV/RT}\right)},$$

$A_m = C_m \beta_{myo}/V_{myo}$, c_{ext} is the extracellular Ca^{2+} concentration, and $[\text{Na}^+]_{myo}$ and $[\text{Na}^+]_{ext}$ are the intracellular and extracellular sodium concentrations, respectively (for parameters see [Williams et al., 2007]). The SERCA-type Ca-ATPase flux that appears in Eqs. 4.1 and 4.2 includes both forward and reverse modes [Shannon et al., 2000] and is given by

$$J_{serca} = v_{serca} \frac{(c_{myo}/K_{fs})^{\eta_{fs}} - (c_{nsr}/K_{rs})^{\eta_{rs}}}{1 + (c_{myo}/K_{fs})^{\eta_{fs}} + (c_{nsr}/K_{rs})^{\eta_{rs}}}$$

with parameters as in [Williams et al., 2007]. In addition, Eqs. 4.1 and 4.2 include a leakage Ca^{2+} flux given by

$$J_{leak} = v_{leak}(c_{nsr} - c_{myo}).$$

Following [Rice et al., 2000], Eq. 4.1 includes a constant background Ca^{2+} influx that takes the form $J_{in} = -A_m I_{in}/zF$ where $I_{in} = g_{in}(V - E_{Ca})$ and $E_{Ca} = (RT/2F)\ln(c_{ext}/c_{myo})$.

The effective volume ratios λ_{nsr} and λ_{jsr} that appear in Eqs. 4.2 and 4.3 are defined with respect to the physical volume (V_{myo}) and include a constant-fraction Ca^{2+} buffer capacity for the myoplasm (β_{myo}). For example, the effective volume ratio associated with the network SR is

$$\lambda_{nsr} = \frac{\hat{V}_{nsr}}{\hat{V}_{myo}} = \frac{V_{nsr}/\beta_{nsr}}{V_{myo}/\beta_{myo}}$$

with effective volumes defined by $\hat{V}_{nsr} = V_{nsr}/\beta_{nsr}$ and $\hat{V}_{myo} = V_{myo}/\beta_{myo}$. Because each individual junctional SR compartments is assumed to have the same physical volume (V_{jsr}) and buffering capacity (β_{jsr}), the effective volume ratio that occurs in Eq. 4.3 is

$$\lambda_{jsr} = \frac{\hat{V}_{jsr}}{\hat{V}_{myo}} = \frac{V_{jsr}/\beta_{jsr}}{V_{myo}/\beta_{myo}} = \frac{1}{N}\left(\frac{V_{jsr}^T/\beta_{jsr}}{V_{myo}/\beta_{myo}}\right) \tag{4.1}$$

where the second expression defines λ_{jsr} in terms of the total physical volume of all the junctional SR compartments in aggregate $(V_{jsr}^T = NV_{jsr})$. Similar assumptions and equations apply for the diadic subspaces so that the definition of λ_{ds} follows Eq. 4.1. However, when rapid equilibration of diadic subspace $[Ca^{2+}]$ is assumed, the volume ratio λ_{ds} no longer influences the steady state (see Eqs. 4.8–4.11 and Eqs. 4.21–4.23).

In the Monte Carlo model the trigger Ca^{2+} flux into each of the N diadic spaces through DHPR channels (J_{dhpr}^n in Eq. 4.8) is given by

$$J_{dhpr}^n = -\frac{A_m}{zF}I_{dhpr}^n \tag{4.2}$$

where $A_m = C_m\beta_{myo}/V_{myo}$. The inward Ca^{2+} current ($I_{dhpr}^n \le 0$) is given by

$$I_{dhpr}^n = \gamma_{dhpr}^n \frac{P_{dhpr}^T}{N}\left(\frac{zFV}{V_\theta}\right)\left(\frac{\bar{c}_{ds}^n e^{V/V_\theta} - c_{ext}}{e^{V/V_\theta} - 1}\right) \tag{4.3}$$

where $V_\theta = RT/zF$, P_{dhpr}^T is the total (whole cell) permeability of the L-type Ca^{2+} channels, and γ_{dhpr}^n is a random variable that is 0 when the L-type Ca^{2+} channel associated with the nth CaRU is closed and 1 when this channel is open. Thus, the quantities $J_{dhpr}^0 = J_{dhpr}^{T,0}/N$ and $J_{dhpr}^1 = J_{dhpr}^{T,1}/N$ required to evaluate $\bar{c}_{ds,0}^n$ (Eq. 4.10) and $\bar{c}_{ds,1}^n$ (Eq. 4.11) are defined through

$$J_{dhpr}^{T,0} = \frac{A_m P_{dhpr}^T V}{V_\theta}\left(\frac{c_{ext}}{e^{V/V_\theta} - 1}\right)$$

$$J_{dhpr}^{T,1} = \frac{A_m P_{dhpr}^T V}{V_\theta}\left(\frac{e^{V/V_\theta}}{1 - e^{V/V_\theta}}\right),$$

consistent with Eq. 4.12. In the univariate probability density approach and moment closure method the total flux through L-type Ca^{2+} channels is given by

$$J_{dhpr}^{T} = -A_m P_{dhpr}^{T} \frac{V}{V_\theta} \left(\frac{\bar{c}_{ds}^{n} e^{V/V_\theta} - c_{ext}}{e^{V/V_\theta} - 1} \right) \qquad (4.4)$$

and the quantities $J_{dhpr}^{T,0}$ and $J_{dhpr}^{T,1}$ are used to evaluate $\bar{c}_{ds,0}^{i}$ (Eq. 4.22) and $\bar{c}_{ds,1}^{i}$ (Eq. 4.23).

Chapter 5

Summary of results

Considerable insight into intracellular Ca^{2+} responses has been obtained through the development of whole cell models that are based on molecular mechanisms, e.g., the kinetics of intracellular Ca^{2+} channels and the feedback of Ca^{2+} upon these channels. However, a limitation of most deterministic whole cell models to date is the assumption that channels are globally coupled by a single $[Ca^{2+}]$, when in fact channels experience individual "domain" Ca^{2+} concentrations. More realistic stochastic Monte Carlo simulations are capable of representing individual domain Ca^{2+} concentrations but suffer from increased computational demand. This dissertation introduced an alternative approach where local Ca^{2+} concentrations are represented by either univariate or bivariate probability densities. The probability density approach was shown to capture important aspects of local Ca^{2+} signaling while improving computational efficiency.

In Chapter 2 we validated and benchmarked a probability density model for modeling calcium release in cells with diffusely distributed IP_3Rs. While others have presented simulations of one or more Ca^{2+} channels stochastically gating under the influence of a time-dependent or time-independent Ca^{2+} domain [Sherman et al., 1990b, Mazzanti et al., 1991], the whole cell model of local and global Ca^{2+} responses

presented here includes $2N+2$ compartments and $N=100{,}000$ diffusely distributed IP$_3$Rs, each represented by a four-state Markov chain. Two of these compartments correspond to bulk cytosolic and luminal [Ca^{2+}], and the remaining $2N$ compartments represent time-dependent cytosolic and luminal Ca^{2+} domains associated with each IP$_3$R. This formulation is significantly more complex and realistic than traditional whole cell models that assume IP$_3$Rs are globally coupled by a continuously stirred bulk cytosolic [Ca^{2+}], and thereby neglect the influence of local Ca^{2+} signaling on channel dynamics.

Using this $2N+2$-compartment Monte Carlo model as a starting point, we created a probability density formulation that solves a system of advection-reaction equations for the distribution of cytosolic and luminal domain Ca^{2+} concentrations jointly distributed with IP$_3$R state. These advection-reaction equations were coupled to ODEs for the bulk cytosolic and luminal [Ca^{2+}] to create a realistic but minimal model of whole cell Ca^{2+} dynamics that accounts for the influence of local Ca^{2+} signaling on channel gating and global Ca^{2+} responses. This probability density approach was then validated by comparison with Monte Carlo simulations when the number of channels was large. The probability density calculation was more computationally efficient than the corresponding Monte Carlo simulation when $N > 1000$.

In Section 2.4.4 the probability density approach was used to demonstrate how the time scale of Ca^{2+} domain formation and collapse (both cytosolic and luminal) may influence the amplitude, frequency, and existence of global Ca^{2+} oscillations. While prior work has investigated how residual Ca^{2+} from previous channel openings [Mazzag et al., 2005b] and luminal depletion [Huertas and Smith, 2007a] can influence the stochastic gating of Ca^{2+}-regulated channels, Fig. 2.7 demonstrates that the time constants for cytosolic domain collapse (v_{cyt}) and luminal domain refilling (v_{er}) can influence the stochastic gating of IP$_3$Rs and have dramatic consequences on the dynamics of bulk cytosolic and luminal [Ca^{2+}].

In cardiac myocytes, localized Ca^{2+} influx via L-type Ca^{2+} channels triggers the release of large amounts of intracellular Ca^{2+} mediated by clusters of RyRs, a process known as Ca^{2+}-induced Ca^{2+} release (CICR). In Chapter 3 we validated and benchmarked a novel probability density approach to modeling CICR in cardiac myocytes. To illustrate the approach we have focused on a minimal whole cell model of cardiac EC coupling that includes a four-state CaRU including voltage-dependent activation of an L-type Ca^{2+} channel and calcium-dependent activation of an RyR cluster that includes influence from both diadic subspace and junctional SR Ca^{2+}. However, it is important to note that the probability density formulation does not require a minimal Ca^{2+} release unit model; in fact, the approach is fully generalizable to CaRUs with an arbitrary number of states.

The probability density approach to modeling local control of Ca^{2+} release was validated against traditional Monte Carlo simulations with a physiologically realistic number of CaRUs. In simulated voltage-clamp protocols, the univariate probability density formulation of our whole cell model of cardiac EC coupling produced high-gain Ca^{2+} release that was graded to the Ca^{2+}influx. Indeed, the voltage-dependence of trigger Ca^{2+} influx via L-type Ca^{2+} channels, the resulting Ca^{2+} release via RyR clusters, and the observed EC coupling gain obtained using the univariate probability density formulation are nearly identical to that seen in corresponding Monte Carlo calculations. This agreement validates the conceptually novel aspects of the probability density formulation as well as our implementation of both approaches.

While the probability density and Monte Carlo calculations are essentially equivalent in terms of the dynamic cellular responses they predict, the probability density approach can be significantly faster than Monte Carlo simulation. When both methods are applied using the same time step, our current implementation of the univariate probability density approach is approximately 35 times faster than Monte Carlo simulations that employ a physiologically realistic number of CaRUs. Intriguingly, when

this comparison is made using time steps that are distinct and as large as possible while ensuring numerical stability and accuracy of each calculation, we find that the univariate probability density approach can be up to 650 times faster than the corresponding Monte Carlo simulations. This suggests that the probability density approach could be further investigated and developed as a computationally efficient alternative to Monte Carlo simulations of the local control of EC coupling in cardiac myocytes.

Expanding upon the computational advantages of the probability density approaches presented in Chapters 2 and 3 we introduced a moment closure technique in Chapter 4 for simulating whole cell models of cardiac myocytes when the dynamics of subspace [Ca^{2+}] are much faster than those of junctional SR [Ca^{2+}]. The moment closure technique presented in this manuscript most notably resulted in simulations that were nearly 10,000 times faster than Monte Carlo while leading to nearly identical results. While the CaRU model used here to introduce and validate the moment closure approach includes a two-state DHPR model and a six-state RyR megachannel, the success of the moment closure technique does not depend on the CaRU model; rather, any CaRU that takes the form of Eq. 4.17 could be employed. Future work could involve using a more realistic DHPR model that includes voltage and Ca^{2+}-dependent inactivation allowing the addition of action potentials modeled using Hodgkin-Huxley-style membrane currents. Similarly, a more realistic CaRU model could be constructed as the composition of multiple RyR single channel models. This approach will therefore allow for the development of mechanistic local control models that can examine phenomena such as stochastic SR calcium leak and bidirectional interactions between calcium transients and action potential morphology.

However, to maintain the computational advantage of the moment closure approach it is important to consider the state-space explosion that inevitably occurs in compositional models. For example, using one 12-state L-type channel and ten

4-state RyRs leads to a CaRU model with $M = 3432$ distinguishable states. In general, however, the computational demands of the Monte Carlo, probability density and moment closure approaches can be "roughly" estimated in advance. Recall that N represents the number of CaRUs, M indicates the number of CaRU states, and L is the length of mesh required to resolve the Ca^{2+} densities. Using this notation the Monte Carlo, probability density, and moment closure approaches require $2N$, ML or ML^2 (univariate vs bivariate densities), and $3M$ worth of computational effort, respectively. From this estimation one can see that using a CaRU with a large number of states (more that 1,000) would diminish the advantages of the moment closure or probability density techniques over the traditional Monte Carlo approach. For this reason, future work could also involve investigations into different methods to reduce the state space of CaRUs created from multiple RyR single channel models.

Afterword

Much of the material in this dissertation has been submitted for publication in peer reviewed journals. Chapter 2 entitled "Modeling local and global intracellular calcium responses mediated by diffusely distributed inositol 1,4,5-trisphosphate receptors" was accepted for publication in the Journal of Theoretical Biology. Chapter 3 entitled "A probability density approach to modeling local control of calcium-induced calcium release in cardiac myocytes" was accepted for publication in Biophysical Journal. Finally, Chapter 4 entitled "Moment closure for local control models of calcium-induced calcium release in cardiac myocytes" has been submitted to Biophysical Journal and is currently under review.

Bibliography

[Allbritton et al., 1992] Allbritton, N. L., Meyer, T., and Stryer, L. (1992). Range of messenger action of calcium ion and inositol 1,4,5-trisphosphate. *Science*, 258(5089):1812–5.

[Berridge, 1997a] Berridge, M. (1997a). Elementary and global aspects of Ca^{2+} signalling. *J Physiol (London)*, 499(Pt 2):291–306.

[Berridge, 1993] Berridge, M. J. (1993). Inositol trisphosphate and calcium signalling. *Nature*, 361(6410):315–25.

[Berridge, 1997b] Berridge, M. J. (1997b). Elementary and global aspects of calcium signalling. *J Physiol*, 499 (Pt 2):291–306.

[Berridge, 1998] Berridge, M. J. (1998). Neuronal calcium signaling. *Neuron*, 21(1):13–26.

[Berridge et al., 2003] Berridge, M. J., Bootman, M. D., and Roderick, H. L. (2003). Calcium signalling: dynamics, homeostasis and remodelling. *Nat. Rev. Mol. Cell Biol.*, 4(7):517–29.

[Berridge et al., 2000] Berridge, M. J., Lipp, P., and Bootman, M. D. (2000). The versatility and universality of calcium signalling. *Nat. Rev. Mol. Cell Biol.*, 1(1):11–21.

[Bers, 2002] Bers, D. (2002). Cardiac excitation-contraction coupling. *Nature*, 415(6868):198–205.

[Bers and Stiffel, 1993] Bers, D. and Stiffel, V. (1993). Ratio of ryanodine to dihydropyridine receptors in cardiac and skeletal muscle and implications for E-C coupling. *Am J Physiol*, 264(6 Pt 1):C1587–93.

[Bertram and Sherman, 1998] Bertram, R. and Sherman, A. (1998). Population dynamics of synaptic release sites. *SIAM J Appl Math*, 58(1):142–69.

[Bertram et al., 1999] Bertram, R., Smith, G., and Sherman, A. (1999). Modeling study of the effects of overlapping Ca^{2+} microdomains on neurotransmitter release. *Biophys J*, 76(2):735–50.

[Bezprozvanny, 2005] Bezprozvanny, I. (2005). The inositol 1,4,5-trisphosphate receptors. *Cell Calcium*, 38(3-4):261–72.

[Bezprozvanny and Ehrlich, 1994] Bezprozvanny, I. and Ehrlich, B. E. (1994). Inositol (1,4,5)-trisphosphate (IP_3)-gated ca channels from cerebellum: conduction properties for divalent cations and regulation by intraluminal calcium. *J. Gen. Physiol.*, 104(5):821–56.

[Bondarenko et al., 2004] Bondarenko, V., Bett, G., and Rasmusson, R. (2004). A model of graded calcium release and L-type Ca^{2+} channel inactivation in cardiac muscle. *Am J Physiol Heart Circ Physiol*, 286(3):H1154–69.

[Bootman et al., 1997] Bootman, M., Berridge, M., and Lipp, P. (1997). Cooking with Ca^{2+}: the recipes for composing global signals from elementary events. *Cell*, 91(3):367–73.

[Brochet et al., 2005] Brochet, D., Yang, D., Maio, A. D., Lederer, W., Franzini-Armstrong, C., and Cheng, H. (2005). Ca^{2+} blinks: rapid nanoscopic store calcium signaling. *Proc Natl Acad Sci U S A*, 102(8):3099–104.

[Burgoyne and Morgan, 1998] Burgoyne, R. D. and Morgan, A. (1998). Calcium sensors in regulated exocytosis. *Cell Calcium*, 24(5-6):367–76.

[Cannell et al., 1995a] Cannell, M., Cheng, H., and Lederer, W. (1995a). The control of calcium release in heart muscle. *Science*, 268(5213):1045–1049.

[Cannell et al., 1995b] Cannell, M., Cheng, H., and Lederer, W. (1995b). The control of calcium release in heart muscle. *Science*, 268(5213):1045–9.

[Cannell et al., 1995c] Cannell, M. B., Cheng, H., and Lederer, W. J. (1995c). The control of calcium release in heart muscle. *Science*, 268(5213):1045–9.

[Casti et al., 2002] Casti, A., Omurtag, A., Sornborger, A., Kaplan, E., Knight, B., Victor, J., and Sirovich, L. (2002). A population study of integrate-and-fire-or-burst neurons. *Neural Comput*, 14(5):957–86.

[Chelu and Wehrens, 2007] Chelu, M. G. and Wehrens, X. H. T. (2007). Sarcoplasmic reticulum calcium leak and cardiac arrhythmias. *Biochem. Soc. Trans.*, 35(Pt 5):952–6.

[Chen-Izu et al., 2006] Chen-Izu, Y., McCulle, S., Ward, C., Soeller, C., Allen, B., Rabang, C., Cannell, M., Balke, C., and Izu, L. (2006). Three-dimensional distribution of ryanodine receptor clusters in cardiac myocytes. *Biophys J*, 91(1):1–13.

[Cheng et al., 1996] Cheng, H., Lederer, M., Lederer, W., and Cannell, M. (1996). Ca^{2+} sparks and $[Ca^{2+}]$ waves in cardiac myocytes. *Am J Physiol*, 270(1 Pt 1):C148–59.

[Cheng et al., 1993a] Cheng, H., Lederer, W., and Cannell, M. (1993a). Ca^{2+} sparks: elementary events underlying excitation-contraction coupling in heart muscle. *Science*, 262(5134):740–4.

[Cheng et al., 1993b] Cheng, H., Lederer, W., and Cannell, M. (1993b). Calcium sparks: elementary events underlying excitation-contraction coupling in heart muscle. *Science*, 262(5134):740–4.

[Cheng et al., 1993c] Cheng, H., Lederer, W. J., and Cannell, M. B. (1993c). Calcium sparks: elementary events underlying excitation-contraction coupling in heart muscle. *Science*, 262(5134):740–4.

[Cleemann et al., 1998] Cleemann, L., Wang, W., and Morad, M. (1998). Two-dimensional confocal images of organization, density, and gating of focal Ca^{2+} release sites in rat cardiac myocytes. *Proc Natl Acad Sci U S A*, 95(18):10984–9.

[Colquhoun and Hawkes, 1995] Colquhoun, D. and Hawkes, A. (1995). A Q-matrix cookbook: how to write only one program to calculate the sigle-channel and macroscopic predictions for any kinetic mechanism. In Sakmann, B. and Neher, E., editors, *Single-Channel Recording*, pages 589–633. Plenum Press, New York.

[Colquhoun, 1995] Colquhoun, H. (1995). *Single-Channel Recording*, pages 589–633. Plenum Press.

[Dibb et al., 2007] Dibb, K. M., Graham, H. K., Venetucci, L. A., Eisner, D. A., and Trafford, A. W. (2007). Analysis of cellular calcium fluxes in cardiac muscle to understand calcium homeostasis in the heart. *Cell Calcium*, 42(4-5):503–12.

[DiFrancesco and Noble, 1985] DiFrancesco, D. and Noble, D. (1985). A model of cardiac electrical activity incorporating ionic pumps and concentration changes. *Philos Trans R Soc Lond B Biol Sci*, 307(1133):353–98.

190

[Dolmetsch et al., 1997] Dolmetsch, R. E., Lewis, R. S., Goodnow, C. C., and Healy, J. I. (1997). Differential activation of transcription factors induced by Ca^{2+} response amplitude and duration. *Nature*, 386(6627):855–8.

[Dupont et al., 1991a] Dupont, G., Berridge, M., and Goldbeter, A. (1991a). Signal-induced Ca^{2+} oscillations: properties of a model based on Ca^{2+}-induced Ca^{2+} release. *Cell Calcium*, 12(2–3):73–85.

[Dupont et al., 1991b] Dupont, G., Berridge, M. J., and Goldbeter, A. (1991b). Signal-induced Ca^{2+} oscillations: properties of a model based on Ca^{2+}-induced Ca^{2+} release. *Cell Calcium*, 12(2-3):73–85.

[Dupont and Goldbeter, 1992a] Dupont, G. and Goldbeter, A. (1992a). Oscillations and waves of cytosolic Ca^{2+}: insights from theoretical models. *Bioessays*, 14(7):485–93.

[Dupont and Goldbeter, 1992b] Dupont, G. and Goldbeter, A. (1992b). Oscillations and waves of cytosolic calcium: insights from theoretical models. *Bioessays*, 14(7):485–93.

[Dupont and Goldbeter, 1994] Dupont, G. and Goldbeter, A. (1994). Properties of intracellular Ca^{2+} waves generated by a model based on Ca^{2+}-induced Ca^{2+} release. *Biophys J*, 67(6):2191–204.

[Fabiato, 1985a] Fabiato, A. (1985a). Time and calcium dependence of activation and inactivation of calcium-induced release of calcium from the sarcoplasmic reticulum of a skinned canine cardiac purkinje cell. *J Gen Physiol*, 85(2):247–89.

[Fabiato, 1985b] Fabiato, A. (1985b). Time and calcium dependence of activation and inactivation of calcium-induced release of calcium from the sarcoplasmic reticulum of a skinned canine cardiac purkinje cell. *J. Gen. Physiol.*, 85(2):247–89.

[Falcke, 2003a] Falcke, M. (2003a). Buffers and oscillations in intracellular Ca^{2+} dynamics. *Biophys J*, 84(1):28–41.

[Falcke, 2003b] Falcke, M. (2003b). On the role of stochastic channel behavior in intracellular Ca^{2+} dynamics. *Biophys J*, 84(1):42–56.

[Fernández-Chacón et al., 2001] Fernández-Chacón, R., Königstorfer, A., Gerber, S. H., García, J., Matos, M. F., Stevens, C. F., Brose, N., Rizo, J., Rosenmund, C., and Südhof, T. C. (2001). Synaptotagmin I functions as a calcium regulator of release probability. *Nature*, 410(6824):41–9.

[Fill and Copello, 2002] Fill, M. and Copello, J. A. (2002). Ryanodine receptor calcium release channels. *Physiol Rev*, 82(4):893–922.

[Foskett et al., 2007a] Foskett, J., White, C., Cheung, K., and Mak, D. (2007a). Inositol Trisphosphate Receptor Ca^{2+} Release Channels. *Physiological Reviews*.

[Foskett et al., 2007b] Foskett, J. K., White, C., Cheung, K.-H., and Mak, D.-O. D. (2007b). Inositol trisphosphate receptor Ca^{2+} release channels. *Physiol Rev*, 87(2):593–658.

[Franzini-Armstrong, 1999] Franzini-Armstrong, C. (1999). The sarcoplasmic reticulum and the control of muscle contraction. *FASEB J*, 13 Suppl 2:S266–70.

[Franzini-Armstrong et al., 1999] Franzini-Armstrong, C., Protasi, F., and Ramesh, V. (1999). Shape, size, and distribution of Ca^{2+} release units and couplons in skeletal and cardiac muscles. *Biophys J*, 77(3):1528–1539.

[Gardiner, 2004] Gardiner, C. (2004). *Handbook of stochastic methods for physics, chemistry, and the natural sciences.* Springer, Berlin, 3rd edition.

[Glukhovsky et al., 1998a] Glukhovsky, A., Adam, D., Amitzur, G., and Sideman, S. (1998a). Mechanism of Ca^{2+} release from the sarcoplasmic reticulum: a computer model. *Ann Biomed Eng*, 26(2):213–29.

[Glukhovsky et al., 1998b] Glukhovsky, A., Adam, D. R., Amitzur, G., and Sideman, S. (1998b). Mechanism of Ca^{2+} release from the sarcoplasmic reticulum: a computer model. *Annals of biomedical engineering*, 26(2):213–29.

[Greenstein et al., 2006] Greenstein, J., Hinch, R., and Winslow, R. (2006). Mechanisms of excitation-contraction coupling in an integrative model of the cardiac ventricular myocyte. *Biophys J*, 90(1):77–91.

[Greenstein and Winslow, 2002a] Greenstein, J. and Winslow, R. (2002a). An integrative model of the cardiac ventricular myocyte incorporating local control of Ca^{2+} release. *Biophys J*, 83(6):2918–45.

[Greenstein and Winslow, 2002b] Greenstein, J. L. and Winslow, R. L. (2002b). An integrative model of the cardiac ventricular myocyte incorporating local control of Ca^{2+} release. *Biophys. J.*, 83(6):2918–45.

[Haak et al., 2001] Haak, L., Song, L., Molinski, T., Pessah, I., Cheng, H., and Russell, J. (2001). Sparks and puffs in oligodendrocyte progenitors: cross talk between ryanodine receptors and inositol trisphosphate receptors. *J Neurosci*, 21(11):3860–70.

[Hajnóczky et al., 1995] Hajnóczky, G., Robb-Gaspers, L. D., Seitz, M. B., and Thomas, A. P. (1995). Decoding of cytosolic calcium oscillations in the mitochondria. *Cell*, 82(3):415–24.

[Hilgemann and Noble, 1987] Hilgemann, D. and Noble, D. (1987). Excitation-contraction coupling and extracellular calcium transients in rabbit atrium: recon-

struction of basic cellular mechanisms. *Proc R Soc Lond B Biol Sci*, 230(1259):163–205.

[Hille, 2001] Hille, B. (2001). *Ionic Channels of Excitable Membranes, 3rd edition.* Sinauer Associates, Sunderland, MA.

[Hinch, 2004] Hinch, R. (2004). A mathematical analysis of the generation and termination of calcium sparks. *Biophys J*, 86(3):1293–307.

[Huertas and Smith, 2006a] Huertas, M. and Smith, G. (2006a). The effect of luminal depletion on the dynamics of Ca^{2+}-regulated Ca^{2+} channels. *Biophysical Society Annual Meeting*, 1078-Pos.

[Huertas and Smith, 2006b] Huertas, M. and Smith, G. (2006b). A multivariate population density model of the dLGN/PGN relay. *J Comput Neurosci*, 21(2):171–89.

[Huertas and Smith, 2007a] Huertas, M. and Smith, G. (2007a). The dynamics of luminal depletion and the stochastic gating of Ca^{2+}-activated Ca^{2+} channels and release sites. *J. Theor. Biol.*

[Huertas and Smith, 2007b] Huertas, M. and Smith, G. (2007b). The dynamics of luminal depletion and the stochastic gating of Ca^{2+}-activated Ca^{2+} channels and release sites. *J. Theor. Biol.*, 246(2):332–54.

[Hundsdorfer and Verwer, 2003] Hundsdorfer, W. and Verwer, J. (2003). *Numerical solution of time-dependent advection-diffusion-reaction equations.* Springer.

[Jafri et al., 1998a] Jafri, M., Rice, J., and Winslow, R. (1998a). Cardiac Ca^{2+} dynamics: the roles of ryanodine receptor adaptation and sarcoplasmic reticulum load. *Biophys J*, 74(3):1149–68.

[Jafri et al., 1998b] Jafri, M. S., Rice, J. J., and Winslow, R. L. (1998b). Cardiac Ca^{2+} dynamics: the roles of ryanodine receptor adaptation and sarcoplasmic reticulum load. *Biophys. J.*, 74(3):1149–68.

[Jiang et al., 2007] Jiang, D., Chen, W., Wang, R., Zhang, L., and Chen, S. R. W. (2007). Loss of luminal Ca^{2+} activation in the cardiac ryanodine receptor is associated with ventricular fibrillation and sudden death. *Proc Natl Acad Sci USA*, 104(46):18309–14.

[Keizer et al., 1995] Keizer, J., Li, Y. X., Stojilković, S., and Rinzel, J. (1995). IP_3-induced Ca^{2+} excitability of the endoplasmic reticulum. *Mol Biol Cell*, 6(8):945–51.

[Kepler and Elston, 2001] Kepler, T. B. and Elston, T. C. (2001). Stochasticity in transcriptional regulation: origins, consequences, and mathematical representations. *Biophys. J.*, 81(6):3116–36.

[Kirichok et al., 2004] Kirichok, Y., Krapivinsky, G., and Clapham, D. E. (2004). The mitochondrial calcium uniporter is a highly selective ion channel. *Nature*, 427(6972):360–4.

[Lai et al., 1989] Lai, F. A., Misra, M., Xu, L., Smith, H. A., and Meissner, G. (1989). The ryanodine receptor-Ca^{2+} release channel complex of skeletal muscle sarcoplasmic reticulum. Evidence for a cooperatively coupled, negatively charged homotetramer. *J Biol Chem*, 264(28):16776–85.

[Li et al., 1995] Li, Y. X., Keizer, J., Stojilkovi, S. S., and Rinzel, J. (1995). Ca^{2+} excitability of the er membrane: an explanation for ip3-induced Ca^{2+} oscillations. *Am J Physiol*, 269(5 Pt 1):C1079–92.

[Li and Rinzel, 1994] Li, Y. X. and Rinzel, J. (1994). Equations for IP_3 receptor-mediated $[Ca^{2+}]i$ oscillations derived from a detailed kinetic model: a hodgkin-huxley like formalism. *J. Theor. Biol.*, 166(4):461–73.

[Luo and Rudy, 1994] Luo, C. and Rudy, Y. (1994). A dynamic model of the cardiac ventricular action potential. II. Afterdepolarizations, triggered activity, and potentiation. *Circ Res*, 74(6):1097–113.

[Mak and Foskett, 1997] Mak, D. and Foskett, J. (1997). Single-channel kinetics, inactivation, and spatial distribution of inositol trisphosphate (IP$_3$) receptors in Xenopus oocyte nucleus. *J Gen Physiol*, 109(5):571–87.

[Mazzag et al., 2005a] Mazzag, B., Tignanelli, C., and Smith, G. (2005a). The effect of residual Ca^{2+} on the stochastic gating of Ca^{2+}-regulated Ca^{2+} channel models. *J Theor Biol*, 235(1):121–50.

[Mazzag et al., 2005b] Mazzag, B., Tignanelli, C., and Smith, G. (2005b). The effect of residual Ca^{2+} on the stochastic gating of Ca^{2+}-regulated Ca^{2+} channel models. *Journal of theoretical biology*, 235:121–50.

[Mazzanti et al., 1991] Mazzanti, M., DeFelice, L., and Liu, Y. (1991). Gating of L-type Ca^{2+} channels in embryonic chick ventricle cells: dependence on voltage, current and channel density. *J Physiol*, 443:307–34.

[Means et al., 2006] Means, S., Smith, A. J., Shepherd, J., Shadid, J., Fowler, J., Wojcikiewicz, R. J. H., Mazel, T., Smith, G. D., and Wilson, B. S. (2006). Reaction diffusion modeling of calcium dynamics with realistic er geometry. *Biophys. J.*, 91(2):537–57.

[Murayama and Ogawa, 1996] Murayama, T. and Ogawa, Y. (1996). Properties of Ryr3 ryanodine receptor isoform in mammalian brain. *J Biol Chem*, 271(9):5079–84.

[Naraghi and Neher, 1997] Naraghi, M. and Neher, E. (1997). Linearized buffered Ca^{2+} diffusion in microdomains and its implications for calculation of [Ca^{2+}] at the mouth of a calcium channel. *J Neurosci*, 17(18):6961–73.

[Neher, 1986] Neher, E. (1986). Concentration profiles of intracellular Ca^{2+} in the presence of diffusible chelator. *Exp Brain Res*, 14:80–96.

[Neher, 1998a] Neher, E. (1998a). Usefulness and limitations of linear approximations to the understanding of Ca^{2+} signals. *Cell Calcium*, 24(5-6):345–57.

[Neher, 1998b] Neher, E. (1998b). Vesicle pools and Ca^{2+} microdomains: new tools for understanding their roles in neurotransmitter release. *Neuron*, 20(3):389–99.

[Nguyen and Jafri, 2005] Nguyen, M.-H. T. and Jafri, M. S. (2005). Mitochondrial calcium signaling and energy metabolism. *Ann N Y Acad Sci*, 1047:127–37.

[Nguyen et al., 2005] Nguyen, V., Mathias, R., and Smith, G. D. (2005). A stochastic automata network descriptor for markov chain models of instantaneously coupled intracellular Ca^{2+} channels. *Bull. Math. Biol.*, 67(3):393–432.

[Niggli, 1999] Niggli, E. (1999). Localized intracellular Ca^{2+} signaling in muscle: Ca^{2+} sparks and Ca^{2+} quarks. *Annu Rev Physiol*, 61:311–35.

[Nordin, 1993a] Nordin, C. (1993a). Computer model of membrane current and intracellular Ca^{2+} flux in the isolated guinea pig ventricular myocyte. *Am J Physiol*, 265(6 Pt 2):H2117–36.

[Nordin, 1993b] Nordin, C. (1993b). Computer model of membrane current and intracellular Ca^{2+} flux in the isolated guinea pig ventricular myocyte. *Am. J. Physiol.*, 265(6 Pt 2):H2117–36.

[Nykamp and Tranchina, 2000] Nykamp, D. and Tranchina, D. (2000). A population density approach that facilitates large-scale modeling of neural networks: analysis and an application to orientation tuning. *J Comput Neurosci*, 8(1):19–50.

[Parker et al., 1996] Parker, I., Choi, J., and Yao, Y. (1996). Elementary events of IP$_3$-induced Ca^{2+} liberation in Xenopus oocytes: hot spots, puffs and blips. *Cell Calcium*, 20(2):105–21.

[Rice et al., 1999a] Rice, J., Jafri, M., and Winslow, R. (1999a). Modeling gain and gradedness of Ca^{2+} release in the functional unit of the cardiac diadic space. *Biophys J*, 77(4):1871–84.

[Rice et al., 2000] Rice, J., Jafri, M., and Winslow, R. (2000). Modeling short-term interval-force relations in cardiac muscle. *Am J Physiol Heart Circ Physiol*, 278(3):H913–31.

[Rice et al., 1999b] Rice, J. J., Jafri, M. S., and Winslow, R. L. (1999b). Modeling gain and gradedness of Ca^{2+} release in the functional unit of the cardiac diadic space. *Biophys. J.*, 77(4):1871–84.

[Rios and Stern, 1997] Rios, E. and Stern, M. (1997). Calcium in close quarters: microdomain feedback in excitation-contraction coupling and other cell biological phenomena. *Annu Rev Biophys Biomol Struct*, 26:47–82.

[Shannon et al., 2000] Shannon, T., Ginsburg, K., and Bers, D. (2000). Reverse mode of the sarcoplasmic reticulum calcium pump and load-dependent cytosolic calcium decline in voltage-clamped cardiac ventricular myocytes. *Biophys J*, 78(1):322–33.

[Sherman et al., 1990a] Sherman, A., Keizer, J., and Rinzel, J. (1990a). Domain model for Ca^{2+}-inactivation of Ca^{2+} channels at low channel density. *Biophys. J.*, 58(4):985–95.

[Sherman et al., 1990b] Sherman, A., Keizer, J., and Rinzel, J. (1990b). Domain model for Ca^{2+}-inactivation of Ca^{2+} channels at low channel density. *Biophys J*, 58(4):985–95.

[Shiferaw et al., 2003] Shiferaw, Y., Watanabe, M., Garfinkel, A., Weiss, J., and Karma, A. (2003). Model of intracellular calcium cycling in ventricular myocytes. *Biophys J*, 85(6):3666–86.

[Shuai and Jung, 2003] Shuai, J. and Jung, P. (2003). Selection of intracellular calcium patterns in a model with clustered Ca^{2+} release channels. *Phys Rev E Stat Nonlin Soft Matter Phys*, 67(3 Pt 1):031905.

[Smith, 2002a] Smith, G. (2002a). An extended DeYoung-Keizer-like IP_3 receptor model that accounts for domain Ca^{2+}-mediated inactivation. In Condat, C. and Baruzzi, A., editors, *Recent Research Developments in Biophysical Chemistry, Vol. II*, pages 37–55. Research Signpost.

[Smith, 2002b] Smith, G. (2002b). Modeling the stochastic gating of ion channels. In Fall, C., Marland, E., Wagner, J., and Tyson, J., editors, *Computational Cell Biology*, pages 291–325. Springer-Verlag.

[Smith et al., 2001] Smith, G., Cox, C., Sherman, S., and Rinzel, J. (2001). A firing-rate model of spike-frequency adaptation in sinusoidally-driven thalamocortical relay neurons. *Thalamus and Related Systems*, 1:135–156.

[Smith et al., 2002] Smith, G., Pearson, J., and Keizer, J. (2002). Modeling intracellular Ca^{2+} waves and sparks. In Fall, C., Marland, E., Wagner, J., and Tyson, J., editors, *Computational Cell Biology*, pages 200–232. Springer-Verlag.

[Smith, 1996] Smith, G. D. (1996). Analytical steady-state solution to the rapid buffering approximation near an open Ca^{2+} channel. *Biophys. J.*, 71(6):3064–72.

[Smith et al., 1998] Smith, G. D., Keizer, J. E., Stern, M. D., Lederer, W. J., and Cheng, H. (1998). A simple numerical model of calcium spark formation and detection in cardiac myocytes. *Biophys. J.*, 75(1):15–32.

[Smith et al., 1996] Smith, G. D., Wagner, J., and Keizer, J. (1996). Validity of the rapid buffering approximation near a point source of calcium ions. *Biophys. J.*, 70(6):2527–39.

[Snyder et al., 2000a] Snyder, S., Palmer, B., and Moore, R. (2000a). A mathematical model of cardiocyte Ca^{2+} dynamics with a novel representation of sarcoplasmic reticular Ca^{2+} control. *Biophys J*, 79(1):94–115.

[Snyder et al., 2000b] Snyder, S. M., Palmer, B. M., and Moore, R. L. (2000b). A mathematical model of cardiocyte Ca^{2+} dynamics with a novel representation of sarcoplasmic reticular Ca^{2+} control. *Biophys. J.*, 79(1):94–115.

[Sobie et al., 2002a] Sobie, E., Dilly, K., dos Santos Cruz, J., Lederer, W., and Jafri, M. (2002a). Termination of cardiac Ca^{2+} sparks: an investigative mathematical model of calcium-induced calcium release. *Biophys J*, 83(1):59–78.

[Sobie et al., 2002b] Sobie, E. A., Dilly, K. W., dos Santos Cruz, J., Lederer, W. J., and Jafri, M. S. (2002b). Termination of cardiac Ca^{2+} sparks: an investigative mathematical model of calcium-induced calcium release. *Biophys. J.*, 83(1):59–78.

[Sobie et al., 2005] Sobie, E. A., Song, L.-S., and Lederer, W. J. (2005). Local recovery of ca2+ release in rat ventricular myocytes. *J Physiol*, 565(Pt 2):441–7.

[Stern, 1992a] Stern, M. (1992a). Theory of excitation-contraction coupling in cardiac muscle. *Biophys J*, 63(2):497–517.

[Stern et al., 1999a] Stern, M., Song, L., Cheng, H., Sham, J., Yang, H., Hoheler, K., and Rios, E. (1999a). Local control models of cardiac excitation-contraction coupling. a possible role for allosteric interactions between ryanodine receptors. *J Gen Physiol*, 113(3):469–89.

[Stern, 1992b] Stern, M. D. (1992b). Theory of excitation-contraction coupling in cardiac muscle. *Biophys. J.*, 63(2):497–517.

[Stern et al., 1999b] Stern, M. D., Song, L. S., Cheng, H., Sham, J. S., Yang, H. T., Boheler, K. R., and Ríos, E. (1999b). Local control models of cardiac excitation-contraction coupling. A possible role for allosteric interactions between ryanodine receptors. *J. Gen. Physiol.*, 113(3):469–89.

[Stern et al., 1999c] Stern, M. D., Song, L. S., Cheng, H., Sham, J. S., Yang, H. T., Boheler, K. R., and Ríos, E. (1999c). Local control models of cardiac excitation-contraction coupling. A possible role for allosteric interactions between ryanodine receptors. *J. Gen. Physiol.*, 113(3):469–89.

[Sun et al., 1998] Sun, X., Callamaras, N., Marchant, J., and Parker, I. (1998). A continuum of IP_3-mediated elementary Ca^{2+} signalling events in Xenopus oocytes. *J Physiol*, 509(Pt 1):67–80.

[Swillens and Champeil, 1998] Swillens, S. and Champeil, P. (1998). Stochastic simulation of a single inositol 1,4,5-trisphosphate-sensitive Ca^{2+} channel reveals repetitive openings during 'blip-like' Ca^{2+}transients. *Cell Calcium*, 23(5):291–302.

[Swillens et al., 1998] Swillens, S., Champeil, P., Combettes, L., and Dupont, G. (1998). Stochastic simulation of a single inositol 1,4,5-trisphosphate-sensitive Ca^{2+} channel reveals repetitive openings during 'blip-like' Ca^{2+} transients. *Cell Calcium*, 23(5):291–302.

[Swillens et al., 1994] Swillens, S., Combettes, L., and Champeil, P. (1994). Transient inositol 1,4,5-trisphosphate-induced Ca^{2+} release: a model based on regulatory Ca^{2+}-binding sites along the permeation pathway. *Proc. Natl. Acad. Sci. U.S.A.*, 91(21):10074–8.

[Swillens and Dupont, 1999] Swillens, S. and Dupont, G. (1999). From calcium blips to calcium puffs: theoretical analysis of the requirements for interchannel communication. *Proc Natl Acad Sci U S A*, 96(24):13750–5.

[Szentesi et al., 2004] Szentesi, P., Pignier, C., Egger, M., Kranias, E., and Niggli, E. (2004). Sarcoplasmic reticulum Ca^{2+} refilling controls recovery from Ca^{2+}-induced Ca^{2+} release refractoriness in heart muscle. *Circ Res*, 95(8):807–13.

[Tang and Othmer, 1994a] Tang, Y. and Othmer, H. (1994a). A model of calcium dynamics in cardiac myocytes based on the kinetics of ryanodine-sensitive calcium channels. *Biophys J*, 67(6):2223–35.

[Tang and Othmer, 1994b] Tang, Y. and Othmer, H. G. (1994b). A model of calcium dynamics in cardiac myocytes based on the kinetics of ryanodine-sensitive calcium channels. *Biophys. J.*, 67(6):2223–35.

[Terentyev et al., 2002a] Terentyev, D., Viatchenko-Karpinski, S., Valdivia, H., Escobar, A., and Gyrke, S. (2002a). Luminal Ca^{2+} controls termination and refractory behavior of Ca^{2+}-induced Ca^{2+} release in cardiac myocytes. *Circ Res*, 91(5):414–20.

[Terentyev et al., 2002b] Terentyev, D., Viatchenko-Karpinski, S., Valdivia, H. H., Escobar, A. L., and Györke, S. (2002b). Luminal Ca^{2+} controls termination and refractory behavior of Ca^{2+}-induced Ca^{2+} release in cardiac myocytes. *Circ Res*, 91(5):414–20.

[Wang et al., 2004] Wang, S., Stern, M., Rios, E., and Cheng, H. (2004). The quantal nature of Ca^{2+} sparks and in situ operation of the ryanodine receptor array in cardiac cells. *Proc Natl Acad Sci U S A*, 101(11):3979–3984.

[Whitaker, 2006] Whitaker, M. (2006). Calcium at fertilization and in early development. *Physiol Rev*, 86(1):25–88.

[Wier et al., 1994a] Wier, W., Egan, T., Lpez-Lpez, J., and Balke, C. (1994a). Local control of excitation-contraction coupling in rat heart cells. *J Physiol*, 474(3):463–71.

[Wier, 1990] Wier, W. G. (1990). Cytoplasmic [Ca^{2+}] in mammalian ventricle: dynamic control by cellular processes. *Annu. Rev. Physiol.*, 52:467–85.

[Wier et al., 1994b] Wier, W. G., Egan, T. M., López-López, J. R., and Balke, C. W. (1994b). Local control of excitation-contraction coupling in rat heart cells. *J Physiol*, 474(3):463–71.

[Williams et al., 2006] Williams, G., Huertas, M., Sobie, E., Jafri, M., and Smith, G. (2006). A probability density model of stochastic functional unit activity in cardiac myocytes. *Biophysical Society Annual Meeting*, 1079-Pos.

[Williams and Smith, 2006] Williams, G. and Smith, G. (2006). A probability density approach to modeling local and global Ca^{2+} dynamics in cells with diffusely distributed intracellular Ca^{2+} channels. In *Biophysical Society Annual Meeting Abstracts, 1077-Pos*, Salt Lake City, UT.

[Williams et al., 2007] Williams, G. S. B., Huertas, M. A., Sobie, E. A., Jafri, M. S., and Smith, G. D. (2007). A probability density approach to modeling local control of calcium-induced calcium release in cardiac myocytes. *Biophys J*, 92(7):2311–28.

[Wilson et al., 1998] Wilson, B., Pfeiffer, J., Smith, A., Oliver, J., Oberdorf, J., and Wojcikiewicz, R. (1998). Ca^{2+}-dependent clustering of inositol 1,4,5-trisphosphate receptors. *Mol Biol Cell*, 9(6):1465–78.

[Wilson et al., 2006] Wilson, L. D., Wan, X., and Rosenbaum, D. S. (2006). Cellular alternans: a mechanism linking calcium cycling proteins to cardiac arrhythmogenesis. *Ann. N. Y. Acad. Sci.*, 1080:216–34.

[Wilson et al., 2002] Wilson, S. M., Mason, H. S., Smith, G. D., Nicholson, N., Johnston, L., Janiak, R., and Hume, J. R. (2002). Comparative capacitative calcium entry mechanisms in canine pulmonary and renal arterial smooth muscle cells. *J Physiol*, 543(Pt 3):917–31.

[Winslow et al., 2000] Winslow, R. L., Scollan, D. F., Holmes, A., Yung, C. K., Zhang, J., and Jafri, M. S. (2000). Electrophysiological modeling of cardiac ventricular function: from cell to organ. *Annual review of biomedical engineering*, 2:119–55.

[Wong et al., 1992] Wong, A., Fabiato, A., and Bassingwaigthe, J. (1992). Model of calcium-induced calcium release in cardiac cells. *Bull. Math. Biol.*, 54:95–116.

[Yao et al., 1995] Yao, Y., Choi, J., and Parker, I. (1995). Quantal puffs of intracellular Ca^{2+} evoked by inositol trisphosphate in Xenopus oocytes. *J Physiol*, 482(Pt 3):533–53.

[Young and Keizer, 1992] Young, G. W. D. and Keizer, J. (1992). A single-pool inositol 1,4,5-trisphosphate-receptor-based model for agonist-stimulated oscillations in Ca^{2+} concentration. *Proc. Natl. Acad. Sci. U.S.A.*, 89(20):9895–9.

[Zador and Koch, 1994] Zador, A. and Koch, C. (1994). Linearized models of calcium dynamics: formal equivalence to the cable equation. *J Neurosci*, 14(8):4705–15.

Vita

George S. B. Williams was born in 1978 in Virginia. In 1997 he graduated from Wilson Memorial High School as co-valedictorian and that fall he began his undergraduate career at the College of William & Mary as a Monroe Scholar. During the summer of 1998 he completed his Monroe Scholar project entitled "Golf: Walk or Ride" that studied the effects of physical exertion on a golfer's score. In May of 2001 he graduated with a Bachelor of Science degree in chemistry. Following graduation he began work towards a Master of Arts degree in chemistry under the guidance of Carey K. Bagdassarian. George successfully defended his Master's thesis entitled "Evolution and analysis of a catalytically effective model enzyme: The importance of active site orientation and tuned conformational fluctuations " in May of 2003. In August of 2003, he began his doctoral work in Applied Science under the guidance of Gregory D. Smith and also served as the systems administrator for the Computational Biology Laboratory.